MASARYK UNIVERSITY
FACULTY OF SCIENCE
UNIVERSITY OF TURIN
FACULTY OF SCIENCE

Ph.D. Thesis

BRNO 2021 **ROMANA GROSSOVÁ**

Masaryk University
Faculty of Science
Department of Theoretical Physics
and Astrophysics

&

University of Turin
Faculty of Science
Physics Department

Multifrequency observations of radio galaxies and their interaction with the intergalactic medium

Ph.D. Thesis

Romana Grossová

Thesis Supervisors:
doc. (Assoc. Prof.) Norbert Werner Ph.D.
Assoc. Prof. Francesco Massaro Ph.D.

Brno 2021

Bibliografický záznam

Autor:	Mgr. Romana Grossová Ústav teoretické fyziky a astrofyziky, Přírodovědecká fakulta, Masarykova univerzita Ústav fyziky, Turínska Univezita

Název práce:	Multifrekvenční pozorování rádiových galaxií a jejich interakce s intergalaktickým médiem
Studijní program:	Fyzika
Studijní obor:	Teoretická fyzika a astrofyzika
Specializace:	Astrofyzika
Vedoucí práce:	doc. (Assoc. Prof.) Norbert Werner, Ph.D. Assoc. Prof. Francesco Massaro, Ph.D.
Akademický rok:	2020/2021
Počet stran:	XI+125
Klíčová slova:	obří eliptické galaxie, radio-mechanický režim AGN zpětné vazby, synchrotronová rádiová emise, jety a laloky, rentgenové atmosféry

Bibliographic Entry

Author:	Mgr. Romana Grossová Department of Theoretical Physics and Astrophysics, Faculty of Science, Masaryk University Physics Department, University of Turin

Title of Thesis:	Multifrequency observations of radio galaxies and their interaction with the intergalactic medium
Degree Programme:	Physics
Field of Study:	Theoretical Physics and Astrophysics
Specialization:	Astrophysics
Supervisors:	doc. (Assoc. Prof.) Norbert Werner, Ph.D. Assoc. Prof. Francesco Massaro, Ph.D.
Academic Year:	2020/2021
Number of Pages:	XI+125
Keywords:	giant elliptical galaxies, radio-mechanical mode of AGN feedback, radio synchrotron emission, jets and lobes, X-ray atmospheres

Abstrakt

Galaxie raného typu, nacházející se v centrálních oblastech skupin galaxií a kup galaxií, jsou největší, nejstarší a nejpodivnější galaktické struktury ve vesmíru. Na jejich vznik a vývoj má zásadní vliv centrální aktivně akreující supermasivní černá díra, nazývaná také aktivní galaktické jádro (active galactic nucleus = AGN). AGN v galaxiích raného typu v rádio-mechanickém režimu zpětné vazby vytvářejí jety ultra-relativistických částic viditelných hlavně na rádiových frekvencích. Jety interagují s okolním horkým rentgenovým plynem a nafukují rentgenové dutiny a tak brání tomu, aby docházelo k ochlazování plynu a formování nových hvězd v centrálních oblastech.

Radio-mechanický režim zpětné vazby byl značně studován v posledních dvou desetiletích, ale podrobnosti o jeho pracovním cyklu a příslušných fyzikálních procesech zůstávají nejasné. Hloubková analýza vícefrekvenčních dat s primárním zaměřením na rádiovou emisi na gigahertzových frekvencích, nám umožňuje zkoumat jety a jejich roli v radio-mechanické zpětné AGN vazbě. Hlavní nezodpovězené otázky jsou: jak tento režim zpětné vazby udržuje rovnováhu mezi zahříváním a chlazením okolního média na různých škálách, čímž udržuje jejich hostitelské galaxie raného typy "rudé a mrtvé"? Jaký je aktuální stav aktivity AGN v objemově omezeném vzorku rentgenových a opticky jasných galaxií? Je AGN zapnutá nepřetržitě a fouká bubliny relativistického plynu do horké atmosféry? Nebo se AGN zapíná a vypíná?

Naše statistická studie je založena především na rádiové emisi ze 42 nejbližších a zároveň rentgenově a opticky nejjasnějších galaxií raného typu, pozorovaných pomocí Very Large Array (VLA) při frekvencích mezi 1–2 GHz na různých škálách a rozlišeních. Abychom mohli studovat vliv rádiových jetů na okolní plyn, zahrnuli jsme analýzu archivních rentgenových dat z dalekohledu *Chandra*.

Analýza ukázala, že rádiová emise, detekována v 41/42 galaxií, je rozsáhlá pro 27/42 zdrojů. 34/42 galaxií ukazuje interakce ve formě rentgenových dutin. 7/14 galaxií s bodovou rádiovou emisí (Fanaroff-Riley Class 0; FR 0) vykazuje rentgenové dutiny. To naznačuje, že navzdory nedostatku rozšířených rádiových struktur na frekvenci 1–2 GHz, tyto AGN vypouštějí jety schopné nafouknout laloky a dutiny. Při zkoumání vztahů mezi rádiovými a rentgenovými nebo optickými vlastnostmi emise z těchto galaxií nenacházíme žádné významně silné korelace. Centrální rádiové spektrální indexy galaxií jsou většinou strmé, pouze 1/3 systémů vykazuje plochá a obrácená spektra.

Touto studií jsme prokázali, že aktivita AGN v rádiovém režimu je rozšířená v masivních galaxiích raného typu, kde jsou AGN v naprosté většině případů v zapnutém stavu a liší se pouze v intenzitě jejich aktivity.

Abstract

Early-type galaxies, located in the central regions of groups and clusters, are among the largest, oldest, and most peculiar structures in the Universe. Their formation and evolution are strongly affected by their central accreting supermassive black holes, so-called active galactic nuclei (AGN). AGN in early-type galaxies operate in radio mechanical mode, producing jets of ultra-relativistic particles mainly visible at radio frequencies. These are interacting with the ambient hot gas and inflating cavities seen in X-ray images. This interaction prevents the gas from cooling and forming new stars in the central regions.

The radio-mechanical feedback mode has been studied extensively in the last two decades, but the details about its duty cycle and relevant physical processes are still missing. The in-depth analysis of multifrequency data, with a primary focus on the radio emission at gigahertz frequencies, allowed us to investigate the jets and their role in the feedback. The main open questions are: how does this feedback mode maintain the balance between heating and cooling of the ambient medium at different scales, thus keeping their host early-type galaxies 'red and dead'? What is the current state of the AGN activity in a volume-limited sample of X-rays and optically bright galaxies? Are these AGN always turned on and blowing bubbles of relativistic plasma into the hot atmosphere continuously? Or are AGN turning on and off?

Our statistical study is mainly based on the radio emission of the 42 nearest and X-ray and optically brightest early-type galaxies observed with Very Large Array (VLA) at frequencies between 1–2 GHz at various spatial scales and resolutions. To study the influence of radio jets on the ambient gas, we included the analysis of archival X-ray observations from *Chandra*.

The analysis shows that the radio emission detected in 41/42 galaxies in our sample, is extended for 27/42 cases. 34/42 galaxies show signatures of interactions featuring X-ray cavities. Then 7/14 galaxies, even if being point-like at radio frequencies (Fanaroff-Riley Class 0; FR 0) have X-ray cavities. This indicates that despite the lack of extended radio structures at 1–2 GHz, these AGN can launch jets capable of inflating lobes and cavities. We find no significant strong correlations between radio, X-rays or optical properties. Finally, the radio spectral indices are mostly steep with only 1/3 of the galaxies showing flat and inverted spectra.

Thanks to our investigation, we showed that radio-mode AGN activity is widespread in massive early-type galaxies, where the AGN are in the vast majority of cases in a switched-on state varying only in the intensity of their activity.

Acknowledgment

My deepest gratitude goes to my supervisor Norbert Werner, for his exceptional support, help, guidance, and patience throughout my entire study. I'm also very thankful to him for believing in me and offering me a co-tutoring program in Italy, where I gained another great supervisor, Francesco Massaro. I admire both of them for their terrific scientific accomplishments and unstoppable enthusiasm and ideas on how to explore our Universe. Their vast experiences and knowledge gave me different perspectives on the topic of my research and I'm grateful to be able to learn from them. Moreover, their kindness, openness, friendly approach and their great sense of humor made the whole study much more pleasant. I'm also thankful to Francesco for supporting my summer internships in Boston or Bologna. Profoundly valuable for my progress and personal growth are also their teams of scientists, Ph.D., master and bachelor students both in Brno (or Budapest), and Turin. Lastly, I appreciate help, assistance, comments and notes on my writing and I hope that after this paragraph ', dude' is acceptable.

Furthermore, I am also very grateful to Kamlesh Rajpurohit, who immensely helped me to learn the radio data reduction. Moreover, I want to thank to INAF/IRA in Bologna, especially Elisabetta Liuzzo who kindly hosted and supervised me during my ALMA project. My sincere thanks goes to Paul Nulsen for supervision and useful discussions and important insides in the topic of the AGN feedback during my stay at CfA.

I also would like to thank the NRAO help-desk staff for their assistance, discussions, and help with the VLA data reduction and analysis. Special thanks go to Amy E. Kimball.

A huge thanks goes to my entire great family, my parents, grandparents, the best sisters ever Domi and Micha, and Endži :), who supported and encouraged me during my study. They are the most devoted fans of my work.

Finally, I would like to thank all of my closest (climbing and non-climbing:)) friends, who supported me throughout my study in Brno, Italy, Krakow, and Boston.

Special thanks goes to Jozef, who helped me to remove some white spaces here-and-there and supported me in every other way.

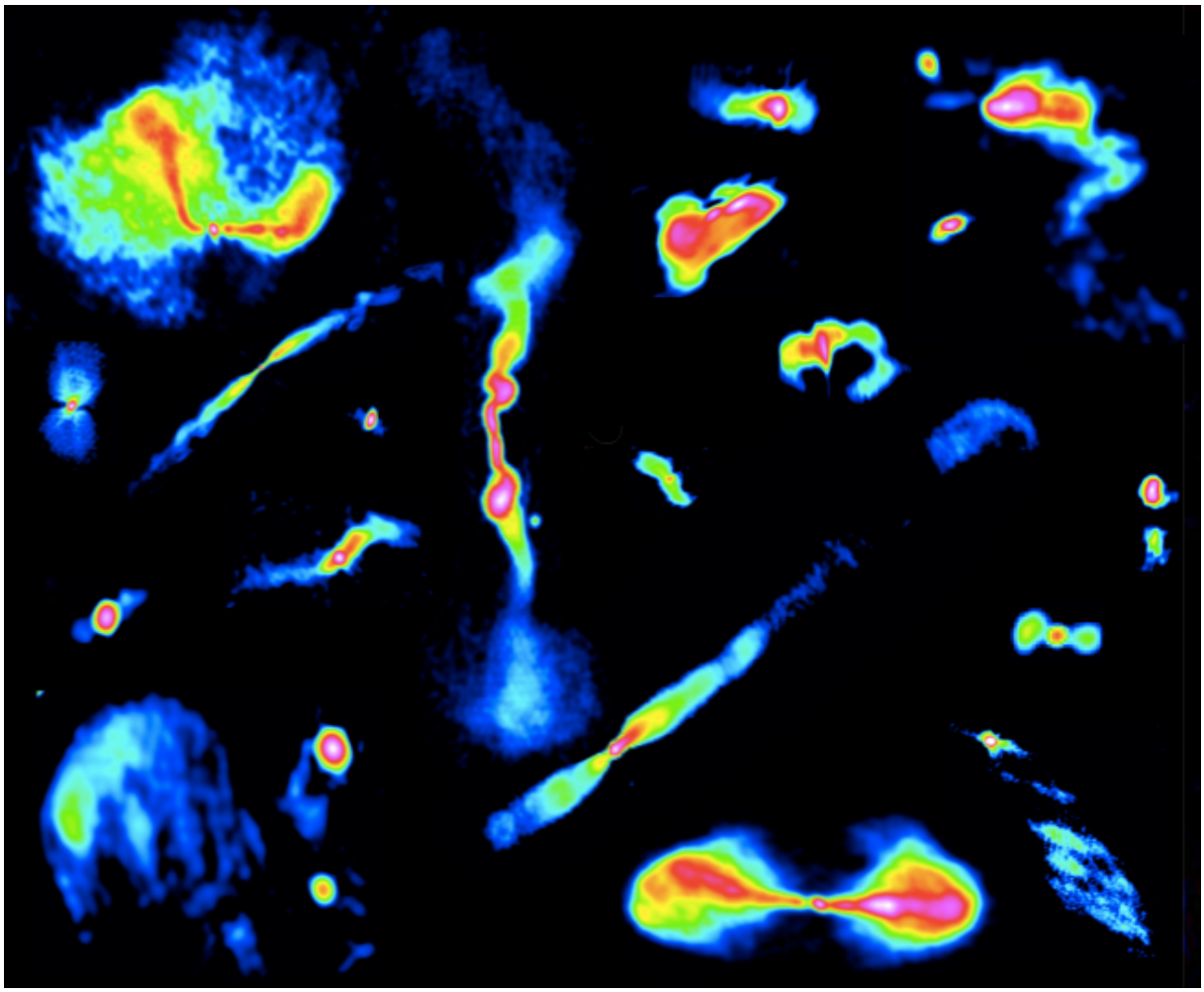

Cover image: VLA radio emission at 1–2 GHz in a subsample of studied early-type galaxies (not to the scale).

Contents

Introduction

Giant elliptical galaxies belong to early-type galaxies in the Hubble sequence and are the oldest and largest galactic structures in the Universe, residing mostly in the centers of groups and clusters of galaxies. Their mass is dominated by dark matter and they are embedded in large reservoirs of hot ionized gas in the form of low-density X-ray emitting atmospheres. The central regions are inhabited by an actively accreting supermassive black hole or so-called active galactic nucleus (AGN).

The X-ray atmospheres are expected to lose their energy via radiative cooling through line emission and bremsstrahlung. The cooling is faster towards the denser, central regions of the galaxy. As the gas cools, its temperature drops, which leads to the decrease in its pressure. Therefore, the cooling gas should flow inwards and provide material for new stars to be formed. With younger populations of stars, the galaxies themselves should appear more blue in color. This, however, does **not** correspond to the observations, which lack signatures of cooling gas or significant star formation in the central regions and only indicate the presence of older populations of stars. Therefore, massive ellipticals appear 'red and dead'.
At the beginning of the 90's, this 'Cooling flow problem' was formulated and extensively studied first for galaxy clusters (Fabian 1994). This study was followed by many research groups since then, concentrating not only on clusters of galaxies, but also galaxy groups and giant elliptical galaxies (e.g.: Peterson & Fabian 2006; Gaspari et al. 2011; McNamara & Nulsen 2007; McDonald et al. 2018; Werner et al. 2019). By studying high resolution spectra of the X-ray atmospheres in the central region, they found missing cooling lines (Peterson et al. 2001; Kaastra et al. 2001) and a minimal temperature at 1/3 of its peak temperature (Allen et al. 2001). Question arose, what is heating the gas, offsetting the cooling, and thus preventing star formation? One of the possible mechanisms is closely related to the beating hearts of these galaxies, the actively accreting supermassive black holes or AGN, and their interaction with the ambient hot X-ray atmosphere.

Over the last 20 years, there has been countless of evidences from the observations and simulations that the activity of the AGN is responsible for balancing the heating and cooling of the ambient medium in so-called radio-mechanical AGN feedback mode. This mode affects the formation and evolution not only of large-scale clusters of galaxies, but also smaller-scale structures from galaxy groups up to individual giant elliptical galaxies (see reviews by McNamara & Nulsen 2007, 2012; Fabian 2012; Werner et al. 2019; Gaspari et al. 2020).

The activity of accreting supermassive black holes can manifest itself in the form of so-called radio jets: well-collimated and powerful streams of highly relativistic particles, which emit a non-thermal radio continuum synchrotron radiation when accelerated in magnetic fields. As these jets expand, they interact with the surrounding medium by inducing weak shocks and turbulence, which then dissipates into heat. They also displace the hot ambient gas and create surface brightness depressions in the X-ray atmosphere, so-called X-ray cavities. Moreover, radio jets can also uplift lower entropy gas from the central regions, thus reducing the cool and

cold gas supplies otherwise available for star formation. The uplifted gas can then 'precipitate' back onto the supermassive black hole by condensing into cool clouds and falling inwards. This way, the fresh fuel is supplied to the central AGN to launch the radio jets again and start another loop of AGN feedback. The mechanism described above is often called the 'precipitation model' and it is recently one of the most popular models to explain the radio-mechanical AGN feedback loop. The popularity arises from the ability of this feedback loop to balance the radiative losses of the X-ray atmosphere (see e.g.: Churazov et al. 2000; Bîrzan et al. 2004; Rafferty et al. 2006; Nulsen et al. 2009; Hlavacek-Larrondo et al. 2015) to quench the star formation in massive ellipticals, and to fuel the central supermassive black hole by condensing circumnuclear medium. Important is also its high efficiency and self-regulating nature.

Many research groups are trying to understand this radio-mechanical feedback loop mechanism in more detail. Especially intriguing questions are: how does the AGN feedback operate from the central regions up to further distances from the core, or even outside of the host galaxy? What is the duty cycle of the AGN feedback? Is the activity in the form of jets continuous, or always on, just blowing out bubbles of relativistic plasma inflated by radio jets similar to the dripping tap or blowing bubbles through the straw? Or is it intermittent, turning on and off, possibly when cold clouds chaotically fall towards the black hole and increase the accretion rate and supply new fuel for the jets to be launched? What is the dominant mechanism of energy transport from the radio jets to the X-ray emitting ambient medium?

High resolution and high quality observations at the radio, X-ray, optical, and infra-red frequencies for a large sample of the closest early-type galaxies are thus crucial for trying to address the above-mentioned outstanding questions.

Comprehensive multi-band statistical analysis of 18 early-type galaxies was performed by Dunn et al. (2010). They searched for radio emission at 1.4 GHz in Very Large Array (VLA) observations of volume-limited sample of nearby ($d < 100$ Mpc) early-type galaxies (mostly giant ellipticals) which inhabit large and bright X-ray atmospheres that are also bright in the optical band to ensure that the investigated galaxies really inhabit massive halos. Remarkably, their study revealed that nuclear radio emission was detected in almost all galaxies (17/18). Moreover, more than half of the galaxies (10/18) revealed spatially-extended radio emission. Their results suggest that the active 'radio-mechanical' feedback could be the dominant state for large elliptical galaxies, which is, however, in disagreement with previously published models in which radio jets are considered a relatively rare and sporadic phenomenon (e.g. Binney & Tabor 1995; Kaiser & Binney 2003). Moreover, Dunn et al. (2010) proposed an extension to his main sample, containing an additional 24 sources, for which only survey radio observations at 1.4 GHz were available.

Higher signal-to-noise observations with a variety of spatial resolutions at gigahertz frequencies would offer more details of the fine structure and morphology of the radio jets in the central region. With the use of interferometric aperture synthesis telescope observations taken by the VLA in New Mexico at frequencies between 1–2 GHz, we investigate the radio detection rate in the nearest X-ray and optical brightest early-type galaxies (mostly giant ellipticals) and the morphology of the radio emission. We also compare the observed radio emission with the emission from the hot X-ray emitting atmospheres and search for signatures of interaction between radio jets and the X-ray atmospheres. The radio jets can mechanically displace the hot gas and inflate X-ray cavities. The duty cycle of the AGN, or how long AGN remain active during their lifetime, is investigated with the analysis of radio spectral indices.

Open Questions

Although the radio-mechanical AGN feedback mode has been studied extensively in the last two decades, the details about its duty cycle and relevant physical processes are still missing. The in-depth analysis of multifrequency data, with a primary focus on the radio emission at gigahertz frequencies, offers us an opportunity to investigate the radio jets and their role in the AGN feedback. Some of the remaining and most intriguing open questions are: how does the AGN feedback operate from the central regions up to further distances from the core, or even outside of the host galaxy? What is the duty cycle of the AGN feedback? Is the activity in the form of jets continuous, always on, blowing out bubbles of relativistic plasma inflated by radio jets, similar to a dripping tap? Or is it intermittent, turning on and off, possibly when cold clouds chaotically fall towards the black hole and increase the accretion rate and supply new fuel for the jets to be launched? What is the dominant mechanism of energy transport from the radio jets to the X-ray emitting ambient medium?

Chapter 1

Giant Elliptical Galaxies

In the late 1920's, Edwin Hubble, while studying local galaxies, defined morphological categories containing: early-type galaxies consisting of elliptical (E) and lentilcular (S0) and late-type including spiral (S; both with and without bars) as well as irregular galaxies (Hubble 1926).

Almost 90 years later, Kormendy et al. (2009) suggested a revision of this diagram, where the E galaxies were divided into 'normal' and 'massive' (also called 'giant') ellipticals. Main differences of the two classes are: the evolution process and specifically the presence/absence of gas during merging activity, the amount of 'excess' of light in the core, disky/boxy isophotes, the speed of rotation[1], high/low accretion rates and the presence of large hot ambient medium together with actively accreting supermassive black hole sustained over large fraction of their lives. The latter property, significant for massive ellipticals, is preventing further star formation, therefore leaving the galaxies with only older populations of stars and they appear red in color. This is also the reason why giant elliptical galaxies are often called 'red and dead'.

The total masses of giant ellipticals are dominated by dark matter. Furthermore, they host hot X-ray emitting atmospheres with luminosities of $L_{\rm Xray}$ $\sim$$10^{39}$– 10^{44} erg/s and magnetic fields with strengths of the order of a micro-Gauss, central supermassive black holes with masses of $M_\bullet$ $\sim$$10^{7}$– 10^{10} $\rm M_\odot$, mostly old populations of stars with total stellar mass of M_* $\sim$$10^{11}$–$10^{12}$ $M_\odot$, as well as a large number of globular clusters (Lidman et al. 2012; Kormendy & Ho 2013; Lakhchaura et al. 2018, 2019; Werner et al. 2019).

The central regions of groups and galaxy clusters usually host giant elliptical galaxies, which are often central dominant galaxies or CDGs[2]. As for example, the giant elliptical NGC 4649 residing inside of a galaxy sub-group within the Virgo cluster (Figure 1.1). A small fraction of giant elliptical galaxies are located in the outskirts of clusters or are field galaxies with their own hot X-ray emitting atmospheres.

[1]Cappellari et al. (2011) suggested another update of the early-type part the Hubble sequence to distinguish between slow and fast rotators. The giant ellipticals are usually in the category of slow rotators.

[2]The CDGs include the brightest cluster (BCGs) or group-dominant early-type galaxies (BGEs).

Figure 1.1: The 'red and dead', spherical, giant elliptical galaxy, NGC 4649, located in a subgroup of the Virgo cluster and interacting with a bluer, star-forming, spiral galaxy NGC 4647 (in the top right corner) imaged by the Hubble Space Telescope (HST). Credit to NASA/ESA.

1.1 The Evolution and Formation of giant Elliptical Galaxies

The progenitors of giant elliptical galaxies, together with their stellar populations, were formed within 1 billion years after the Big Bang (Conroy et al. 2014), when the Universe was less than 10% of its current age.

From the study of the age and metallicity via absorption line indices with variable alpha-elements to iron ratios, Thomas et al. (2002) concluded that giant ellipticals do not follow the standard hierarchical formation scenario, in which the largest galactic structures form by mergers of smaller structures like spiral galaxies. Giant ellipticals underwent very brief and explosive star formation, which was afterwards ceased almost completely, and they further grew only by dry, dissipation-free (or gas-free) mergers (Thomas et al. 2010; Onodera et al. 2015). This short star formation period is supported by the enhanced alpha-elements to iron ratio, e.g.: [Mg/Fe] ≈ 0.3 (Thomas et al. 1999; Milone et al. 2000; Maraston et al. 2003). On the one hand, massive ellipticals have been enriched by alpha-elements produced in the outburst of massive stars, which ended their lives as a core collapsed or type II supernovae (SNe II). On the other hand, however, they have not yet been enriched by the heavier elements created via thermonuclear or type Ia supernovae explosions (SNe Ia), which happened at on average on longer timescales than the SNe II outbursts. The relative abundances of heavier elements reach those of lighter elements and the dominance of the lighter elements will not be recovered again.

It is worth asking why the star formation was and still remains to be quenched? What mechanism is connecting the main components of massive ellipticals explaining their unusual properties? Lets discuss all components of the giant elliptical galaxies in more detail.

1.1.1 Hot X-ray Atmospheres

Giant ellipticals, groups, and clusters of galaxies are embedded in hot low density X-ray emitting atmospheres (see recent review by: Werner et al. 2019; Werner & Mernier 2020).

According to our definition, hot atmospheres include the X-ray emitting plasma in the interstellar medium (ISM) at kiloparsec scales up to the circumgalactic medium (CGM) at megaparsec scales. If the galaxy is embedded in a galaxy cluster or group, the intracluster (ICM) and intragroup (IGM) medium also belong into our definition of hot X-ray atmospheres.

The progenitors of the most massive galaxies[3] are thought to have been formed in the most massive early dark matter haloes (White et al. 1991; Cattaneo et al. 2009). When the mass of these halos reached $\sim 10^{12}\,M_{\odot}$ (Correa et al. 2018), the gas falling inward, passing through the shocks, got heated to temperatures of several million Kelvin, thus forming hot X-ray emitting atmospheres.

The hot atmospheres of galaxies, groups, and clusters have low densities of 10^{-1}–$10^{-4}\,\mathrm{cm}^{-3}$, high temperatures of 5×10^{6}–10^{8} K (or $k_{B}T \sim 0.5$–10 keV[4]) and consists of fully ionized hydrogen and helium as well as highly ionized heavier elements.

The elastic collision times for free electrons and ions in the hot atmospheres are much shorter than the time scales for cooling, thus we can assume a thermal equilibrium between free electrons and ions as well as the ionization and recombination rates. The hot atmospheres are in a collisional ionisation equilibrium. The atmospheres are largely optically thin thus the emitted X-ray photons rarely interact with free electrons or ions. Therefore, the observed X-ray emission represents the projected gas distribution very well and the spectrum is defined solely by the temperature of the gas and the chemical abundances.

Line emission and bremsstrahlung

At the temperatures of hot atmospheres the cooling is dominated by line emission (bound-bound process). Electrons in the ions get excited to higher energy levels after collisions and during the de-excitation to the ground energy state, they emit X-ray photons with the energy corresponding to particular X-ray emission lines, for instance: O, Fe (blended L-shell lines), Mg, Si, S, Ar, and so on (Figure 1.2; left).
The continuum emission is created by the radiative recombination, when free electrons are captured by ions (free-bound process) and by the breaking radiation or bremsstrahlung (free-free process). The free electrons are deflected and accelerated in the Coulomb field of ions. This way, the atmospheres lose energy and cool.

It is worth noting that the bremsstrahlung process is the dominant mechanism of cooling in the atmospheres of clusters of galaxies. These atmospheres can reach higher temperatures (up to 10^{8} K) than atmospheres of a single massive galaxy. Therefore, the gas is almost fully ionized and atomic transitions of only highly ionized heavier elements, like iron or nickel, can occur (Figure 1.2; right).

[3] One of the candidates for the progenitors of giant elliptical galaxies are massive, compact, high-redshift galaxies called 'red nuggets' (see e.g.: Daddi et al. 2005). Werner et al. (2018) and Buote & Barth (2018) discovered hot atmospheres around these potential candidates in the local universe and thus supported their relevance as progenitors.

[4] The temperatures in high energy astrophysics are usually expressed in term of particle energies in kiloelectronvolts.

Detailed description of following radiative process can be found in Rybicki & Lightman (1979), Longair (2011), or in online-available lectures e.g.: by Pfrommer[5] (Potsdam Univesity)

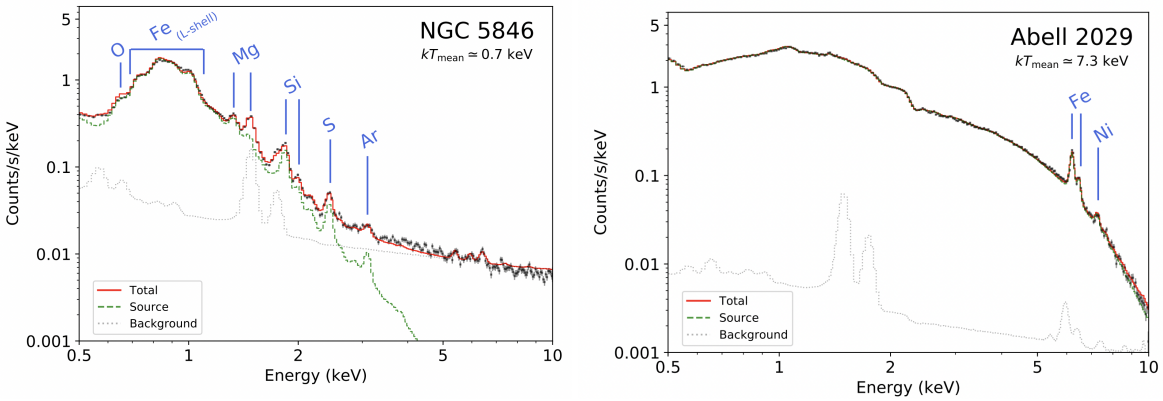

Figure 1.2: **Left:** At lower temperatures, relevant for giant ellipticals, radiative losses through line emission are more prominent. **Right:** At higher temperatures the dominant mechanism is bremsstrahlung (Werner & Mernier 2020).

X-ray Emissivity and Spectra

The X-ray emissivity, $\epsilon_{\rm ff}$, of the thermal bremsstrahlung (free-free) process is defined as: $\epsilon_{\rm ff} = {\rm d}^3E/({\rm d}\nu{\rm d}t{\rm d}V)$, the amount energy, E, released by photons with frequency, ν, per unit frequency interval ${\rm d}\nu$) unit time (${\rm d}t$), and gas volume, ${\rm d}V$. It scales with the product of the number density of electron (n_e) and ion (n_i). The time period for the scattering process is defined as: $t \sim l/\Delta v$, where $\Delta v = (k_{\rm B}T/m_e)^{1/2}$ is the typical velocity of the relative thermal motion between the electrons and ions, $k_{\rm B}$ is the Boltzmann constant, m_e is mass of the electron, $g_{\rm ff}$ is the Gaunt factor and h is the Planck's constant. Considering the Maxwell-Boltzmann distribution of the electron velocities at a given temperature, we get:

$$\epsilon_{\rm ff} = g_{\rm ff} n_e n_i \Delta v^{-1} e^{-h\nu/k_{\rm B}T} \propto n_e n_i T^{-1/2}. \tag{1.1}$$

The emissivity, $\epsilon_{\rm ff}$, defined in Equation 1.1, is dependent on the product of the number density of electrons and ions, $n_e \cdot n_i$, and the temperature, T, but independent on frequencies, ν, except the turn-over point, where the frequency, $\nu_{\rm turn\_over}$, is $\approx k_{\rm B}T/h$. Thus, we observe flat spectra at low frequencies with an exponential decline[6] at frequencies higher than the turn-over point.

Thermodynamical properties of the X-ray atmosphere

As was demonstrated, the analysis of the X-ray spectra provides information about thermodynamic properties of the hot X-ray atmosphere. From the normalization of the spectra, we get the number densities of electrons, n_e, whereas from the turn over point the gas temperature, T.

Furthermore, we can define the pressure of gas in the hot atmosphere from above obtained properties. Considering its low density, this gas can be approximated by the ideal gas, for

[5]The Physics of Galaxy Clusters: https://pages.aip.de/pfrommer/Lectures/

[6]In comparison with power-law spectra from inverse Compton scattering, where the relativistic electrons loose energy (thus cool) by upscattering the low-energy cosmic microwave background (CMB) photons into X-rays.

which the pressure is defined as:

$$p = \frac{\rho k_{\rm B} T}{\mu m_p} = nkT, \tag{1.2}$$

where ρ is the density of the gas and μ is the mean molecular mass in the units of proton mass, m_p.

We can estimate how much of the total energy of the gas is released by the radiation from the X-ray regime (10^6 to 10^8 K) to the cool gas regime (10^4 K) or the cooling time, $t_{\rm cool}$:

$$t_{\rm cool} = \frac{\epsilon_{\rm tot}}{\epsilon_{\rm ff}} = \frac{\frac{3}{2} n k_{\rm B} T}{n_e n_i \Lambda(Z,T)} \approx \left(\frac{T}{10^8\,{\rm K}}\right)^{1/2} \left(\frac{n_e}{0.01\,{\rm cm}^{-3}}\right)^{-1}, \tag{1.3}$$

where $\Lambda(Z,T)$ is the cooling function (Schure et al. 2009) dependent on the temperature and metalicities.

Another important property, which stores the information of the thermodynamic history of the ionised gas and determines the structure of the atmosphere is entropy, K (Voit et al. 2002, 2005; Werner & Mernier 2020). It is defined as follows:

$$K = \frac{k_{\rm B} T}{n_e^{2/3}}, \tag{1.4}$$

thus the lower entropy gas is observed in the central region of giant elliptical galaxies.

Cooling flow problem

The 'cooling flow problem' was first described almost 30 years ago in clusters of galaxies by Fabian (1994) and will be briefly discuss in this section.

As Equation 1.3 shows, the radiative cooling of the hot atmosphere is faster in the denser central regions of galaxy clusters than in their outskirts. If the timescales for cooling are much smaller than the Hubble time ($< 10^9$ yr), the material in the center cools out relatively fast and the overlaying layers of gas slowly flow inward to balance the pressure and form so-called 'cooling flow'. Thus, large cold gas supplies are expected in the central regions, providing fuel for new stars to be born. The problem of the cooling flow is that the rate at which the mass is being deposited in the core seems to be a magnitude smaller than theoretically estimated. Moreover, there is little evidence for cooling lines in the X-ray spectra of galaxy clusters (Peterson et al. 2001; Kaastra et al. 2001) and the gas temperature does not drop below 1/3 of its peak temperature (Allen et al. 2001).

In the case of giant ellipticals, this 'cooling flow problem' is even more severe with shorter cooling times and larger amount of gas returned by the stellar populations over the lifetime of the galaxy (Pellegrini et al. 2018).

The main questions arise: How it is possible that such large reservoirs of hot gas are not able to cool enough to initiate star formation? What is the heating mechanism to prevent the rapid cooling within the central regions of clusters of galaxies and giant ellipticals?
One of the main candidates to satisfyingly answer those outstanding questions is hidden in the central regions of massive ellipticals. The activity of the central supermassive black hole seems to be able to maintain the observed properties of the X-ray atmospheres (Churazov et al. 2000; McNamara & Nulsen 2007, 2012; Fabian 2012; Werner et al. 2019; Gaspari et al. 2020).

1.1.2 Active Galactic Nucleus

Before we continue to present more details about the interaction of the active galactic nucleus (AGN) and the hot atmosphere, we take a closer look at the AGN itself and describe the radiative processes responsible for the observed emission.

The main components of AGN are shown in Figure 1.3. The central regions of giant ellipticals are occupied by an actively accreting and spinning supermassive black hole (or AGN) as well as collimated outflows of highly relativistic particles in form of radio jets. These AGN emit radiation across the entire electromagnetic spectrum. The most energetic *gamma-rays* are observed from the jets emitting synchrotron self-Compton radiation, followed by *X-rays* emitting via the inverse Compton emission from the corona and K-shell iron line emission produced in the accretion disk[7] and from the radio jets. The 'warm' accretion disk[8] itself shines in the *ultraviolet (UV)* band. *Optical and infrared (IR)* radiation come from the blackbody emission of the individual stars, 'warm' ionized nebula, dust, obscuring torus as well as powerful jets. The lower energy bands are represented by *radio waves*, which we are mostly focusing on in this thesis, are dominated by the emission from the activity of the AGN. And finally, *microwaves* can be observed from the dense regions of the dusty torus (de Menezes et al. 2020; Haardt & Maraschi 1991; Blandford et al. 2019; Algaba et al. 2021; Laor 1990; López-Gonzaga et al. 2016; Imanishi et al. 2018).

Jets

The most prominent AGN features at radio frequencies are the so-called radio jets, which are collimated plasma streams along the angular momentum axis of the accretion disk. They consists of several components. In the central region, at the base of the jets, is a radio core hosted by the supermassive black hole. The jets expand at first supersonically and continuously loose energy and slow down due to the interaction with the ambient medium in the form of shocks and turbulence. Finally, they inflate radio lobes, which then continue to rise via buoyancy. These kind of jets are more prominent for Fanaroff-Riley Class I (FR I) radio sources. If the jets remain supersonic up to large distances from the core, they will form hotspots, the brightest features in the powerful (FR II) radio sources (see Figure 1.4 and for more details about FR dichotomy, see Section 1.3.1).

Currently, one of the most popular jet-formation scenario follows the Blandford-Znajek mechanism (see Figure 1.5; Blandford & Znajek 1977). In this mechanism, the energy to launch the jets seems to be extracted from the spinning central supermassive back hole electromagnetically. The rotating black hole is dragging in and twisting magnetic fields generated within the accretion disk as well as inducing electric fields that accelerate electrons. Accelerated electrons destabilize vacuum, what initiate production of electron-positron pairs. Neutral plasma is formed, that slides along the twisted magnetic field lines threading the black hole and therefore forming jets.

Handful of numerical general relativistic magneto-hydrodynamic (GRMHD) simulations confirm underlying mechanisms described by Blandford and Znajek (McKinney & Gammie 2004; Komissarov 2004; Krolik & Hawley 2010; McKinney et al. 2014).

Moreover, recent ground-breaking discovery by the Event Horizon Telescope (EHT) team

[7] The ultraviolet (UV) photons from the accretion disk are up-scattered by the relativistic electrons in the corona to X-ray energies and some photons are back-scattered to the disk and causing the fluorescent K-shell iron line emission.

[8] The temperatures in the accretion disk for the supermassive black hole reach up to 10^5 K.

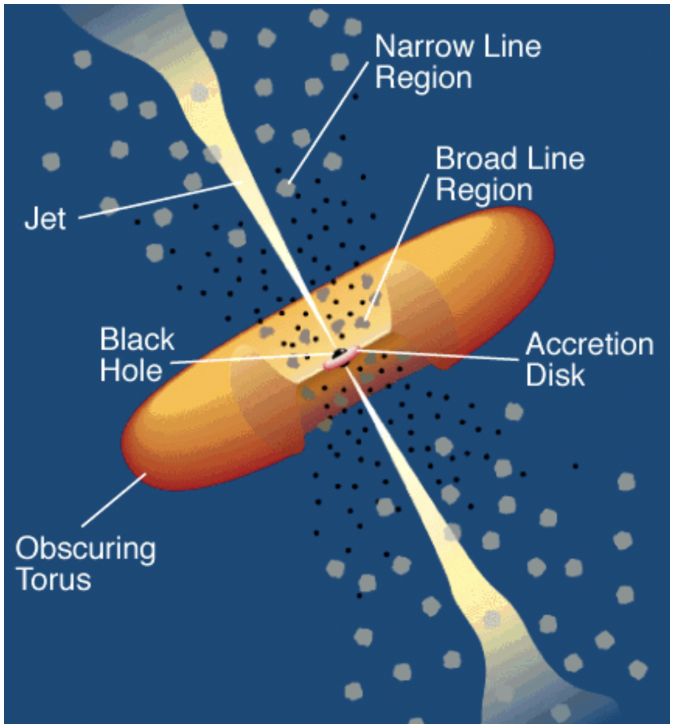

Figure 1.3: Schematic diagram of the main AGN components. The central supermassive black hole is surrounded by an accretion disk. Broad emission lines (black dots) are produced in clouds orbiting around the disk and perhaps by the disk itself and are surrounded by a thick dusty obscuring torus. Much further from the central source lies a narrow line region (gray spherical dots). Lastly, the picture shows radio jets emanating from the region near the supermassive black hole, which expands initially at relativistic speeds (Urry & Padovani 1995).

(Event Horizon Telescope Collaboration et al. 2021) revealed in great detail the structure of magnetic fields based on polarization measurements of the inner region around the supermassive black hole in M 87 (or NGC 4486; Section 5.29). It is considered to be the first significant evidence in favor of the Blandford-Znajek mechanism, which seems to be a viable mechanism to launch jets in M 87 with a jet power (Equation 1.24) of $P_{\rm jet} \sim 10^{42}{\rm erg/s}$ and a magnetic field, B of ≤ 5 G. Furthermore, a spiral structure of the field lines as revealed by the polarimetric EHT image appears to be better described by the Magnetically Arrested Disk (MAD, e.g.: Narayan et al. 2003) model rather than the Standard and Normal Evolution (SANE, De Villiers et al. 2003; Narayan et al. 2012) model.

For a recent review of the radio jets, see Blandford et al. (2019).

Non-thermal Continuum Synchrotron Emission

The synchrotron radiation is one of the dominant radiative processes in high energy astrophysics responsible for the observed emission from jets in the giant elliptical galaxies at radio[9], optical and X-ray frequencies[10] (e.g.: M 87 or NGC4486; Algaba et al. 2021).

[9] Although, radio waves have a long wavelengths, thus short frequencies and small energies, the processes that causing them are very energetic. Therefore, radio emission from early-type galaxies is considered to be part of the domain of high energy astrophysics.

[10] Synchrotron emission from the same population of electron responsible for observed radio emission is also

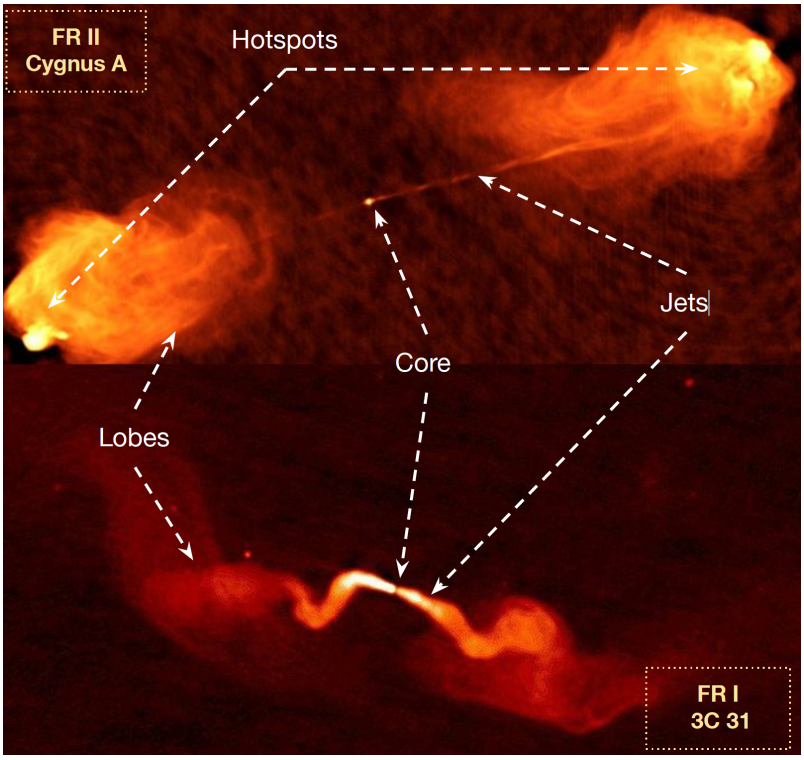

Figure 1.4: Individual components of radio jets for low (FR I) and high (FR II) power radio sources (see discussion in Section 1.3.1). Credit to: NRAO/AUI (Galaxies/) by R.Laing, A. Bridle, R. Perley, L. Feretti, G. Giovannini, and P. Parma & NRAO/AUI by Chris Carilli.

This non-thermal[11] continuum process describes acceleration of ultra-relativistic charged particles (e.g., electrons) gyrating in the uniform magnetic field.

Detailed descriptions of this radiative process can be found, for example in Rybicki & Lightman (1979), Longair (2011), Condon & Ransom (2016)[12], or in the online-available lectures by e.g.: Tolstoy[13] (University of Groningen) and Garret[14] (University of Oxford).

The relativistic form of the equation of motion of an electron with charge, e, mass, $m_{\rm e}$, velocity, $\mathbf{v}$ and Lorentz factor, $\gamma = \left(1 - v^2/c^2\right)^{-1/2}$, in a uniform magnetic field, B, is described by:

$$\frac{\mathrm{d}}{\mathrm{d}t}\left(\gamma m_{\rm e}\mathbf{v}\right) = e\left(\frac{\mathbf{v}}{c} \times \mathbf{B}\right). \tag{1.5}$$

responsible for observed X-ray and optical emission especially for lower-power FR I, like sources in our sample. The origin of X-rays in higher-power FR II source is not that straightforward (Blandford et al. 2019).

[11] In high energy astrophysics, the term 'non-thermal' describes continuum emission from high energy particles with non-Maxwellian energy distribution (Longair 2011).

[12] Book Essential Radio Astronomy is also available online at https://www.cv.nrao.edu/ sransom/web/xxx.html.

[13] https://www.astro.rug.nl/ etolstoy/astroa07/

[14] https://www-astro.physics.ox.ac.uk/ garret/teaching/

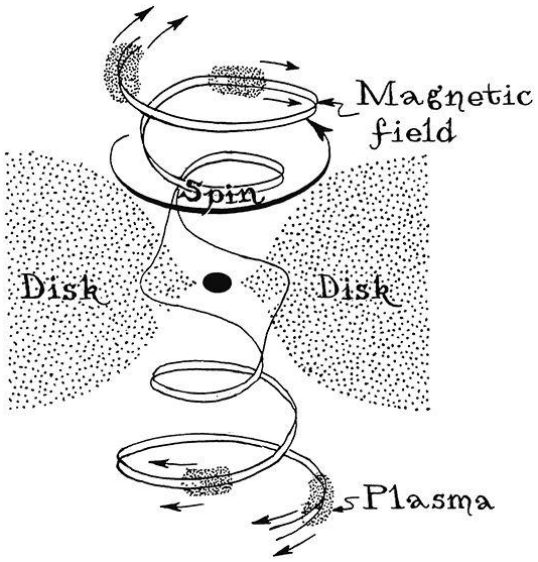

Figure 1.5: Graphic scheme of the main components of the Blandford-Znajek jet formation mechanism (Blandford & Znajek 1977). The spinning central supermassive black hole is threaded by magnetic field lines generated within the accretion disk. The material from the disk is sliding along the twisted field lines and forms radio jets. The drawing done by Matt Zimet is based on a sketch in the book by Thorne (1994).

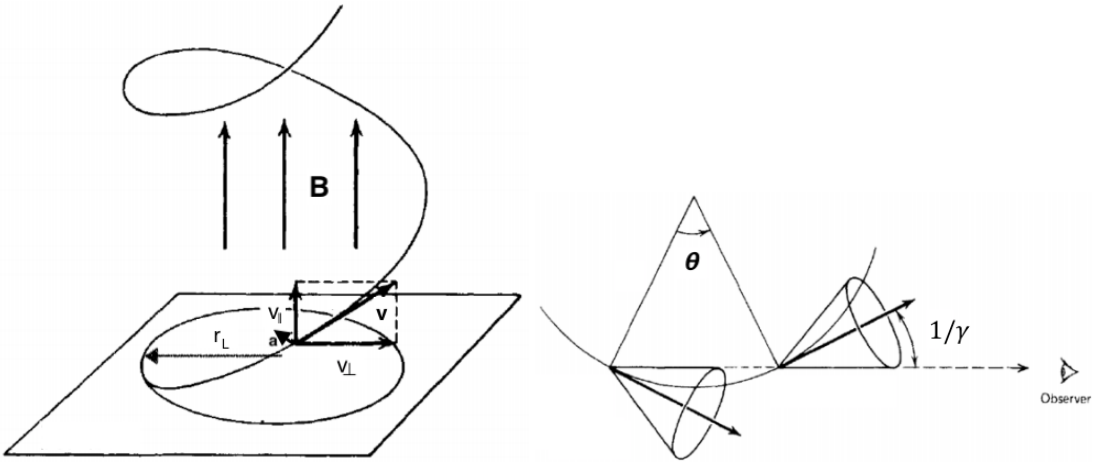

Figure 1.6: **Left:** Scheme of the helical motion of a relativistic particle with labelled velocity components (parallel, $v_{\parallel}$, and perpendicular, $v_{\perp}$), acceleration, a, magnetic field, B, perpendicular to the main plane, Larmor radius, $r_{\rm L}$, (Carroll & Ostlie 2006). **Right:** The radiation from the relativistic electron gets visible only for a short time and a small fraction $\sim 1/\gamma$ of electron's orbit, when the beam is pointed at our line of sight (Rybicki & Lightman 1979).

If we separate the velocity to its perpendicular $v_{\perp}$ and parallel $v_{\parallel}$ components:

$$\frac{\mathrm{d}\mathbf{v}_{\parallel}}{\mathrm{d}t} = 0 \quad \& \quad \frac{\mathrm{d}\mathbf{v}_{\perp}}{\mathrm{d}t} = \frac{e}{\gamma m_{\mathrm{e}} c} \left(\mathbf{v}_{\perp} \times \mathbf{B}\right), \tag{1.6}$$

it shows, that $v_{\parallel}$ is constant, as well as γ, then also $v_{\perp}$ is constant. Therefore, electron performs a circular motion with a Larmor radius $r_{\rm L}$ together with an uniform motion along the magnetic

field lines with a constant pitch angle θ[15]. This is a helical motion (Figure 1.6; left) along the field lines with an orbital angular frequency or angular gyrofrequency, $\omega_{\rm g}$, with Larmor radius, $r_{\rm L}$:

$$\omega_{\rm g} = \frac{v_\perp}{r_{\rm L}} = \frac{eB}{\gamma m_{\rm e} c} \Rightarrow r_{\rm L} = \frac{\gamma m_{\rm e} v_\perp c}{eB}. \tag{1.7}$$

There is a corresponding gyrofrequency, $\nu_{\rm g} = \omega_{\rm g}/2\pi$, associated with the Larmor frequency:

$$\nu_{\rm g} = \frac{\nu_{\rm L}}{\gamma} \Rightarrow \nu_{\rm L} = \frac{eB}{2\pi m_{\rm e} c}. \tag{1.8}$$

Electrons, spiraling around along the magnetic field lines, accelerate (again only perpendicular acceleration $a_\perp$ is considered) and therefore radiate. They emit over a wide range of frequencies and due to the relativistic beaming effect, the radiation gets visible only for a short time and a small fraction $\sim 1/\gamma$ of electron's orbit, when the core of the beam is pointed at our line of sight (Figure 1.6; right).

Synchrotron Power

The radiated power, P, follows Larmor formula (recalling that: $c^2 = (\mu_0 \varepsilon_0)^{-1}$) we get:

$$\begin{aligned} P &= -\frac{{\rm d}E}{{\rm d}t} = \frac{e^2 |a_\perp|^2}{6\pi\varepsilon c^3} \\ &= \frac{e^2}{6\pi\,\epsilon\, c^3} \left(\frac{e\gamma B |\mathbf{v}| sin\theta}{m_e} \right)^2 \\ &= 2 \left(\frac{e^4}{6\pi\varepsilon^2 c^4 m_e^2} \right) \left(\frac{v}{c} \right)^2 \frac{cB^2}{2\mu_0} \gamma^2 sin^2\theta, \end{aligned} \tag{1.9}$$

where the first bracket on the right-hand side of the equation is the Thompson cross-section of the electrons, $\sigma_{\rm T}$, defined as $\sigma_{\rm T} = \frac{8\pi}{3} \left(\frac{e^2}{m_{\rm e} c^2} \right)^2$. Therefore:

$$P = 2\sigma_{\rm T} \frac{cB^2}{8\pi} \left(\frac{v}{c} \right)^2 \gamma^2 sin^2\theta. \tag{1.10}$$

It is worth noting, that the ratio $\frac{B^2}{8\pi}$ is the magnetic energy density, $U_{\rm B}$.

The pitch angles of the electrons can vary, but assuming their isotropic distribution, we can average over all angles and get the average power emitted by the synchrotron radiation:

$$\langle P \rangle = \frac{4}{3} \sigma_T c \left(\frac{v}{c} \right)^2 \gamma^2 \frac{B^2}{8\pi}, \tag{1.11}$$

and if we consider that:

$$\gamma = \frac{E}{m_{\rm e} c^2}, \tag{1.12}$$

[15]The pitch angle is the angle between the velocity vector and the magnetic field lines and for the case, when the motion is perpendicular to the magnetic field the pitch angle is $\pi/2$.

and use this relation in Equation 1.11, we get that synchrotron power is proportional to a square of both, E and B:

$$P \propto E^2 B^2. \tag{1.13}$$

Synchrotron Spectra

The total synchrotron spectrum of a radio source is a sum of the spectra of each individual ultra-relativistic electrons (Figure 1.7; left). Lets consider first, the spectrum of a single electron, which can be calculated using a reasonable approximation that each electron radiates its average power at a single frequency with a maximum at $\nu_{\rm max} = 0.29\nu_{\rm c}$ (see Figure 1.7; right), where $\nu_{\rm c}$ is the critical frequency defined as:

$$\begin{aligned} \nu_{\rm c} &= \frac{3}{2} sin\theta \gamma^2 \nu_{\rm L} \\ &= \frac{3}{2} sin\theta \left(\frac{E}{m_{\rm e}}\right)^2 \frac{eB}{2\pi m_{\rm e} c} \propto E^2 B. \end{aligned} \tag{1.14}$$

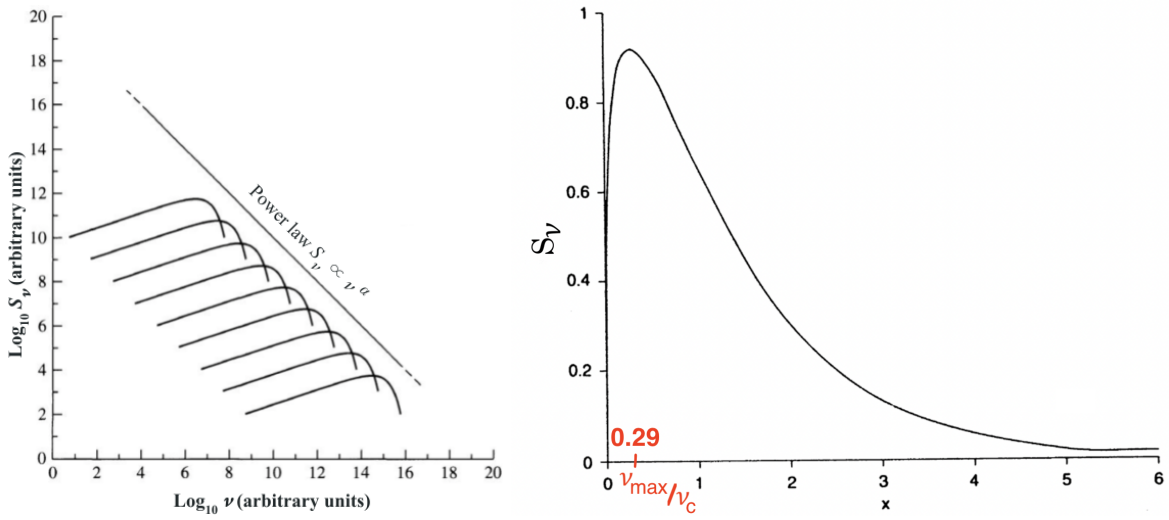

Figure 1.7: **Left:** Final synchrotron spectrum in log-log scale is a sum of the spectra of each individual ultra-relativistic electrons with a power-law slope (Longair 2011). **Right:** Synchrotron spectrum of single relativistic electron peaking at $\nu_{\rm max}/\nu_{\rm c} \simeq 0.29$ with $x = \nu/\nu_c$ (in linear scale; Longair 2011).

We consider a power-law distribution of electron energies with a slope, p, and $N(E)\mathrm{d}E$ as the number of electrons per unit volume with energies E to $E + \mathrm{d}E$:

$$N(E)dE \propto E^{-p}dE. \tag{1.15}$$

The power radiated at energies: E and $E+\mathrm{d}E$ is equal to the power radiated by ν and $\nu+\mathrm{d}\nu$, therefore we can substitute the energy by frequency. Considering the relation in Equation 1.14,

we get $E \propto \nu^{1/2}$ and $\mathrm{d}E \propto \nu^{-1/2}\mathrm{d}E$ and the spectrum will have the following form:

$$\begin{aligned} S(\nu)\mathrm{d}\nu &= P(E)N(E)\mathrm{d}E \\ &\propto E^2 B^2 E^{-p}\mathrm{d}E \\ &\propto \nu^{-(p-1)/2}\mathrm{d}\nu, \end{aligned} \tag{1.16}$$

where we obtain the well-know dependence of the flux density on the frequency, $S(\nu) \propto \nu^{\alpha}$ with the spectral index $\alpha = -(p-1)/2$.

This essentially tells us how fast the electrons, responsible for synchrotron radiation, loose their energy or simply how fast they age. The time it takes to radiate away the energy from the total power is described by the synchrotron cooling time ($t_{\mathrm{cool\_synch}}$). As already mentioned in Equation 1.13, we know there is a square-dependence of power on energy. Thus, we find that the cooling time ($t_{\mathrm{cool\_synch}}$) or rate at which electron looses energy, scales as $1/E$:

$$t_{\mathrm{cool\_synch}} \propto E/P \propto E/E^2 \propto 1/E, \tag{1.17}$$

the more energetic are the particles, the shorter are their cooling times. The critical frequency is also proportional to E^2 (Equation 1.14), therefore the synchrotron losses steepen the spectra at higher frequencies.

There are three different types of spectrum depending on the inclination of the spectral slope. A *flat* spectrum with a spectral index larger or equal to -0.5, is observed if there is a continuous supply of fresh newly injected electrons within the central regions or the re-accelerated electrons in the hot-spots away from the radio core. The final spectra are then the superposition of the individual spectra from many unresolved[16] sub-components in that region. The innermost central regions of the source can also show *inverted* spectral index due to synchrotron self-absorption (see new Subsection). In the jet-inflated radio lobes, the particles that were once injected progressively start to loose their energy and the spectrum *steepens* ($\alpha < -0.5$). The high energy particles loose their energy faster and some of them are moved to the lower-energy part of the spectrum.

Synchrotron self-absorption

In the above-derivation of synchrotron spectrum, we are assuming that all of the synchrotron radiation emitted by each electron reaches the observer. This, however, could be not only linked. Especially in the optically thick environment of the inner parsec-scale region of giant ellipticals, there is a chance that the emitted photon propagating through the plasma, will be scattered by one of the synchrotron electrons. This process is called synchrotron self-absorption (SSC). To investigate the spectral shape of self-absorbed spectrum, we consider the electrons to have an effective temperature, T_{eff}. It is worth noting, that such a particle energy distribution is non-thermal, but the effective temperature can be still defined according to:

$$k_{\mathrm{B}} T_{\mathrm{eff}} \sim \gamma m_{\mathrm{e}} c^2. \tag{1.18}$$

And due to energy dependence on frequency, we get:

$$k_{\mathrm{B}} T_{\mathrm{eff}} \propto E \propto v^{1/2}. \tag{1.19}$$

[16]Unresolved sources have their observed radio emission not encompassed by the resolution, or beam size, of the observation with the radio antennas.

Finally, we can estimate the maximum brightness of the self-absorbed synchrotron plasma using the Rayleigh-Jeans limit ($h\nu << k_{\rm B}T$) of the Plank formula:

$$B_\nu = \frac{2k_{\rm B}T\nu^2}{c^2}. \tag{1.20}$$

And if we use $T_{\rm eff}$ in the above equation, we get:

$$\begin{aligned} B_\nu &\propto T_{\rm eff}\nu^2 \\ &\propto \nu^{1/2}\nu^2 \\ &\propto \nu^{5/2}. \end{aligned} \tag{1.21}$$

Thus, the spectrum of the relativistic electrons can produce an 'inverted' spectrum with α as large as $\alpha = 2.5$. The turn-over frequency, ν_1, (see Figure 1.8) is reached, when the mean free path between scatterings reaches the size of the source.

It is worth noting, that especially, for low redshift galaxies, the SSC is one of the possible mechanisms in producing high energy photons observed in X-rays.

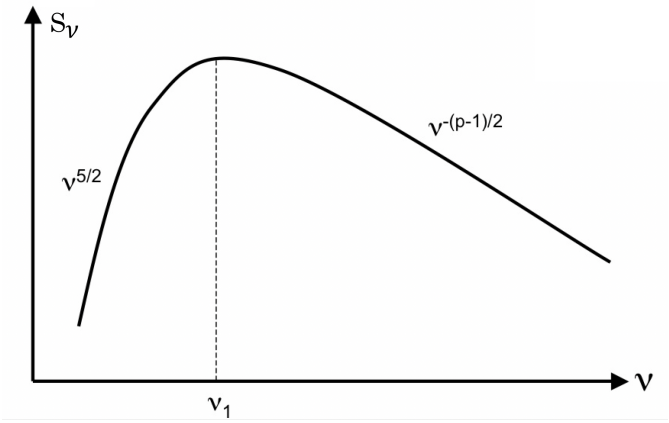

Figure 1.8: Self-absorbed synchrotron spectrum shows a steep rise at lower frequencies with spectral slope (index) up to 5/2. The turnover frequency, v_1, is shown after which the spectrum exponentially drops with a spectral index $\alpha = -(p-1)/2$. Credit to Ch. Stuardi.

1.1.3 Cold Gas and Dust

Study of cool and cold gas receives a considerable attention due to their important role in feeding of the central, active supermassive black hole. It is supplying the necessary fuel for the radio jets to be launched and likely cooling from hot atmospheres (Werner et al. 2019).

Recent surveys have found the presence of warm and cold, atomic and molecular gas as well as dust in nearby early-type galaxies (Lauer et al. 2005; Werner et al. 2014; Werk et al. 2014; Babyk et al. 2019; Werner et al. 2019; Olivares et al. 2019). Some of the cold gas is turning into stars, as shown by the UV observations (Yi et al. 2005), even though the star formation rates are usually low (0.01 –1 $M_\odot$; Donahue et al. 2010; Kolokythas et al. 2018, and see Section 4.5.2).

Lakhchaura et al. (2018) found that in approximately half of the galaxies the Hα+[NII] line emission is observed including nuclear and filamentary extended emission. This results are consistent with the previous findings (e.g.: Werner et al. 2014; Babyk et al. 2019).

1.2 Feedback Processes

Feedback in galaxies can be provided by numerous mechanisms. Star formation or supernova feedback and AGN feedback in the form of galactic outflows or radio jets are some of the potential mechanisms. More detailed investigation of supernova feedback in the most massive giant elliptical galaxies has shown not provide enough energy to uplift gas from the potential wells (Croton et al. 2006; McNamara & Nulsen 2007, 2012).

Within the last decade, AGN feedback turned out to be the most likely mechanism to quench the star formation in massive ellipticals due to its high efficiency, self-regulating nature, the ability to balance the radiative losses of the X-ray atmospheres as well as to fuel the central black hole by condensing the circumnuclear medium. This AGN feedback also explains the observed shape of the stellar mass function, where the high-mass end is balanced by AGN feedback and the low-mass end by the supernovae feedback (Figure 1.9, Harrison 2017).

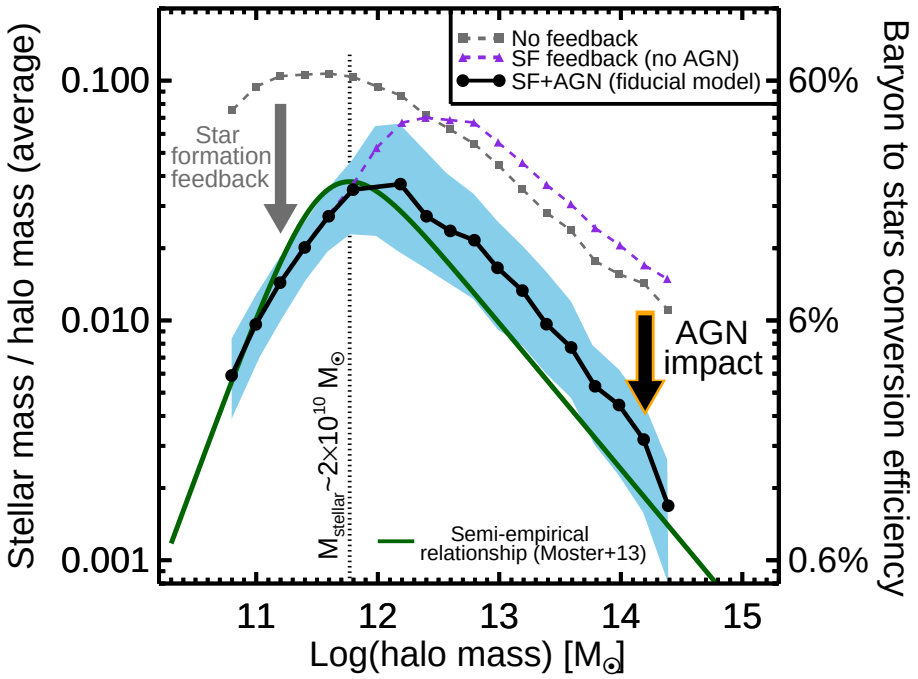

Figure 1.9: Stellar mass function, where the high-mass end is balanced by AGN feedback and the low-mass end by the supernovae feedback. Based on Harrison (2017).

The following sections will discuss the AGN feedback in more detail. There are two modes of feedback in massive galaxies: quasar (or radiative) and radio-mechanical (or maintenance mode) AGN feedback.

1.2.1 Quasar Mode

Within the first billion years, when the massive galaxies were formed, the cold gas was falling onto the supermassive black hole and fueling a vicious accretion at rates of about 10% of the Eddington luminosity. At such a high accretion rates quasars are producing high luminosities which far exceed the luminosties of their host galaxies. The quasar feedback mechanism was probably dominant in giant elliptical galaxies during the very early stage of their formation and evolution. However, due to the presence of hot atmospheres from relatively early in the process of galaxy evolution the accretion rate slowed to 10^{-5} of the Eddington rate and the AGN switched to the radio-mechanical mode, which is described in the following section.

1.2.2 Radio-mechanical Mode

The radio mechanical maintenance mode is dominant at the later stages of giant elliptical galaxies and seems to have a crucial role in preventing and offsetting the gas cooling in the central regions, therefore maintaining low star formation rates in the central regions. This way giant ellipticals remain 'dead and red'.

For comprehensive reviews of hot atmospheres and AGN feedback mechanisms, see McNamara & Nulsen (2012); Werner et al. (2019); Werner & Mernier (2020); Gaspari et al. (2020) and Eckert et al. (2021).

Investigation of different scales on which AGN feedback operates, ranging from *clusters of galaxies*, through *galaxy groups* to *early-type galaxies*, is crucial for understanding the big picture of this feedback mode and fine-tuning the theoretical models and simulations.

The lower-masses of giant ellipticals result in smaller binding energies due to shallower potential wells. Therefore, the energy provided by the AGN can overcome their binding energies more easily (Eckert et al. 2021). Moreover, as already mentioned the 'cooling flow problem' is more severe in giant ellipticals than in galaxy clusters due to the shorter cooling times and larger amount of gas returned by the stellar populations over the lifetime of giant elliptical galaxies (Pellegrini et al. 2018). Therefore, a larger amount of cooled gas can be provided to the supermassive black hole.

Many observational evidences show that powerful radio jets are tuned to provide just the right amount of energy to balance the radiative losses of the X-ray emitting atmospheres, regardless if their are hosted by clusters of galaxies, galaxy groups or giant elliptical galaxies (Churazov et al. 2000; Bîrzan et al. 2004; Rafferty et al. 2006; Nulsen et al. 2009; Hlavacek-Larrondo et al. 2015).

Radio jets inflate X-ray dark cavities by displacing the hot atmospheric gas. Initially, the radio lobes/X-ray cavities expand supersonically, driving weak shocks into the surrounding medium, increasing its entropy. As the radio jets displace the hot gas at the location of the cavities, they perform pdV work on the gas with pressure, p, (see Equation 1.2) and supply internal energy, U, to the cavity with the volume, V. Thus, the total energy required to create the cavity is equal to its enthalpy:

$$H = U + pV = \frac{1}{(\gamma_{\rm bubble} - 1)}\, pV + pV = 4pV \tag{1.22}$$

For the relativistic plasma filling the lobe, we assume $\gamma_{\rm bubble} = 4/3$.

Moreover, to investigate the total mechanical power of the jet, $P_{\rm jet}$, which inflated the radio lobes and displaced the X-ray gas, we need to estimate the age of the cavities. Considering ongoing inflation of radio lobes/bubbles (or cavities) that are reaching the projected distance, R,

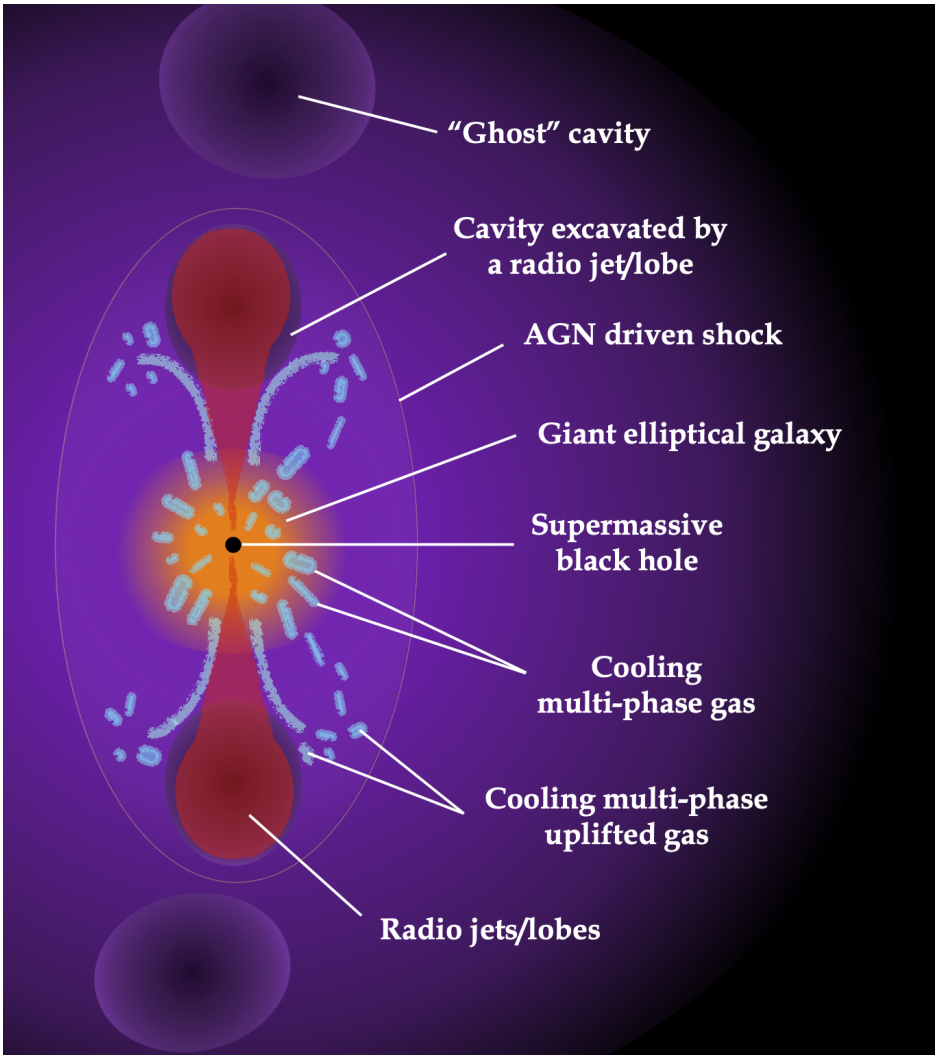

Figure 1.10: An illustration of processes involved in radio-mechanical AGN feedback. The jets inflate lobes, displacing the hot gas, creating X-ray dark cavities. Initially, the lobes expand supersonically, driving weak shocks into the hot atmosphere and increasing its entropy. After detaching from the jets, the lobes/cavities rise buoyantly, driving turbulence and uplifting low entropy gas in their updraft. The uplifted low entropy gas may cool and fall back towards the centre. As the relativistic plasma filling the bubbles looses energy it stops shining in the radio band and the cavities become 'ghost' cavities. Based on Werner & Mernier (2020).

from the nuclear regions at the sound speed[17], which is defined as $c_{\rm s} = \sqrt{\frac{\gamma p}{\rho}}$ and is $\sim$500 km/s for 1 keV gas, we assume a cavity age[18] of:

$$t_{\rm age} = R/c_{\rm s}. \tag{1.23}$$

[17] Another approach is considering that radio lobes rise buoyantly with velocities of $v_{\rm buoy} = \sqrt{2gV/\sigma C}$, where V and $\sigma \approx \pi r^2_{\rm lobe}$ is the volume and the cross-section of the lobe, C is the drag coefficient depending on the lobe geometry and property of the flow ($C \sim 0.6$ for a Mach number $M \sim 0.7$, Bîrzan et al. 2004).

[18] We note that this method will provide only lower limits on the cavity inflation time. Alternatively, one can consider the buoyancy time-scale.

Thus, the enthalpy for two radio lobes inflated in the outburst is twice the $4pV$ work and when divided by the cavity age, $t_{\rm age}$, it gives:

$$P_{\rm jet} = \frac{2 \times 4pV}{t_{\rm age}} \qquad (erg/s). \tag{1.24}$$

This can be interpreted as the ability of the AGN to heat the ambient gas, therefore it should be compared to the cooling luminosity of the X-ray atmosphere.

Most of the jet energy is stored as a thermal energy of the bubbles and potential energy of the displaced gas and not immediately used for heating the atmosphere. As the bubbles rise through the atmosphere, all this energy will be release to the surrounding plasma (Churazov et al. 2001, 2002). Processes that likely contribute to the energy transfer include generation of turbulence in the wakes of bubbles, viscous dissipation, uplift of low entropy gas entrained in the wakes of bubbles, or excitation of internal waves. However, there is no consensus yet about the dominant mechanism (see e.g. Werner et al. 2019, for discussion).

Thermally unstable accretion

Currently, the most popular explanation for the feeding and the radio-mode AGN feedback mechanism is the so called 'precipitation' model, also known as 'chaotic cold accretion' or 'stimulated feedback' (Pizzolato & Soker 2005; Gaspari et al. 2013; Voit et al. 2015b; McNamara et al. 2016; Voit et al. 2019). In favor of this model is the observational evidence of the boosted feedback, when the ambient gas transitions to the multi-phase state, mainly represented by by the ratio of the radiative cooling time $t_{\rm cool}$ and free-fall time $t_{\rm ff}$ (Rafferty et al. 2008; Voit et al. 2015b; Hogan et al. 2017). Moreover, numerous simulations show that gas, disturbed by turbulence, mergers, or uplift (Voit 2018; Gaspari et al. 2018; Tremmel et al. 2019), becomes thermally unstable[19] when the ratio $t_{\rm cool}/t_{\rm tff}$ is between 10–20 (Sharma et al. 2012; Gaspari et al. 2012a, 2013). For a recent review see Voit et al. (2019) and Gaspari et al. (2020).

The main idea behind the 'precipitation' model can be summarized as: an actively accreting supermassive black hole is launching outflows of relativistic plasma in the form of radio jets. These jets are well-collimated and moving supersonically at first, and as they expand and inflate radio lobes, they interact with the ambient gas inducing weak shocks[20] and turbulence, which over time dissipate into heat. Hence, the ambient gas gets heated. Moreover, radio jets can uplift a lower entropy gas from the center, which then 'precipitates' by condensing into cool clouds, which loose angular momentum and randomly fall onto the AGN. The accretion rate increases locally and provides new fuel for the radio jets. This way the well-balanced loop of cool-gas-feeding and radio-jet-heating-and-uplifting is maintained. The graphical representation of this model is shown in Figure 1.10.

AGN duty cycle

The activity of the AGN in giant ellipticals can be described by its duty cycle, or simply: how long the central radio source is 'on duty' and shows activity in the form radio emission from a core, jets and lobes.

[19] In the late 70's, Fabian & Nulsen (1977) and Nulsen et al. (1982) found that hot atmospheres with the typical cooling times seen in early-type galaxies are prone to thermal instability.

[20] The Mach number of these shocks is the order of unity (see for example: Million et al. 2010). For comparison, the Mach numbers of supernova-induced shocks are at least 10 or 100 times larger (Ellison et al. 1994).

In our study of local AGN embedded in a volume-limited sample of massive ellipticals, we found that radio emission is detected in almost all central regions of the galaxies (see Section 6.3 for more details). This indicates a very high duty cycle of local AGN. Moreover, the sign of radio jets-X-ray gas interaction in the form of X-ray cavities is observed for $\sim 80\%$ massive galaxies, what suggests that most of these systems are operating in the radio-mechanical or maintenance mode AGN feedback. Such a high detection rate of radio sources and X-ray cavities appears to be consistent with previous findings (e.g.: Dunn et al. 2010; Brown et al. 2011; Sabater et al. 2019). At first glance, these high rates indicate that AGN duty cycle is very high. It is, however, worth noting that the detected extended radio emission could not always represent the current state of AGN activity and can be just a remnant from a previous outburst.

There are still ongoing debates if the AGN is 'flickering' (switching on and off in some intervals) or is continuously active (always on). Observed outbursts in our sample of massive ellipticals vary in scale and number. Top images of Figure 1.11 shows a single outburst spanning up to 70 kpc from the radio core in NGC 1399 and outburst on a smaller scale in NGC 4649 (Shurkin et al. 2008). Bottom images of Figure 1.11 present galaxies NGC 5813 (Randall et al. 2011, 2015; Eckert et al. 2021) and NGC 5044 (Schellenberger et al. 2020a; Eckert et al. 2021), in which multiple outbursts or generations of cavities are observed. Dashed rings (white, and black) encircle the X-ray cavities displaced by the expanding radio jets and red lines depicts the location of the shocks. Most of the cavities in the images are so-called 'ghost' cavities. The aged radio plasma stops to be visible at radio frequencies and the X-ray brightness dips are the only sign of the past interaction.

The synchrotron spectrum (see Section 1.1.2) could help to better constrain the details of the duty cycle. The spectral slope or so-called spectral index, essentially gives the information about the age of the synchrotron emitting electrons. Therefore, we attempted to estimate the spectral indices in the innermost central regions of the subsample of our massive ellipticals and found that majority of the studied sources show a steep spectral index, indicating that the relativistic plasma aged significant since the last major cycle of AGN activity. For the rest of the galaxies, flat and inverted spectral indices are observed. This suggests the presence of relativistic particles injected recently by the AGN as well as the presence of an older population of particles.

It is worth noting that the AGN activity may be variable, but that is not necessarily what causes the separate bubbles, which are probably more related to magnetic tension in the hot gas. Just like a dripping tap, where the separated drips are due to surface tension. Therefore, the observations could still be consistent with the AGN being always on.

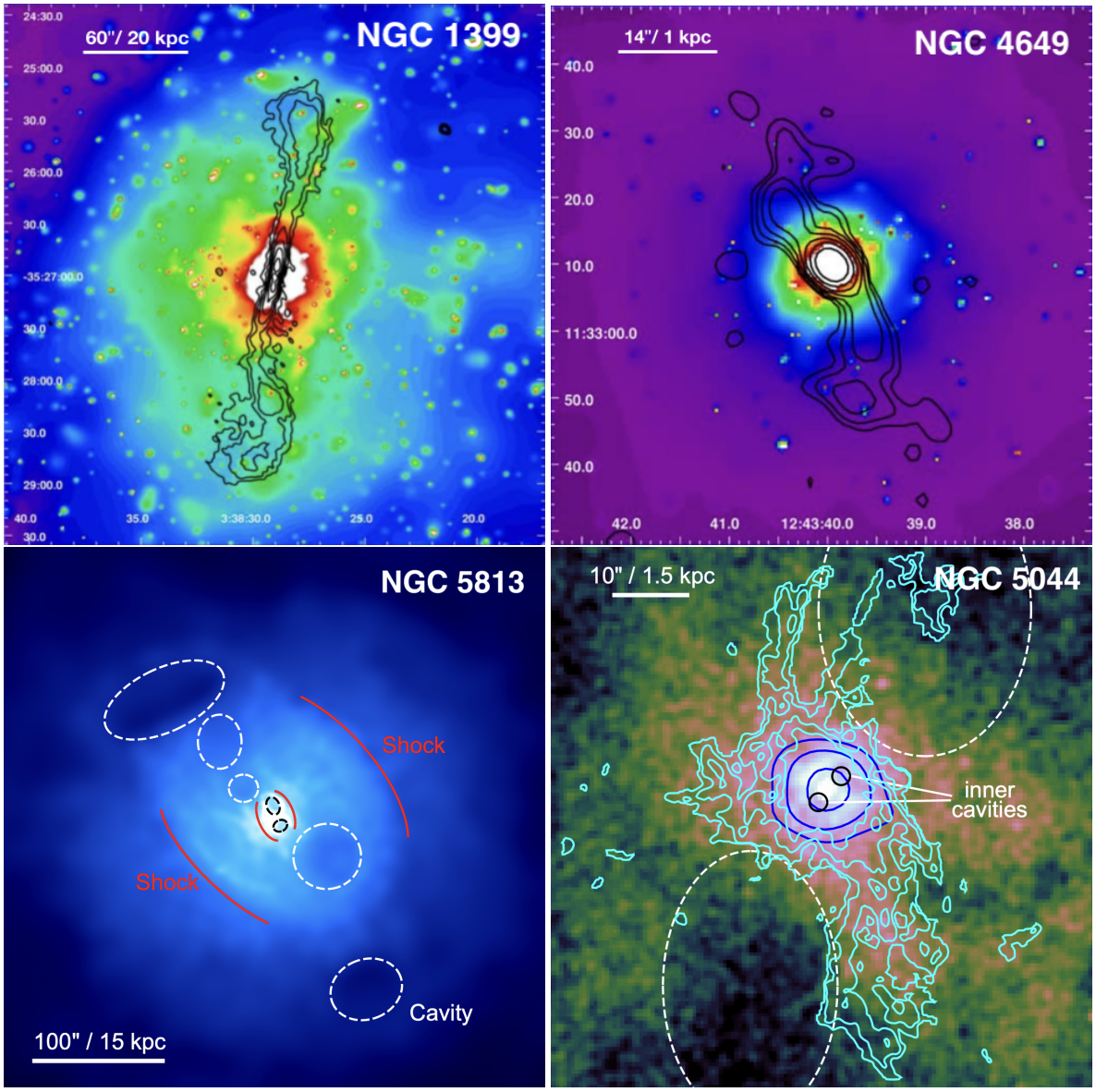

Figure 1.11: **Top images:** Large and small scale radio outbursts shown in black contours on *Chandra* X-ray images of NGC 1399 and NGC 4649, respectively. Both images are published in Shurkin et al. (2008). **Bottom images:** Examples of cavities (white and black circles) from multiple outburst in *Chandra* images of NGC 5813 and NGC 5044. Both images are published in Eckert et al. (2021).

1.3 Radio Emission in Giant Elliptical Galaxies

1.3.1 Radio Classification

In the early 1970's, Fanaroff and Riley first noticed morphological differences between radio sources at 178 MHz (Fanaroff & Riley 1974).

FR I and FR II

Back then, there were only two main classes, which consisted of Fanaroff-Riley Class I (FR I) radio sources, where the radio brightness decreases as a function of distance from the center or so-called 'edge-darkened' sources and Fanaroff-Riley Class II (FR II) radio sources with the brightest features, 'hotspots', created far from the center, where the supersonically expanding jet interacts with the ambient medium. This type is therefore called 'edge-brightened' source. In Figure 1.4, the famous radio galaxy Cygnus A (3C 405) is representing FR II radio sources with the brightest features (hotspots) far from the center (top image; Carilli & Barthel 1996) and 3C 31, a prototypical example of FR I sources, shows continuous decrease in brightness as a function of distance from the nucleus (bottom image; Laing et al. 2008).
Although the two classes are based on morphological differences, there is a clear division in the radio powers too. FR IIs are brighter than the FR I sources with a boundary limit at 2×10^{25} W/Hz (at the frequency of 178 MHz), which is approximately $10^{24.5}$ W/Hz when extrapolated to 1.4 GHz, which is a frequency used in our study (if we consider the average spectral index of -0.7). Capetti et al. (2017a) and Capetti et al. (2017b) build two catalogues of FR I (FRICAT) and FR II (FRIICAT) radio sources.

Majority of the X-ray and optically bright local early-type galaxies in our sample are low-power FR I sources with two potential exceptions of FR II galaxies: NGC 533 and NGC 1600 (Chapter 4; Section 4.5.8).

FR 0

More recent category of Fanaroff-Riley classification includes low-power radio sources with only point-like morphology, which lack of prominent extended radio emission. There is ongoing discussion if the radio emission from these sources can be dominated by the star formation rather than the AGN activity (see Section 4.5.2).

The catalogue FR0CAT of these compact radio sources with linear sizes $\leq 5\,\mathrm{kpc}$ was published by Baldi et al. (2018). They found, from their low redshift ($z \leq 0.05$) sample of giant elliptical galaxies, a possible explanation for the origin and classification of these low-power radio sources. FR 0s are 5 times more frequent in the local Universe in comparison with FR Is or FR II. They could be young radio galaxies (see Section 1.3.2) with a short duty cycle. Due to the fact, that FR 0s tent to have due to lower black hole spin also lower jet bulk speeds than FR Is or FR IIs. Thus, they are likely prone to instabilities in the entrainment, which can disrupt their morphologies causing the point-like, non-extended radio appearance.

In our sample, we found 14 galaxies with point-like radio morphologies that are potential candidates for FR 0 (for more details see Section 4.5.6).

Wide-Angle Tailed

Galaxies with wide-angle tailed radio morphology tend to be related to the interaction of the radio jets with the dynamic ambient X-ray medium. Properties, significant for the wide-angle tailed (WAT) radio sources, are two-sided bend (with wide opening angles) radio jets with clear "warmspots"[21] (Figure 1.12). The radio emission is extending beyond 30 kpc from central host galaxies (Owen & Rudnick 1976; O'Donoghue et al. 1990; Leahy 1993; Missaglia et al. 2019).

Missaglia et al. (2019) published a redshift-limited ($z \leq 0.15$) catalogue of wide-angle tailed galaxies and showed that, while on the one hand, multifrequency properties of WATs are re-

[21] 'Warmspots' are re-brightenings in the jets with the brightness around 1/5 of the radio core brightness.

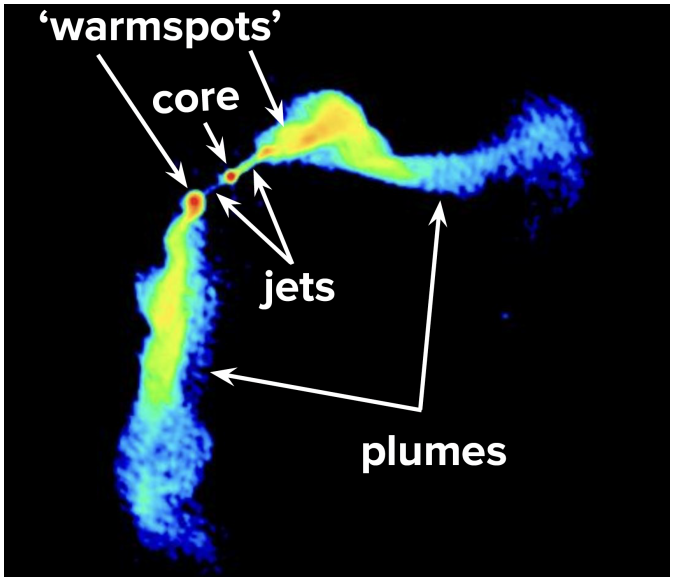

Figure 1.12: Prototypical wide-angle tailed radio galaxy 3C 465 with labeled components. Credit to F. N. Owen; published in Atlas of DRAGNs by Leahy (1993); Leahy et al. (2013).

sembling those of FR I sources, on the other hand, the radio powers are similar to FR II radio sources.

In our sample, we found only a few sources, which could resemble the morphology of WATs: NGC 4782 (see Chapter 4; Section 5.35), 3C 449 (see Chapter 4; Section 5.1) and IC 4296 (see Chapter 4; Section 5.3).

Compact Double

Jimenez-Gallardo et al. (2019) published an COMP2CAT, redshift-limited ($z \leq 0.15$) catalogue of compact double radio galaxies. Their morphologies partially resemble those of FR II and FR 0 radio sources with their radio powers falling into the low-power tail of FR II sources. Moreover, the radio emission of compact double sources is entirely encompassed within their host galaxies and thus their projected linear sizes do not exceed 60 kpc.

In our study, we found one giant elliptical galaxy, NGC 533 (Chapter 4; Section 5.9), the morphology of which could resemble the morphologies of sources in the COM2CAT catalog.

1.3.2 Young Radio Sources

A compact double morphology of the radio emission within the host galaxy without extended features as well as cavities in X-ray atmospheres as a sign of a small-scale interaction of the radio and X-ray plasma are some of the main properties, which describes young radio sources (O'Dea 1998).

We found two candidates in our sample of giant ellipticals which could potentially be classified as young radio sources: NGC 507 (Chapter 4; Section 5.8) and NGC 708 (Chapter 4; Section 5.10).

Chapter 2

Radio Observational Techniques and Data Reduction

Radio studies of giant elliptical galaxies are crucial for our understanding of the physics of maintenance mode AGN feedback. The analysis of complementary X-ray and optical data provides a comprehensive, multifrequency view on the heating and cooling of the X-ray emitting atmospheres, AGN feeding and feedback, and jet-ICM interaction.

In the following sections, we briefly summarize the details of VLA radio observations and data analysis at gigahertz frequencies. The reduction and analysis of the data for of 42 early-type galaxies, from which 19 galaxies are newly observed, are considered as the main contribution of this thesis.

The X-ray data from *Chandra* are adopted from a parent X-ray study of this sample by Lakhchaura et al. (2018). The latter work provides more details of the X-ray data reduction and analysis (for a brief summary see Chapter I or II; Section 4.3.2 and 6.2.2). Moreover, Lakhchaura et al. (2018) also summarize the results of narrow-band imaging and long slit spectroscopic observations of Hα+[NII] line emission with the 4.1 meter Southern Astrophysical Research (SOAR) telescope.

Following sections are also inspired by numerous online-available lectures on radio interferometry and data reduction, e.g.: the VLA Synthesis Workshop[1], CASA-VLBI workshop[2], ANITA lectures[3], and lectures at Charles University, AVČR[4].

2.1 Radio Observational Techniques

2.1.1 Aperture Synthesis Telescope

To compare the *Chandra* X-ray data with the radio synchrotron emission at 1–2 GHz of the early-type galaxies in our sample, high resolution observations of 1 arcseconds are needed. From the diffraction theory, the angular resolution θ in radians is inversely proportional to the diameter, D, of the antenna and studied frequency, ν (with c as speed of light):

$$\theta \propto \frac{c}{\nu}\frac{1}{D} \tag{2.1}$$

[1]VLA, e.g.: R. Perley: http://www.cvent.com/events/virtual-17th-synthesis-imaging-workshop/agenda-0d59eb6cd1474978bce811194b2ff961.aspx.

[2]VLBI, e.g.: C. Spingola https://www.jive.eu/casa-vlbi2020/programme.php.

[3]ANITA, D. Wilner: http://anita.edu.au/lectures/.

[4]AVČR, P. Jachym: https://astro.troja.mff.cuni.cz/vyuka/AST021/.

The largest single-dish radio telescope, the Five-hundred-meter Aperture Spherical Telescope (FAST) in China with a (obvious) diameter of 500 m, does not (by far) satisfy our resolution requirements of 1 arcsecond. A quick calculation will give us a resolution of $\sim 90\,\mathrm{arcsec}$ (considering the frequency of 1.4 GHz and the diameter of 500 m). Therefore, a larger radio dish is needed. However, a larger single-dish telescope would be impossible to build. The solution is offered by a technique known as aperture synthesis, which combines smaller radio antennas (dishes) to simulate/synthesise a larger radio antenna with a diameter of the longest separation between two antennas. In the radio jargon, the separation between two radio antennas is called baseline.

Sir Martin Ryle received a Nobel Prize in 1974 for his pioneering research in this field of radio astronomy (Ryle 1972).

2.1.2 Radio Interferometry

Radio interferometry is used to transform the observed source brightness from the sky or image plane into the total intensity image in the interferometer plane.

The individual pairs of antennas are forming a simplified two-element interferometer, which measures so-called visibilities or coherence (or correlation) of the electric field in both antennas and converts the measured electric fields into voltages. Therefore, the visibilities, $V(u, v$[5]$)$, are the 2D Fourier transform of the sky brightness, $B(l, m)$, or the double integral of the actual brightness of the radio source on the sky with coordinates, l, m, multiplied by the fringe/interference/sine wave pattern produced by the two antennas in the uv- (Fourier) plane on the Earth (with the coordinates, u, v, w). This is demonstrated by Figure 2.1 (left) and defined by van Cittert–Zernike theorem (van Cittert 1934; Zernike 1938):

$$V(u, v) \approx \int\int B(l, m) e^{-i2\pi(ul+vm)} dl dm. \tag{2.2}$$

Moreover, the spacing of the fringe pattern is inversely proportional to the baseline length, B, over the observed wavelength, λ. Thus, as shown in Figure 2.1 (right), the shorter the distance between the two antennas, the broader the sine wave or the larger the separation of the two fringe components. It is worth noting that, on the one hand, when the radio source (smiley-face) is completely covered in one amplitude of the sine wave, the entire signal is recovered, but the individual components of this source cannot be distinguished. The radio source is smaller than the resolution of the baseline and thus unresolved. On the other hand, for larger sources and with shorter baselines, we are able to recover the more diffuse and more extended radio emission, while longer baselines capture the fine details and structures of the source. The source is resolved but to recover the entire emission is more difficult and the combination of several baseline lengths and orientations is necessary.

Importantly, the conversion of the electric field into voltages preserves the properties of the incoming signal, like the amplitude and phase. The visibilities are complex functions with their real and imaginary components or amplitude and phase, respectively. The *amplitude* is the measure of how bright the source is, whereas the *phase* information gives the position of the signal in the Fourier plane. And since the sky brightness distribution, $B(l, m)$, is a real function, the visibility, $V(u, v)$, is Hermitian[6]. Therefore, one pair of antennas or one baseline

[5]The coordinates 'u' ans 'v' are so called spacial frequencies measured in the wavelengths and are essentially tell us how many sinus waves can we fit into the unit space in the plane of the two antennas on the Earth (in the Fourier plane). The 'w' coordinate can be neglected due to small field of view.

[6]For the visibility in $-u$ and $-v$ coordinates, its complex conjugate is: $V(-u, -v) = V^*(u, v)$.

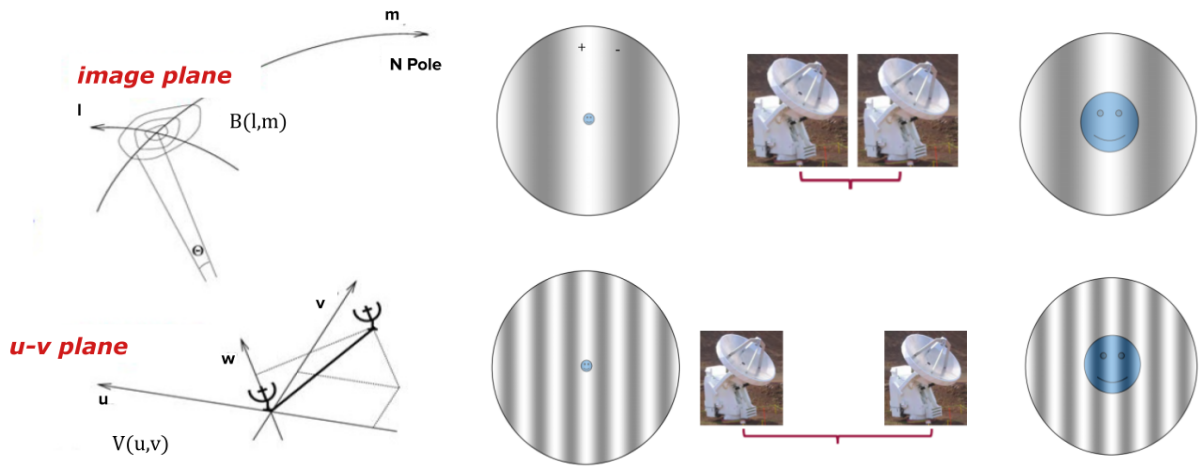

Figure 2.1: **Left:** Sketch of two-element interferometer in the uv-plane with spatial coordinates: u, v, w. The position of the source in the image plane with sky coordinates: l, m is also shown. **Right:** The shorter the distance between two antennas (shorter baseline), the wider the sine (interference) pattern. The '+' and '-' waves of the sinusoidal pattern are shown on the first image of our observed radio signal (top left image). Credit to D. Wilner, CfA.

is represented by two uv-points in the uv-plane. That is the reason why we see horizontally mirrored VLA Y-shape with the mirroring axis passing through the centre of the uv-coverage (Figure 2.2a; top left).

2.1.3 Imaging: CLEAN Algorithm

In the early 70's, Hogbom (Högbom 1974, 2003) used Green Bank 3-antenna interferometer for snapshot observations of radio morphologies from 3C radio sources[7]. Later on, during the data reduction he found that the direct inverse Fourier transform of the observed visibilities to get the sky brightness of the sources would be mathematically incorrect and would result in unreliable outputs with significant artefacts in the image. Problems arise because the uv-plane is not continuously filled (see Figure 2.2a; left). To gain the properly sampled uv-coverage defined by a sampling function, $S(u, v)$[8], long observations of about 12 hours[9] (see Figure 2.2**c**) are required. Combined with the Earth rotation, the gaps in the coverage can be better filled. This would be, however, very ineffective and expensive to perform for each target.

Therefore, Hogbom developed an iterative process to reduce the artefacts in the sky brightness, the so-called 'clean' algorithm[10].

The basic idea of the Hogbom's cleaning loop starts with the assumption that the observed targets on the sky are a collection of discrete point sources. Taking the Fourier transform of the sampling function, $S(u, v)$, will give an idea on the shape of the point source response or PSF (Point Spread Function). In the radio jargon, PSF is also called a 'dirty beam', $s(l, m)$, and it leaves a 'finger-print' or its specific pattern on each observed point on the sky.

[7] 3C stands for the Third Cambridge Catalogue of Radio Sources.

[8] Sampling (coverage) function, $S(u, v)$, is defined to be 1, if there is a measurement in uv-plane and otherwise 0.

[9] Majority of our source in the sample, where observed for around 1 hour. The 2.2b shows the shape of the beam (PSF) and thus the pattern of the artefacts, we should expect in our images.

[10] See also commentary on Hogbom's algorithm by Cornwell (2009).

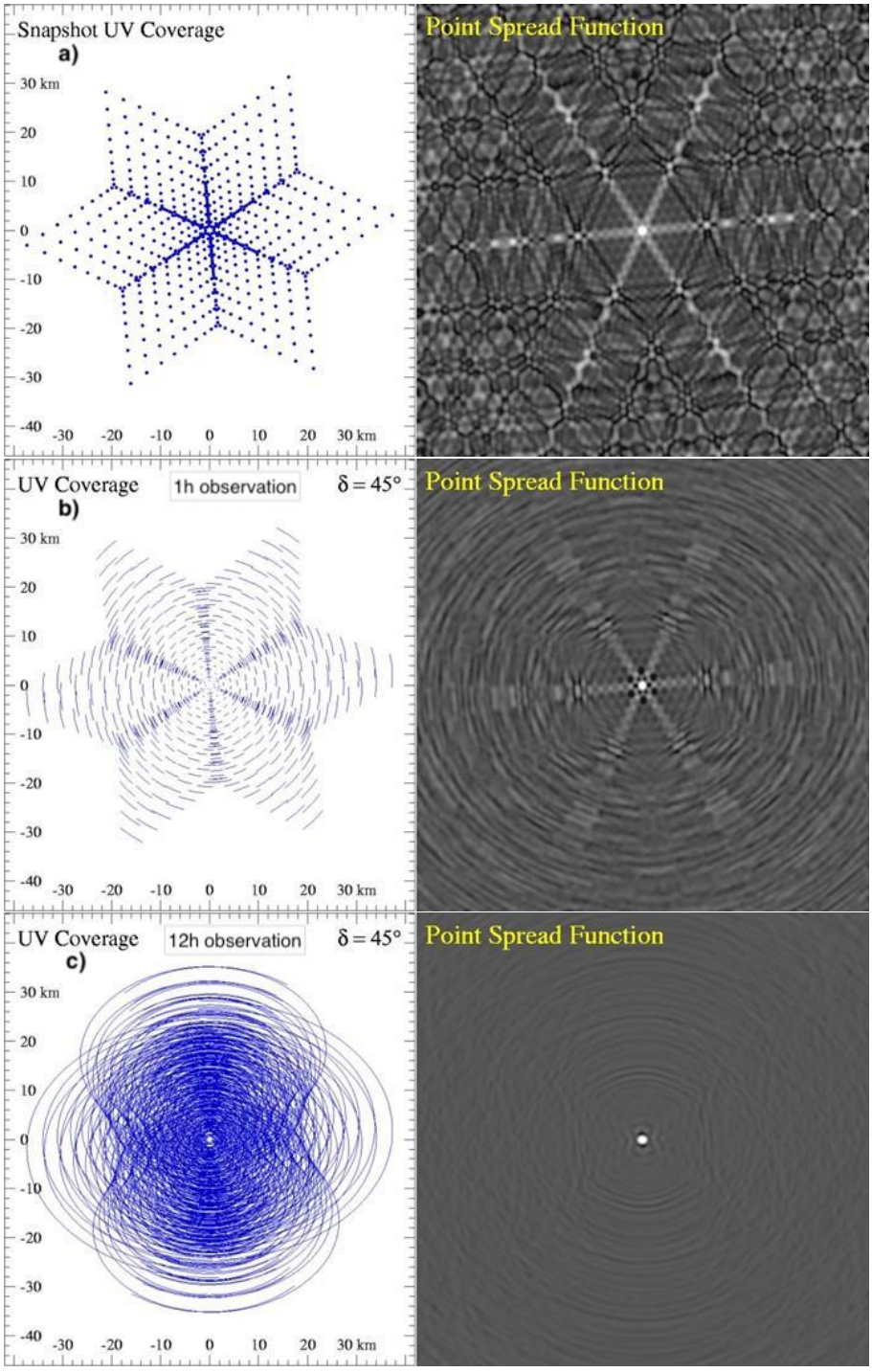

Figure 2.2: The Fourier transform of the sampled visibilities (or uv-coverage) gives a 'dirty beam' or Point Spread Function (PSF) with significant artefacts in form of asterisk shape due to VLA Y-shape design (**a**) for source observed at the declination of 45°. The artefacts are reduced if the Earth rotation is accounted for (especially for 12-hour synthesis observations, **c**). Targets in our sample are usually observed for $\sim$1 hour (**b**). Credit C. Walker, NRAO.

$$S(u,v) \xrightarrow{FT} s(l,m) \tag{2.3}$$

The clean algorithm attempts to remove this pattern or artefacts from the image using deconvolution[11]. First of all, the so-called 'dirty image', $D(l,m)$, is obtained via the inverse Fourier transform of the sampled visibility (the product of sampling function and measured visibilities), $S(u,v) \cdot V(u,v)$. From the Fourier theory, we know that the multiplication in one domain (u,v) is a convolution ($\circledast$) in the other domain (l,m). Thus, $S(u,v) \cdot V(u,v)$ can be approximated by the true image of the sky, $B(l,m)$, convolved by the 'dirty beam' $s(l,m)$:

$$D(l,m) \xrightarrow{FT^{-1}} S(u,v) \cdot V(u,v) \approx s(l,m) \circledast B(l,m), \tag{2.4}$$

Hence, deconvolving the 'dirty image', we can recover this sky brightness of the source, $B(l,m)$.

Hogbom's CLEAN in practice

The clean algorithm is implemented in the Common Astronomy Software Applications[12] (CASA) package (McMullin et al. 2007), where also calibration and analysis on 'cleaned' images can be performed (see Section 2.3.2 and 2.3.3). The CASA version 4.7.2 and 5.0.0 is used (as well as pipeline version 1.3.11.)

The first step of this cleaning loop in CASA is to initialize a residual map to the 'dirty image'. Next, we need to identify the strongest intensity peak (pixel with maximum intensity) in the residual map as a point source and add it into the model or 'clean component list' via creating a mask around it. Afterwards, the component is convolved with the 'dirty beam' and the fraction of the peak is subtracted from the residual map. We iteratively continue to identify the next strongest peaks in the residual map, until some stopping criteria are reached like: the desired flux density threshold in the residual image, the maximum number of clean components, and so on. The next step of the loop is producing the final 'restored' image, which includes the creation of a model with all sources in the 'clean component list'. Afterwards, we convolve the model with an elliptical Gaussian, which is fitted to the main lobe of the 'dirty beam' called 'clean beam'. Lastly, we add the residual map including noise and the source structure below the threshold as well as the shape of the 'clean beam' and thus create the final total intensity image or 'cleaned' image of the target.

This way, we recover the total flux densities of the observed target in the common radio astronomy unit of Jansky (Jy), named after Karl Jansky, who first observed the radio emission from the center of our galaxy. The Jy units are connected to metric and cgs units in following way: $1\,\mathrm{Jy} = 10^{-26}\,\mathrm{Wm^{-2}Hz^{-1}} = 10^{-23}\mathrm{ergs^{-1}cm^{-2}Hz^{-1}}$.

Cotton-Schwab CLEAN

More advanced algorithm is called the Cotton-Schwab CLEAN (CSCLEAN), that works in two cycles: minor and major. First of all, the visibilities are gridded and weighted. Then the Fast Fourier transform (FFT) is used to create a 'dirty image'. The inner loop or minor cycle operates solely in the image domain: finding the 'clean components', adding them into the model, and iteratively finding the next bright points and subtracting the beam from the image. The outer loop or major cycle implements the FFT between the image and visibilities domains. The

[11] Deconvolution is widely used in radio astronomy, an inverse process of convolution. From the signal distorted by some filter (PSF), this original signal can be restored.

[12] https://casa.nrao.edu/

model of the image produced in the minor cycle is FFT-ed back to the visibility domain, re-gridded, and subtracted from the visibilities, what creates a new residual image that is then gridded, weighted, and FFT-ed again to the image domain for the next iteration. This iterative process is continued until the previously-mentioned stopping criteria are reached. And the recovery of the final image is consistent with Hogbom's cleaning loop as described in the previous Section 2.1.3.

Weighting

Three types of weighting can be used to obtain rather higher surface brightness, sensitivity, or resolution of the image: natural, robust, and uniform as well as tapering[13].

The main aim of our statistical study is to detect radio emission and its morphology in nearby X-ray and optically bright early-type galaxies, therefore we use Briggs weighting scheme (Briggs 1995, with CASA parameter `robust=0`), which offers a compromise between the spatial resolution and surface brightness sensitivity. For sources with a point-like emission, the natural weighting is used, whereas for some sources with extended emission uv-tapering is applied.

MultiTerm MultiFrequency CLEAN

The major upgrade of the VLA in 2011 allowed observations in multiple frequencies. This thesis works solely with the VLA L-band receiver data, which spans the frequency range between 1–2 GHz.
Simultaneously imaging with many frequencies across the entire band is called MultiFrequency Synthesis (MFS) (Rau & Cornwell 2011). On the one hand, the multifrequency observations add uv-points to cover the uv-plane in more detail than single-frequency observations. On the other hand, it also introduces frequency-dependent variation that needs to be accounted for, otherwise they result in additional image artefacts. Moreover, the MultiTerm MultiFrequency Synthesis (`MTMFS`) algorithm provides the ability to simultaneously image and fit for the spectral behaviour of bright sources in each pixel. Polynomial Taylor-term expansion in frequency is used to approximate the spectrum or the frequency dependence of the sky emission.

Half of the targets in our sample are obtained with the post-upgraded VLA, thus the use of `MTMFS` with the second-order Taylor polynomial CASA `clean/tclean`[14] parameter `nterms=2`) is preferred. In the case of pre-upgraded VLA observations, most of them contain at least two frequencies and thus the `MTMFS clean` provides a reliable solution as well.

Self-calibration

If the image artefacts are not reduced by the standard calibration steps (see Section 2.3.2) and `cleaning` loop, another useful approach can be used called self-calibration. When the ratio of the peak intensity to the RMS noise, or the so-called dynamic range of the total intensity images, reaches values of about 100, the source itself can be used to calibrate the phases and potentially the amplitudes of the visibility as a function of time.

[13] More details about different weigthings can be found in the CASA Cookbook and User Reference Manual (https://casa.nrao.edu/Release4.1.0/doc/UserMan/UserMansu257.html).

[14] `tclean` stands for 'test `clean`' and it is an improved version of `clean` algorithm.

2.2 Very Large Array

Most of our results are based on observations with the VLA, thus the main properties of this array will be discussed.

The technology of aperture synthesis telescopes is also used by the Very Large Array (VLA)[15] spreading over the Plains of San Agustin. VLA is located at around 80 km from Socorro in New Mexico, US and consists of 27[16] parabolic radio dishes of 25 meters in diameter which all together form a shape resembling the letter Y[17] (see Figure 2.3; left).

Figure 2.3: **Left:** The famous 'Y'-shaped configuration of VLA antennas spreaded over the Plains of San Agustin in New Mexico. Credit: D. Finley. **Right:** Zoom-in on one 25-m antenna from the array. Several dish components are depicted. Especially important is the position of the L-band receiver feed, which is the only receiver used for our observations.

2.2.1 VLA Receiver Bands

Each VLA antenna is receiving the signal in a wide range of frequencies, from 54 MHz–50 GHz. To focus only on a specific frequency range, one of the 8 cryogenically cooled feed-horn receivers can be used.

The most relevant for this work is the L-band receiver spanning the frequency range 1–2 GHz and centered at 1.5 GHz (see Figure 2.3; right, for the location on the dish).

2.2.2 VLA Configurations and Resolution

VLA operates in four different configurations (Figure 2.4). The dishes can be put closer or further from each other (through the 64 km-long rail tracks). When the pairs of antennas are closest to each other, they simulate a radio antenna with the diameter of $\approx$ 1 km and the array is in the D configuration. This leads to the largest spacial sensitivity, but the smallest angular resolution with VLA. Thus, the D configuration is used to detect more diffuse and extended emission.

[15]The array is under the administration of the National Radio Astronomy Observatory (NRAO) based in Socorro (New Mexico, US) with another institution located in the West Virginia, US. More details can be found on their websites: https://science.nrao.edu/facilities/vla.

[16]There is one more antenna as a back-up, when the others need to maintained.

[17]The Y-shape of the array gives an uniform coverage of the uv-plane at almost all declinations (from 90 to -30°).

VLA Configuration	B_{max} (km)	B_{min} (km)	Resolution (arcsec)	LAS (arcsec)
A	36	0.7	1.3	36
B	11	0.2	4.3	120
C	3	0.04	14	970
D	1	0.04	46	970

Table 2.1: The properties of VLA configurations. The maximum (B_{max}) and minimum (B_{min}) baseline length (antenna' separation), the resolution in L-band at frequencies 1–2 GHz for each configuration and the largest angular scale (LAS) of the structure visible to the array. This information can be found at the NRAO websites (https://science.nrao.edu/facilities/vla/docs/manuals/oss/performance/resolution).

On the other hand, the largest separation of the antennas is 35 km for the A configuration, resulting in the highest angular resolution possible with VLA on the expense of the lowest sensitivity to the extended diffuse structures. VLA antennas in the A configuration are the best to resolve the fine structure of the central region. Table 2.1 summarizes the properties of each VLA configuration like the minimum and maximum baseline length, its resolution in L-band (in the frequency range between 1–2 GHz), as well as the largest angular scale (LAS) of the structure observable with the particular configuration.

In our work, we concentrated on each of the four VLA configurations in order to be sensitive to both the high resolution details of the fine radio structures of the central region and the diffuse, extended radio emission further from the core in the form of radio jets and lobes. This mechanism can be explained on the basis of radio interferometry (see Section 2.1.2).

Figure 2.4: Radio source Hercules A shown in all four VLA configurations. The longest baseline of each configuration is given in kilometers. Images are adapted from NRAO/AUI/NSF.

2.3 Radio Data Reduction and Analysis

2.3.1 VLA Observations

The radio data of early-type galaxies in our sample observed by the VLA between 1984 and 2020 spanning the frequency range between 1–2 GHz are available in the NRAO VLA archive[18].

We reduced and image VLA data obtained both before (*historical* data) and after the major upgrade of the Very Large Array in 2011 (*Karl G. Jansky* VLA data; Perley et al. 2009, 2011).
To study multiscale features of giant elliptical galaxies, we gathered data from all available configurations (A, B, C, and D) for each source (see Chapter 4; Table 3.1).
The historical data consist of only one or two spectral windows with tens of 100–1000 kHz-wide channels, whereas the Karl G. Jansky VLA data have tens of spectral windows with up to hundreds of 3000 kHz-wide channels, which makes the size of those data sets significantly larger. This fact affects our approach to the calibration methods, which we used for historical and Karl G. Jansky VLA data.
The pre-upgrade or historical VLA data sets were analysed for 33 galaxies and Karl G. Jansky VLA data for 20 massive ellipticals in the sample in various configurations (details are given in Chapter 6; Table 3.1). For all data, the primary flux, amplitude and bandpass calibrator were observed at the beginning or end of the observation and the secondary calibrator used for phase calibration was observed in between each scan of the main target.

Moreover, to complete the VLA A configuration data for the sample of early-type galaxies, new VLA radio observations were obtained in 2015 (marked in Chapter 4; Table 3.1) by *). It is worth nothing that the priority to have VLA A configuration observation for all galaxies lies in its high resolution of around 1 arcsecond, which matches with the on-axis point-spread function (PSF) for the *Chandra* X-ray observatory. This allows the comparison of the emission at both radio and X-ray frequencies on the same scale.

2.3.2 Calibration

We used the NRAO's Common Astronomy Software Applications (CASA)[19] package (McMullin et al. 2007) versions 4.7.2 and 5.0.0 for data calibration, reduction, imaging, and analysis. It is a powerful tool that helps us to obtain calibrated total intensity images of the observed radio emission from our sample of galaxies.

Two calibration methods are used for the historical and Karl G. Jansky VLA data sets. The data sizes of later observations are larger than the historical due to the increased bandwidth of the observations after the upgrade to the Wideband Interferometer Digital ARchitecture (WIDAR) correlator system. For the Karl G. Jansky VLA data ($\sim$ 20-100 GB), we use the more effective pipeline calibration method (CASA pipeline version 1.3.11). In the case of historical data, a manual calibration approach is chosen following the 'Jupiter continuum calibration tutorial' available on the VLA NRAO website[20]. Both approaches are using essentially very similar steps to calibrate the data, that will be briefly described in the following section (see also radio data reduction sections in Chapter 4 and 6, Sections 6.2 and Sections 6.2.1, respectively).

Initial step[21] of the calibration includes corrections for antenna position offsets. Afterwards, a careful approach was followed to flag the Radio Frequency Interferences (RFIs). First, the

[18]https://archive.nrao.edu/archive/advquery.jsp
[19]https://casa.nrao.edu/
[20]https://casaguides.nrao.edu/index.php/Jupiter:_continuum_polarization_calibration
[21]Historical VLA data were recorded in '.xp*' format, thus they first need to be imported into measurement set ('.ms') format.

auto-flagging with CASA algorithm `tfcrop` identifies the outliers in the time-frequency plane. Then, we use manual inspection of data in the CASA viewing tool `plotms` and flag the remaining high and low amplitude RFIs and outliers. The RFIs usually severely affect certain spectral windows around 1.4 GHz[22]. Therefore, spectral windows 8 and 9 are entirely flagged for every data set. The amount of flagged data varies for each observation. In general, from 40% to 80% of the unflagged data are left for further analysis. For example, in our single source study of IC 4296, around 50% of the target data remains unflagged (see Chapter 6, Section 6.2.1).

Next, we use a L-band model by Perley & Butler (2013) to set the flux density scale for the flux calibrators. The names of the VLA flux calibrators used in each observation are given in Chapter 6; Table 3.2. The initial gain calibration of the central channels accounts for the small phase variations with time in the bandpass. Then, the bandpass calibration for VLA flux calibrator is performed, including the relative delays of each antenna with respect to the reference antenna and derivation of complex bandpass solutions in order to include variations of gain with frequency. Afterwards, we determine the complex gains for both calibrators. And finally, the obtained calibration solutions are applied to our target.

2.3.3 Imaging

After calibration, we proceed to determine the total flux density maps or images of our targets. The various spatial scales of radio emission require an individual approach to each source with different combinations of weightings, gridders, convolvers, and uv-tapers[23]. However, due to the fact that the majority of sources were obtained in multiple frequencies CASA `clean` or TCLEAN algorithm in the MultiTerm MultiFrequency (MTMFS) synthesis mode (Rau & Cornwell 2011), a second order Taylor polynomial parameter (`nterms = 2`, McMullin et al. 2007), and the briggs weighing (Briggs 1995) with `robust=0` is used.

When the dynamic range (or the ratio between the peak brightness and RMS noise of the image) reaches values about 100 in the VLA image, two or three cycles of phase and possibly one cycle of amplitude and phase self-calibration are performed[24].

[22] https://science.nrao.edu/facilities/vla/docs/manuals/obsguide/rfi

[23] More details of different parameters can be found at e.g. CASA tutorial for imaging (https://casaguides.nrao.edu/index.php?title=VLA_CASA_Imaging-CASA5.7.0)

[24] Recent comprehensive tutorial on self-calibration can be found at https://casaguides.nrao.edu/index.php?title=VLA_Selfcalibration_TutorialCASA5.7.0

Chapter 3

A Complete Sample of Giant Elliptical Galaxies in the Local Universe

3.1 Sample Selection

We base our study on the extended sample of the nearest X-ray and optically brightest massive early-type galaxies discussed in Dunn et al. (2010). Their parent sample is the catalog of Beuing et al. (1999), which contains 530 elliptical and elliptical/lentilcular galaxies brighter than the total Johnson B-band magnitude of $B_{\rm T} = 13.5$ and has a 90 per cent completeness. Beuing et al. (1999) also provide X-ray luminosities or upper limits for 293 galaxies, based on *ROSAT* All-Sky Survey (RASS) data. These measurements were updated by O'Sullivan et al. (2001), who also used data from *ROSAT* pointed observations.

An extensive *Chandra* X-ray study of this sample was performed by Lakhchaura et al. (2018), who slightly modified the selection criteria and increased its completeness. Our paper is a radio counterpart to the X-ray study of Lakhchaura et al. (2018). Our final selection criteria combine the criteria of Dunn et al. (2010) and Lakhchaura et al. (2018) and are as follows:

- lower limit of the X-ray luminosity within 10 kpc from the center of galaxy: $L_{\rm X} > 10^{40}\,{\rm erg\,s^{-1}}$ in the 0.5–7 keV band
- upper limit of the optical absolute magnitudes: $B_T < -20$ (total Johnson B-band magnitudes)
- volume restriction: all sources are within the distance of 100 Mpc
- declination cut: DEC $>$ -40 degrees to ensure radio coverage with the VLA

We note that while the X-ray luminosities of O'Sullivan et al. (2001) were total luminosities, which also included the contribution from point sources, such as the central AGN and X-ray binaries, our X-ray luminosities based on the measurements of Lakhchaura et al. (2018) only refer to the hot X-ray emitting atmospheres within 10 kpc from the center of the galaxy. Additionally, the intrinsic 2–10 keV central X-ray point source luminosities were estimated from the power-law components of the spectral models for a sub-sample of galaxies, for which central X-ray point source emission was detected (Lakhchaura et al. 2018).

Given these selection criteria, our volume-limited sample of the X-ray and optically brightest nearby early-type galaxies (41 giant elliptical galaxies and 1 lenticular) has a high degree of completeness. However, one source, NGC 1521, which meets our volume and X-ray/optical

brightness criteria, has no dedicated VLA L-band observations in the VLA National Radio Astronomy Observatory (NRAO) archive[1]. This source is a part of the NRAO VLA Sky Survey (NVSS) and the radio source detection was published at the $2\,\sigma$ significance (Brown et al. 2011). Although, we did not confirm the presence of the radio emission within the sensitivity limit of the NVSS survey[2]. Thus, we decided not to include this source in our further analysis.

The main goal of our study is to extend the radio sample of Dunn et al. (2010) to the 42 nearest X-ray and optically brightest galaxies with the highest resolution VLA A configuration data in the L-band spanning the frequency range 1–2 GHz and centered at $\sim$ 1.5 GHz.
We obtained new VLA A observations for 20 giant elliptical galaxies (proposal ID: 15A-305, PI: N. Werner) to complement the available archival radio data for the entire sample[3]. The highest resolution array configuration was chosen to match the resolution of images from the *Chandra* X-ray observatory. Moreover, to be sensitive not only to the fine structure of the central region, but also to more diffuse and extended radio emission, we decided to complement the high resolution VLA A configuration data with data from the more compact C and D VLA configurations.

[1] https://archive.nrao.edu/archive/advquery.jsp
[2] The Root Mean Square (RMS) noise in the total intensity NVSS survey images is $\sim$ 2.5 mJy (Condon et al. 1998)
[3] Unfortunately, NGC 1521 was missed while proposing for the new VLA observations.

3.2 Observational Details

Table 3.1: The main VLA observational information about the early-type galaxies in our sample between 1–2 GHz. The columns are ordered as follows: (1) source name; (2) VLA configuration; (3) NRAO VLA archive project code; (4) date (year-month-day; some source has been observed during multiple days or within multiple VLA projects); (5) VLA primary flux density calibrators from the NRAO VLA archive: details can be found at https://science.nrao.edu/facilities/vla/observing/callist.

Source Name	Config VLA	Project (Code)	Date (year-month-day)	Primary Flux Density Calibrator
3C 449	A	AB920	1999-Jul-18	3C 84
3C 449	C	AM0740	2002-Dec-21	3C 84
IC 1860	A	AG0748	2009-Jun-19	3C 84
IC 4296*	A	15A-305	2015-Jul-11	3C 286
IC 4296	D	18A-317	2018-Oct-26	3C 286
NGC 57*	A	15A-305	2015-Jul-03	3C 48
NGC 315	A	AM670/AB920	1999-Jul-18/2000-Dec-04	3C 286
NGC 315	B	AL538	2001-Mar-10	3C 286
NGC 315	C	AL538	2001-Jul-17	3C 48
NGC 410*	A	15A-305	2015-Jun-28	3C 48
NGC 499	A	AG748	2007-Jun-09/14	3C 84
NGC 507*	A	15A-305	2015-Jun-19	3C 48
NGC 507	C	AC0785	2005-Aug-17	3C 84
NGC 533*	A	15A-305	2015-Jun-27	3C 48
NGC 533	B	AC0849	2006-Sep-02/04/10	3C 84
NGC 708	AB	AC470	1987-Nov-06	3C 84
NGC 708	C	13A-131	2013-Aug-18	3C 286
NGC 741	A	AB920	1999-Jul-18	3C 84
NGC 741	C	13A-387	2013-Jul-26	3C 48
NGC 777*	A	15A-305	2015-Jun-21	3C 48
NGC 777	C	AC0488	1997-Sep-18	3C 286
NGC 1132	C	AC0488	1997-Sep-18	3C 286
NGC 1316	BA	AH787	2002-May-31/Jun-01	3C 84
NGC 1316	CD	AW0110	1985-Nov-03	3C 48
NGC 1399*	A	15A-305	2015-Jun-20	3C 138
NGC 1404*	A	15A-305	2015-Jun-20	3C 138
NGC 1404	CD	AT0285/6	2003-Jan-31/Feb-01	3C 84
NGC 1407*	A	15A-305	2015-Jun-28	3C 138
NGC 1407	B	12A-139	2012-Jun-10	3C 147
NGC 1407	C	12A-139	2012-Apr-22	3C 147
NGC 1550*	A	15A-305	2015-Jun-24	3C 138
NGC 1550	C	AC0488	1997-Sep-18	3C 286
NGC 1600	A	AB0289	1984-Dec-15	3C 48
NGC 2300*	A	15A-305	2015-Jun-18	3C 147
NGC 2300	D	AS0552	1995-Mar-27	3C 48
NGC 3091*	A	15A-305	2015-Jun-19	3C 286
NGC 3091	AB	AM0344	1991-Dec-15	3C 286
NGC 3923*	A	15A-305	2015-Jul-01	3C 286
NGC 3923	C	AW0110	1984-Jun-10	3C 286
NGC 4073*	A	15A-305	2015-Jun-24	3C 286
NGC 4125	D	14B-396	2015-Oct-17	3C 286
NGC 4261	A	AL0693	2007-Jun-08/09	3C 286
NGC 4261	C	AL0693	2008-May-24/25	3C 286
NGC 4374	A	BH210	2015-Jul-17	3C 286
NGC 4374	B	BW0003	1994-Aug-04	3C 286

Table 3.1 - continued. The CASA imaging results for our VLA sample.

Source Name	Config VLA	Project (Code)	Date (year-month-day)	Primary Flux Density Calibrator
NGC 4374	C	14A-468	2014-Dec-24	3C 286
NGC 4406*	A	15A-305	2015-Jul-02	3C 286
NGC 4406	D	AS623	1997-Nov-29	3C 286
NGC 4472*	A	15A-305	2015-Jun-27	3C 286
NGC 4472	C	AB0412	1986-Nov-26	3C 286
NGC 4486	A	AB0920	1999-Jul-18	3C 286
NGC 4486	B	16A-245	2016-Sep-17	3C 286
NGC 4486	C	AO0149	2000-May-15	3C 286
NGC 4552	A	AC301	1991-Aug-24	3C 286
NGC 4552	C	16A-275	2016-Apr-04	3C 286
NGC 4636	A	AF389	2002-Mar-12	3C 286
NGC 4636	C	17A-073	2017-May-25	3C 286
NGC 4649	A	AC301	1991-Aug-24	3C 48
NGC 4649	D	17A-073	2017-Jun-01	3C 286
NGC 4696	A	AT211	1998-Apr-23	3C 286
NGC 4696	BC	AB623	1992-Feb-06	3C 286
NGC 4778	AB	AL0227	1990-Jul-09	3C 286
NGC 4778	C	AB1150	2005-Jul-30/31	3C 286
NGC 4782	A	AC0104	1984-Dec-26	3C 286
NGC 4782	BA	AL0227	1990-Jul-09	3C 286
NGC 4936*	A	15A-305	2015-Jun-20	3C 295
NGC 5044	A	AD294	1992-Nov-27	3C 286
NGC 5044	BA	15A-243	2015-May-25	3C 286
NGC 5044	D	11B-093	2011-Dec-03	3C 286
NGC 5129*	A	15A-305	2015-Jun-30	3C 286
NGC 5419*	A	15A-305	2015-Jun-18	3C 295
NGC 5419	B	AE31	1984-Feb-26	3C 286
NGC 5419	CD	AE31	1984-Jul-07/8	3C 286
NGC 5813	A	AF188	1990-Apr-19	3C 48
NGC 5813	B	AW202	1988-Jan-30	3C 286
NGC 5813	C	AC0488	1997-Sep-17	3C 286
NGC 5846	A	AF389	2002-Mar-12	3C 286
NGC 5846	B	AW0202	1988-Jan-30	3C 286
NGC 5846	CD	AM0197	1987-Feb-24	3C 48
NGC 7619*	A	15A-305	2015-Jul-05	3C 48
NGC 7619	C	AC0488	1997-Sep-17	3C 286

(1) sources marked with * sign are our new VLA A observations within project 15A-305)

3.3 Radio Data Analysis: Results

Table 3.2: Radio imaging results for the sample of 42 early-type galaxies in several VLA configurations. The columns are listed as follows: (1) 3C, IC and NGC source names; (2) VLA configuration; (3) luminosity distance mostly derived from surface brightness fluctuations, a redshift-independent method (see Note); (4) the linear scale in kiloparsecs per arcseconds; (5) the radio morphology classification (Figure 4.1 and Section 4.2); (6) the largest linear extent in kpc; (7) the restoring beam from the CASA clean algorithm in arcseconds and corresponding (8) position angle; (9) the peak intensity in Jy/beam of the radio source in the total intensity image in the L-band (the frequency range between 1–2 GHz, centered at 1.5 GHz); (10) the integrated total flux density in Jy in L-band; (11) the total radio power in W/Hz; (12) the RMS noise ($\sigma_{\rm RMS}$) values of each total intensity image in Jy/beam. Details of each observation can be found in Table 3.1.

Source Name	Config VLA	Distance (Mpc)	Scale (kpc/″)	Radio Class	Extend (kpc)	Beam (″ × ″)	PA (deg)	$\mathbf{S_{peak} \pm eS_{peak}}$ (Jy/b)	$\mathbf{S_{1.5\,GHz} \pm eS_{1.5\,GHz}}$ (Jy)	$\mathbf{P_{1.5\,GHz} \pm eP_{1.5\,GHz}}$ (W/Hz)	RMS (Jy/b)
3C 449	A	$72.5^{L\#}$	0.352	J/L	36.6	1.9×1.4	78.2	$(1.46 \pm 0.06) \times 10^{-2}$	$(2.55 \pm 0.10) \times 10^{-1}$	$(1.60 \pm 0.06) \times 10^{23}$	1.0×10^{-4}
3C 449	C	$72.5^{L\#}$	0.352	J/L	446.7	13.2×11.7	5.5	$(1.16 \pm 0.05) \times 10^{-1}$	$(3.13 \pm 0.12) \times 10^{0}$	$(1.97 \pm 0.08) \times 10^{24}$	1.1×10^{-4}
IC1860	A	95.75^{L}	0.465	PS	-	3.0×1.2	8.9	$(1.28 \pm 0.05) \times 10^{-2}$	$(1.30 \pm 0.06) \times 10^{-2}$	$(1.43 \pm 0.06) \times 10^{22}$	1.0×10^{-4}
IC 4296*	A	47.31^{L}	0.230	J/L	108.1	4.0×3.3	-12.5	$(2.20 \pm 0.09) \times 10^{-1}$	$(3.84 \pm 0.15) \times 10^{0}$	$(1.03 \pm 0.04) \times 10^{24}$	6.0×10^{-5}
IC 4296	D	47.31^{L}	0.230	J/L	437.0	84.3×22.6	-7.7	$(5.31 \pm 0.21) \times 10^{-1}$	$(8.56 \pm 0.34) \times 10^{0}$	$(2.29 \pm 0.09) \times 10^{24}$	1.8×10^{-4}
NGC 57*	A	77.15^{L}	0.375	PS	-	1.8×1.0	70.1	$(3.26 \pm 0.13) \times 10^{-4}$	$(5.41 \pm 0.29) \times 10^{-4}$	$(3.85 \pm 0.21) \times 10^{20}$	1.0×10^{-5}
NGC 315	A	56.01^{L}	0.272	J/L	13.4	1.6×1.4	66.4	$(4.40 \pm 0.18) \times 10^{-4}$	$(3.39 \pm 0.37) \times 10^{-2}$	$(1.27 \pm 0.14) \times 10^{22}$	8.9×10^{-5}
NGC 315	B	56.01^{L}	0.272	J/L	154.2	4.2×3.7	82.0	$(4.61 \pm 0.18) \times 10^{-1}$	$(1.27 \pm 0.05) \times 10^{0}$	$(4.77 \pm 0.19) \times 10^{23}$	4.9×10^{-5}
NGC 315	C	56.01^{L}	0.272	J/L	326.1	13.4×11.8	-13.2	$(4.62 \pm 0.18) \times 10^{-1}$	$(2.04 \pm 0.08) \times 10^{0}$	$(7.66 \pm 0.31) \times 10^{23}$	7.3×10^{-5}
NGC 410*	A	66.0^{L}	0.320	PS	-	3.1×1.2	66.6	$(4.62 \pm 0.18) \times 10^{-3}$	$(4.95 \pm 0.21) \times 10^{-3}$	$(2.58 \pm 0.11) \times 10^{21}$	2.8×10^{-5}
NGC 499	A	60.74^{L}	0.295	NS	-	1.4×1.2	-61.5	-	-	-	1.2×10^{-4}
NGC 507*	A	59.83^{L}	0.290	D	13.2	2.7×1.1	67.9	$(1.70 \pm 0.07) \times 10^{-3}$	$(7.20 \pm 0.40) \times 10^{-3}$	$(3.08 \pm 0.17) \times 10^{21}$	2.8×10^{-5}
NGC 507	C	59.83^{L}	0.290	D†	36.0	13.6×12.7	62.8	$(8.92 \pm 0.36) \times 10^{-3}$	$(1.00 \pm 0.04) \times 10^{-1}$	$(4.28 \pm 0.17) \times 10^{22}$	7.8×10^{-5}
NGC 533*	A	61.58^{L}	0.299	C†	1.1	1.2×1.1	-62.3	$(1.02 \pm 0.04) \times 10^{-2}$	$(2.41 \pm 0.10) \times 10^{-2}$	$(1.09 \pm 0.04) \times 10^{22}$	1.9×10^{-5}
NGC 533	B	61.58^{L}	0.299	C	2.8	4.8×3.7	-12.5	$(4.26 \pm 0.17) \times 10^{-1}$	$(6.95 \pm 0.30) \times 10^{-1}$	$(3.15 \pm 0.13) \times 10^{23}$	4.4×10^{-3}
NGC 708	AB	64.19^{L}	0.312	D†	15.0	3.9×3.1	89.6	$(1.42 \pm 0.06) \times 10^{-2}$	$(6.49 \pm 0.31) \times 10^{-2}$	$(3.20 \pm 0.15) \times 10^{22}$	3.0×10^{-4}
NGC 708	C	64.19^{L}	0.312	D†	38.6	8.3×5.0	-72.7	$(1.29 \pm 0.05) \times 10^{-2}$	$(4.49 \pm 0.18) \times 10^{-2}$	$(2.21 \pm 0.09) \times 10^{22}$	9.3×10^{-6}
NGC 741	A	64.39^{L}	0.313	D†	16.1	2.8×1.4	50.9	$(1.38 \pm 0.06) \times 10^{-2}$	$(1.64 \pm 0.07) \times 10^{-1}$	$(8.14 \pm 0.33) \times 10^{22}$	6.2×10^{-5}
NGC 741	C	64.39^{L}	0.313	C†	137.7	15.8×14.1	0.2	$(6.80 \pm 0.27) \times 10^{-2}$	$(9.12 \pm 0.37) \times 10^{-1}$	$(4.52 \pm 0.18) \times 10^{23}$	7.0×10^{-4}
NGC 777*	A	58.08^{L}	0.282	C	1.6	1.5×1.0	73.7	$(2.67 \pm 0.11) \times 10^{-3}$	$(5.82 \pm 0.24) \times 10^{-3}$	$(2.35 \pm 0.10) \times 10^{21}$	2.1×10^{-5}
NGC 777	C	58.08^{L}	0.282	NS	-	3.2×3.0	30.4	-	-	-	6.5×10^{-4}
NGC 1132	C	87.9^{L}	0.427	PS	-	16.9×15.1	-7.4	$(4.26 \pm 0.17) \times 10^{-3}$	$(4.28 \pm 0.28) \times 10^{-3}$	$(3.96 \pm 0.26) \times 10^{21}$	1.4×10^{-4}
NGC 1316	BA	21.0^{B}	0.102	D†	11.8	4.5×3.5	29.9	$(9.15 \pm 0.37) \times 10^{-2}$	$(2.62 \pm 0.10) \times 10^{-1}$	$(1.38 \pm 0.06) \times 10^{22}$	8.5×10^{-5}
NGC 1316	CD	21.0^{B}	0.102	J/L	257.7	60.3×34.4	-28.5	$(2.04 \pm 0.08) \times 10^{-1}$	$(3.30 \pm 0.18) \times 10^{1}$	$(1.74 \pm 0.09) \times 10^{24}$	4.7×10^{-2}
NGC 1399*	A	20.09^{B}	0.098	J/L	22.5	3.9×2.6	13.6	$(1.63 \pm 0.07) \times 10^{-2}$	$(2.72 \pm 0.11) \times 10^{-1}$	$(1.31 \pm 0.05) \times 10^{22}$	2.5×10^{-5}
NGC 1404*	A	20.02^{B}	0.097	PS	-	3.9×2.6	13.6	$(2.04 \pm 0.08) \times 10^{-4}$	$(2.15 \pm 0.32) \times 10^{-4}$	$(1.03 \pm 0.15) \times 10^{19}$	2.5×10^{-5}
NGC 1404	CD	20.02^{B}	0.097	NS	-	47.8×42.8	25.4	-	-	-	3.6×10^{-5}
NGC 1407	A	23.27^{L}	0.113	D	4.0	2.1×1.1	36.1	$(1.26 \pm 0.05) \times 10^{-2}$	$(5.87 \pm 0.24) \times 10^{-2}$	$(3.80 \pm 0.15) \times 10^{21}$	2.4×10^{-5}

Table 3.2 - continued. The CASA imaging results for our VLA sample.

Source Name	Config VLA	Distance (Mpc)	Scale (kpc/″)	Radio Class	Extend (kpc)	Beam (″ × ″)	PA (deg)	$S_{peak} \pm eS_{peak}$ (Jy/b)	$S_{1.5\,GHz} \pm eS_{1.5\,GHz}$ (Jy)	$P_{1.5\,GHz} \pm eP_{1.5\,GHz}$ (W/Hz)	RMS (Jy/b)
NGC 1407	B	23.27^{L}	0.113	D	6.0	5.1×2.7	-10.7	$(2.24 \pm 0.09) \times 10^{-2}$	$(7.12 \pm 0.29) \times 10^{-2}$	$(4.61 \pm 0.18) \times 10^{21}$	1.4×10^{-5}
NGC 1407	C	23.27^{L}	0.113	D	7.1	15.7×8.4	-3.0	$(3.86 \pm 0.15) \times 10^{-2}$	$(7.60 \pm 0.30) \times 10^{-2}$	$(4.92 \pm 0.20) \times 10^{21}$	2.5×10^{-5}
NGC 1550*	A	67.30^{L}	0.327	C†	10.1	1.8×1.0	56.3	$(8.52 \pm 0.34) \times 10^{-4}$	$(2.35 \pm 0.13) \times 10^{-3}$	$(1.27 \pm 0.07) \times 10^{21}$	2.1×10^{-5}
NGC 1550	C	67.30^{L}	0.327	D†	36.2	17.3×15.3	-11.9	$(3.13 \pm 0.12) \times 10^{-3}$	$(1.70 \pm 0.11) \times 10^{-2}$	$(9.21 \pm 0.60) \times 10^{21}$	2.3×10^{-4}
NGC 1600	A	45.77^{L}	0.222	D†	4.0	1.5×1.3	-3.5	$(3.72 \pm 0.15) \times 10^{-3}$	$(3.81 \pm 0.15) \times 10^{-2}$	$(9.55 \pm 0.38) \times 10^{21}$	1.1×10^{-5}
NGC 2300*	A	41.45^{L}	0.201	PS	-	1.7×1.0	89.4	$(1.67 \pm 0.07) \times 10^{-3}$	$(1.70 \pm 0.08) \times 10^{-3}$	$(3.49 \pm 0.16) \times 10^{20}$	2.1×10^{-5}
NGC 2300	D	41.45^{L}	0.201	PS	-	66.4×36.8	15.2	$(2.32 \pm 0.09) \times 10^{-3}$	$(1.99 \pm 0.19) \times 10^{-3}$	$(4.09 \pm 0.40) \times 10^{20}$	1.4×10^{-4}
NGC 3091*	A	48.32^{L}	0.235	PS	-	1.9×0.9	-24.3	$(7.53 \pm 0.30) \times 10^{-4}$	$(7.39 \pm 0.51) \times 10^{-4}$	$(2.06 \pm 0.14) \times 10^{20}$	2.8×10^{-5}
NGC 3923*	A	20.97^{L}	0.102	PS	-	2.2×0.8	5.0	$(3.76 \pm 0.15) \times 10^{-4}$	$(4.90 \pm 0.40) \times 10^{-4}$	$(2.58 \pm 0.21) \times 10^{19}$	2.3×10^{-5}
NGC 3923	CD	20.97^{L}	0.102	NS	-	40.7×32.1	-88.2	-	-	-	7.9×10^{-5}
NGC 4073*	A	60.08^{L}	0.292	PS	-	1.5×1.1	-51.5	$(7.23 \pm 0.29) \times 10^{-4}$	$(7.15 \pm 0.43) \times 10^{-4}$	$(3.09 \pm 0.19) \times 10^{20}$	2.0×10^{-5}
NGC 4125	D	21.41^{L}	0.104	PS	-	44.0×34.2	17.7	-	-	-	6.7×10^{-4}
NGC 4261	A	29.0^{M}	0.141	J/L	7.9	1.4×1.3	-22.9	$(1.13 \pm 0.05) \times 10^{-2}$	$(1.72 \pm 0.07) \times 10^{-2}$	$(1.73 \pm 0.07) \times 10^{21}$	8.2×10^{-6}
NGC 4261	C	29.0^{M}	0.141	J/L	55.5	18.8×13.5	51.8	$(2.11 \pm 0.08) \times 10^{-1}$	$(1.27 \pm 0.05) \times 10^{-1}$	$(1.28 \pm 0.05) \times 10^{22}$	1.4×10^{-3}
NGC 4374	A	18.5^{B}	0.090	J/L	4.3	1.5×1.3	47.6	$(1.18 \pm 0.05) \times 10^{-1}$	$(4.78 \pm 0.23) \times 10^{-1}$	$(1.96 \pm 0.09) \times 10^{22}$	2.0×10^{-3}
NGC 4374	B	18.5^{B}	0.090	J/L	13.3	4.6×4.4	-4.5	$(1.30 \pm 0.05) \times 10^{-1}$	$(4.18 \pm 0.17) \times 10^{0}$	$(1.71 \pm 0.07) \times 10^{23}$	1.4×10^{-3}
NGC 4374	C	18.5^{B}	0.090	J/L	18.7	38.8×32.4	-45.2	$(1.28 \pm 0.05) \times 10^{0}$	$(5.94 \pm 0.24) \times 10^{0}$	$(2.43 \pm 0.10) \times 10^{23}$	5.8×10^{-3}
NGC 4406*	A	17.9^{B}	0.087	PS	-	1.1×1.0	-1.4	$(3.57 \pm 0.14) \times 10^{-4}$	$(2.77 \pm 0.53) \times 10^{-4}$	$(1.06 \pm 0.20) \times 10^{19}$	4.5×10^{-5}
NGC 4406	D	17.9^{B}	0.087	NS	-	45.0×43.2	-6.0	-	-	-	2.610^{-4}
NGC 4472*	A	16.7^{B}	0.081	C†	2.6	1.4×1.0	-72.7	$(2.79 \pm 0.11) \times 10^{-2}$	$(1.20 \pm 0.05) \times 10^{-1}$	$(4.00 \pm 0.16) \times 10^{21}$	2.2×10^{-5}
NGC 4472	C	16.7^{B}	0.081	D†	12.4	16.2×13.8	-32.6	$(1.21 \pm 0.05) \times 10^{-1}$	$(2.28 \pm 0.09) \times 10^{-1}$	$(7.61 \pm 0.31) \times 10^{21}$	3.1×10^{-4}
NGC 4486	A	16.7^{B}	0.081	J/L	4.4	1.4×1.2	49.1	$(3.31 \pm 0.13) \times 10^{0}$	$(2.03 \pm 0.09) \times 10^{1}$	$(6.77 \pm 0.29) \times 10^{23}$	2.8×10^{-2}
NGC 4486	B	16.7^{B}	0.081	D†	9.7	6.5×3.6	-51.1	$(8.14 \pm 0.33) \times 10^{0}$	$(1.23 \pm 0.05) \times 10^{2}$	$(4.10 \pm 0.16) \times 10^{24}$	1.3×10^{-2}
NGC 4486	C	16.7^{B}	0.081	D†	46.5	13.4×12.2	0.8	$(2.03 \pm 0.08) \times 10^{1}$	$(1.52 \pm 0.06) \times 10^{2}$	$(5.07 \pm 0.20) \times 10^{24}$	1.8×10^{-2}
NGC 4552	A	16.0^{B}	0.078	PS	-	1.4×1.1	13.6	$(5.89 \pm 0.24) \times 10^{-2}$	$(5.97 \pm 0.25) \times 10^{-2}$	$(1.83 \pm 0.08) \times 10^{21}$	2.7×10^{-4}
NGC 4552	C	16.0^{B}	0.078	C†	7.8	11.4×10.4	-26.5	$(1.09 \pm 0.04) \times 10^{-1}$	$(1.65 \pm 0.07) \times 10^{-1}$	$(5.05 \pm 0.21) \times 10^{21}$	2.6×10^{-4}
NGC 4636	A	15.96^{L}	0.077	C	2.9	2.7×1.6	-74.7	$(7.84 \pm 0.31) \times 10^{-3}$	$(5.95 \pm 0.24) \times 10^{-2}$	$(1.81 \pm 0.07) \times 10^{21}$	4.4×10^{-6}
NGC 4636	C	15.96^{L}	0.077	C	3.7	13.8×10.7	116.7	$(2.99 \pm 0.12) \times 10^{-2}$	$(6.91 \pm 0.28) \times 10^{-2}$	$(2.11 \pm 0.08) \times 10^{21}$	7.4×10^{-5}
NGC 4649	A	16.5^{B}	0.080	C	0.3	1.4×1.3	-8.5	$(9.68 \pm 0.39) \times 10^{-3}$	$(1.44 \pm 0.06) \times 10^{-2}$	$(4.69 \pm 0.19) \times 10^{20}$	2.2×10^{-5}
NGC 4649	D	16.5^{B}	0.080	D†	6.4	11.5×9.1	-6.8	$(2.02 \pm 0.08) \times 10^{-2}$	$(2.83 \pm 0.11) \times 10^{-2}$	$(9.22 \pm 0.37) \times 10^{20}$	4.2×10^{-5}
NGC 4696	A	37.48^{L}	0.182	D†	7.9	5.0×1.0	8.5	$(2.42 \pm 0.10) \times 10^{-1}$	$(2.80 \pm 0.11) \times 10^{0}$	$(4.71 \pm 0.19) \times 10^{23}$	3.8×10^{-4}
NGC 4696	BC	37.48^{L}	0.182	D†	10.9	31.3×10.1	-34.6	$(1.36 \pm 0.05) \times 10^{-1}$	$(2.43 \pm 0.10) \times 10^{-1}$	$(4.08 \pm 0.16) \times 10^{22}$	4.5×10^{-5}
NGC 4778	A B	$59.29^{L\#}$	0.288	PS	-	6.7×5.6	-41.5	$(5.57 \pm 0.22) \times 10^{-3}$	$(5.15 \pm 0.53) \times 10^{-3}$	$(2.17 \pm 0.22) \times 10^{21}$	3.5×10^{-4}
NGC 4778	C	$59.29^{L\#}$	0.288	PS	-	18.1×11.5	-2.0	$(3.81 \pm 0.15) \times 10^{-3}$	$(3.95 \pm 0.73) \times 10^{-3}$	$(1.66 \pm 0.31) \times 10^{21}$	4.4×10^{-4}
NGC 4782	A	48.63^{L}	0.236	J/L	30.2	0.5×0.4	-177.1	$(7.55 \pm 0.30) \times 10^{-2}$	$(1.24 \pm 0.05) \times 10^{0}$	$(3.51 \pm 0.14) \times 10^{23}$	3.6×10^{-5}
NGC 4782	BA	48.63^{L}	0.236	D†	55.9	5.8×3.9	16.0	$(7.48 \pm 0.30) \times 10^{-2}$	$(5.43 \pm 0.22) \times 10^{0}$	$(1.54 \pm 0.06) \times 10^{24}$	2.7×10^{-4}
NGC 4936*	A	31.36^{L}	0.152	PS	-	3.3×1.2	12.9	$(3.33 \pm 0.13) \times 10^{-3}$	$(3.34 \pm 0.14) \times 10^{-3}$	$(3.93 \pm 0.17) \times 10^{20}$	2.6×10^{-5}
NGC 5044	A	35.75^{L}	0.174	C†	1.4	2.1×1.3	-17.6	$(2.72 \pm 0.11) \times 10^{-2}$	$(2.95 \pm 0.12) \times 10^{-2}$	$(4.51 \pm 0.18) \times 10^{21}$	3.0×10^{-5}
NGC 5044	BA	35.75^{L}	0.174	D†	23.1	5.3×3.6	-54.2	$(2.78 \pm 0.11) \times 10^{-2}$	$(3.25 \pm 0.13) \times 10^{-2}$	$(4.97 \pm 0.20) \times 10^{21}$	2.7×10^{-5}
NGC 5044	D	35.75^{L}	0.174	D	24.3	62.1×37.2	2.1	$(3.34 \pm 0.13) \times 10^{-2}$	$(3.40 \pm 0.14) \times 10^{-2}$	$(5.20 \pm 0.21) \times 10^{21}$	1.7×10^{-4}
NGC 5129*	A	86.85^{L}	0.422	C†	4.0	2.3×1.6	-5.5	$(5.50 \pm 0.22) \times 10^{-3}$	$(5.05 \pm 0.21) \times 10^{-3}$	$(4.56 \pm 0.19) \times 10^{21}$	3.0×10^{-5}
NGC 5419*	A	50.87^{L}	0.247	D	6.1	3.7×1.1	16.4	$(3.84 \pm 0.15) \times 10^{-3}$	$(2.11 \pm 0.08) \times 10^{-2}$	$(6.53 \pm 0.26) \times 10^{21}$	2.3×10^{-6}
NGC 5419	B	50.87^{L}	0.247	D	13.5	10.7×3.8	0.6	$(1.24 \pm 0.05) \times 10^{-1}$	$(3.23 \pm 0.13) \times 10^{-1}$	$(1.00 \pm 0.04) \times 10^{23}$	2.5×10^{-4}

Table 3.2 - continued. The CASA imaging results for our VLA sample.

Source Name	Config VLA	Distance (Mpc)	Scale (kpc/″)	Radio Class	Extend (kpc)	Beam (″ × ″)	PA (deg)	$\mathbf{S_{peak} \pm eS_{peak}}$ (Jy/b)	$\mathbf{S_{1.5\,GHz} \pm eS_{1.5\,GHz}}$ (Jy)	$\mathbf{P_{1.5\,GHz} \pm eP_{1.5\,GHz}}$ (W/Hz)	RMS (Jy/b)
NGC 5419	CD	50.87^{L}	0.247	D	181.8	33.6×28.3	19.8	$(2.97 \pm 0.12) \times 10^{-1}$	$(5.54 \pm 0.22) \times 10^{-1}$	$(1.72 \pm 0.07) \times 10^{23}$	1.3×10^{-4}
NGC 5813	A B	29.23^{L}	0.142	D	2.7	5.3×4.5	-33.3	$(4.04 \pm 0.16) \times 10^{-3}$	$(7.66 \pm 0.36) \times 10^{-3}$	$(7.83 \pm 0.37) \times 10^{20}$	6.9×10^{-5}
NGC 5813	B	29.23^{L}	0.142	D	4.1	6.2×4.7	-21.9	$(3.60 \pm 0.14) \times 10^{-3}$	$(5.34 \pm 0.38) \times 10^{-3}$	$(5.46 \pm 0.38) \times 10^{20}$	1.7×10^{-4}
NGC 5813	D	29.23^{L}	0.142	D	19.5	45.2×36.5	20.2	$(1.27 \pm 0.05) \times 10^{-2}$	$(1.46 \pm 0.06) \times 10^{-2}$	$(1.49 \pm 0.06) \times 10^{21}$	6.5×10^{-5}
NGC 5846	A	27.13^{L}	0.132	C	4.2	1.5×1.3	8.3	$(9.25 \pm 0.37) \times 10^{-3}$	$(2.07 \pm 0.09) \times 10^{-2}$	$(1.82 \pm 0.08) \times 10^{21}$	2.6×10^{-5}
NGC 5846	B	27.13^{L}	0.132	C	2.7	8.0×5.7	-20.3	$(1.02 \pm 0.04) \times 10^{-2}$	$(1.57 \pm 0.09) \times 10^{-2}$	$(1.38 \pm 0.08) \times 10^{21}$	2.2×10^{-4}
NGC 5846	CD	27.13^{L}	0.132	D	19.4	58.7×25.6	-61.7	$(1.82 \pm 0.07) \times 10^{-2}$	$(2.00 \pm 0.10) \times 10^{-2}$	$(1.76 \pm 0.08) \times 10^{21}$	3.0×10^{-4}
NGC 7619*	A	50.53^{L}	0.245	C	2.2	2.2×1.1	58.8	$(1.20 \pm 0.05) \times 10^{-2}$	$(1.91 \pm 0.08) \times 10^{-2}$	$(5.84 \pm 0.24) \times 10^{21}$	2.8×10^{-5}
NGC 7619	C	50.53^{L}	0.245	PS	104.2	15.6×15.2	-47.0	$(2.1 \pm 0.1) \times 10^{-2}$	$(2.5 \pm 0.1) \times 10^{-2}$	$(7.64 \pm 0.34) \times 10^{21}$	2.4×10^{-4}

(1) sources marked with * are our new VLA A observations obtained within the project 15A-305; (3) distances marked with # are based on redshift measurements; **References:** L:Lakhchaura et al. (2018); B:Blakeslee et al. (2009); M: Mieske et al. (2005); (5) radio morphological categories: J/L: jets/lobes; D: diffuse and D†: diffuse with signatures of jet/lobe-like morphology; C: compact and C† with signatures of small-scale jet/lobe-like morphology; PS: point source-like radio emission; NS: no radio source detected.

3.4 Radio and X-ray Comparison

3.4.1 Point-like Radio Sources

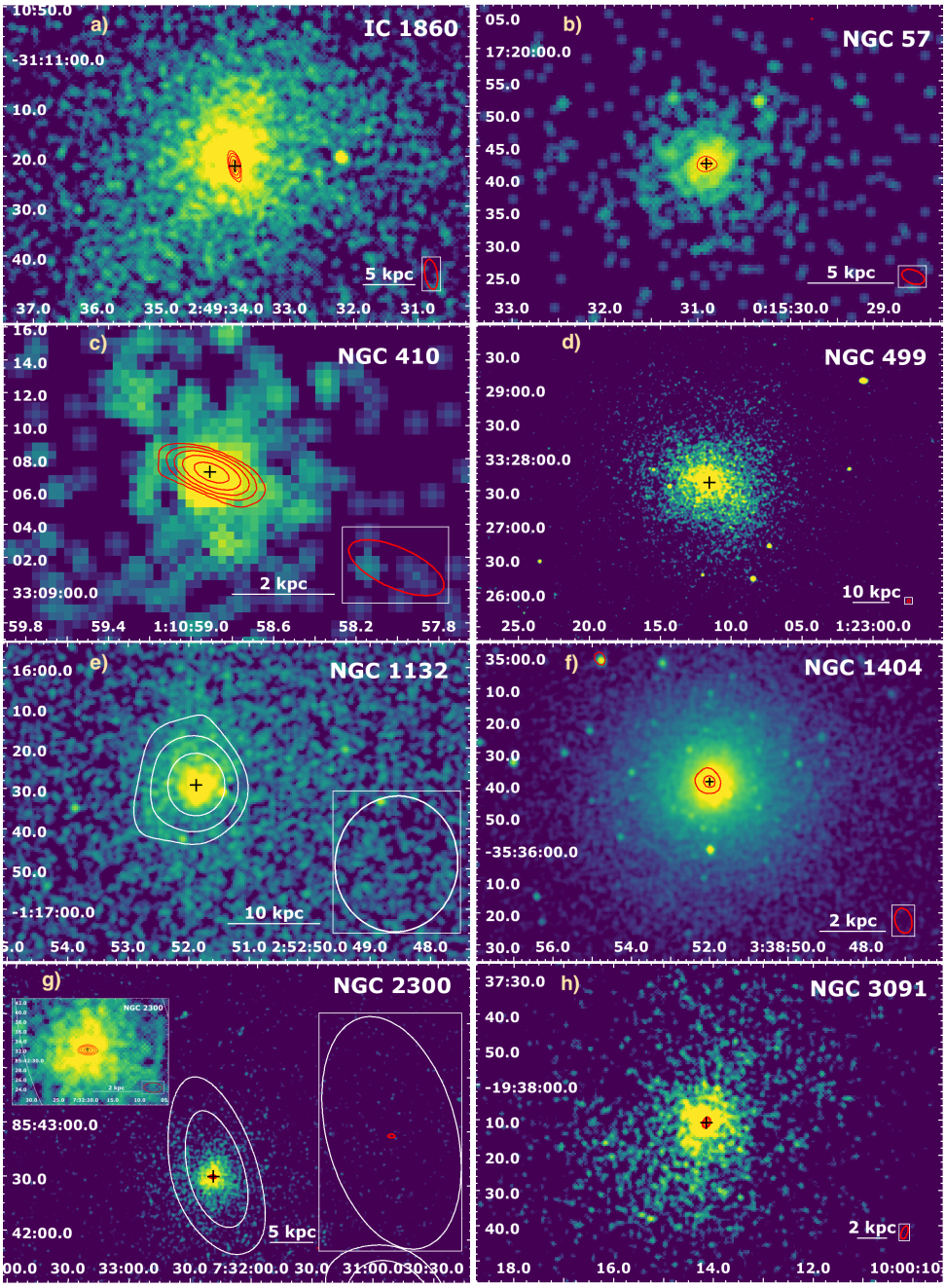

Figure 3.1: The *Chandra* smoothed (by two-sigma Gaussian kernel) images overlaid by 1.5 GHz VLA A, AB/B and C/D configuration contours in the red, cyan and white, respectively. In all cases, the contours are created at $5 \times \sigma_{\rm RMS}$ and increase by the power of 2 up to the peak intensity. The radio center of the galaxy is represented by a black '+' sign. RMS noise ($\sigma_{\rm RMS}$) and peak intensity values are given in Table 3.2.

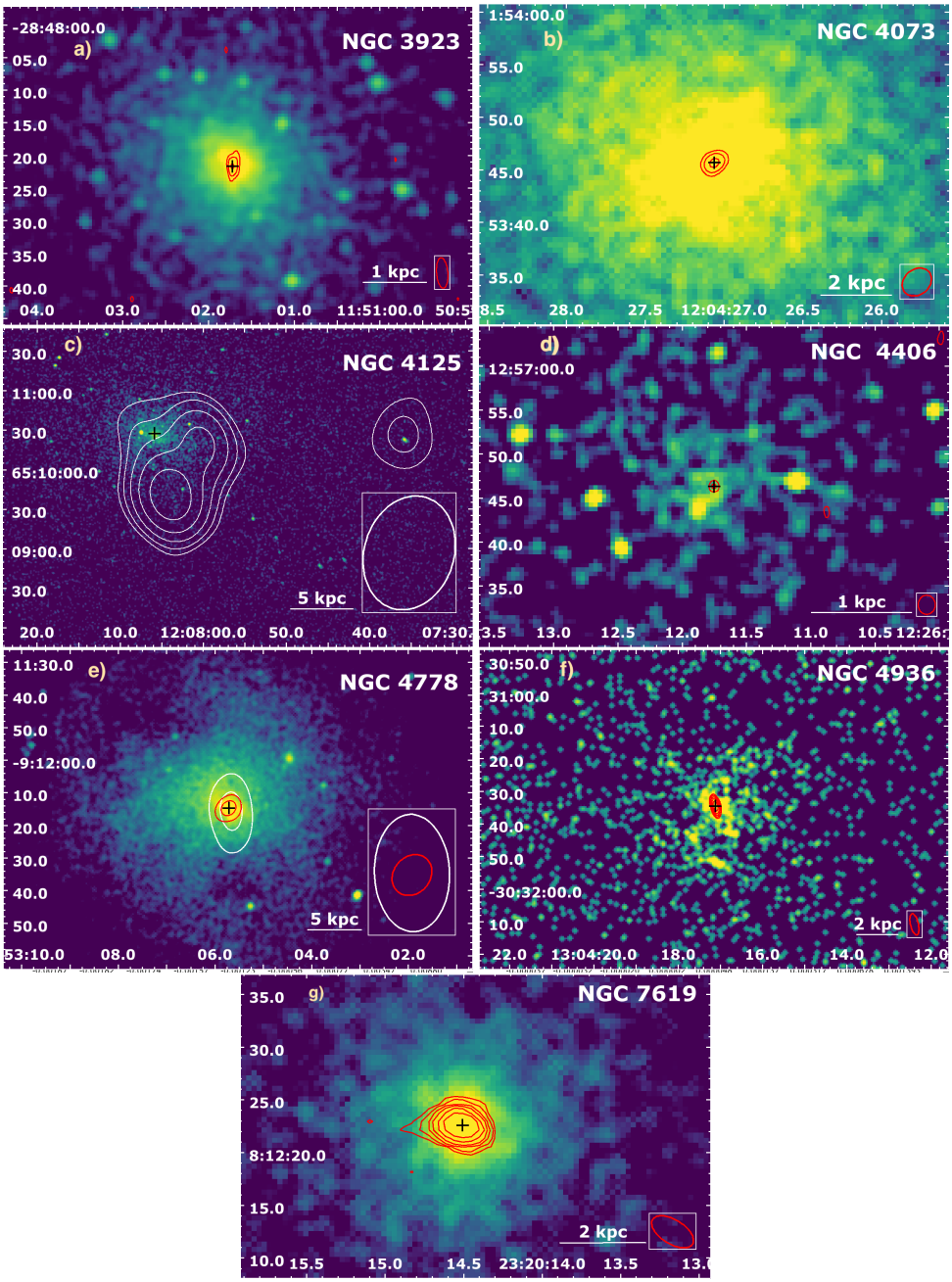

Figure 3.2: The X-ray *Chandra* smoothed (by two-sigma Gaussian kernel) images overlaid by 1.5 GHz VLA A, AB/B and C/D configuration contours in the red, cyan and white, respectively. In all cases, the contours are created at $5 \times \sigma_{\rm RMS}$ and increase by the power of 2 up to the peak intensity. The radio center of the galaxy is represented by a black '+' sign. RMS noise ($\sigma_{\rm RMS}$) and peak intensity values are given in Table 3.2.

3.4.2 Extended Radio Sources

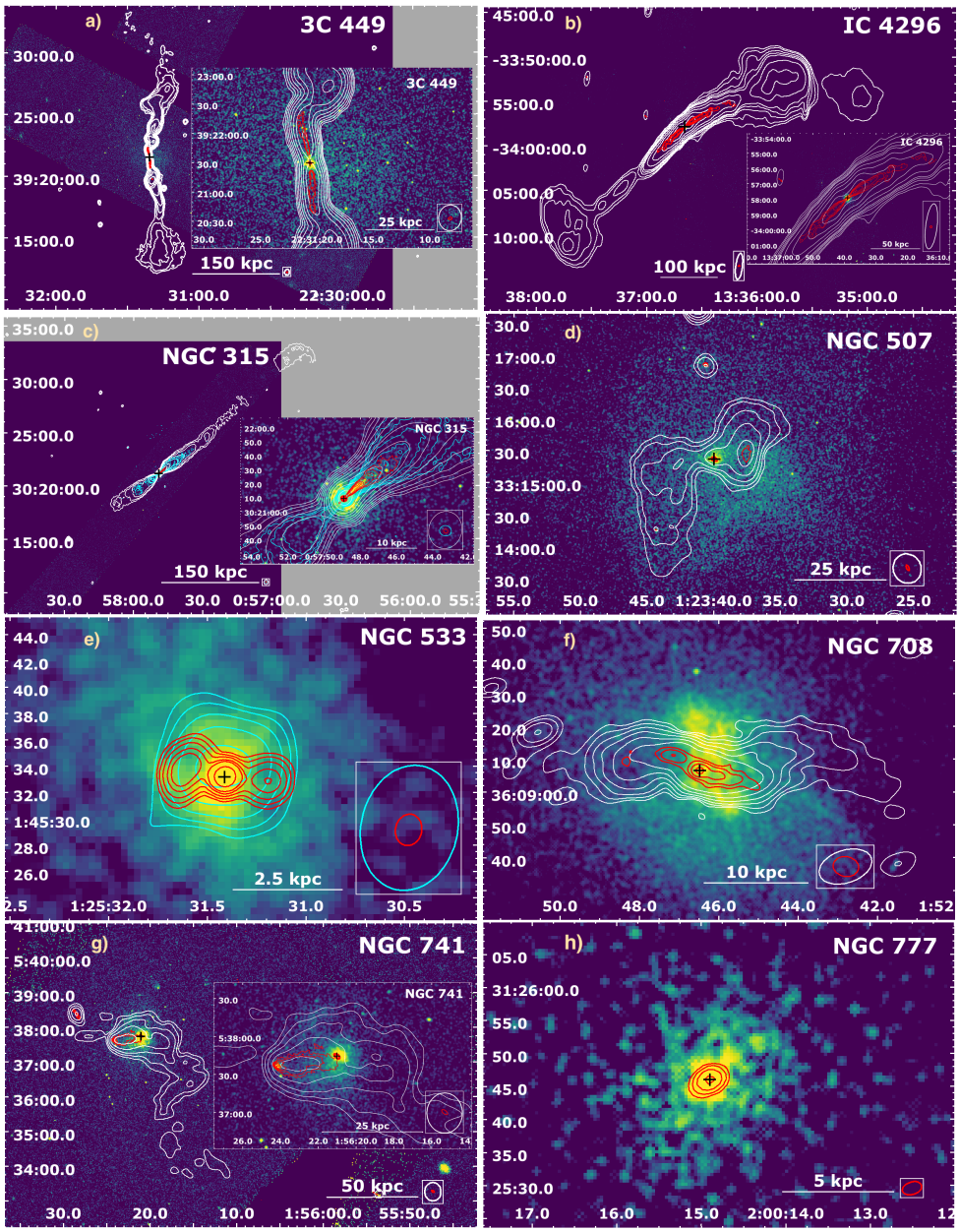

Figure 3.3: The X-ray *Chandra* smoothed (by two-sigma Gaussian kernel) images overlaid by 1.5 GHz VLA A, AB/B and C/D configuration contours in the red, cyan and white, respectively. In all cases, the contours are created at $5 \times \sigma_{\rm RMS}$ and increase by the power of 2 up to the peak intensity. The radio center of the galaxy is represented by a black '+' sign. RMS noise ($\sigma_{\rm RMS}$) and peak intensity values are given in Table 3.2.

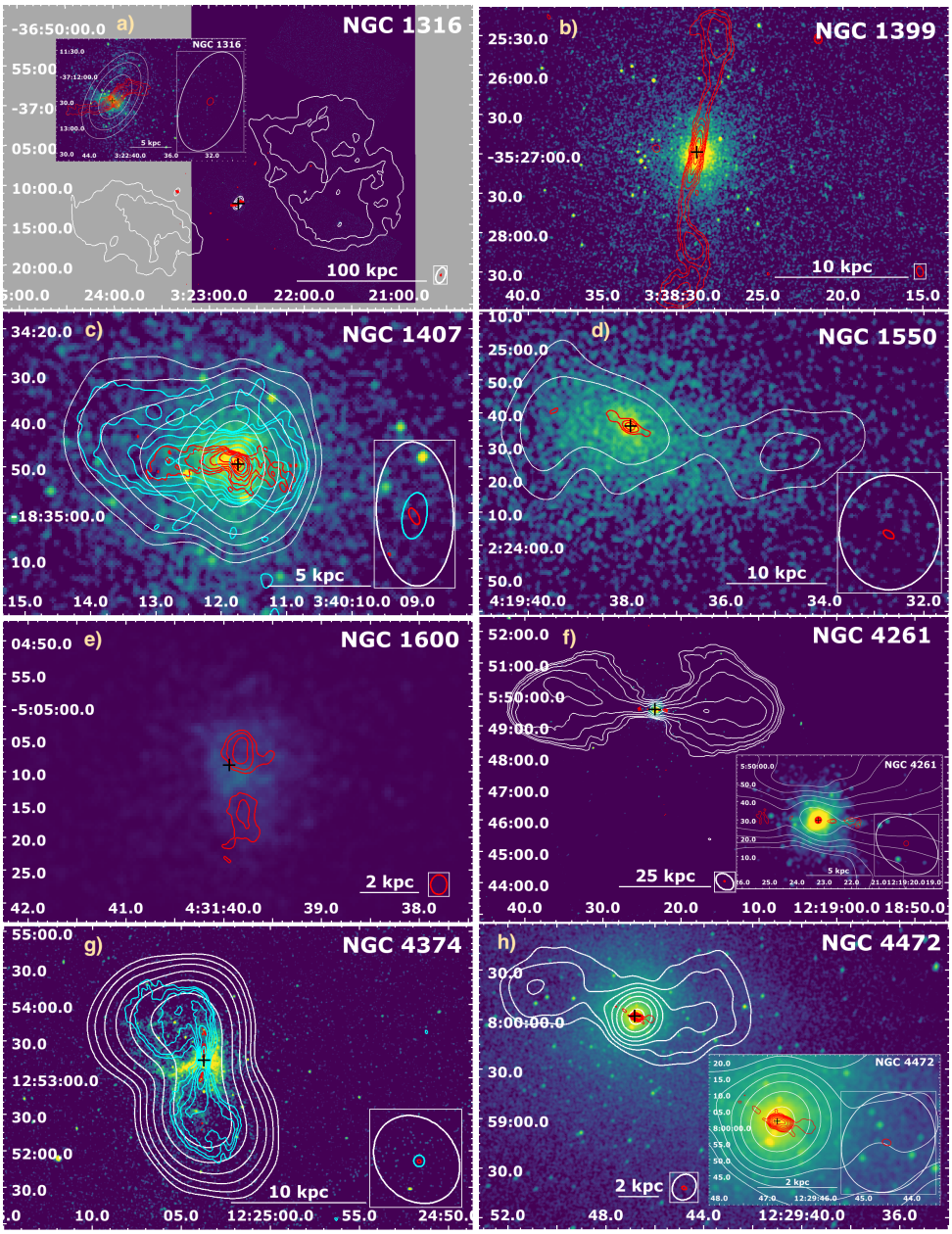

Figure 3.4: The X-ray *Chandra* smoothed (by two-sigma Gaussian kernel) images overlaid by 1.5 GHz VLA A, AB/B and C/D configuration contours in the red, cyan and white, respectively. In all cases, the contours are created at $5 \times \sigma_{\mathrm{RMS}}$ and increase by the power of 2 up to the peak intensity. The radio center of the galaxy is represented by a black '+' sign. The RMS noise and peak intensity values are given in Table 3.2.

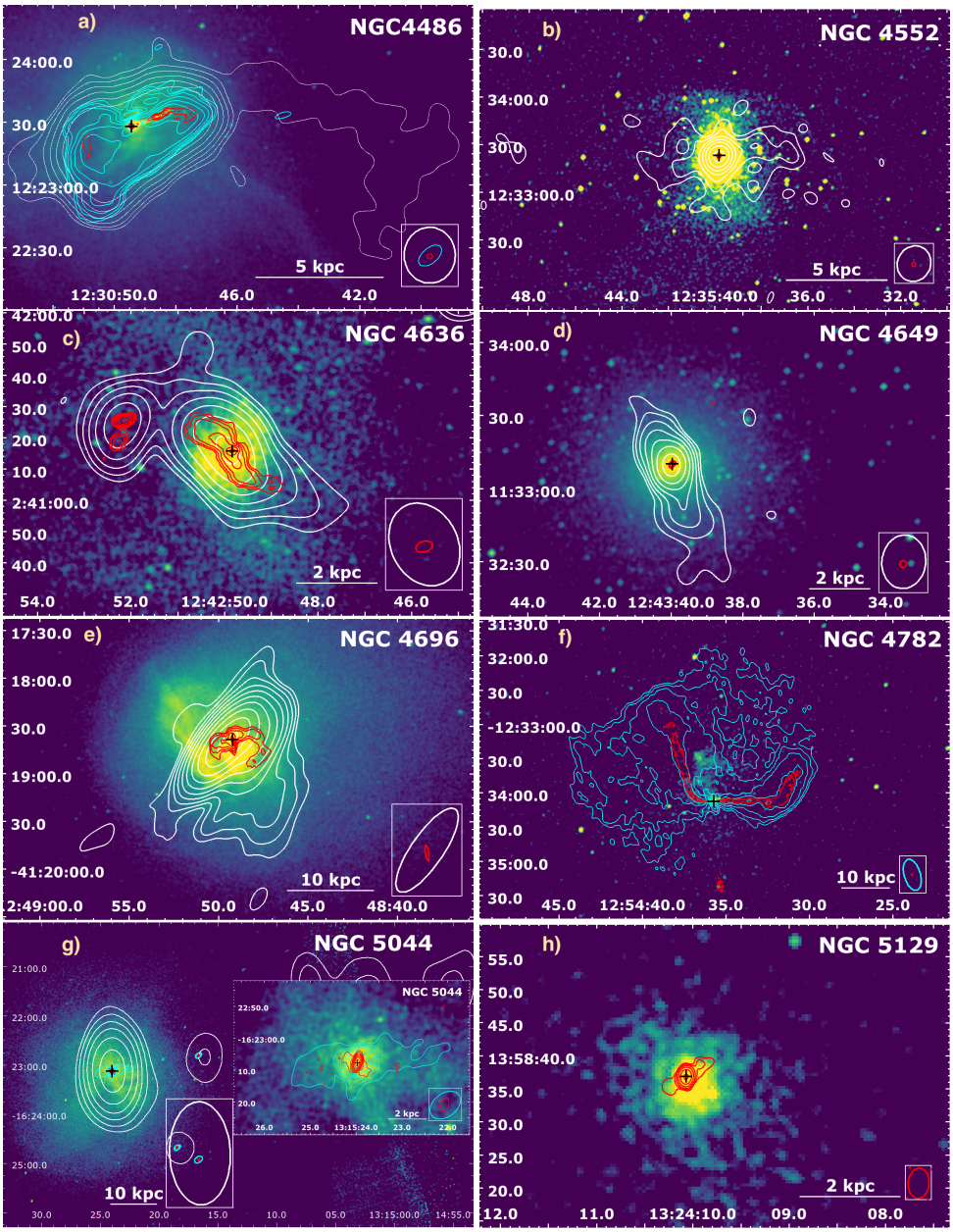

Figure 3.5: The X-ray *Chandra* smoothed (by two-sigma Gaussian kernel) images overlaid by 1.5 GHz VLA A, AB/B and C/D configuration contours in the red, cyan and white, respectively. In all cases, the contours are created at $5 \times \sigma_{\mathrm{RMS}}$ and increase by the power of 2 up to the peak intensity. The radio center of the galaxy is represented by a black '+' sign. The RMS noise and peak intensity values are given in Table 3.2.

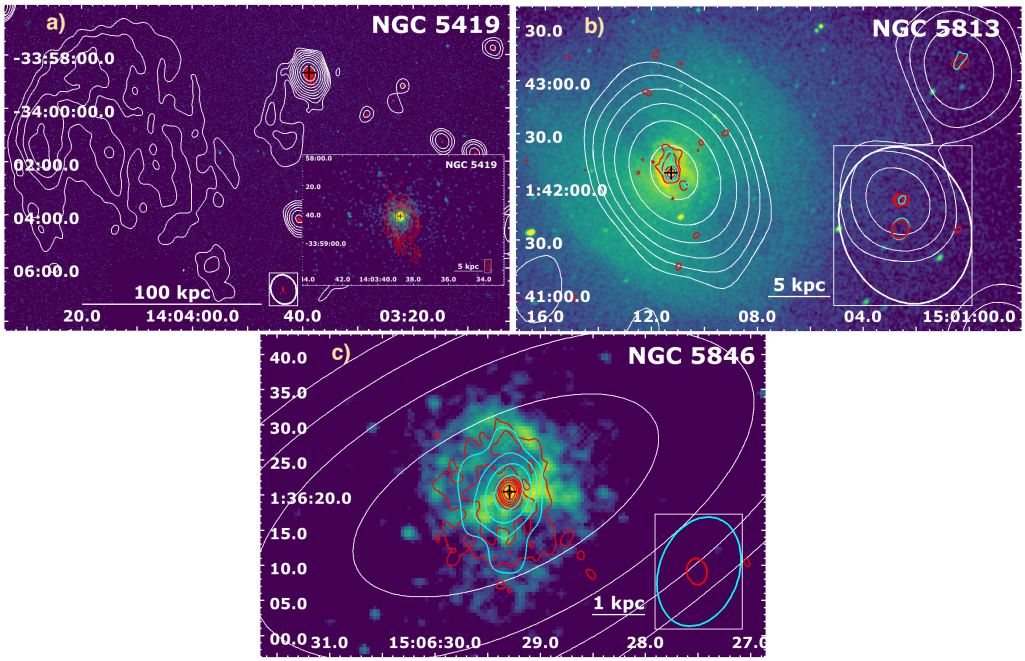

Figure 3.6: The X-ray *Chandra* smoothed (by two-sigma Gaussian kernel) images overlaid by 1.5 GHz VLA A, AB/B and C/D configuration contours in the red, cyan and white, respectively. In all cases, the contours are created at $5 \times \sigma_{\mathrm{RMS}}$ and increase by the power of 2 up to the peak intensity. The radio center of the galaxy is represented by a black '+' sign. The RMS noise and peak intensity values can be found in Table 3.2.

3.5 Additional Sources

Additionally, we provide a list of giant elliptical galaxies that are omitted from our main sample. The reason for each omission is given in Table 3.3 and varies from missing radio VLA data in the frequency range of 1–2 GHz or insufficient/missing archival *Chandra* data up to strong dominance by the central X-ray point source, thus diminishing the contribution from the hot X-ray atmosphere. Moreover, Table 3.3 also contains the VLA observational details together with information about the properties of the observed radio emission from the VLA in the frequency range between 1–2 GHz.

Source Name	**Config VLA**	**Project Code (Code)**	**VLA Obs. Date (year-month-day)**	$\mathbf{S_{1.5\,GHz} \pm eS_{1.5\,GHz}}$ **(mjy)**	**RMS (mjy)**	**Exclusion Reason**
IC2006	CD	NVSS	1993-09-20	-	0.47	no archival VLA at 1–2 GHz & insufficient *Chandra* (4.55 ks)
IC310*	A	15A-305	2015-Jun-23	330 ± 13	0.03	dominant X-ray point source
IC310	C	AB0412	1986-Dec-05	460 ± 20	1.8	dominant X-ray point source
NGC 1521	CD	NVSS	1993-09-20	-#	0.47	no archival VLA at 1–2 GHz
NGC 2329*	A	15A-305	2015-Jun-20	220 ± 9	0.014	insufficient *Chandra* (2.86 ks)
NGC 2329	C	AB0476	1988-Apr-14	650 ± 27	0.6	insufficient *Chandra* (2.86 ks)
NGC 2340*	A	15A-305	2015-Jun-19	2.00 ± 0.08	0.002	insufficient *Chandra* (1.92 ks)
NGC 4203*	A	15A-305	2015-Jul-03	7.8 ± 0.3	0.027	dominant X-ray point source
NGC 4203	D	AB0506	1988-Jul-13	-	2.8	dominant X-ray point source
NGC 5090	A	AG0454	1995-Jul-23	350 ± 25	4.5	no *Chandra*
NGC 5090	BC	AS0225	1985-Jul-07/08	3300 ± 130	0.67	no *Chandra*
NGC 5328	CD	NVSS	1993-09-20	-	0.47	no archival VLA at 1–2 GHz & insufficient *Chandra* (2.6 ks)

Table 3.3: The list of early-type galaxies omitted from the main sample. The columns are: (1) source name; ' * ': sources observed within our project 15A-305 (2) VLA configuration; (3) the NRAO VLA archive project code. Missing VLA archival data were supplemented by the NRAO VLA Sky Survey (NVSS) data (4) observation date (year-month-day) (5) VLA total flux density of the image; ' - ': non-detection of radio emission at 1.5 GHz and '#': a weak radio source with an integrated flux density of 2.0 mJy detected at the lower threshold of $4\times\,\sigma_{\rm RMS}$ (6) the RMS noise value of the image (7) the reason for the exclusion of a certain source from the main sample.

3.6 Multifrequency information

Table 3.4: The multifrequency information of the gas in our sample of early-type galaxies. The column order is following: (1) the 3C, NGC, IC source name; (2) radio morphology from VLA in the L-band at 1–2 GHz (centered at 1.5 GHz), LOFAR or GMRT (3) X-ray morphology from *Chandra* at 0.5–7 keV within the innermost $\sim$ 10 kpc or *XMM-Newton*; (4) Optical and infrared morphology of the dust and corresponding diameter of the dusty disk from HST or *Spitzer*; (5) Atomic gas observed from SOAR through the presence of a warm ionized nebulae Hα+[N II]; (6) Molecular gas in form of molecular CO lines observed from ALMA and IRAM.

Source Name	**Radio VLA/GMRT/LOFAR**	**X-rays** *Chandra/XMM-Newton*	**Dust/extend HST/***Spitzer*	**Atomic gas SOAR**	**Molecular gas ALMA/IRAM**
3C 449	FR I^{Fan74}	inCav$^{Har98;Cro03}$, CFs^{Lal13}	dustyDisk$^{Fer99;Tre06}$	unkHa^{Lak18}	CO(1-0)^{Leo01}
IC 1860	PS^{Dun10}	CFs$^{Gas07;Gas13}$	-	nucHa^{Lak18}	-
IC 4296	FR I/FR II^{Gro19}	outCav^{Gro19}	dustyDisk$^{Schm02;Boi17}$	extHa^{Lak18}	CO(2-1)$^{Boi17;Ruf19}$
NGC 57	PS^{Gro}	compact	noDust^{Gou18}	noHa^{Lak18}	-
NGC 315	FR I^{Cap02}	X-jet$^{Wor03;Don04}$	dustyDisk$^{Ver99;Cap00;Boi21}$	unkHa^{Lak18}	CO(1-0)^{Fla10}/(2-1)^{Boi21}
NGC 410	PS^{Con98}	compact^{Lak18}	noDust^{Tan9}	nucHa^{Lak18}	uppCO(1-0)/(2-1)$^{O'Sul18}$
NGC 499	NS^{Dun10}/PS^{Bir20}	gCav(in^{Pls}/out^{Pan24b,Kim19})	-	nucHa^{Lak18}	-
NGC 507	FR I^{Cap02,Par86}	inCav$^{Don10;Pls}$; CF$^{Fab02;Kra04}$	noDust^{Tem07}	noHa^{Lak18}	-
NGC 533	FR II?/young?^{Gro}	inCav^{Dun10}	dust^{Tem07}	extHa^{Lak18}	-
NGC 708	FR I^{Par86,Bla04}/young?^{Gro}	inCav$^{Bla04;Pan14b}$	centDust^{Sah16}	extHa^{Lak18}	CO(1-0)^{Fla10}/(2-1)^{Oli19,Nor21}
NGC 741	radioTail^{Sche17,Ven94}	in^{Sche17}/outCav^{Jet08}	noDust^{Ver05}	noHa^{Lak18}	noCO^{Wik95}
NGC 777	compact$^{Bha14;Kol18}$	pos-Cav^{Pan14b}	lowDust^{Pah04}	noHa^{Lak18}	uppCO(1-0/2-1)$^{O'sul15}$
NGC 1132	PS^{Kim18}	gCav$^{Don10;Pls}$	dustLanes^{Ala12}	noHa^{Lak18}	noCO^{Dav16}
NGC 1316	FR I$^{Fom89;Mac20a}$	in/out(g)-Cav^{Lan10}	dust$^{Schw80;Gri99;Dua14}$	extHa^{Lak18}	CO(1-0)^{Sag93}/CO(2-1)^{Hor01}
NGC 1399	FR I$^{Dun10;Shu08}$	inCav^{Pan14b}	dust^{Tem07}/noDust^{Dok95,Pra10}	noHa^{Lak18}	CO(2-1)^{Pra10}
NGC 1404	PS$^{Dun10;Gro}$	CFs$^{Mach05;Su17}$	dust^{Tem07}	noHa^{Lak18}	-
NGC 1407	disturbed^{Gia12}	disturbed^{For06}	dust$^{Kul14;Tem07}$	noHa^{Lak18}	uppCO(1-0)^{Bab19}
NGC 1550	disturbed$^{Dun10;Kol18}$	Cav^{Pan14b} CFs^{Kol20}	-	noHa^{Lak18}	uppCO(1-0)/(2-1)$^{O'sul18}$
NGC 1600	FR II?$^{Bir85;Gro}$	inCav^{Siv04}	dust^{Ferr99}	noHa^{Lak18}	-
NGC 2300	PS^{Gro}	pot-gCav^{Pls}	noDust^{Xil04}	noHa^{Lak18}	-
NGC 3091	PS^{Gro}	pot-gCav^{Pls}	noDust^{Col01}	noHa^{Lak18}	-
NGC 3923	PS$^{Dis77;Gro}$	pot-gCav^{Pls}	filDust^{Pen86,Bil16}	noHa^{Lak18}	-
NGC 4073	PS$^{Hog14;Gro}$	pot-gCav^{Pls}	-	noHa^{Lak18}	-
NGC 4125	PS$^{Kra02;Gro}$	pot-gCav^{Pls}	dust$^{Ver05;Tem07;Kul14}$	noHa^{Lak18}	noCO(1-0)^{Wel10}/CO(2-1)^{Wel10}
NGC 4261	FR I$^{Kol15;O'sul11}$	Xjet$^{Gli03;Wor10}$; outCav$^{Cro08;O'su11}$	dustyDisk	nucHa^{Lak18}	uppCO(1-0)$^{O'sul18}$/CO(2-1)/(3-2)^{Boi21}
NGC 4374	FR I^{Lai87}	outCav^{Fin01,Dev10}	dustLanes$^{Ver99;Boi17}$	nucHa^{Lak18}	CO(1-0)/(2-1)^{Fla10,Boi17}
NGC 4406	PS$^{Dun10;Gro}$	X-ray tail/plume^{For79,Kim19}	dust^{Smi12}	extHa$^{Ken08;Lak18}$	noCO$^{Wik95;You11}$
NGC 4472	FR I$^{Con88;Gro}$	inCav$^{Bil04;Su19}$	dust^{Tem07}	noHa^{Lak18}	CO(1-0)/(2-1)^{Huch88,Huch99}
NGC 4486	FR I^{Fan74}	in/outCav$^{You02;For05;For07}$; Xjet^{Mar02}	dustyDisk	extHa^{Lak18}	CO(1-0)^{Fla10}/(2-1)$^{Sim18;Oli19}$
NGC 4552	FR I$^{Fil04;Gro}$	outCav$^{Mach06;All06}$, CF$^{Mach06;Kra17}$	dust$^{Tem07;Kul14}$	noHa^{Lak18}	uppCO(1-0)/(2-1)^{Com07}
NGC 4636	FR I$^{Dun10;Gia11}$	inCav$^{Sta86;Bal09}$	dust^{Tem07}	nucHa^{Lak18}	uppCO(1-0)$^{O'sul18}$/CO(2-1)$^{O'sul18;Tem18}$
NGC 4649	FR I?$^{Shu08;Dun10}$	Cav$^{Shu08;Dun10}$	dust$^{Kul14;Tem07}$	noHa^{Lak18}	CO(1-0)$^{Sag89;You11}$
NGC 4696	FR I^{Tay02}	inCav$^{Tay06;San16}$	filDust$^{Tem07;Fab16}$	extHa^{Lak18}	CO(1-0)^{Bab19,Oli19}/(2-1)^{Fab16}
NGC 4778	PS$^{Vrt02;Gro}$	gCav^{Mor06,Pan14b}	-	nucHa^{Lak18}	-
NGC 4782	FR I$^{Bor96;Mach06}$	in/outCav$^{Bor96;Mach06}$	-	nucHa^{Lak18}	-
NGC 4936	PS$^{Bha14;Gro}$	disturbed$^{Bha14;Lak18}$		extHa^{Lak18}	-
NGC 5044	jets$^{Dun10;Sche20a}$	in/outCav$^{Gas09;Sche20a}$; CFs^{Gas09}	dust^{Tem07}	extHa^{Lak18}	CO(2-1)$^{Lau14;Dav14;Tem18}$
NGC 5129	jets$^{Con98;Bha14;Gro}$	disturbed^{Bha14}	-	nucHa^{Lak18}	-

Table 3.4 - continued. The multifrequency information of the gas in our sample of early-type galaxies.

Source	Radio	X-rays	Dust/extend	Atomic gas	Molecular gas
Name	VLA/GMRT/LOFAR	*Chandra/XMM-Newton*	HST/*Spitzer*	SOAR	ALMA/IRAM
NGC 5419	relic-like$^{Gos87;Sub03}$	central^{Bal06}	-	noHa^{Lak18}	-
NGC 5813	jets$^{Ran11;Ran15}$	in/outCav^{Ran11}	dust^{Tem07}	extHa^{Lak18}	uppCO(1-0)/(2-1)$^{O'sul18}$
NGC 5846	disturbed$^{Dun10;Bir20}$	in/outCav$^{Tri02;All06}$, CF^{Mach11}	dust^{Tem07}	nucHa^{Lak18}	CO(1-0)$^{O'sul18}$/(2-1)$^{O'sul18;Tem18}$
NGC 7619	PS$^{Con98;Gia11}$	RPS tails^{Ran09}	dust^{Tem07}	noHa^{Lak18}	-

(2) the Fanaroff-Riley (Fanaroff & Riley 1974) (FR) radio morphology classification: 'FR I' = edge-darkened, 'FR II' = edge-brightened; 'FR II?': potential FR II radio source; 'PS': point-source radio morphology (< twice the beam size; unresolved source); NS: no radio source; young: young radio source; *References column (2):* Bir85: Birkinshaw & Davies (1985); Bir20: Bîrzan et al. (2020); Bha14: Bharadwaj et al. (2014); Bla04: Blanton et al. (2004); Bor96: Borne & Colina (1996); Cap02: Capetti et al. (2002); Con88L Condon & Broderick (1988); Con98: Condon et al. (1998); Dun10: Dunn et al. (2010); Dis77: Disney & Wall (1977); Fan74: Fanaroff & Riley (1974); Fil04: Filho et al. (2004); Fom89: Fomalont et al. (1989); Gia12: Giacintucci et al. (2012); Gia11: Giacintucci et al. (2011); Gos87: Goss et al. (1987); Gro: (submitted); Hog14: Hogan (2014); Kim18: Kim et al. (2018); Kol15: Kolokythas et al. (2015); Kol18: Kolokythas et al. (2018); Kra02: Krajnović & Jaffe (2002); Lai87: Laing & Bridle (1987); Mac20a: Maccagni et al. (2020); Mach06: Machacek et al. (2006); O'sul11: O'Sullivan et al. (2011a); Par86: Parma et al. (1986); Ran11: Randall et al. (2011); Ran15: Randall et al. (2015); Sche17: Schellenberger et al. (2017); Sche20a: Schellenberger et al. (2020b); Shu08: Shurkin et al. (2008); Sub03: Subrahmanyan et al. (2003); Tay02: Taylor et al. (2002); Ven94: Venkatesan et al. (1994); Vrt02:Vrtilek et al. (2002); **(3)**'inCav': inner cavities, corresponding to innermost jets/lobes and located within innermost 5 kpc; 'outCav': outer cavities, corresponding to outer jets/cavities; 'gCav': ghost cavities, no radio counterpart; 'pot-()Cav': potential cavities; 'CF': cold fronts as a sign of sloshing;'compact': smooth compact morphology of the hot X-ray atmosphere within the host galaxy (up to 10 kpc from the center); 'RPS tail': ram pressure stripped tail; *References column (3):* All06: Allen et al. (2006); Bal09: Baldi et al. (2009); Bal06: Balmaverde & Capetti (2006); Bha14: Bharadwaj et al. (2014); Bil04; Biller et al. (2004); Bla04: Blanton et al. (2004); Bor96: Borne & Colina (1996); Cro03: Croston et al. (2003); Cro08: Croston et al. (2008); Dev10: Devereux et al. (2010); Don10: Dong et al. (2010); Dun10: Dunn et al. (2010); Fab02: Fabbiano et al. (2002); Fin01: Finoguenov et al. (2001); For79: Forman et al. (1979); For05: Forman et al. (2005); For07: Forman et al. (2007); For06: Forbes et al. (2006); Gas07: Gastaldello et al. (2007); Gas09: Gastaldello et al. (2009); Gas13: Gastaldello et al. (2013); Gli03: Gliozzi et al. (2003); Gro19: Grossová et al. (2019); Har98: Hardcastle et al. (1998); Jet08: Jetha et al. (2008); Kol20: Kolokythas et al. (2020); Kra04: Kraft et al. (2004); Kra17: Kraft et al. (2017); Kim19: Kim et al. (2019); Lal13: Lal et al. (2013); Lak18: Lakhchaura et al. (2018); Lan10: Lanz et al. (2010); Mach05: Machacek et al. (2005); Mach06: Machacek et al. (2006); Mar02: Marshall et al. (2002); Mor06: Morita et al. (2006); Pan14b: Panagoulia et al. (2014); Pls: Plšek et al. (in prep.); Ran09: Randall et al. (2009); Ran11: Randall et al. (2011); San16: Sanders et al. (2016); Sche17: Schellenberger et al. (2017); Sche20: Schellenberger et al. (2020b); Shu08: Shurkin et al. (2008); Siv04: Sivakoff et al. (2004); Sta86: Stanger & Warwick (1986); Su17:Su et al. (2017); Su19: Su et al. (2019); Tay06: Taylor et al. (2006); Tri02: Trinchieri & Goudfrooij (2002); Wor10: Worrall et al. (2010); You02: Young et al. (2002) **(4)** 'dustyDisk': morphology of dust in form of disk; 'noDust': no dust observed; 'centDust': centrally located dust; dustLanes: dust in form of lanes; 'filDust': filamentary dust *References column (4):*; Ala12: Alamo-Martínez et al. (2012); Bil16: Bílek et al. (2016); Boi17: Boizelle et al. (2017); Cap00: Capetti et al. (2000); Dua14: Duah Asabere et al. (2014); Kim19: Kim et al. (2019); Col01: Colbert et al. (2001); Kul14: Kulkarni et al. (2014); Fab16: Fabian et al. (2016); Fer99: Feretti et al. (1999); Ferr99: Ferrari et al. (1999); Gou18: Goullaud et al. (2018); Gri99: Grillmair et al. (1999); O'sul18:O'Sullivan et al. (2018); Pah04: Pahre et al. (2004); Pen86: Pence (1986); Schm02: Schmitt et al. (2002); Smi12: Smith et al. (2012); Schw80: Schweizer (1980); Tan9: Tang et al. (2009); Tem07: Temi et al. (2007a); Tre06: Tremblay et al. (2006); Sah16: Sahu et al. (2016); Ver99: Verdoes Kleijn et al. (1999); Ver05: Verdoes Kleijn & de Zeeuw (2005); Xil04: Xilouris et al. (2004) **(5)** 'noHa': no detection of Hα+[N II] emission in the narrow-band imaging and confirming long slit spectroscopic observation, 'unkHa': the detection could not be confirmed, 'extHa': Hα+[N II] is extending to $\leq$ 2 kpc, 'nucHa': nuclear Hα+[N II] line emission, the extent is smaller than 2 kpc; *Reference column (25):* Ken08: Kenney et al. (2008); Lak18: Lakhchaura et al. (2018); **(6)** 'noCO': not dectected CO line emission; uppCO(..): upper limit on the CO line emission *References column (6):* Bab19: Babyk et al. (2019); Boi17: Boizelle et al. (2017); Boi21: Boizelle et al. (2021); Com07: Combes et al. (2007); Dav14: David et al. (2014a); Dav16: Davis et al. (2016); Fab16: Fabian et al. (2016); Fla10:Ocaña Flaquer et al. (2010); Hor01: Horellou et al. (2001); Huch88: Huchtmeier et al. (1988); Lau14: David et al. (2014b); Leo01: Leon et al. (2001); Nor21: North et al. (2021); O'sul15: O'Sullivan et al. (2015); O'sul18: O'Sullivan et al. (2018); Oli19: Olivares et al. (2019); Pra10: Prandoni et al. (2010); Ruf19: Ruffa et al. (2019); Sag89: Sage & Wrobel (1989); Sag93: Sage & Galletta (1993); Sim18: Simionescu et al. (2018); Tem18: Temi et al. (2018); You11: Young et al. (2011); Wik95: Wiklind et al. (1995); Wel10: Welch et al. (2010); (all) '-': not investigated yet

Chapter 4

VLA Radio Study of a Sample of Nearby X-ray and Optically Bright Early-Type Galaxies

R. Grossová,[1,2] *N. Werner,*[1] *F. Massaro,*[2] *K. Lakhchaura,*[3] *T. Plšek,*[1] *K. Gabányi,*[4,5,6] *K. Rajpurohit,*[7] *R. E. A. Canning,*[8] *P. Nulsen,*[9,10] *E. O'Sullivan,*[9] *S. W. Allen,*[11] *A. C. Fabian*[12]

[1]Department of Theoretical Physics and Astrophysics, Faculty of Science, Masaryk University, Kotlářská 2, Brno, 611 37, Czech Republic
[2]Dipartimento di Fisica, Universita degli Studi di Torino, via Pietro Giuria 1, I-10125 Torino, Italy
[3]MTA-Eötvös University Extragalactic Astrophysics Research Group, Pázmány Péter sétány 1/A, Budapest, 1117, Hungary
[4]ELKH-Eötvös University Extragalactic Astrophysics Research Group, Pázmány Péter sétány 1/A, Budapest, 1117, Hungary
[5]Konkoly Observatory, MTA Research Center for Astronomy and Earth Sciences, Konkoly Thege Miklós út 15-17, H-1121 Budapest, Hungary
[6]Department of Astronomy, Eötvös University, Pázmány Péter sétány 1/A, Budapest, 1117, Hungary [7]Dipartimento di Fisica e Astronomia, Universitá di Bologna, Via Gobetti 93/2, 40131, Bologna, Italy [8]University of Portsmouth, Winston Churchill Ave, Portsmouth PO1 2UP, UK
[9]Harvard Smithsonian centre for Astrophysics, 60 Garden Street, Cambridge, MA 02138, USA
[10]ICRAR, University of Western Australia, 35 Stirling Hwy, Crawley,WA 6009, Australia
[11]Kavli Institute for Particle Astrophysics and Cosmology, Stanford University, 452 Lomita Mall, Stanford, CA 94305-4085, USA
[12]Institute of Astronomy, University of Cambridge, Madingley Road, Cambridge CB3 0HA, UK

Submitted to Astrophysical Journal Supplement

Abstract

Many massive early-type galaxies host central radio sources and hot X-ray atmospheres indicating the presence of radio-mechanical active galactic nucleus (AGN) feedback. The duty cycle and detailed physics of the radio-mode AGN feedback is still a matter of debate. To address these questions, we present 1–2 GHz Karl G. Jansky Very Large Array (VLA) radio observations of a sample of the 42 nearest optically and X-ray brightest early-type galaxies. We detect radio emission in 41/42 galaxies. However, the galaxy without

a radio source, NGC 499, has recently been detected at lower frequencies by the Low-Frequency Array (LOFAR). Furthermore, 27/42 galaxies in our sample host extended radio structures and 34/42 sources show environmental interactions in the form of X-ray cavities. We find a significant correlation between the radio flux density and the largest linear size of the radio emission and between the radio power and the luminosity of the central X-ray point-source. The central radio spectral indices of the galaxies span a wide range of values, with the majority of the systems having steep spectra and the rest flat spectra. These results are consistent with AGN activity, where the central radio sources are mostly switched on, thus the duty cycle is very high. 7/14 galaxies with point-like radio emission (Fanaroff-Riley Class 0; FR 0) also show X-ray cavities indicating that, despite the lack of extended radio structures at 1–2 GHz, these AGN do launch jets capable of inflating lobes and cavities.

4.1 Introduction

The radio-mechanical feedback mode is thought to play a dominant role in the evolution of massive early-type galaxies, which host hot (10^7 K) X-ray emitting atmospheres. In the absence of balancing heating, the atmospheric gas should cool radiatively and form stars, building much larger and bluer galaxies than are seen. X-ray studies with *Chandra* and *XMM-Newton* as well as radio observations have shown that in these galaxies jet-inflated radio lobes displace the hot gas, creating 'cavities' in the X-ray emitting plasma (e.g. Fabian et al. 2003) and driving weak shocks and turbulence that heat the surrounding medium essentially isotropically (for a recent review see Werner et al. 2019). This feedback mode appears to be maintaining a remarkably long-lived delicate balance between heating and cooling in the hot X-ray emitting atmospheres of these systems (McNamara & Nulsen 2007).

Burns (1990) showed that as much as 70% of the central dominant galaxies (CDGs) in clusters are radio loud. Later, Mittal et al. (2009) found that all strong cool cores host a central radio source and Sun (2009) argued that all central brightest cluster and group galaxies with a radio emitting active galactic nucleus (AGN) are located in cool cores. Kolokythas et al. (2018) used the Giant Metrewave Radio Telescope (GMRT) to study the Complete Local-volume Groups Sample (CLoGS), consisting of 53 local galaxy groups, at 235 MHz and 610 MHz and also found a high radio detection rate of 87%. These results showed that the duty cycle of AGN in clusters and groups with short cooling times must be high. Moreover, the duty cycle for the X-ray cavities in clusters of galaxies of around 70% was found, although lower mass systems like groups and giant elliptical galaxies showed also lower duty cycles (between 30-50%) (Dunn et al. 2005; Dunn & Fabian 2006; Nulsen et al. 2009; Dong et al. 2010; Bîrzan et al. 2012, 2020). The ability to detect cavities depends on a number of factors including their location, size, age, the level of disturbance of the surrounding halo, the depth of the observation, and the instrument used, so estimates are likely subject to bias, and perhaps systematically underestimated as you go from the brightest clusters to fainter systems.

Results for the duty cycle in a population of massive galaxies are, however, somewhat less clear. Best et al. (2005) studied galaxies in the redshift range of $0.03 < z < 0.1$ and found that the fraction of galaxies with a radio-loud AGN increased with the stellar mass of the galaxy, reaching a maximum fraction of 30-40%. For a volume limited sample of very local (up to 15 Mpc) infrared luminous galaxies, Goulding & Alexander (2009) found that only 27% of the galaxies host an AGN. Other studies found a higher fraction. The K-band absolute magnitude limited ($M_K < -24$) sample of 396 early-type galaxies (Brown et al. 2011) showed the presence of radio continuum emission for all sources in the NRAO Very Large Array Sky Survey (NVSS) data combined with the single-dish data from the Green Bank Telescope (GBT), and Parkes Radio Telescope survey (PKS). Sabater et al. (2019) used observations at lower frequencies (120–168 MHz) from the LOw-Frequency ARray's (LOFAR's) Two-Metre Sky Survey (LoTSS) to investigate sources up to redshift 0.3 and confirmed previous findings of the high rate of radio source detection in the central region of massive galaxies.

A different approach was taken by Dunn et al. (2010), who focused on a volume-limited study of the 18 nearest ($d < 100$ Mpc) optically and X-ray brightest early-type galaxies. Compared to other studies,

their selection criteria also included X-ray luminosity, ensuring that the investigated galaxies really inhabit massive halos. Remarkably, their study revealed that nuclear radio emission is present in 17 out of the observed 18 galaxies. Furthermore, at least 10 of the galaxies with observed central radio emission also exhibited obvious spatially-extended jets in the Very Large Array (VLA) images. The authors concluded that the results present a severe challenge for models in which radio jets are considered a relatively rare and sporadic phenomenon (e.g. Binney & Tabor 1995; Kaiser & Binney 2003) and the active 'radio-mode' feedback most likely represents the default state for large elliptical galaxies.

Here, we extend the Dunn et al. (2010) study to the 42 optically and X-ray brightest, nearest ($d < 100$ Mpc) early-type galaxies, with declination greater than -40 degrees (to ensure coverage by the VLA) to observe their radio properties, investigate the duty cycles, and search for correlations between the radio plasma and their hot atmospheres, as well as emission line nebulae. Our sample includes both galaxies at the centres of groups and clusters and field ellipticals with their own hot X-ray emitting atmosphere. Our focus on the nearest systems, as well as the relatively long baseline of the VLA A configuration (35 km), ensures a good sensitivity and spatial resolution.

Sections in this paper are arranged as follows: The selection criteria for our sample are stated in Section 3.1. The radio morphology categories used in the paper are described in Section 4.2 and followed by Section 6.2, which presents the observations and data reduction for radio (Section 4.3.1) and X-ray (Section 4.3.2) data. The main results are summarized in Section 6.3 and discussed in Section 6.4. Section 3.5 presents additional sources excluded from the main sample. In Section 7.1, we conclude with a summary of our results.
Observed radio morphologies and relevant multifrequency data for every source are described in Section 5. *Chandra* X-ray data overlaid by radio contours obtained in multiple VLA configurations at 1–2 GHz, for all sources in our sample, are presented in Section 3.4, for both point-source-like (Section 3.4.1) and those showing extended (Section 3.4.2) radio morphologies. Finally, the Table in Section 3.3 includes information about the radio observations.

Throughout the paper, the spectral indices, α, are defined by flux density, $S_\nu \propto \nu^\alpha$ and radio powers as $P_\nu = 4\pi D_l^2 S_\nu$[1]. The distances were determined through the redshift-independent surface brightness fluctuation method due to proximity of the sources in our sample (see Table 3.2). The following cosmological parameters were used in this paper: $\mathrm{H}_0 = 67.8\,\mathrm{km\,s^{-1}\,Mpc^{-1}}$ (Planck Collaboration et al. 2016), $\Omega_\mathrm{M} = 0.308$ and $\Omega_\Lambda = 0.692$.

4.2 Radio Morphology Categories

We define four categories of radio sources (see Figure 4.1) depending on the total extent of radio emission: point sources, compact sources, diffuse sources, and sources with prominent jets and lobes. In some cases, the compact and diffuse sources reveal small-/large-scale jets and lobes, which we classify as a subcategory of the compact (e.g. NGC 5129) or diffuse (e.g. NGC 741) sources with jets/lobes.

The *point-source* category (PS) is defined for those sources with an extent smaller than twice the restoring beam size of their total intensity VLA map. Galaxies with radio emission larger than this threshold are indeed labeled as extended. In addition, *compact* sources (C) are defined when showing their total extent smaller than 5 kpc. On the other hand, *diffuse* (D) sources are those classified as having their radio emission extending to more than 5 kpc from the nucleus with a rather dispersed morphology, without well-defined large-scale jets/lobes. Lastly, for the sources in the category of *prominent jets/lobes* (J/L), the radio jets and lobes are the most prominent features (e.g. IC 4296) and well collimated and narrow (i.e., with opening angles less than a few tenths of degrees) extending more than 5 kpc from their radio core.

[1]The K correction was not applied given the redshift distribution of sources in our sample.

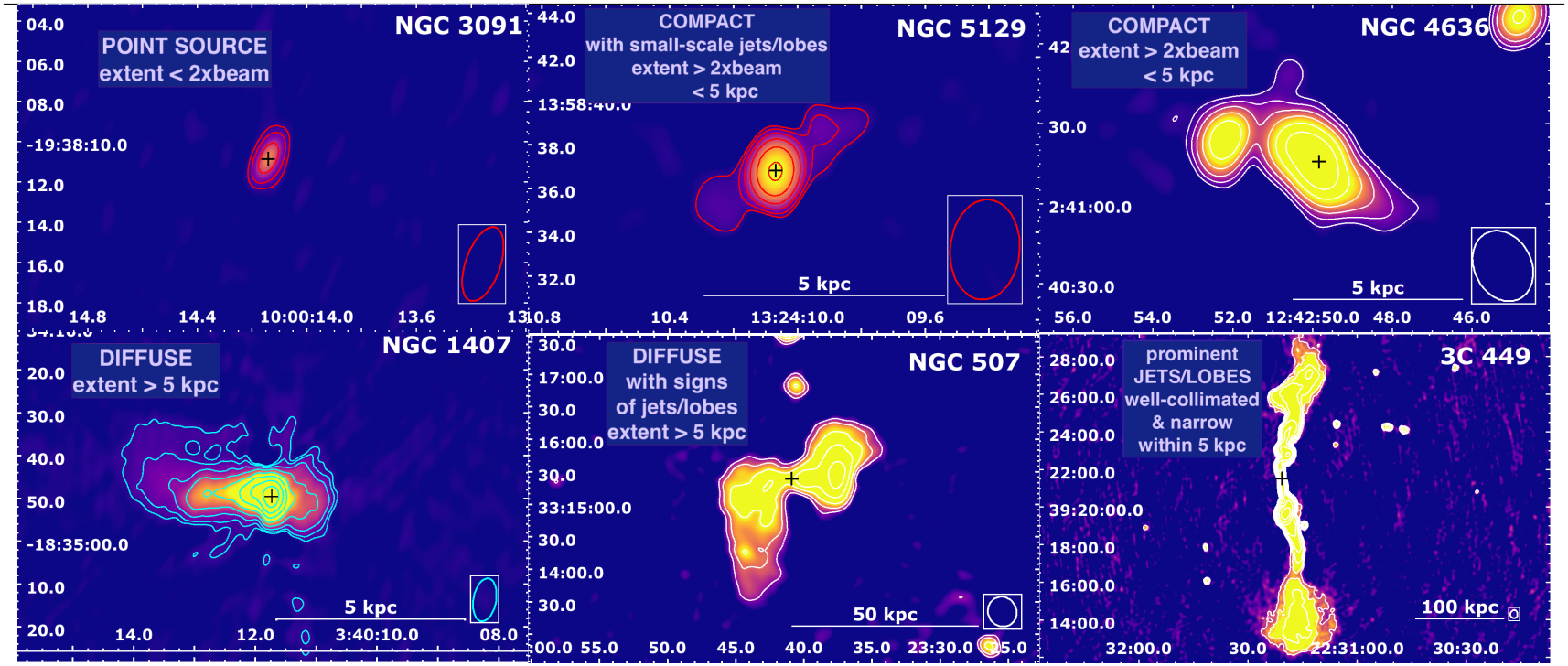

Figure 4.1: Examples of radio morphology categories. The lowest level of the red/cyan/white (configuration A/ B/ C or D) radio contours corresponds to $5\times$ RMS noise ($\sigma_{\rm RMS}$) in the image and the subsequent contours increase by factor of 2. The corresponding RMS noise and restoring beam size of the elliptical Gaussian for each source can be found in Table 3.2. The black cross depicts the position of the radio center of the galaxy.

4.3 Observations and Data Reduction

4.3.1 VLA Radio Observations and Analysis

We reduce and analyse VLA data obtained both before (historical VLA data) and after the major upgrade in 2011 (Karl G. Jansky VLA/EVLA data; Perley et al. 2009, 2011).

The major data size difference is in the increased bandwidth of the observations due to the upgrade to the Wideband Interferometer Digital ARchitecture (WIDAR) correlator system. The older historical data consisted of only one or two spectral windows with tens of channels with a channel width of 100–1000 kHz, whereas the Karl G. Jansky VLA data have tens of spectral windows with up to hundreds of channels with a channel width of 3000 kHz, which makes the size of the data set significantly larger. This affects our approach to the calibration methods we used for the two different data sets. For the Karl G. Jansky VLA data ($\sim$ 20-100 GB), we used the more effective pipeline calibration method and in the case of historical data, a manual calibration approach was chosen, following the 'Jupiter continuum calibration tutorial' available on the VLA NRAO website[2].

Historical VLA data

The pre-upgrade or historical VLA data sets were analysed for 33 galaxies in multiple configurations (details are given in Table 3.1) and observed for a large fraction of sources in our sample (i.e., more than $\sim$80%) in two spectral windows between 1.4–1.7 GHz. The important calibration steps for the historical data sets can be summarized as follows: The first step is to flag the imported data according to the suggestions from the NRAO observation log[3] (if available), then we run `tfcrop` (Time-Frequency Crop), the automatic flagging algorithm. The flux density for the corresponding VLA primary flux calibrators (Table 3.1) is set from a model (Perley & Butler 2013) with the CASA task `setjy`. Since there are only one or two single-channel spectral windows for most of the pre-upgrade historical data, we do not need to solve for the antenna delays and do the bandpass calibration. The next step is to determine the solution of the total gains for the flux density calibrator and finally, apply those gain solutions to the target.

Karl G. Jansky VLA data

The new Karl G. Jansky VLA observations at 1–2 GHz presented here include 20 sources in A configuration from our project (ID: 15A-305, PI: Werner) and 10 archival observations in various VLA configurations (Table 3.1). The details of the data reduction and imaging were described in our recent paper on the giant elliptical galaxy IC 4296 (Grossová et al. 2019).A similar approach is used to calibrate[4] and image all sources from the 2015 project. The corresponding flux density calibrators for each observation are listed in Table 3.1.

The imaging was performed with the MultiTerm MultiFrequency synthesis (`MTMFS`) `clean` algorithm (Rau & Cornwell 2011) with the `briggs` (`robust=0`) weighting scheme (Briggs 1995). The second order Taylor polynomial (`nterms=2`; McMullin et al. 2007) was used to account for the spectral behaviour of the sources. The various spatial scales of radio emission require an individual approach to each source with different combinations of weightings, gridders, convolvers, and uv-tapers. When the dynamic range of the total intensity images reaches high enough values[5], a few cycles of phase and possibly one cycle of amplitude and phase self-calibration are performed.

[2] https://casaguides.nrao.edu/index.php/Jupiter:_continuum_polarization_calibration

[3] http://www.vla.nrao.edu/cgi-bin/oplogs.cgi

[4] CASA pipeline version 1.3.11 and CASA version 4.7.2.

[5] We consider the dynamic range high enough when the ratio of the peak intensity to the RMS noise of the image is about 100.

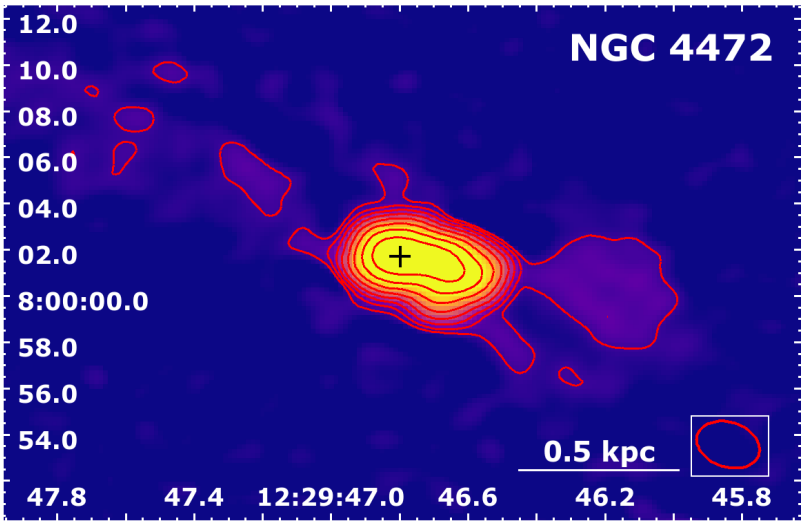

Figure 4.2: Example of the calibrated, final total intensity image of the giant elliptical galaxy NGC 4472 in the upgraded VLA A configuration data observed in 2015. The red contour levels are created at [1,2,4,8,16,...]$\times\, 5\,\sigma_{\rm RMS}$ up to peak intensity at 1.5 GHz ($S_{\rm peak}$). The RMS noise and peak intensity values are $22\,\mu{\rm Jy\,beam^{-1}}$ and $(2.79 \pm 0.11) \times 10^{-2}$ Jy (Table 3.2). The red ellipse in the white box represents the restoring beam of the final image. The black cross shows the position of the radio center of the giant elliptical galaxy.

An example of the final total intensity map is presented for the giant elliptical galaxy NGC 4472 in Figure 4.2. All details including the rms noise, peak intensity, scale and restoring beam are given in Table 3.2.

Total flux densities and uncertainties

The final total flux densities centered at 1.5 GHz ($S_{\rm 1.5GHz}$) for each source are derived using the `imstat` CASA task. It is worth noting that, for sources in the sample observed only in A or B configuration, the final flux density could be lower than the 'true' total flux density, because of the missing short baselines. On the other hand, we are mainly interested in central cores, where the flux density values are not effected by this missing short baselines.

The corresponding measurement uncertainties for the flux densities ($\Delta S_{\rm 1.5\,GHz}$) are determined as follows (e.g.: Klein et al. 2003; Rajpurohit et al. 2018):

$$\begin{aligned}\Delta S_{\rm 1.5GHz} &= \sqrt{(S_{\rm 1.5\,GHz}\cdot S_{\rm cal})^2 + S_{\rm n}^2 + S_{\rm z}^2} \\ &= \sqrt{(S_{\rm 1.5GHz}\cdot S_{\rm cal})^2 + \left(\sigma_{\rm RMS}\cdot\sqrt{npts/A_{\rm beam}}\right)^2},\end{aligned} \tag{4.1}$$

where $S_{\rm cal}$ is the specific calibration uncertainty, which is about 4% for VLA observations (Perley & Butler 2013). $S_{\rm n}$, the noise uncertainty, is defined as the off-source root-mean-square (RMS) noise ($\sigma_{\rm RMS}$) of the image multiplied by the square-root of *the number of points* ($npts$) in pixels per area, which covers the entire radio emission of the source divided by *the beam area* ($A_{\rm beam}$) in pixels. The term $S_{\rm z}$ accounts for a possibly wrong zero level, but may be neglected for interferometric observations (Klein et al. 2003).
The RMS noise values were determined from four circular off-source regions in the image using `casaviewer` and the median was taken as the final $\sigma_{\rm RMS}$. The CASA tool for image analysis, `ia.beamarea`, gives an area that is covered by the beam or $A_{\rm beam}$ in pixels. Finally, we create a polygonal region enclosing the source's entire radio emission and save it into a CASA region file with the extension '.crtf'. The CASA task `imstat` with a parameter `region='*.crtf'` is used to determine the integrated flux density at 1.5 GHz ($S_{\rm 1.5GHz}$) and

the number of points (*npts*) or pixels within that specific region of the source emission.
The value of the peak intensity at 1.5 GHz ($S_{\rm peak}$) and the corresponding uncertainties are determined accordingly.

Spectral index maps

To investigate the most recent activity of the AGN in our sample, we produce in-band spectral index maps from our 15A-305 VLA A configuration project for 18 giant elliptical galaxies. Each observation contains 16 spectral windows spanning the frequency range between 1–2 GHz.

We adopted two different approaches to estimate the spectral index. First, we used the MultiTerm Multi-Frequency (MTMFS) deconvolution algorithm in the TCLEAN CASA task. It produces two Taylor coefficient images: *tt0* as an equivalent of a Stokes I image, thus containing the information on the emission at a reference frequency, and *tt1* as a Taylor expansion term. The spectral index α is then defined as: $\alpha = {\rm tt1/tt0}$. The final output of the spectral index map is stored in the CASA product file, '.alpha.image.tt0' with the corresponding measurement uncertainty values saved in the CASA product, '.alpha.image.alpha.error.tt0'. To focus only on the emission above $5\times \sigma_{\rm RMS}$, we applied this threshold value through the task `widebandpbcor` to the final 'alpha image' and with a parameter `calcalpha`, we recalculated the spectral index map. In the `casaviewer`, a circular region for each source with the diameter of 0.7 kpc is defined to investigate the spectral index at the same physical scale in all 18 galaxies. The size of the central region (0.7 kpc) was chosen to be applicable to all of our sources taking into account the different distances. This region was then used to extract the mean spectral index values from the threshold-adjusted CASA 'alpha images'.

For our second approach, we estimated the spectral index fitting flux densities measured in the central regions as described in the following. We split the 12 spectral windows[6] into 4 chunks and 'cleaned' them separately with specific reference frequencies (1.1, 1.3, 1.7 and 1.9 GHz). Then, we smoothed the image chunks with the CASA task `imsmooth` to gain the same restoring beam size (resolution). Lastly, in `casaviewer`, we extracted the flux densities from a circle of 0.7 kpc diameter centered at the radio core (consistent with the peak of radio intensity or the point from which the symmetrical jets/lobes are streaming out and are confirmed by the position of the center listed in the literature or NASA/IPAC Extragalactic Database (NED)[7]) and calculated the spectral indices as a slope of the log-log fit with the extracted flux densities on the y-axis and the corresponding frequencies on the x-axis.

Comparison between the two methods adopted to estimate the spectral index are shown in Figure 4.3 for the case of NGC 4472 and results appear in good agreement. Although, the latter method is simpler, because the spectral index maps ('alpha images') are automatically created during the TCLEAN task with the parameter `nterms=2`. For further analysis of spectral indices, we concentrate only on this approach.

Potential contribution of star formation to radio emission

To estimate the potential radio contribution from star formation, we follow the analysis of Kolokythas et al. (2018). We determine the far-ultraviolet (FUV) fluxes of the galaxies with point-source-like radio emission using the Galaxy Evolution Explorer (GALEX) Survey GR6 catalog[8] to estimate the star formation rate (SFR) (Bell 2003), from which we determine the expected radio power (Salim et al. 2007). If the expected radio power from the FUV estimated SFR is at least half of the observed radio power, star-formation could potentially be the dominant radio emission mechanism.

[6] The 12 spectral windows were left after flagging the original 16 spectral windows.
[7] https://ned.ipac.caltech.edu/
[8] https://galex.stsci.edu/GR6/?page=mastform

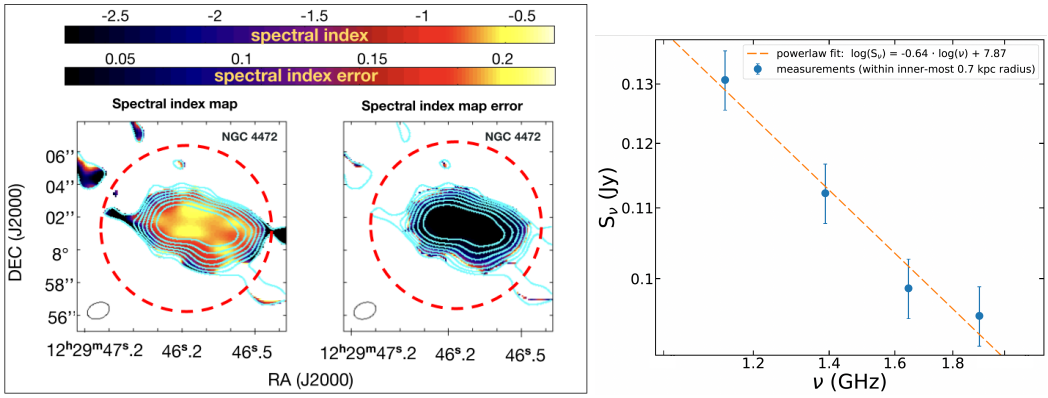

Figure 4.3: Example of determining the spectral index for NGC 4472 from a red circle with a diameter of 0.7 kpc. **Top:** The CASA output 'alpha image' and its corresponding uncertainty values. In CASAVIEWER, we extracted the mean spectral index of (-0.55±0.05). **Bottom:** The manual fitting of 4 frequency chunks and their corresponding flux densities gives a final spectral index value for NGC 4472 of -0.64, which is comparable with the mean spectral index from the CASA 'alpha image'.

4.3.2 X-ray *Chandra* Observations and Analysis

We use archival *Chandra* Advanced CCD Imaging Spectrometer (ACIS) observations first reported and described in Lakhchaura et al. (2018).

The archival *Chandra* observations were processed using the standard CIAO 4.13 (Fruscione et al. 2006) procedures and a most recent calibration files (CALDB 4.9.4). For galaxies observed multiple times, the individual observations were reprojected and merged. Most galaxies were observed in the VFAINT mode using the ACIS-S chip, however, for a couple of galaxies we combined the ACIS-S and ACIS-I observations and for some of the galaxies there were only ACIS-I observations available.

The observations were deflared using the `lc_clean` algorithm within the `deflare` routine. The images were generated from the merged observations using the `fluximage` procedure with a binsize of 1 pixel (0.492 arcsec). The images were background-subtracted using `blanksky` background files, which were scaled to match the observations in the $9-12$ keV band, and exposure corrected using the corresponding exposure maps. The point sources were found using the `wavdetect` tool, inspected visually and filled with a mean surrounding surface brightness using the `dmfilth` procedure (CIAO 4.13).

The two-dimensional surface brightness distribution of each image obtained by this procedure was modelled using a projected version (Ettori & Fabian 2000) of a classical beta model (Cavaliere & Fusco-Femiano 1976). The fitting was performed in the SHERPA 4.13 package (Freeman et al. 2001) using the Cash statistics (Cash 1979) and Monte Carlo optimization method (Storn 1995). The fitted models were subtracted from the original images and the resulting residual images were used for further analysis. Individual X-ray cavities were searched by eye using residual images and their reliability was checked using the Poisson statistics to be at least 4σ under the surrounding background. The detection of these cavities is further supported also by a novel machine learning method (a.k.a CADET; Plšek et al. in prep.).

4.4 Results

Here, we report the results of radio observations for a sample of 42 early-type galaxies (41 giant elliptical galaxies and 1 lenticular galaxy). Our sample contains the most optically and X-ray luminous early-type galaxies within the luminosity distance of ~ 100 Mpc at declinations that are accessible by the VLA (for more details see Section 3.1). All details are reported in Table 3.2.

4.4.1 Multiscale Radio Emission

Central radio emission

Our results show a high radio core[9] detection rate of 98% (41/42) for the early-type galaxies in our sample within the frequency range between 1–2 GHz, centered at 1.5 GHz (Table 3.2).

For the remaining galaxy, NGC 499, no central radio emission has been detected in the available VLA observations in the L-band (1–2 GHz). However, an archival single-dish Arecibo observation at 2.38 GHz (Dressel & Condon 1978), an observation by the NVSS survey at 1.4 GHz (Brown et al. 2011, although, only with a 2σ detection) and most recently a low-frequency observation with LOFAR (Bîrzan et al. 2020) detect a faint nuclear point-like radio source in the centre of NGC 499. Thus, due to the previously confirmed presence of radio emission from NGC 499 in the above-mentioned studies, the detection rate in our sample could be considered to be 100%.

The non-detection of the radio emission from NGC 499 in the highest resolution VLA A configuration data could be due to the shallow observations with a resulting RMS noise of $\sim 12.0\times10^{-5}$ Jy/beam, which is twice the sensitivity limit for our faintest detected radio source in our sample: NGC 4406 (Table 3.2). Observations with LOFAR at $\sim$150 MHz detected a radio core with a total integrated flux density of 0.046 ± 0.009 Jy. Assuming a spectral index of about -0.7, we estimate that NGC 499 would have a radio source with the total flux density of 0.009 Jy at 1.5 GHz, which is still above the threshold of the archival VLA A observation, potentially indicating a steeper spectrum. We note that the much higher flux density of 0.26 Jy reported by Condon & Broderick (1988) at 1.4 GHz frequency does not agree with all other available radio measurements.

Extended radio emission

For 67% (28/42) of the galaxies in our sample, we detect a diffuse, extended morphology.

It is worth noting that we present only a lower limit for the number of galaxies with extended radio emission. Due to our main interest in detecting the radio cores, the highest resolution A configuration data are prioritized. Sensitivity to the diffuse, extended emission was sacrificed at the expense of the higher resolution of the fine structures in the central region. The more compact configuration observations (C or D) are missing for a fraction of sources (11 sources out of 42) in our sample.

4.4.2 Radio morphology

The morphology of the radio emission at 1–2 GHz varies widely within our sample of early-type galaxies.

On the one hand, the total intensity radio maps reveal well-collimated large-scale radio jets and lobes extending up to hundreds of kiloparsecs (e.g. NGC 315 ; Figure 3.3c) or small-scale jets residing within a few kpc from the radio nucleus (e.g. NGC 5129; Figure 3.5h). On the other hand, we also observe many galaxies, where the jets and lobes are disturbed by the influence of the surrounding hot gas or interaction with other galaxies: narrow or wide angle tails (e.g. NGC 507; Figure 3.3d; and IC 4296; Figure 3.3b), tails tracing the path of the interaction with another galaxy (e.g. NGC 741; Figure 3.3g), S-shaped radio emission (e.g. NGC 1316; Figure 3.4a), diffuse morphology with no clear jets or lobes (e.g. NGC 1407; Figure 3.4c) and relic-like large-scale diffuse emission (e.g. NGC 5419; Figure 3.6a). A more detailed definition of our categories is given in Section 4.2.

For IC 4296 (Figure 3.3b), NGC 57 (Figure 3.1b), NGC 533 (Figure 3.3e), NGC 1550 (Figure 3.4d), NGC 4261 (Figure 3.4f), NGC 4374 (Figure 3.4g), NGC 4472 (Figure 3.4h), NGC 4552 (Figure 3.5b), NGC 5129,(Figure 3.5h) and NGC 5419 (Figure 3.6a), we found new, previously unobserved and undescribed radio morphology at the high resolution of about 1–2 arcseconds in the frequency range of 1–2 GHz (red contours in Figures in

[9] A radio core is point-like radio emission within twice the beam size located at the center of host galaxy.

Section 3.4.2).

Details of radio morphologies (together with relevant information on the multifrequency data) for each source are given in Section 5.

4.4.3 Comparison with X-ray Data

X-ray cavity rate

The hot X-ray emitting atmospheres embedded in galaxies are closely related to the activity of their central radio-emitting AGN (e.g.: McNamara et al. 2005; Werner et al. 2019).

In our sample, we compared *Chandra* X-ray images with the total intensity radio images searching for signatures of interaction as X-ray cavities. We reported also all known X-ray cavities from the literature.

We also detected X-ray cavities for 7 sources with only point-like radio morphology and for NGC 499 (Panagoulia et al. 2014; Kim et al. 2019). Cavities in NGC 1132 and NGC 4778, which host point-like radio sources were previously detected by Dong et al. (2010) and Morita et al. (2006). Additionally, Plšek et al. (in prep.) found potential cavities for another five point-like radio sources: NGC 2300, NGC 3091, NGC 3923, NGC 4073, NGC 4125 (see Discussion 4.5.5 for more details).

In our sample we can summarize that 34 out of 42 (81%) early-type galaxies show detectable X-ray cavities in their hot X-ray atmospheres.

Central X-ray point source rate

In the parent X-ray study, Lakhchaura et al. (2018) found nuclear X-ray point sources for 32% of early-type galaxies (16 out of 49 in their study), from which 14 X-ray point sources are relevant to our study.

It is worth noting that while a radio emission is detected in 98(–100)% sources of our sample, only about 33% (14/42) of the systems also host a detectable central X-ray point source.

4.4.4 Multifrequency Correlations

We investigate the correlations and trends between the radio power at $\sim$1.5 GHz ($P_{1.5\mathrm{GHz}}$) and the X-ray luminosity within 10 kpc from the center of the galaxy (Figure 4.4; top), the luminosity of the central X-ray point source or AGN (Figure 4.4; bottom), entropy and cooling time of the hot X-ray emitting gas (Figure 4.5; top and bottom, respectively), the power of the jet estimated from X-ray cavities (Figure 4.6; left), the luminosity of Hα+[N II] nebulae (Figure 4.6; middle), the mass of the central supermassive black hole (Figure 4.6; right), and the largest linear size of the radio emission (Figure 4.7). Moreover, the flux density distribution for point-like and extended radio sources is presented in Figure 4.8.

The details of the Hα+[N II] nebulae emission extent and other information about multiphase gas is given in Section 3.6 and Table 3.4.

The Spearman and Pearson correlation coefficients are used to derive the trends between two investigated quantities without accounting for the measurement uncertainties. Moreover, a Bayesian approach to linear regression taking into account the corresponding measurement uncertainties for both x and y variables, as well as the upper limits was used within the `linmix` package[10] (Kelly 2007).

The statistical significance of the trends is represented by the probability derived from the null hypothesis test (i.e., the p-value).

[10] https://github.com/jmeyers314/linmix

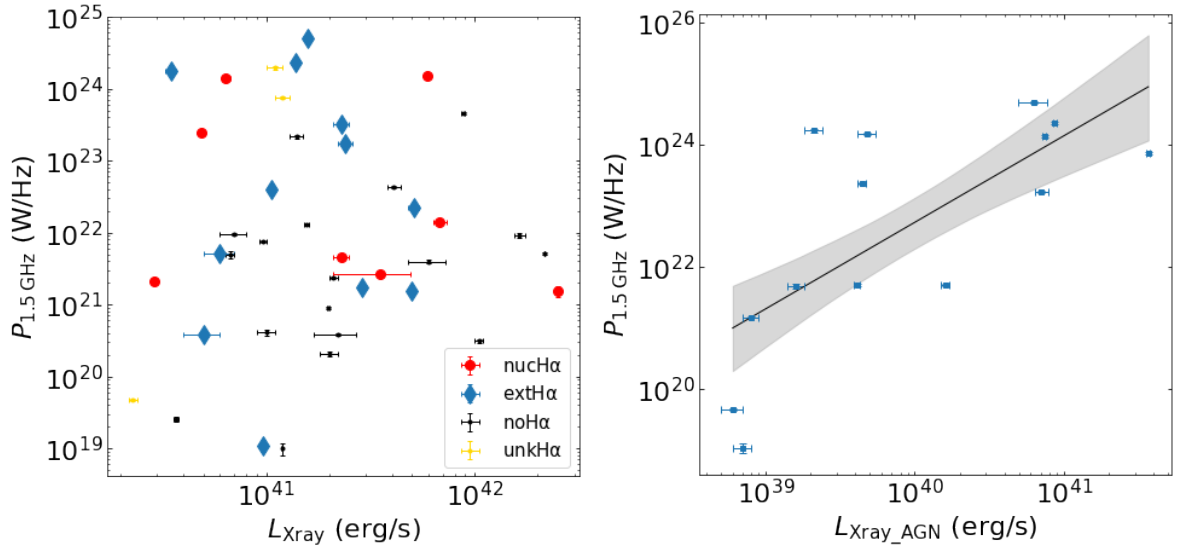

Figure 4.4: **Left:** Relation between radio power at $\sim$1.5 GHz ($P_{1.5\mathrm{GHz}}$) vs. the X-ray luminosity (L_{Xray}) within the 10 kpc from the center of the galaxy shows no correlation. **Right:** Significant correlation ($r \sim 0.68$, P-value$\sim$ 0.01) is seen, when we compare the radio power at $\sim$ 1.5 GHz ($P_{1.5\mathrm{GHz}}$) with the luminosity of the central X-ray point sources ($L_{\mathrm{Xray\_AGN}}$) (Lakhchaura et al. 2018) detected only in a subset of our main sample of early-type galaxies. Error bars on the radio power are mostly smaller than the plotted symbol size. The correlation coefficients and corresponding P-values are given in Table 4.1.

Significant trends, with Spearman and Pearson correlation factor of 0.71 and corresponding p-value of 0.004 are obtained when comparing the radio power with the luminosity of the central X-ray point source (Figure 4.4; bottom) and the radio flux density with the largest linear size of the detected radio emission (Figure 4.7).

Negligible correlations are found when comparing the radio power with the jet power required to inflate the cavities; the luminosity of the X-ray atmosphere (Figure 4.4; top), and the luminosity of the warm ionized nebulae, traced by Hα+[N II] line emission (Figure 4.6; middle), the mass of the supermassive black hole (Figure 4.6; right) as well as various thermodynamical properties of the X-ray emitting hot gas like entropy (Figure 4.5; top) and cooling time (Figure 4.5; bottom) (Lakhchaura et al. 2018).

4.4.5 Nuclear Spectral Indices

To estimate the age of the radio emitting plasma in the innermost central regions (within 0.7 kpc radius of the radio core) of early-type galaxies, we determined in-band spectral indices for 18 out of 42 galaxies observed with the upgraded VLA A configuration. The description of the approach we used to determine the spectral indices for the subsample of our galaxies can be found in Section 4.3.1.

The final central spectral indices are presented in Table 4.2 and Figure 4.9. Interestingly, about 1/3 of our sources have inverted or flat radio spectra ($\alpha \geq -0.5$), while the majority showed steep spectral indices ($\alpha < -0.5$). This result is consistent with a scenario where some of sources were recently active, while for some, the spectral shape is in agreement with synchrotron cooling.

Investigated Relations $P_{1.5\,\mathrm{GHz}}$ vs.	Fitted points	Spearman r	Spearman p-value	Pearson r	Pearson p-value	linmix ρ	linmix α	linmix β
L_{Xray}	all	0.06	0.71	0.06	0.71	$0.06^{+0.17}_{-0.16}$	40.9 ± 1.2	0.02 ± 0.06
	nuc/extHα	-0.12	0.62	-0.10	0.66	$-0.10^{+0.20}_{-0.20}$	42.1 ± 2.0	-0.4 ± 0.9
	no Hα	0.19	0.046	0.33	0.19	$0.32^{+0.22}_{-0.26}$	38.5 ± 2.4	0.1 ± 0.11
$L_{\mathrm{Xray\_AGN}}$	all	0.71	< 0.004	0.71	< 0.004	$0.68^{+0.14}_{-0.21}$	31.9 ± 2.9	0.4 ± 0.13
$K_{10\,\mathrm{kpc}}$	all	0.03	0.37	0.02	0.34	$0.34^{+0.14}_{-0.16}$	0.7 ± 0.4	0.04 ± 0.02
t_{cool}	all	0.29	0.06	0.31	0.05	$0.17^{+0.17}_{-0.15}$	-0.7 ± 0.6	0.04 ± 0.03
P_{jet}	all	0.05	0.83	0.22	0.33	$0.33^{+0.23}_{-0.27}$	39.4 ± 2.4	0.13 ± 0.1
$L_{\mathrm{H}\alpha+[\mathrm{NII}]}$	all	-0.23	0.34	-0.31	0.19	$-0.30^{+0.24}_{-0.22}$	-0.1 ± 0.1	42.3 ± 2.0
M_{BH}	all	0.07	0.75	0.02	0.93	$0.01^{+0.22}_{-0.22}$	9.1 ± 2.1	0.01 ± 0.09
	nuc/extHα	0.41	0.16	0.39	0.18	$0.38^{+0.25}_{-0.31}$	5.8 ± 2.8	0.1 ± 0.1
	no Hα	-0.37	0.29	-0.18	0.62	$-0.16^{+0.35}_{-0.38}$	11.4 ± 5.4	-0.1 ± 0.3
$S_{1.5\,\mathrm{GHz}}$ vs. LLS	all	0.64	< 0.0002	0.64	< 0.0003	$0.63^{+0.11}_{-0.14}$	1.62 ± 0.1	0.4 ± 0.1

Table 4.1: The linmix correlation coefficients between the radio power at 1.5 GHz and the properties of the ambient hot and warm gas and the mass of the central supermassive black hole. The corresponding parameters of the fit are: the Spearman correlation coefficient and Pearson correlation coefficient and the corresponding p-values, the linmix correlation coefficient (ρ), the log normalisation (α) and the power-law index (β).

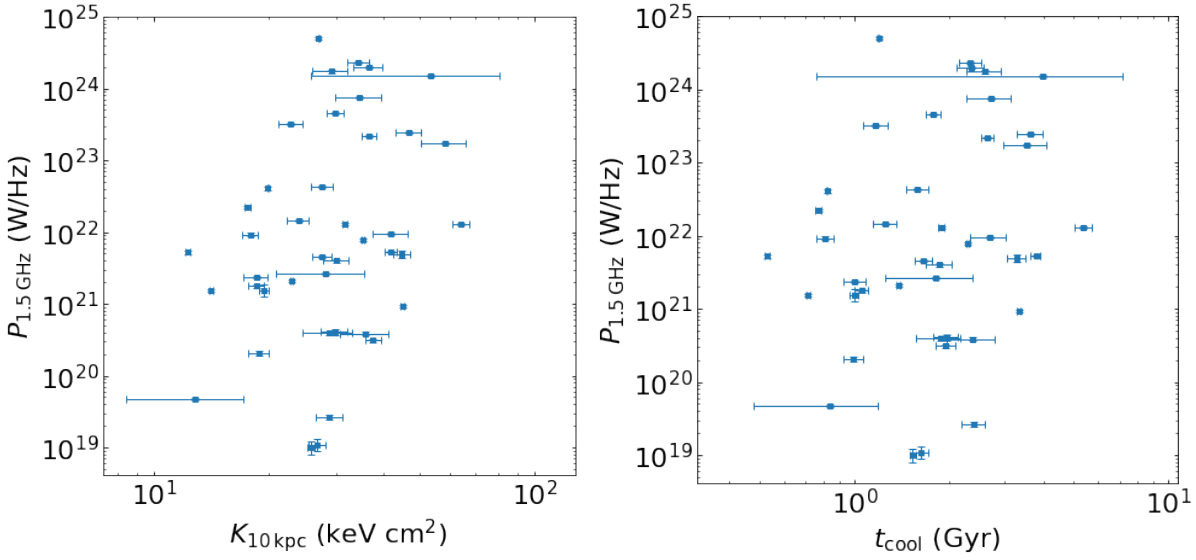

Figure 4.5: The radio power ($P_{1.5\mathrm{GHz}}$) plotted against the entropy (**left**) and cooling time (**right**) of the hot X-ray emitting gas measured within $r < 10$ kpc shows no correlation ($r < 0.2$). Error bars on the radio power are mostly smaller than the plotted symbol size.

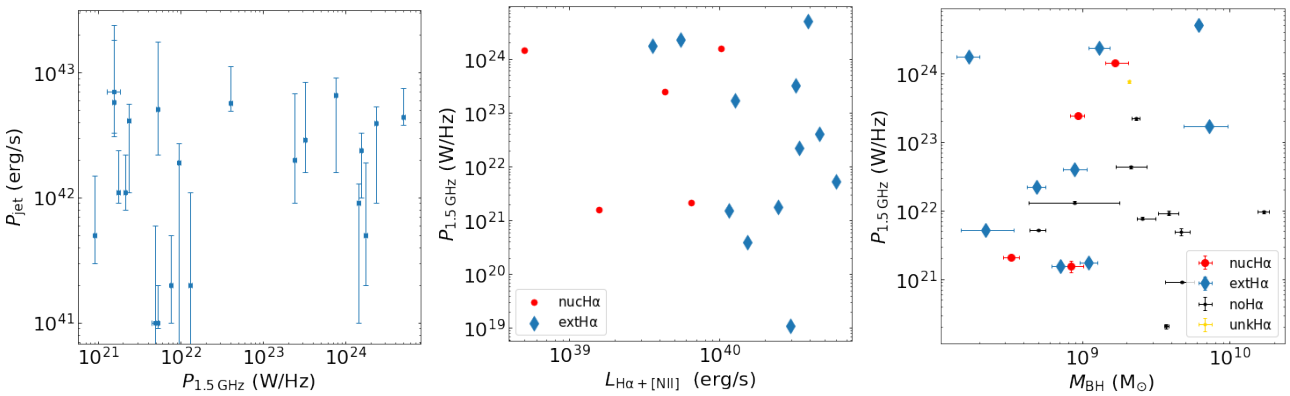

Figure 4.6: No correlation is found between the radio power ($P_{1.5\,\mathrm{GHz}}$) and the jet power (P_{jet}; **left**), the Hα+[N II] luminosity ($L_{\mathrm{H}\alpha+[\mathrm{NII}]}$; **middle**) as well as the supermassive black hole mass (M_{BH}; **right**). The nuclear (nucHα), extended (extHα), undetected (noHα) and unknown (unkHα) H$\alpha+$[NII] emission are distinguished. The correlation coefficients and corresponding p-values are given in Table 4.1. Error bars on the radio power are mostly smaller than the plotted symbol size.

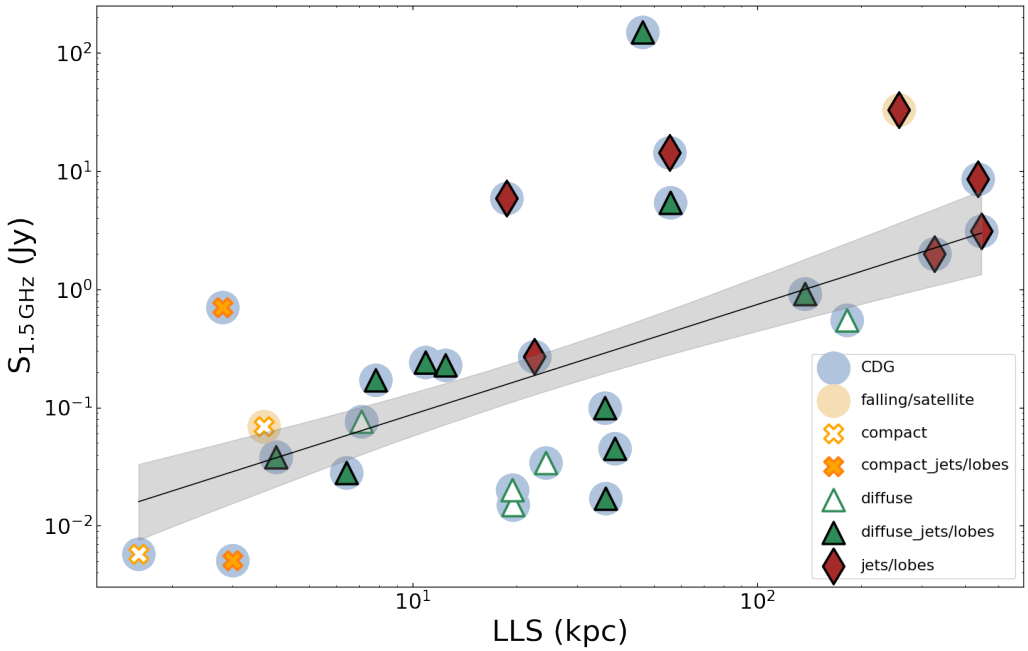

Figure 4.7: The total flux density at 1.5 GHz ($S_{1.5\,\mathrm{GHz}}$) is plotted against the largest linear size (LLS) of the radio source. A positive correlation with a linmix correlation coefficient of 0.66 with P-value of 0.002 is determined. The brighter the radio source, the larger its linear extent. The correlation coefficients and corresponding P-values are given in Table 4.1.

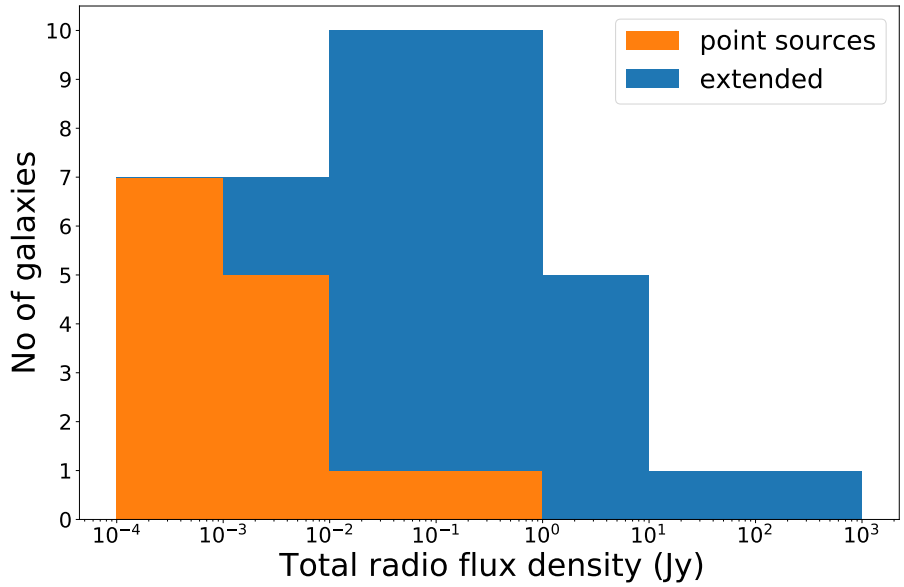

Figure 4.8: The total integrated radio flux density histogram with two morphologically different categories: point sources and extended sources. The fainter sources fall into the point sources category, whereas the brighter galaxies are the extended ones.

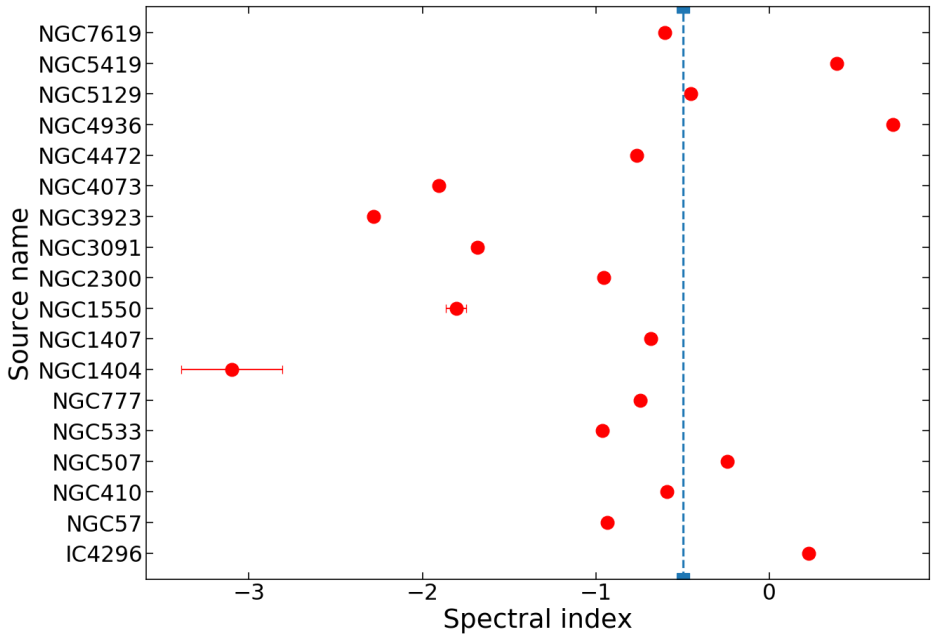

Figure 4.9: Radio spectral indices for a subset of our sample. Approximately, 3/4 of the sources have steep spectra ($\alpha < -0.5$) and the rest have flat and inverted radio spectra ($\alpha \geq -0.5$). The chosen division line at the spectral index of -0.5 is shown by the blue dashed line.

Source	Spectral index
IC 4296	0.224±0.005
NGC 57	-0.934±0.014
NGC 410	-0.698±0.055
NGC 507	-0.289±0.058
NGC 533	-0.978±0.068
NGC 777	-0.757±0.080
NGC 1404	-2.554±0.621
NGC 1407	-0.727±0.025
NGC 1550	-1.628±0.387
NGC 2300	-0.954±0.004
NGC 3091	-1.259±0.227
NGC 3923	-2.074±0.851
NGC 4073	-0.647±0.053
NGC 4472	-0.548±0.054
NGC 4936	0.491±0.042
NGC 5129	-0.506±0.006
NGC 5419	0.342±0.002
NGC 7619	-0.614±0.014

Table 4.2: The mean values of the spectral indices and corresponding uncertainties determined from the central region with diameter of 0.7 kpc for a subset of our early-type galaxies.

4.5 Discussion

4.5.1 High Detection Rate

The early-type galaxies in our sample show a very high radio detection rate at frequencies between 1–2 GHz. For 41 out of the sample of 42 galaxies, we detected at least point-like emission in the central region. A significant fraction, 27/42 galaxies, shows extended radio emission from jets and lobes. For 26 out of these 42 galaxies, the presence of X-ray cavities was detected. Moreover, X-ray cavities were also detected for 8 sources without jets/lobes. Altogether, 34 sources show signatures of interaction with the X-ray emitting medium. This suggests that most of these systems are operating in the radio-mechanical or maintenance mode AGN feedback.

Our high detection rate of radio sources appears to be consistent with previous findings (e.g.: Dunn et al. 2010; Brown et al. 2011; Sabater et al. 2019). At first glance, these results indicate a very high AGN duty cycle. It is, however, worth noting that the detected extended radio emission does most likely not always represent the current state of AGN activity and is often a remnant from a previous cycle.

4.5.2 Origin of Radio Emission

To investigate whether the origin of the observed radio emission is solely related to AGN activity or could also be linked to star formation[11], we follow the analysis of Kolokythas et al. (2018). We determine the far-ultraviolet (FUV) fluxes of the galaxies with point-source-like radio emission using the Galaxy Evolution Explorer (GALEX) Survey GR6 catalog[12] to estimate the star formation rate (SFR) (Bell 2003), from which we determine the expected radio power (Salim et al. 2007). If the expected radio power from the FUV estimated SFR is at least half of the observed radio power, star formation could potentially be the dominant radio emission mechanism.

Our analysis shows that for 5 out of the 14 galaxies with point-like radio morphology, namely NGC 1404, NGC 3091, NGC 3923, NGC 4073 and NGC 4406, star formation could dominate the observed radio emission (see Table 4.3). However, 3/5 sources where the radio emission could potentially be dominated by star-formation activity, also host ghost cavities, indicating that radio-mode AGN activity is also present in these galaxies (see Section 4.5.5). Importantly, 7/14 point-like galaxies display cavities indicating that despite the lack of extended radio structures at 1–2 GHz, these galaxies host a radio AGN capable of inflating lobes and cavities. The two galaxies, which lack observable signatures of radio mode AGN feedback are NGC 1404 and NGC 4406, which are falling through and being stripped by the ICM of the Fornax and Virgo clusters, respectively.

Using FUV fluxes as an indicator of star formation, Kolokythas et al. (2018) found that for 5 of the 26 galaxies in their high richness subsample of the Complete Local-volume Groups Sample (CLoGS), the star formation could have a significant contribution to the radio emission.

Table 4.3: The star formation contribution to the radio emission in the case of early-type galaxies with point-source radio morphologies. The columns: (1) the source name; ' * ': sources observed within our project 15A-305; (2) the far-ultraviolet flux from GALEX-DR5 (GR5) catalogue(Bianchi et al. 2011); (3) the estimated star fomation rate (SFR) according to relation by Bell (2003); (4) the expected radio power from the SFR (Salim et al. 2007); (5) the half value of the radio power; if the expected power dominates of 1/2 of the observed power, star formation dominates.

Source Name	**$\mathbf{FUV_{flux}}$ VLA**	**$\mathbf{SFR_{FUV}}$ (Code)**	$P_{\mathbf{1.5GHz\_exp}}$ **(year-month-day)**	**50% of $\mathbf{P_{1.5GHz\_obs}}$ Calibrator**
IC1860	(60.3 ± 6.3)	(7.10 ± 0.70)	$(1.29 \pm 0.13) \times 10^{20}$	$(7.13 \pm 0.33) \times 10^{21}$
NGC 57*	(94.5 ± 7.2)	(7.30 ± 0.60)	$(1.32 \pm 0.10) \times 10^{20}$	$(1.93 \pm 0.10) \times 10^{20}$
NGC 410	(77.8 ± 9.3)	(4.40 ± 0.50)	$(7.92 \pm 0.90) \times 10^{19}$	$(1.29 \pm 0.05) \times 10^{21}$
NGC 410	(97.6 ± 2.7)	(5.49 ± 0.15)	$(9.95 \pm 0.28) \times 10^{19}$	$(1.29 \pm 0.05) \times 10^{21}$
NGC 1132	(59.7 ± 9.4)	(6.00 ± 0.90)	$(1.08 \pm 0.17) \times 10^{20}$	$(1.98 \pm 0.13) \times 10^{21}$
NGC 1404*	(550.1 ± 27.2)	(2.85 ± 0.14)	$(5.16 \pm 0.26) \times 10^{19}$	$(5.20 \pm 0.80) \times 10^{18}$
NGC 1404*	(702.9 ± 1.5)	(3.64 ± 0.01)	$(6.60 \pm 0.01) \times 10^{19}$	$(5.20 \pm 0.80) \times 10^{18}$
NGC 1404*	(778.2 ± 3.9)	(4.03 ± 0.02)	$(7.30 \pm 0.04) \times 10^{19}$	$(5.20 \pm 0.80) \times 10^{18}$
NGC 1404*	(732.3 ± 5.7)	(3.79 ± 0.03)	$(6.90 \pm 0.06) \times 10^{19}$	$(5.20 \pm 0.80) \times 10^{18}$
NGC 2300*	(150.8 ± 6.7)	(3.35 ± 0.2)	$(6.07 \pm 0.27) \times 10^{19}$	$(2.05 \pm 0.20) \times 10^{20}$
NGC 2300*	(163.0 ± 4.2)	(3.62 ± 0.01)	$(6.56 \pm 0.17) \times 10^{19}$	$(2.05 \pm 0.20) \times 10^{20}$
NGC 3091*	(186.4 ± 3.4)	(5.62 ± 0.1)	$(1.02 \pm 0.02) \times 10^{20}$	$(7.60 \pm 0.40) \times 10^{19}$

[11] Especially for low luminosity galaxies with no significant extended emission known as FR 0s (Baldi et al. 2015), the synchrotron emission at GHz frequencies could also be due to particles accelerated in star forming regions (see e.g., Condon 1992; Lacki & Thompson 2013)

[12] https://galex.stsci.edu/GR6/?page=mastform

Table 4.3 - continued. The CASA imaging results for our VLA sample.

Source Name	$\mathbf{FUV_{flux}}$ (μJy)	$\mathbf{SFR_{FUV}}$ ($10^{-2}\,M_{\odot}$/yr)	$P_{\mathbf{1.5GHz\_exp}}$ (W/Hz)	50% of $P_{\mathbf{1.5GHz\_obs}}$ (W/Hz)
NGC 3091*	(163.5 ± 4.2)	(4.93 ± 0.34)	$(8.90 \pm 0.60) \times 10^{19}$	$(7.60 \pm 0.40) \times 10^{19}$
NGC 3923*	(438.4 ± 6.1)	(2.49 ± 0.03)	$(4.51 \pm 0.06) \times 10^{19}$	$(1.29 \pm 0.11) \times 10^{19}$
NGC 3923*	(357.5 ± 21.5)	(2.03 ± 0.12)	$(3.68 \pm 0.22) \times 10^{19}$	$(1.29 \pm 0.11) \times 10^{19}$
NGC 4073*	(191.0 ± 3.9)	(8.91 ± 0.18)	$(1.61 \pm 0.03) \times 10^{20}$	$(1.54 \pm 0.09) \times 10^{20}$
NGC 4073*	(130.0 ± 10.2)	(6.1 ± 0.05)	$(1.10\pm)\,0.09 \times 10^{20}$	$(1.54\pm)\,0.09 \times 10^{20}$
NGC 4125	(206.80 ± 16.6)	(1.22 ± 0.10)	$(2.22 \pm 0.18) \times 10^{19}$	$(2.36 \pm 0.11) \times 10^{19}$
NGC 4406*	(1004.0 ± 9.0)	(4.16 ± 0.04)	$(7.53 \pm 0.07) \times 10^{19}$	$(5.30 \pm 1.00) \times 10^{18}$
NGC 4406*	(1029.6 ± 12.6)	(4.26 ± 0.05)	$(7.72 \pm 0.09) \times 10^{19}$	$(5.30 \pm 1.00) \times 10^{18}$
NGC 4406	(800.7 ± 17.2)	(3.32 ± 0.07)	$(6.01 \pm 0.13) \times 10^{19}$	$(5.30 \pm 1.00) \times 10^{18}$
NGC 4936	(70.0 ± 9.2)	(0.89 ± 0.12)	$(1.61 \pm 0.21) \times 10^{19}$	$(1.96 \pm 0.08) \times 10^{20}$
NGC 7619	(81.2 ± 6.6)	(2.31 ± 0.22)	$(4.20 \pm 0.40) \times 10^{19}$	$(3.82 \pm 0.15) \times 10^{21}$
NGC 7619	(95.4 ± 3.3)	(2.31 ± 0.11)	$(4.18 \pm 0.20) \times 10^{19}$	$(3.82 \pm 0.15) \times 10^{21}$
NGC 7619	(81.6 ± 7.0)	(2.31 ± 0.23)	$(4.20 \pm 0.40) \times 10^{19}$	$(3.82 \pm 0.15) \times 10^{21}$

4.5.3 AGN duty cycle

To study the duty cycle of radio mode AGN activity in more detail, we estimate the spectral indices in the nuclear regions for a subsample of our early-type galaxies (Table 4.2). The distribution of the central spectral indices could help us place better constraints on the duty cycle of the AGN.

From in-band VLA analysis of the mean spectral indices of the radio emission within 0.7 kpc from the central region, we determined that approximately 1/3 of the sources have a relatively flat ($\alpha \geq -0.5$) spectral index. The rest of the galaxies have steep spectra. This result indicates that the age of the radio emitting plasma in the centres of these galaxies spans a range of values and while the radio mode AGN activity is variable, it has a relatively high duty cycle.

This analysis could also motivate a more in-depth investigation of the nuclear activity of these AGN. For example, higher resolution VLBI observations would offer a closer look at the central regions and their most recent state of activity. From our sample, an example is provided by the recently active source NGC 5044, where Schellenberger et al. (2020b) confirm ongoing jet activity using VLBA and summarize the presence of multiple generations of X-ray cavities.

Another example in the sample is NGC 1407, where we see a small-scale young jet in the core (Giacintucci et al. 2012). A recent study of NGC 1316 (Maccagni et al. 2021) using the upgraded Karoo Array Telescope (MeerKAT), as well as VLA and ALMA data, found a highly variable central radio source in the last three cycles of its activity. One cycle, forming large diffuse radio lobes, could have started around 20 Myr ago. The second cycle started possibly around 3 Myr ago, forming a flattened S-shaped structure. The current activity appears to be 1 Myr old.

4.5.4 Correlations with Radio Power

We investigated the possible correlations between the radio power and the X-ray luminosity of the hot halo as well as the central point source, the thermodynamical properties of the hot gas, the Hα+[N II] luminosity, and the jet power calculated from the X-ray cavities and between the radio flux density and the largest linear size of the radio emission (Table 4.1 and Figure 4.4, 4.5, 4.6, 4.7).

We see a significant correlation with Spearman and Pearson coefficient of 0.64 with p-value of 0.004) between the total radio flux density and the largest linear size of the radio emission. The larger the total extent of the radio emission, the more powerful the source is (Singal 1993; Lara et al. 2001; Shabala & Godfrey 2013; Tang et al. 2020). While the distances of our sources span a factor of 6, the radio fluxes span four orders of magnitude. The range of radio power is thus too large to be accounted for by the more powerful sources being more distant.

Similarly, a significant correlation with Spearman and Pearson coefficient of 0.71 with the p-value of 0.004) is found between the radio power and the X-ray luminosity of the central X-ray point source[13]. The correlation is consistent with a scenario where the X-ray emission comes from an unresolved X-ray jet or the base of the jet.

The relation between the luminosity of the hot X-ray atmospheres within 10 kpc radius from the central region and the radio power at 1.5 GHz shows no correlation. The lack of trends could, at the first glance, appear surprising. It is worth noting that the lack of any trend detected here could be affected by the limited range of X-ray luminosities in the innermost regions up to radius of 10 kpc spanning over approximately one order of magnitude in comparison with a large span of radio power values ($\sim$6 orders of magnitude; Figure 4.4; left). Moreover, for a stable continuous accretion of the hot atmospheric gas, at a given black hole mass, one would expect higher accretion rates and thus more powerful jets for lower entropies and shorter cooling times.

[13]To take into account biasing due to the same D_l^2 dependence, we compared X-ray luminosity of the atmosphere ($L_{\rm Xray}$) within 10 kpc radius from the core with the radio flux ($S_{1.5GHz}$) instead of the radio power ($P_{1.5GHz}$), resulting in a slightly lower correlation coefficient of 0.61 and p-value of 0.01

However, the gas with typical cooling times seen in early-type galaxies is expected to be thermally unstable (e.g. Fabian & Nulsen 1977; Nulsen 1986). Assuming that the ambient medium cools and forms dense clouds with very small volume filling fractions that fall toward the central black hole, the accretion rate can for short moments rise by orders of magnitude, triggering a feedback response (Gaspari et al. 2013; Voit et al. 2015b; McNamara et al. 2016). Since the infall of dense clouds with a range of masses is essentially chaotic, the power of a given triggered outbursts can also have a range of values. Thus, we are not expecting any trend between the thermodynamic properties of the atmospheric gas and the observed radio emission.

The radio power showed no correlation with the radio power and the jet power computed using X-ray cavities (Lakhchaura et al. 2018, and references therein) and Hα+[N II] luminosity (Lakhchaura et al. 2018) and the mass of the central supermassive black hole[14].
The Hα+[N II] emitting gas represents only a fraction of the cold/warm gas mass in the centres of these galaxies and the observed nebulae are not necessarily located in the vicinity of the supermassive black hole. Therefore, the lack of correlation is not entirely surprising. Results of the statistical analysis are consistent with previous ones found in the literature (Franceschini et al. 1998; Liu et al. 2006). Weak correlations with CO emitting cold molecular gas have previously been observed by Babyk et al. (2019).

4.5.5 Interaction with the X-ray Gas

Widening radio jets

One of the signatures of the interaction between the radio plasma and the hot X-ray gas could be seen in the widening of the jets after they pierce through the relatively dense galactic atmosphere.

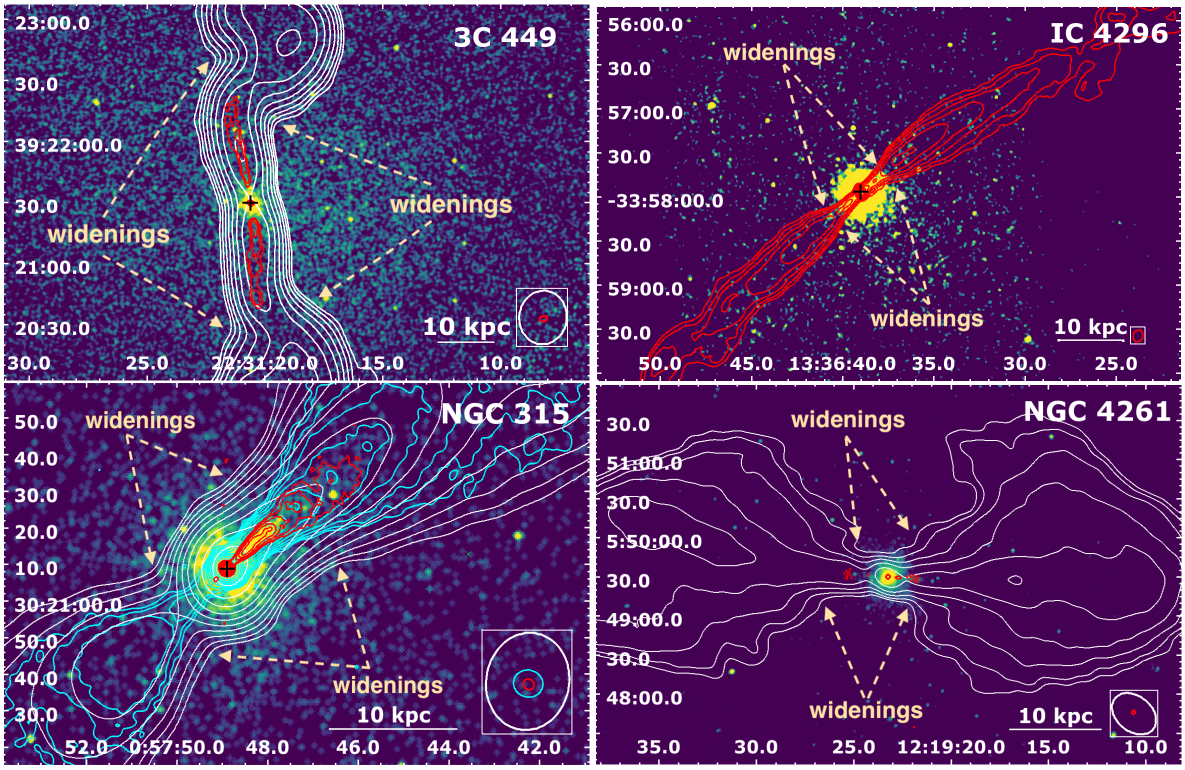

Figure 4.10: Widening of the radio contours visible for 3C 449, IC 4296, NGC 315 and NGC 4261. The radio contour levels are drawn at 5×RMS noise, increasing by factors of 2 up to the peak intensity. The RMS noise and peak intensity values can be found in Table 3.2. The black cross depicts the radio center of the galaxy.

The radio contours in 3C 449, NGC 315, NGC 4261 and IC 4296[15] by e.g.: Killeen & Bicknell (1988); Grossová et al. (2019) (Figure 4.10) widen significantly at about 10-20 kpc as the relativistic plasma in jets is released from the higher pressure environment

[14]The supermassive black hole masses were adapted from Kormendy & Ho (2013) and Saglia et al. (2016) using direct measurements and from Lauer et al. (2007) and Makarov et al. (2014), who derived the masses from the $M_{BH} - \sigma$ scaling relations and taken from (Lakhchaura et al. 2018).
[15]The mechanism was described for IC 4296

of the hot X-ray gas.
The widening and the corresponding brightening of the jets could be connected to the lower ambient ICM pressure and possibly to additional thermal energy from the interaction of the radio and X-ray plasma that will increase the pressure of the radio jet causing it to expand (e.g. Gizani & Leahy 1999).

Ghost X-ray cavities

Evidence for the past interaction between the radio and X-ray plasma, in the form of 'ghost'[16] cavities, was also observed in the giant elliptical galaxy NGC 499 (Panagoulia et al. 2014; Kim et al. 2019), which is the only galaxy in our sample with a non-detection of a radio source at 1–2 GHz (Section 4.4.1) using our VLA data. Similarly, X-ray cavities have been observed in seven galaxies with only a central point source in radio. Those previously known are: NGC 1132 (Dong et al. 2010) and NGC 4778 (Morita et al. 2006). Additionally, Plšek et al. (in prep.) found potential cavities for another five sources: NGC 2300, NGC 3091, NGC 3923, NGC 4073, and NGC 4125.

The lack of radio emission filling the volume of X-ray cavities is most likely due to the old, aged plasma present in lobes. Assuming the lobes rose and expanded at the sound speed $c_s \approx 500\,\mathrm{km/s}$ of 1 keV gas, then the radio plasma in the ghost cavities has aged at the time scales $\sim$ 10 Myr thus barely visible at the observed radio frequencies unless other mechanisms occur.

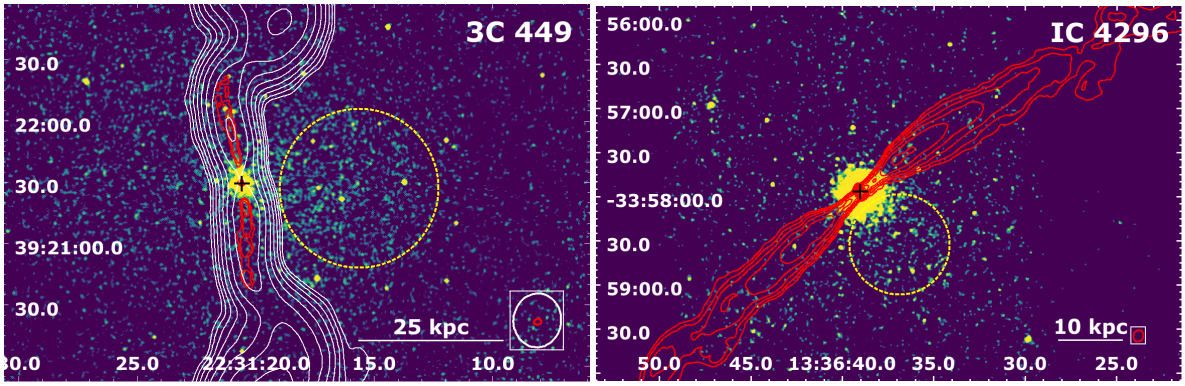

Figure 4.11: The *Chandra* X-ray images smoothed to enhance the X-ray tail enclosed by the radio jets of 3C 449 and IC 4296. The black cross indicates the position of the radio center of the galaxy.

Possible X-ray tail

We observe an X-ray tail in the so-called cross-cone region between the jets (yellow circles in the images of IC 4296 and 3C 449; Figure 4.11) due to the relative motion of the intra-cluster/group medium and the centrally located jetted galaxy in a system that experiences ICM sloshing. With a large opening angle of the jets and the presence of potential 'warm' spots, the galaxies can be categorised as Wide Angled Tail (WAT) galaxies (e.g.: Owen & Rudnick 1976; O'Donoghue et al. 1990; Leahy 1993; Missaglia et al. 2019).

4.5.6 Unresolved, Point-like Central Radio Sources

The origin of the observed radio emission for a few sources in our sample could be also due to other processes rather than being only related to AGN activity as, for example, especially for low luminosity objects, linked to star formation. Despite the presence of non-thermal radio emission occurs in radio galaxies with no significant extended emission at GHz frequencies as FR 0s (Baldi et al. 2015), synchrotron emission could be also due to particles accelerated in star forming regions thus emitting in the GHz regime (see e.g., Condon 1992; Lacki & Thompson 2013).
Our analysis shows that for 5 of the 14 galaxies with point-like radio morphology, star formation could dominate the observed radio emission. Moreover, 7/14 point-like galaxies display cavities indicating that despite the lack of extended radio structures at 1–2 GHz, these galaxies host a radio AGN capable of inflating lobes and cavities. Importantly, 4/5 sources where the radio emission could potentially be dominated by star-formation activity, also host ghost cavities, indicating that radio-mode AGN activity is also present in these galaxies. The only galaxy, which could entirely lack radio mode AGN activity is NGC 1404 falling through and being stripped by the ICM of the Fornax Cluster.

[16] In the systems, where the radio relativistic plasma has aged up to the point, where it stops to shine in radio, the X-ray cavities appear without radio counterpart, thus called 'ghost' cavities.

Using FUV fluxes as an indicator of star formation, Kolokythas et al. (2018) found that 5 of the 26 galaxies in their high richness subsample of the Complete Local-volume Groups Sample (CLoGS), the star formation could have a significant contribution to the radio emission.

4.5.7 Potential Candidates for Recoiled Black Hole

In gas-rich galaxies, the central black holes can coalesce 10^6-10^7 years after the merger of progenitor galaxies (Escala et al. 2005) and due to the asymmetrical gravitational wave recoil, the final coalescent black hole can be kicked out of the system at large velocities, ranging from hundreds to thousands of km s^{-1}. To date, there have been tens of observed candidates for such black holes ejected by gravitational wave recoil (also supported by simulations, e.g. Campanelli et al. 2007; Blecha et al. 2016, 2013; Chiaberge et al. 2017; Condon et al. 2017; Komossa 2012). The broad line region can be carried away by the recoiling black hole and the AGN can continue to be active (e.g.: Komossa 2012).

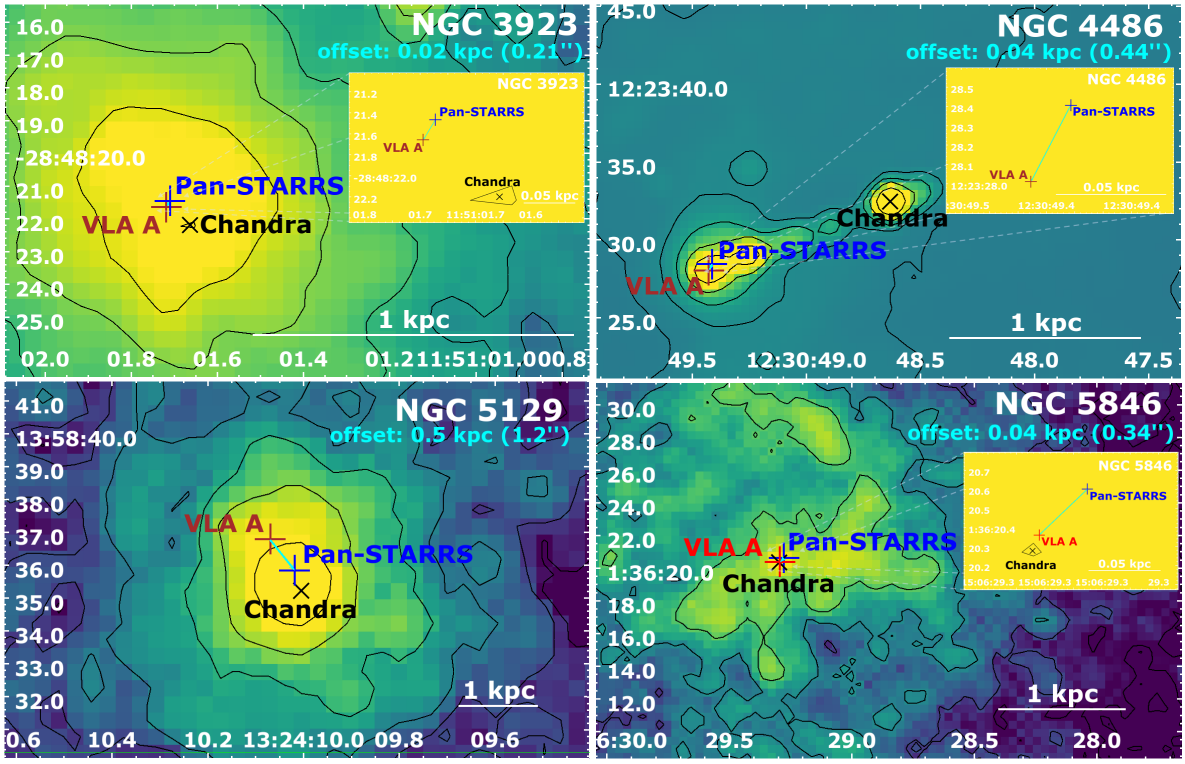

Figure 4.12: *Chandra* images with overlaid black X-ray contours and a black 'X' to mark the central X-ray brightness peak. The innermost X-ray contour is drawn by estimating the peak of the average count value of the *Chandra* image with the DS9 (Joye & Mandel 2003) `projection region tool`. The subsequent contours levels are decreasing as a power of two. The brown cross shows the core of the radio emission from VLA A configuration data and the blue cross represents the position of the optical center from Pan-STARRS in each image (estimated from the innermost optical contour). The offset of the observed radio core emission with respect to the central peak of the optical emission is shown by cyan lines. Small offsets (within 0.5 kpc) are seen for NGC 3923, NGC 4486, NGC 5129 and NGC 5846.

Small offsets: NGC 3923, NGC 4486, NGC 5846, NGC 5129

Multifrequency studies were carried out to search for such recoiling black holes (Lena et al. 2014; Barrows et al. 2016; Skipper & Browne 2018; Ward et al. 2021). Even in the cases of the giant elliptical galaxies M 87 (NGC 4486) and NGC 5846, a pc-scale displacement of the SMBH from the center of the host galaxy was observed and ascribed to the recoil mechanism (Batcheldor et al. 2010; Lena et al. 2014). Although, the apparent supermassive black hole offset in M 87 could be just due to the variation of the flux as suggested by López-Navas & Prieto (2018).

In our analysis, we present a previously unpublished candidate for radio/X-ray offset from the optical core of 1.2 arcsec (0.5 kpc), which may be the result of a displaced supermassive black hole from the central potential of the host giant elliptical

galaxy NGC 5129. And we confirm the previous findings for NGC 4486 and NGC 5846, where we also find small offsets of the central radio emission relative to the optical/X-ray emission. Moreover, we found a previously unpublished small offset of 0.21 kpc for the radio emission in the central regions of NGC 3923.

All small-scale offsets are shown in Figure 4.12.

Intriguing radio lobe emission in NGC 4125

The most intriguing is the offset radio emission located 46 arcseconds (4 kpc) from the radio core of NGC 4125 (Figure 4.13; top). The unusual position of the radio emission has been previously reported by Krajnović & Jaffe (2002), who claimed that due to the missing optical counterpart, it is probably a background source. However, our analysis, where we estimated how distant a potential background source would need to be if its optical counterpart is not seen by the Panoramic Survey Telescope and Rapid Response System (Pan-STARRS)[17] showed that it is quite unlikely that the observed radio emission is connected to a background source.

Our analysis takes into account the limiting apparent magnitude of the Pan-STARRS survey of 23 mag. We derived that a galaxy similar to M 87, with an absolute magnitude of -21.5, would need to be at least at the luminosity distance of $\sim$6300 Mpc (corresponding to a redshift of 0.95) to be missed by the optical survey. At this luminosity distance, the potential background radio source would have a size of $\sim$1 Mpc (assuming a linear scale 8 kpc/arcseconds) and large radio power of 10×10^{25} W/Hz, corresponding to twice the power of the giant radio halo in the cluster merger 'El Gordo' (Lindner et al. 2014) at the redshift of $z = 0.87$.

Moreover, we examined the archival data from TIFR GMRT Sky Survey (TGSS) at 148 MHz and Westerbork Synthesis Radio Telescope (WSRT) data at 1.4 GHz and created a spectral index map between these two frequencies (Figure 4.13; bottom). We found a flat spectral index at the position of the radio/X-ray/optical core of NGC 4125 and steeper spectral indices in a clear double morphology of the radio emission resembling a FR II radio galaxy, which would potentially disfavor the recoiled black hole scenario. A 'kicked-out' black hole, which recoils and moves with a high velocity relative to the galaxy, would be expected to form narrow tail structures along its path (Blecha et al. 2011), whereas we observe an apparently untouched radio emission from potential hotspots (especially in the north-western side).

The analysis of the X-ray *Chandra* data reveals possible X-ray cavities (Plšek et al.; in prep.) perpendicular to the core of NGC 4125, thus they do not correspond to the offset radio emission in the form of radio lobes.

Burke-Spolaor et al. (2017) found a similar offset radio source in the central dominant galaxy (CDG) of the galaxy cluster Abell 2261 with a missing optical and X-ray counterpart (Gültekin et al. 2021). Interestingly, the radio morphology of the emission resembles the one in NGC 4125 with its pear-like shape.

Further analysis needs to be carried out to investigate the origin and source of this unusual double-lobe radio emission.

4.5.8 Potential Fanaroff-Riley Class II Radio Sources

Most of the early-type galaxies in our sample are low power Fanaroff-Riley Class I (FR I, Capetti et al. 2017a) radio sources. Although, two giant ellipticals, NGC 533 and NGC 1600, show morphological similarities to Fanaroff-Riley Class II (FR II, Capetti et al. 2017b) radio sources, but they still have low powers significant for FR Is (see Section 1.3.1).

NGC 533

The radio morphology of NGC 533 (Figure 4.14; top) was observed within our 15A-305 project in the VLA A configuration and has a resolved central region and two inflated almost symmetric small-scale spherical radio jets/lobes with a possible hot spot in the western lobe. We suggest that this source resembles the radio morphology of FR II radio galaxies based on the visual comparison with sources in the FR II FIRST Catalog (FRIICAT) (Capetti et al. 2017b). Further analysis of the in-band spectral index map revealed a flattening of the spectral index at the position of radio lobes especially in the region west of the radio core visible in Figure 4.14 (bottom left). Potentially, due to its small physical size (less than 30 kpc), it could fall into the category of Compact Double Radio galaxies (COMP2CAT) Jimenez-Gallardo et al. (2019). NGC 533 could resemble the compact radio source J132031.47-012718.5 (Figure 4.14; bottom right).

[17] https://panstarrs.stsci.edu/

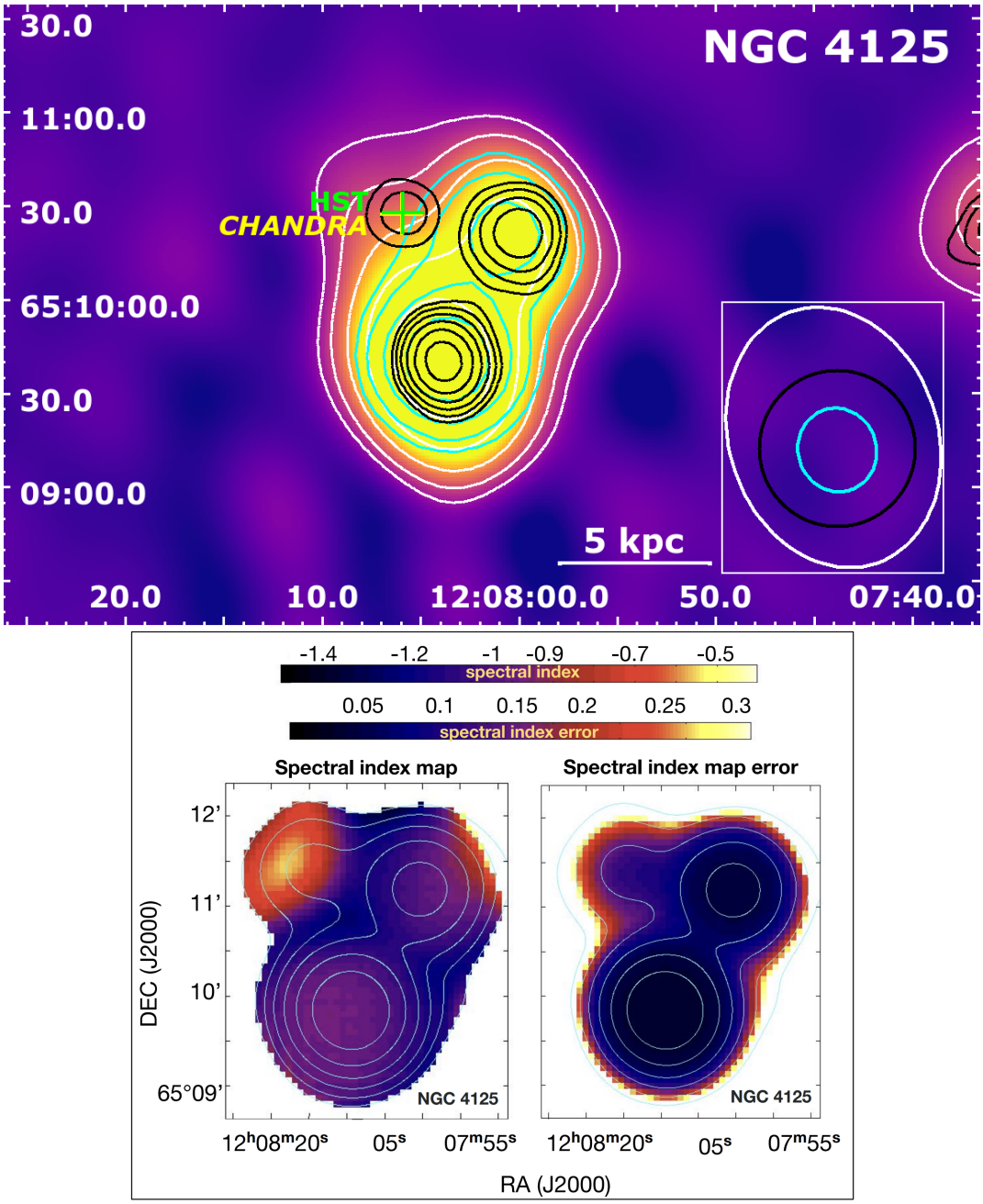

Figure 4.13: **Top:** VLA D configuration total intensity image of NGC 4125 with overlaid radio isophots in white. The contours in cyan and black represent the emission from TGSS at 148 MHz and WSRT at 1.4 GHz, respectively. In all cases the contour levels are at [1, 2, 4, 8, 16,...] $\times 5 \cdot \sigma_{\rm RMS}$. The corresponding RMS noise levels ($\sigma_{\rm RMS}$) for VLA D configuration, TGSS and WSRT data is 67 μJy, 1.7 mJy and 60 μJy, respectively. The restoring beam (resolution) for each observation can be found in the bottom right corner of the image in the white box. The optical (HST) center of the galaxy is shown as a green cross and is consistent with the X-ray center (*Chandra*; a yellow cross) and the radio center, most promint in the WSRT image at 1.4 GHz. **Bottom:** The spectral index map between 148 MHz (TGSS) and 1.4 GHz (WSRT).

NGC 1600

The radio emission of the giant elliptical galaxy NGC 1600 was previously published by Birkinshaw & Davies (1985), where they used VLA C configuration data at 4.885 GHz. They defined the source as a double and stated that the galaxy and lying close to

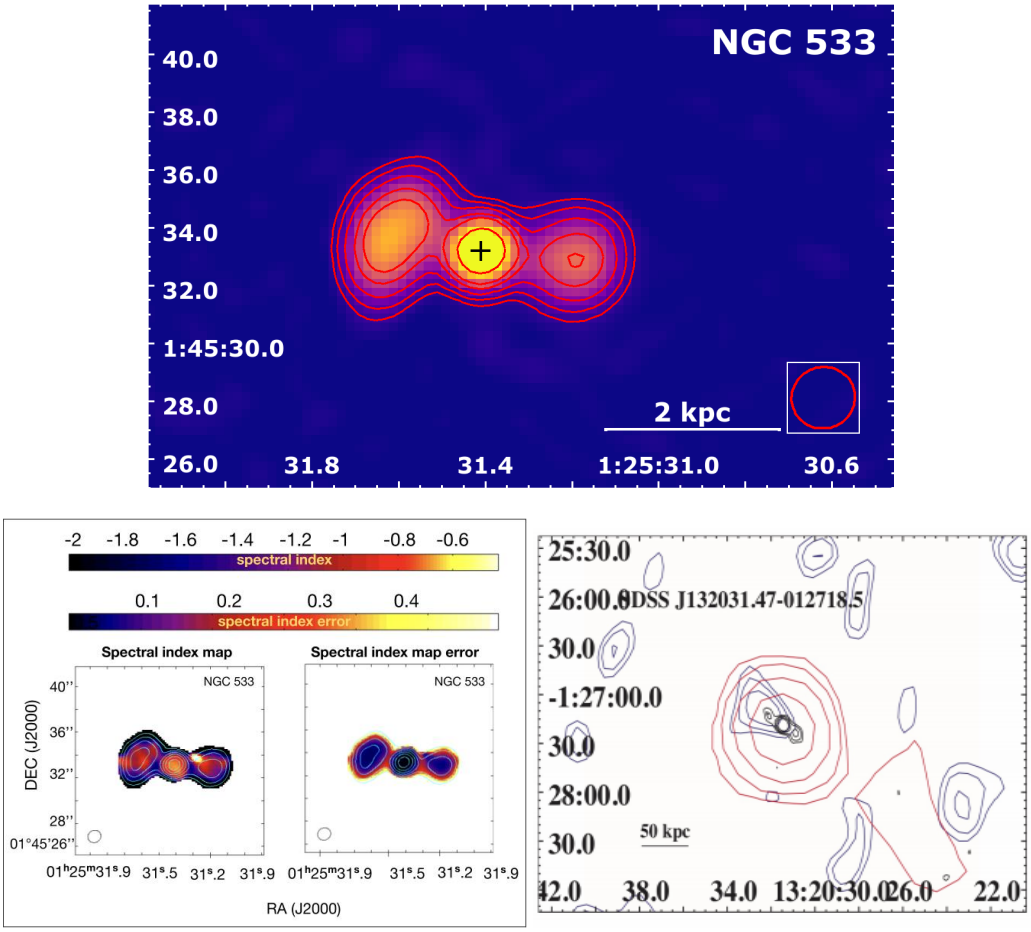

Figure 4.14: **Top:** The total intensity image of NGC 533 in VLA A configuration at 1–2 GHz and (**bottom left:)** its corresponding in-band spectral index map with measurement uncertainties produced by the multi-term 'cleaning' algorithm in CASA. **Bottom right:** The morphological structure of NGC 533 is similar to the structure in the COMP2CAT source J132031.47-012718.5.

the northern radio lobe-like feature. The higher resolution VLA A configuration data at 1.4 GHz shows more clearly the jets/lobes morphology and potential hotspots.

Additionally, we suggest that the radio morphology in NGC 1600 at both frequencies resembles the radio morphology of the source J1423+2501, identified as an FR II radio source in the FRIICAT catalog (Capetti et al. 2017b) with an unidentified radio core (Figure 4.15).

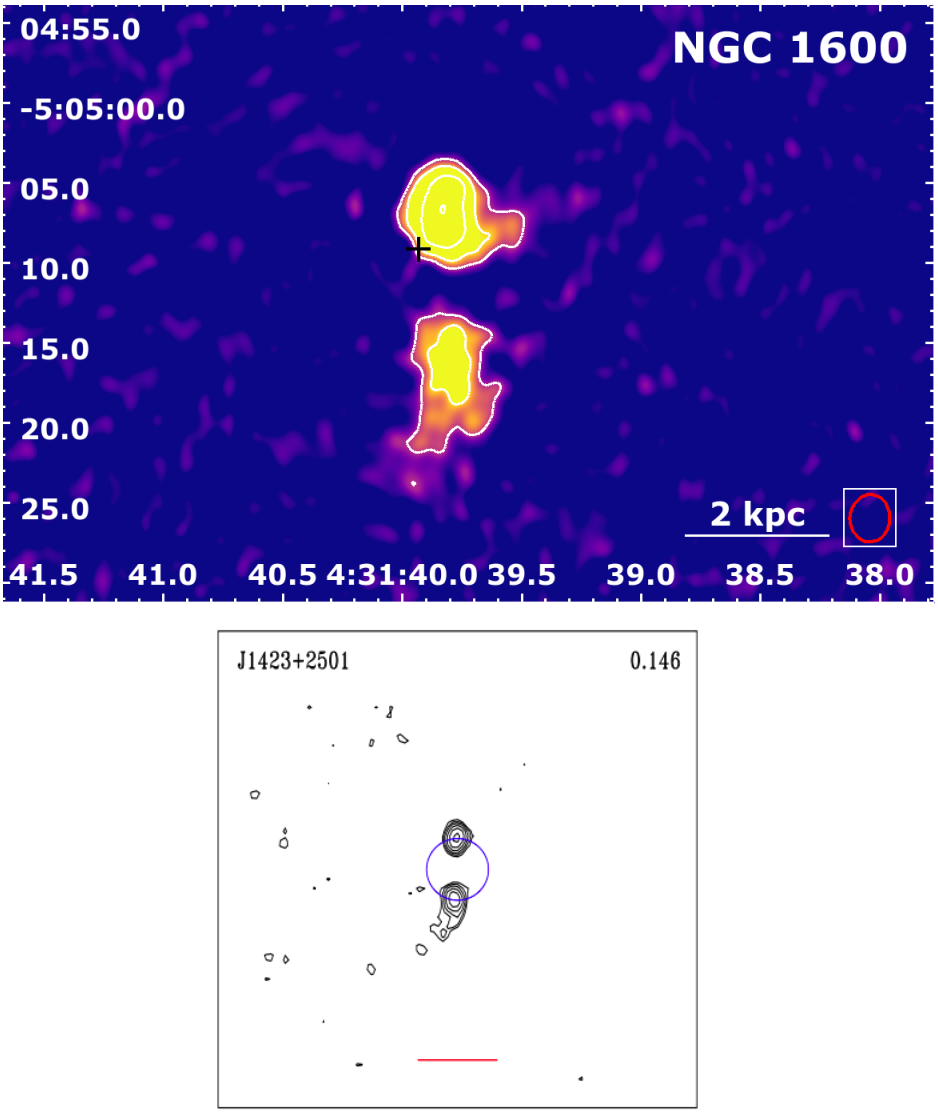

Figure 4.15: **Top:** The total intensity image of NGC 1600 in VLA A configuration at 1–2 GHz has a morphology resembling the FR II radio source J1423+2501 from the FRIICAT catalog (Capetti et al. 2017b) (**bottom**).

Chapter 5

Details on Individual Sources

Detailed description of the radio emission morphologies of each source in our sample and additional relevant information on the multifrequency emission are given in the following sections. An asterisk (' * ') after the name of the source indicates that it was observed as part of our VLA A-configuration project (ID: 15A-305, PI: Werner) from 2015.

5.1 3C 449

The low-power FR I radio source 3C 449 is the central dominant galaxy (CDG) of the 1.5 keV group/poor cluster Zwicky 2231.2+3732 at a luminosity distance of $\sim$ 76 Mpc. The radio emission extends out to almost 500 kpc (Perley et al. 1979; Andernach et al. 1992; Feretti et al. 1999) in the form of relativistic (up to $\sim$ 3.3 kpc) and well-collimated (up to $\sim$ 16.7 kpc) radio jets terminating in large diffuse radio lobes with a slight bent to the west (Figure 3.3a).

Associated X-ray emission from the hot gas and its interaction with the radio source has been studied by Hardcastle et al. (1998), Croston et al. (2003), and Lal et al. (2013). The X-ray cavities were observed coincident with the inner southern radio jet and the *Chandra* X-ray Observatory detected cold fronts, which likely originate from sloshing of the hot gas that could also contribute to the bending of the radio jets.

HST observations revealed a 600 pc dusty disk, the orientation of which is not perpendicular to the orientation of the radio jet axis (Feretti et al. 1999; Tremblay et al. 2006). The CO(1-0) transition line, as a tracer of molecular gas was detected by Ocaña Flaquer et al. (2010). The study of SOAR data revealed Hα+[NII] line emission within the innermost 2 kpc from the core (Lakhchaura et al. 2018).

5.2 IC 1860

IC 1860 is a CDG of the 1.3 keV group IC 1860 (Abell S301; Abell et al. 1989).

The observed radio emission in the VLA A configuration has a form of point-like[1] radio source slightly elongated in the north-eastern and south-western direction (Figure 3.1a).

The *XMM-Newton* and *Chandra* data were analysed by Gastaldello et al. (2013) who found sharp surface brightness discontinuities (cold fronts) which they interpreted as evidence for sloshing, which could be a result of a minor merger with the spiral galaxy IC 1859 (this is also consistent with numerical simulations for relaxed clusters; Ascasibar & Markevitch 2006). Moreover, their radio observations at the lower frequency with Giant Metre-wave Radio Telescope (GMRT) revealed a steep-spectrum diffuse radio emission enclosed by these cold fronts.

5.3 IC 4296*

IC 4296 is a giant elliptical galaxy and CDG of a poor galaxy cluster Abell 3565.

The radio emission identified with the radio source PKS 1333-33, extends well beyond the host galaxy IC 4296.
Our VLA A and D configuration data (Figure 3.3b) show a unresolved central radio source and extended radio emission in the form of two, well-collimated (within the first $\sim$ 10 kpc from the core) radio jets expanding up to $\sim$ 150 kpc on both sides with many knots and wiggles and terminating in large radio lobes with a radius of $\sim$ 60-80 kpc. IC 4296 and its radio source (in VLA C configuration) was extensively studied by Kileen et. al (Killeen et al. 1986b,a; Killeen & Bicknell 1988).

The X-ray emission from this giant elliptical galaxy was described by Pellegrini et al. (2003). Moreover, our analysis of the archival *XMM-Newton* data revealed an X-ray cavity associated with the north-western radio lobe (Grossová et al. 2019). The more in-depth X-ray spectral analysis of thermodynamical profiles show an unusually low central entropy and cooling time.

[1] Point-like morphology was found by Dunn et al. (2010) using observations at 1.4 GHz from 2007.

The presence of cooling gas in the form of warm Hα+[NII] (at kpc scale) (Lakhchaura et al. 2018), molecular CO(2-1) emission (at 100 pc scale) (Boizelle et al. 2017; Ruffa et al. 2019) and a warped dust disk (at $<$ pc scale) (Schmitt et al. 2002) has been revealed in the central region.

More details of the potential unbalanced cooling in the nucleus and the relationship between the radio, X-ray and optical emission for IC 4296 is summarized in our paper (Grossová et al. 2019).

5.4 NGC 57*

NGC 57 is another giant elliptical galaxy from our proposal VLA A configuration data and identified as an isolated elliptical galaxy (Smith et al. 2004; O'Sullivan et al. 2007).

Our high resolution VLA A configuration total intensity image (Figure 3.1b) reveals, for the first time, a point-like radio morphology previously unseen in the TIFR GMRT sky survey (TGSS), the NRAO VLA sky survey (NVSS) or in the study by O'Sullivan et al. (2007). No dusty features (Goullaud et al. 2018) or warm gas (Lakhchaura et al. 2018) were found in this galaxy.

5.5 NGC 315

NGC 315 is well-known giant elliptical galaxy classified as a FR I radio source (Fanaroff & Riley 1974), which resides in the central region of the NGC 315 (WBL 22) group.

The radio emission has been thoroughly studied at various radio frequencies by many research groups (Bridle et al. 1979; Willis et al. 1981; Klein et al. 1994; Mack et al. 1997; Laing et al. 2006; Worrall et al. 2007; Giacintucci et al. 2011, ; and references therein) and has the form of relatively symmetric radio jets with several wiggles and knots, which are inflating wiggles and knots, which extend almost 200 kpc. The SE jet is inflating a radio lobe, while the NW jet undergoes an apparent 180 degree bend and forms an extended plume (Figure 3.3c).

Chen et al. (2012) investigated the kinematic and spatial properties of the close galaxy members of NGC 315 and found a low density ambient X-ray gas environment, which could be the reason why the radio jet can expand to such a large distance from the core.

The X-ray analysis revealed a strong X-ray jet, which traces the radio synchrotron emission and extends up to about $\sim$ 10 kpc (Worrall et al. 2003, 2007; Donato et al. 2004, Figure 3.3c).

The optical emission is represented by a dusty disk perpendicular to the direction of the jets and a few dust patches (Capetti et al. 2000). Moreover, at the position of the HST dust patches, Morganti et al. (2009) found two HI absorption components. The cold molecular gas, traced by CO(1-0) line emission, was found with the IRAM telescope (Ocaña Flaquer et al. 2010). Moreover, Boizelle et al. (2021) detected a sub-kpc CO disk. The warmer nebulae, traced by Hα+[NII] line, was observed by Ho et al. (1997), but not confirmed in the more recent study as presented in Lakhchaura et al. (2018) combing narrow-band imaging with long slit spectroscopic observations with SOAR.

5.6 NGC 410*

Another galaxy from our VLA A configuration project is a giant elliptical NGC 410 (Figure 3.1c), which is the CDG of the LGG 18 group (Kolokythas et al. 2018).

The radio emission with a point source-like morphology was previously observed with the VLA at various frequencies (Condon et al. 1998; Filho et al. 2002). The more recent study by Kolokythas et al. (2018) at lower frequencies (610 MHz) with GMRT found a small extension of the radio emission to north-east with a total extent $\sim$ 10 kpc.

González-Martín et al. (2009) claimed no point source detection in the X-ray hard band (4.5-8.0 keV) with *XMM-Newton* (together with other evidence from the optical, UV and radio bands) and therefore classified NGC 410 as a galaxy without an AGN. The X-ray halo emission was detected in 0.5-7 keV band with *Chandra* (Lakhchaura et al. 2018).

A recent study with SOAR data, as summarized by Lakhchaura et al. (2018), revealed
Hα+[NII] line emission within the innermost 2 kpc from the core.

5.7 NGC 499

NGC 499 is the only one galaxy in our sample of 42 early-type sources without radio emission (Figure 3.1d) observed in the nucleus or in the extended diffuse region.

A faint radio source was observed within the 1.4 GHz NVSS survey (Condon et al. 1998) with a flux density of 0.7 mJy at $2\,\sigma_{\rm RMS}$ (Brown et al. 2011), which is well above the sensitivity limit of our VLA observations (for more details see Section 4.4.1).

NGC 499 is a CDG of the NGC 499 group, which is a part of the Pisces cluster (Kim & Fabbiano 1995). Paolillo et al. (2003) have shown that NGC 499 group is in the process of merging with the NGC 507 group (Section 5.8).

The luminosity of the X-ray halo is relatively high ($\sim 2.3 \cdot 10^{42}$ erg/s; Dunn et al. 2010; Lakhchaura et al. 2018). Moreover, the *Chandra* image shows possible ghost cavities at about ∼10-15 kpc to the north and south of the nucleus, a sign of a previous AGN activity (Panagoulia et al. 2014; Kim et al. 2019).

Lakhchaura et al. (2018) present a detection of a centrally located warm nebular emission.

5.8 NGC 507*

NGC 507 is the CDG of the NGC 507 group, which belongs to the Pisces cluster. As mentioned in the previous section, NGC 507 group is likely to be merging with the NGC 499 group (Section 5.7).

The large-scale diffuse radio emission from a low-power FR I radio source B2 0120+33 (Parma et al. 1986) has shape resembling a letter 'T' formed by two radio lobes with diameters of ∼40 and ∼20 kpc (Dunn et al. 2010; Murgia et al. 2011). Interestingly, this emission has a very steep radio spectrum, possibly due to the 'fossil' radio material from previous AGN activity (Murgia et al. 2011).

The central part of the brighter western lobe was resolved also by our high resolution A configuration data (Figure 3.3d) and coincides with a *Chandra* X-ray cavity at ∼7 kpc to the south-west of the galaxy core (Dong et al. 2010).
On the other hand, the eastern radio lobe is bending to the south with its edge tracing a *Chandra* X-ray cold front (Fabbiano et al. 2002; Kraft et al. 2004), a result of sloshing. The disturbed morphology could be due to the ongoing merger with NGC 499 as studied and simulated by Ascasibar & Markevitch (2006). A different scenario is proposed by Kraft et al. (2004): the sharp-edged X-ray surface brightness profile could be entrained ICM material from the expanding eastern radio lobe.
XMM-Newton data also confirms the observed discontinuity (Fabbiano et al. 2002).

No warm (Lakhchaura et al. 2018) and cold gas was found inside of this giant elliptical galaxy.

5.9 NGC 533*

NGC 533 is the CDG of the NGC 533 group of galaxies.

The new high resolution A configuration data observed within our project 15A-305 revealed a central bow-tie-shaped radio emission with a total extent of ∼5 kpc (Figure 3.3e), which resembles the radio morphology of FR II radio sources (see Discussion 4.5.8).

NGC 533 is one of the two galaxies in our sample (besides NGC 708; Section 5.10) which shows signatures of beeing a young radio galaxy (O'Dea 1998): a compact morphology of the radio emission within the host galaxy without extended features, cavities in X-rays as a sign of small-scale interaction of the radio and X-ray plasma, a double morphology of the radio emission.

In comparison with the central X-ray emission, previously studied using *Chandra* X-ray images by Dunn et al. (2010) and Shin et al. (2016), we suggest that the radio lobes visible in the red contours in Figure 3.3e could correspond to the presence of the north-eastern and especially south-western X-ray cavity.

The optical analysis presented in Ferrari et al. (1999), Temi et al. (2007a), and Lakhchaura et al. (2018) showed co-spatial Hα+[NII] emission coincident with a filamentary dust distribution.

5.10 NGC 708

The giant elliptical galaxy, NGC 708 is a CDG of the cooling flow cluster Abell 262. Parma et al. (1986) and Blanton et al. (2004) defined this galaxy as a low-power FR I radio source.

VLA archival data in the A and C configuration (Figure 3.3f), also studied by Parma et al. (1986), Blanton et al. (2004), and Clarke et al. (2009), reveal a diffuse two-sided radio lobe-like emission with a total extent of ∼40 kpc from the central radio source B2 0149+35.

The radio emission from NGC 708, like NGC 533 (see Section 5.9), resembles the emission of a young radio galaxy (O'Dea 1998) due to its confinement within 10 kpc of the host galaxy without extended emission, interaction with the inner X-ray gas in form of cavities (Blanton et al. 2004; Clarke et al. 2009; Panagoulia et al. 2014), double radio morphology, and presence of the optical emission line [OIII] (Liuzzo et al. 2013).

The X-ray emission shows surface brightness dips, which could be signatures of cavities on both sides (especially on the eastern side of the core) consistent with the expanding diffuse radio emission (Blanton et al. 2004; Clarke et al. 2009). The X-ray analysis shows that the enthalpy of the radio lobes is not sufficient to balance radiative losses from the ICM, suggesting that NGC 708 may have shut down or be in a low-power phase of activity. This is also supported by the non-detection of radio emission on smaller scales with VLBI (Liuzzo et al. 2010).

A search for multiphase gas in NGC 708 was performed by Sahu et al. (2016). A molecular CO gas disk, with a total extent of ∼3 kpc, was discovered with ALMA by Braine & Dupraz (1994) and in more detail studied also by Russell et al. (2019) and Olivares et al. (2019). The peak of the molecular gas emission coincides with the AGN core and is perpendicular to the projected orientation of the radio jets. The cool gas is also surrounded by dust lanes in the nuclear region (Sahu et al. 2016; Kulkarni et al. 2014).

The extended ($\sim$13 kpc) warm nebula traced by Hα+[NII] emission (Lakhchaura et al. 2018) is also consistent with the *Chandra* X-ray surface brightness peaks, which suggests that at least part of the hot X-ray gas is cooling at even larger distances from the core (Blanton et al. 2004).

5.11 NGC 741

NGC 741 is the CDG in the group holding the same name.

The radio structure, first studied by Venkatesan et al. (1994) and Birkinshaw & Davies (1985), was probably formed by the close passage of the second brightest galaxy in the group, the head-tail radio galaxy NGC 742 with the same redshift as NGC 741 (Schellenberger et al. 2017).

Our analysis, using a new high resolution A configuration total intensity image, confirms the radio emission in the form of a bridge connecting NGC 471 and NGC 742 and a prominent bent radio tail (to the southwest) in the C configuration total intensity image (Figure 3.3g).

X-ray analysis by Jetha et al. (2008) and Schellenberger et al. (2017) has shown several generations of X-ray cavities.

The warm gas was found in the nuclear regions of NGC 741 by Macchetto et al. (1996), but more recent narrow-band and long slit spectroscopic SOAR observations are disfavoring their findings (Lakhchaura et al. 2018). Dust is missing in this giant elliptical galaxy (Verdoes Kleijn & de Zeeuw 2005)

5.12 NGC 777*

Compact radio emission is detected in our new VLA A configuration total intensity image with a resolution of $\sim$1.5 arcsec for NGC 777 (Figure 3.3h), the giant elliptical galaxy and the CDG of LGG 42 group.

Additionally, we also imaged the archival VLA C configuration data, where no radio emission was detected at the angular resolution of $\sim$3.2 arcsec, possibly due to the flux density being very close to the sensitivity limit of the VLA observations (see Section 4.4.1).

The X-ray emitting halo has an almost undisturbed morphology ($\sim$40 kpc across) with a quite high luminosity of $\sim 4 \cdot 10^{42}$ erg/s (when compared to the rest of the galaxies in the sample Lakhchaura et al. 2018). The X-ray surface brightness depressions were detected in the hot atmosphere of NGC 777 by Panagoulia et al. (2014).

Lakhchaura et al. (2018) reports a non-detection of any trace of warm ionized nebulae.

5.13 NGC 1132

NGC 1132 is a giant elliptical, which resides inside of the well-known fossil group NGC 1132.

Radio emission from the archival VLA C configuration data (Figure 3.1e) shows a point source morphology from the unresolved central source.

The outer contour level ($5 \times \sigma_{\rm RMS}$; see Table 3.2) coincides with the possible shock front in the X-rays noticed by Kim et al. (2018) and could be connected to the merging history of NGC 1132 as suggested by Mulchaey & Zabludoff (1999) (and predicted by the simulations of Barnes 1989; Governato et al. 1991). Moreover, Dong et al. (2010) found an X-ray cavity at a distance of 4 kpc south of the host galaxy's center, which is consistent with the potential set of cavities detected in the southern regions by Plšek et al. (in prep).

No emission from warm gas emission was detected for this source (Lakhchaura et al. 2018).

5.14 NGC 1316

The giant elliptical galaxy, NGC 1316, hosts a very well-known strong radio source Fornax A located at the outskirts of the Fornax cluster.

Radio emission in the higher resolution BA configuration image extends from the northwest to southeast in the form of an oblong letter 'S' and represents the most recent of its AGN outbursts with the south-eastern extension also visible in the C configuration image (Figure 3.4a), (both previously published; Fomalont et al. 1989; Maccagni et al. 2020, 2021).

Several generations of X-ray cavities are visible in the *XMM-Newton* and *Chandra* images (Lanz et al. 2010).

The S-shaped jet morphology together with the disturbed morphology of the multi-phase gas (Morokuma-Matsui et al. 2019; Lakhchaura et al. 2018) and dust (Duah Asabere et al. 2014) supports the fact that NGC 1316 is in the process of merging into the Fornax cluster (Section 5.15).

5.15 NGC 1399*

The radio emission of NGC 1399, the CDG of the Fornax cluster, has a two-sided extended radio morphology in the form of two well-collimated radio jets terminating in two mildly diffuse radio lobes (Figure 3.4b). Similar morphological features were previously discussed in Shurkin et al. (2008) and Dunn et al. (2010).

Moreover, Paolillo et al. (2002), Shurkin et al. (2008), and Panagoulia et al. (2014) found signatures of the interaction between the AGN and the hot gas, in the form of X-ray cavities, with bright rims coincident with the outer edges of both radio lobes.

Even though the presence of CO(2-1) line emission was confirmed by Prandoni et al. (2010), no dust features were found in the core of NGC 1399. Moreover, Werner et al. (2014) showed that the central regions of this galaxy lack [CII] line emission.

5.16 NCG 1404*

The giant elliptical NGC 1404, also part of our new A configuration VLA observation, is another member of the Fornax cluster. Machacek et al. (2005) suggested that NGC 1404 is falling towards the center of the Fornax cluster, where NGC 1399 (Section 5.15) resides.

Our new VLA A configuration data (Figure 3.1f) at high sensitivity with the RMS noise of the total intensity image reaching $25\,\mu$Jy revealed a faint (flux density of $210\,\mu$Jy) central radio source and thus supporting the previous findings of Dunn et al. (2010), where the detection was very close to the sensitivity limit. On the other hand, a more compact archival VLA CD configuration observation did not detect a radio emission, maybe due to a lower flux density than the sensitivity limit (see Section 4.4.1).

There are no signatures of ongoing AGN-gas interactions in this system, as supported by a quite smooth circumnuclear morphology of the hot X-ray halo (Machacek et al. 2005; Dunn et al. 2010). Cold (Werner et al. 2014) and warm gas (Lakhchaura et al. 2018) is missing in this galaxy.

5.17 NGC 1407*

Another object within our sample with a newly observed VLA A configuration data is
NGC 1407. This giant elliptical galaxy is located inside in the dynamically relaxed NGC 1407 (Eridanus A) group, part of the Eridanus supergroup.

The radio emission from the new A configuration data does not show a very distinctive radio point source in the nucleus (Figure 3.4c). More prominent is the diffuse morphology with asymmetric radio jet-like structures, extending especially to the east as seen also in the archival VLA B and C configuration data (Giacintucci et al. 2012).

From multiband and multifrequency studies (Saikia & Jamrozy 2009; Giacintucci et al. 2012) reoccurring activity of the AGN has been suggested, similar to that found for another fossil giant elliptical galaxy in our sample, NGC 5044 (Section 5.37).
Only an upper limit on the flux density of CO(1-0) emission is found for NGC 1407 (Babyk et al. 2019).

5.18 NCG 1550*

NGC 1550 is the CDG of the group of galaxies having the same name.

The radio emission observed within our new high resolution A configuration observation revealed asymmetric small-scale jets with a physical extent of ~ 4 kpc. At the lowest contour level created at $5 \times \sigma_{\rm RMS}$, we find a small hotspot-like feature at the distance of 6 kpc. This feature seems not to be the extension of the jet and is located within the diffuse lobe-like emission visible in the compact archival C configuration total intensity image (Figure 3.4d), previously published by Dunn et al. (2010).
The lower frequency GMRT study supports the presence of the diffuse lobe-like morphology (Kolokythas et al. 2018). They also found that the inward-bended eastern jet seems to be aligned with the potential hotspot feature seen in the VLA A configuration contours (Figure 3.4d).

Kolokythas et al. (2020), in their recent radio and X-ray study found a sign of sloshing of the ambient IGM around NGC 1550, previously known as relaxed. They present arc-shaped cold fronts together with a potential X-ray cavity (supported by findings of Panagoulia et al. 2014) coincident with the position of the radio lobe.

Neither molecular gas nor cold dusty features have not yet been observed and Lakhchaura et al. (2018) presents non-detection of warm ionized nebulae for this giant elliptical galaxy.

5.19 NCG 1600

NGC 1600 is a relatively isolated CDG of the NGC 1600 group of galaxies (Smith et al. 2008).

The radio emission was previously published by Birkinshaw & Davies (1985) at 4.85 GHz with VLA in C configuration and shows a potential double radio source without a clearly defined radio core. The higher resolution A configuration data at 1.4 GHz (Figure 3.4e) shows in more detail the radio jets/lobes features and potential hotspots, which could resemble the morphology of FR II radio source (see Discussion 4.5.8).

The X-ray emission from *Chandra* X-ray image shows a diffuse structure, which seems to show two surface brightness depressions at the positions of the two radio lobe structures, previously studied by Sivakoff et al. (2004).

Moreover, they found excess emission in the X-rays, which more or less coincides with the Hα+[NII] emission (Singh et al. 1995; Lakhchaura et al. 2018) of the ionized gas (extending up to $\sim$30 arcsec from the core) and dust (extending up to $\sim$10 arcsec from the core; Ferrari et al. 1999).

The signatures of properties similar to the 'fossil group' were for NGC 1600 identified by Santos et al. (2007) and Smith et al. (2008).

5.20 NGC 2300*

The radio emission from our new VLA A configuration data for NGC 2300, the central dominant galaxy of the NGC 2300 group, shows a point-like morphology (Figure 3.1g). The archival VLA D configuration data reveals radio point source emission, as well (Figure 3.1g) .

NGC2300 is known to undergo tidal interactions with a late-type active star-forming galaxy NGC 2276 (Wolter et al. 2015). Plšek et al. in prep. detected potential 'ghost' X-ray cavities in NGC 2300.

The optical study of the HST and SOAR data, done by Xilouris et al. (2004), showed that there is no detection of dust or warm ionized nebulae (Lakhchaura et al. 2018) inside NGC 2300.

5.21 NGC 3091*

NGC 3091 is a part of our VLA high resolution project from 2015 and is the CDG of a poor Hickson Compact Group, HCG 42 (Hickson 1982) (Colbert et al. 2001).

The radio morphology, seen in the highest resolution $\sim$2 arcsec VLA A configuration data (Figure 3.1h), is represented by a faint point source-like radio emission in the center of the galaxy. The AB configuration data with $\sim$14 arcsec resolution at the same frequency (1.4 GHz) reveals no detection, maybe because of a lower flux density limit of our VLA observation (see Section 4.4.1).

Even though radio emission has a point-like morphology, Plšek et al. in prep. detected potential 'ghost' cavities in the X-ray hot atmosphere.

In the analysis of the optical and NIR morphology, no H I, dust features (Colbert et al. 2001) or warm gas (Lakhchaura et al. 2018) have been detected in the central regions of NGC 3091.

5.22 NGC 3923*

The biggest early-type galaxy, NGC 3923, located in the optical group (LGG 255) with only galaxy-scale X-ray halo has an oval-shaped radio morphology in our new VLA A configuration data (Figure 3.2a), while the archival C and CD configuration data show no radio emission. This source was observed in the 5 GHz survey done by Disney & Wall (1977).

Chandra data have shown potential X-ray surface brightness decrements in the form of 'ghost' cavities without corresponding radio emission from radio jets and lobes in this giant elliptical galaxy (Plšek et al. in prep.).

NGC 3923 is a famous shelled[2] giant elliptical with dusty filamentary features and Hα emission in the central region (Bílek et al. 2016; Miller et al. 2017). On the other hand, Lakhchaura et al. (2018) reported non-detection of warm gas in the core.

5.23 NGC 4073*

The giant elliptical NGC 4073 is dominant member of the poor cluster MKW 4 and shows a point source-like radio morphology in our new high resolution VLA A configuration observation (Figure 3.2b). A weak detection of the central radio source has been reported by Hogan (2014) with VLA in the C-band (4–8 GHz).

The X-ray emission was studied by O'Sullivan et al. (2003) who found a 1.7 keV halo within the relaxed system. Moreover, Plšek et al. (in prep.) found potential 'ghost' cavities in the X-ray atmosphere. A warm emission line nebula was not detected in this source (Lakhchaura et al. 2018).

5.24 NCG 4125

NGC 4125 is a luminous giant elliptical galaxy residing in the NGC 4125 group (alternatively called LGG 266).

The radio emission (Figure 3.2c), detected in the archival D configuration data, has a diffuse morphology with an extension to the northeast, corresponding to a point-like radio source visible in the archival 1.4 GHz Westerbork Synthesis Radio Telescope

[2]NGC 3923 has between 22 and 42 shells, the largest number of shells observed in the elliptical galaxy.

(WSRT) observations. More prominent structure has a form of inflated radio lobes, which are offset by 4 kpc (46 arcsec) in projection with respect to the radio, optical, and X-ray core of NGC 4125. This offset was also noticed in the NVSS data at 1.4 GHz by M. Rupen et al. in their online notes[3] about VLA H I data of early-type galaxies and by Krajnović & Jaffe (2002) in the VLA C configuration observations at 8.3 GHz. In both studies, only the central regions of the offset radio lobes were detected. The radio core corresponding to the X-ray and optical center of NGC 4125 was missing and is only clearly visible in the WSRT images. Moreover, due to the missing optical counterpart of the extended radio-lobe like emission, Krajnović & Jaffe (2002) defined NGC 4125 as a background source (see Discussion 4.5.7 for a possible explanation of this unusual emission).

González-Martín et al. (2006) studied NGC 4125 as a part of the X-ray study of LINER galaxies and identified a centrally located hard X-ray point source-like emission, which is a sign of ongoing AGN activity. The extended cold emission from the large amount of dust (Kulkarni et al. 2014), [CII] and [NII] has been observed, but no CO[4], HI (Welch et al. 2010; Wilson et al. 2013) or Hα+[NII] emission (Lakhchaura et al. 2018). This could be explained by a merger-triggered star-formation outburst providing heated gas and dust to the surrounding medium of the galaxy.

5.25 NGC 4261

NGC 4261 is the optical counterpart to the radio source 3C 270, which is a very well known FR I radio source inside the Virgo cluster (W cloud; Garcia 1993) with well-defined radio jets and large radio lobes piercing through the atmosphere of the host galaxy and extending beyond from the core (Figure 3.4f).

A detailed study, combining data from the GMRT and VLA as well as comparing the radio emission with the X-ray emission of the hot gas, was published by Kolokythas et al. (2015) and O'Sullivan et al. (2011a).

From the X-ray point of view, NGC 4261 has an extended X-ray halo (Davis et al. 1995) with features showing the interaction with radio source in the form of X-ray cavities (Croston et al. 2008; O'Sullivan et al. 2011a). On small scales, X-ray jets are present corresponding to the innermost collimated radio jets (Gliozzi et al. 2003; Zezas et al. 2005; Worrall et al. 2010).

On the parsec scale, Jaffe & McNamara (1994) and Ferrarese et al. (1996) found a warped dusty disk with the rotational axis perpendicular to the direction of the radio jets streaming out of the nuclear region and extending up to $\sim$100 pc from the core. The presence of atomic and molecular gas from H I and CO (2–1) was detected too. Moreover, a sub-kpc CO disk was recently detected by Boizelle et al. (2021).

Very similar morphology and multiband features are observed for the giant elliptical galaxy IC 4296 (Section 5.3), which has, however, $\sim$6$\times$larger radio lobes, what leads to $\sim$30$\times$larger total energy output supplies for the inflation of those radio lobes (Frisbie et al. 2020; Grossová et al. 2019).

5.26 NCG 4374

Messier 84 or NGC 4374 is a giant elliptical galaxy in the Virgo A group, which is a part of the Virgo cluster together with NGC 4406 (Section 5.27), NGC 4486 (Section 5.29), and NGC 4552 (Section 5.30).

The radio emission in the archival B configuration data (Figure 3.4g) shows well-defined and in the central regions well-collimated jets terminating in diffuse plum-like lobes (first published by Laing & Bridle 1987) with the northern lobe brighter than the southern and bent to the east. VLA D configuration data reveal pear-like diffuse emission extending beyond the B configuration data. Moreover, the VLBA data analysed by Ly et al. (2004) revealed a jet-like extension in the direction consistent with the northern radio jet from the VLA.

The extended radio lobe emission is filling the region of the drops in the surface X-ray brightness, the X-ray cavities (Finoguenov et al. 2001), and extending far beyond the host galaxy (Devereux et al. 2010).

The nuclear region in NGC 4374 revealed a small ionized gas disk (Bower et al. 1997), faint circumnuclear CO(2-1) absorption and emission together with an asymmetric dust lane (Verdoes Kleijn et al. 1999; Boizelle et al. 2017). All features perpendicular to the innermost radio jets.

5.27 NGC 4406*

NGC 4406, know as M 86, is located in the Virgo cluster and flying in the direction towards us. Our new VLA A configuration data at 1.5 GHz (Figure 3.2d) reveal a faint, point-like radio emission in the center of this giant elliptical. Similarly, Dunn et al. (2010) found point-like radio emission in the nuclear region at higher frequencies at around 4.9 GHz in the C configuration data. On the other hand, complementary archival data in VLA D configuration at 1.4 GHz have not detected any radio emission from the core, possibly due to the high noise level of the observation (for more details see Table 3.2).

NGC 4406 is the second X-ray brightest giant elliptical in Virgo cluster (after M 87) and its negative radial velocity suggests a supersonic movement through the ICM. This could create the observed X-ray features (plume and tail) by ram pressure stripping (Forman et al. 1979; Randall et al. 2008; Ehlert et al. 2013; Kim et al. 2019).

[3] https://www.cv.nrao.edu/$\sim$jhibbard/HIinEs/HIinE.html

[4] Wiklind et al. (1995) claimed detection of CO(1-0) line, which was not confirmed by Welch et al. (2010).

Signs of possible galaxy-galaxy interactions are observed in the distribution of the atomic gas and dust (Smith et al. 2012) as well as the Hα features connected to the neighboring spiral galaxy NGC 4438 (Kenney et al. 2008; Lakhchaura et al. 2018).

5.28 NGC 4472*

NGC 4472, or M 49, is an early-type elliptical and CDG of the M 49 group falling from the south into the Virgo cluster and it is possibly in the second turn around the cluster center (Su et al. 2019).

NGC 4472 was observed in our 2015 project in VLA A configuration (Figure 3.4h). Additionally, we also reduced archival VLA C configuration data (Condon & Broderick 1988). The high angular resolution of the A configuration total intensity image (Figure 3.4h contours) showed the radio emission from the innermost central region in the form of an elongated amorphous feature with the extended tail to the west and a small sign of radio emission to the north-east.
On the other hand, using the more compact C configuration array, the extended radio emission with a total extent of $\sim$10 kpc is seen (Ekers & Kotanyi 1978). The central regions in the C configuration image are consistent with the radio features in the A configuration. The additional extended lobe-like structures are observed to the east and west from the nucleus.

The eastern lobe is consistent with a decrement in the X-ray surface brightness, one of the X-ray cavities observed in this source (for more details see, e.g. Biller et al. 2004; Kraft et al. 2011; Panagoulia et al. 2014; Su et al. 2019). A warm gas is missing in the central or extended regions of this giant elliptical galaxy (Lakhchaura et al. 2018).

5.29 NGC 4486

NGC 4486 or Messier 87, is the central dominant galaxy of the Virgo cluster. Here, we summarize the results obtained from the archival A, B, and C configuration data (Figure 3.5a).

The bright radio core, 3C 274, was detected along with its innermost radio jet, which is coincident with the X-ray emission of the jet (Marshall et al. 2002). On the opposite side of the core, an elongated lobe-like emission is visible and coincides with an X-ray cavity (Young et al. 2002; Forman et al. 2005, 2007). The archival C configuration VLA map, which is more sensitive to extended structures, presents a western tail extending up to $\sim$10 kpc from the nucleus. However, we note that at 300 MHz the entire structure of NGC 4486 is far more extended (up to 80 kpc, e.g.: Owen et al. 2000).

The presence of multi-phase gas in the form of cold molecular CO clouds (e.g.: Simionescu et al. 2018), cool [CII] (Werner et al. 2014), nuclear ionized gas (Arp 1967; Macchetto et al. 1996), as well as extended warm ionized Hα+[NII] nebulae (Lakhchaura et al. 2018) has been reported.

5.30 NGC 4552

The radio emission from the giant elliptical NGC 4552 or M 89, which resides inside of the subgroup A of the Virgo cluster, is present in Figure 3.5b.

The red contours are showing the innermost radio point-like emission from the archival high resolution VLA A configuration. More recent (Project ID: 16A-275) previously unpublished C configuration data revealed a more diffuse butterfly-like emission extending on both sides to about 0.8 kpc.

The relativistic plasma from the jet-like emission is clearly interacting with the hot X-ray emitting gas and forming on both sides X-ray cavities. Machacek et al. (2006) and Allen et al. (2006) analysed the *Chandra* X-ray data and found two bright rings surrounding the two cavities to the north and south, which are perpendicular to the radio structures seen in the VLA images. Moreover, Machacek et al. (2006) also found signatures of ram pressure stripping of hot gas as the galaxy moves through the ICM of the Virgo cluster (see also: Kraft et al. 2017).

Ferrari et al. (1999) has shown that the emission from the ionized gas extends up to 10 arc-
seconds, whereas the dust absorption is very weak. The warm ionized gas, traced by Hα+[NII] has not been confirmed in a more recent study described in Lakhchaura et al. (2018).

5.31 NGC 4636

NGC 4636 is a central early-type galaxy within a poor group in the far outskirts of the Virgo Cluster. VLA A configuration images, as presented in Figure 3.5c, have been previously published and discussed by Dunn et al. (2010). The additional archival C configuration VLA data from 2017 revealed a more diffuse, but still quite compact and weak radio-jet-like emission with a total extent of $\sim$3.5 kpc. Although the majority of detected radio emission in VLA is consistent with the radio emission at lower frequencies (235 and 610 MHz) with GMRT observed by Giacintucci et al. (2011), they also found a more extended north-eastern radio lobe, which is coincident with the observed X-ray (NE) cavity(Stanger & Warwick 1986; Jones et al. 2002; Allen et al. 2006; Baldi et al. 2009; Panagoulia et al. 2014). The SW radio lobes is filled only partially with relativistic plasma.

There have been reports of very weak CO(2-1) emission (indicating a cloud of cold molecular gas; Temi et al. 2018), [CII] emission and warm ionized Hα+[NII] nebulae (Werner et al. 2014), as well as dusty features (Temi et al. 2003).

5.32 NGC 4649

The giant elliptical galaxy NGC 4649, or M 60, is the third most luminous galaxy in the Virgo Cluster. Archival VLA data obtained in the A configuration reveal point-like emission from a weak central radio source in NGC 4649.

Using D-configuration data, Shurkin et al. (2008) and Dunn et al. (2010) found radio lobes filling the innermost X-ray cavities.

Sharp edges seen in the X-ray images are spatially coincident with the radio emission detected in the D configuration (Figure 3.5d). The X-ray properties of the hot gas are discussed in more depth by Shurkin et al. (2008); Dunn et al. (2010); Paggi (2014); Wood et al. (2017) and Kim et al. (2020).

Molecular gas, traced by CO (1-0) emission, was detected by Sage & Wrobel (1989). However, Young et al. (2002) failed to confirm their findings with the observations from IRAM and provide only upper limits on CO flux. The galaxy does not show the presence of warmer gas traced by Hα+[NII] emission.

5.33 NGC 4696

Figure 3.5e reveals a radio emission in NGC 4696, the CDG of Abell 3526 (Centaurus Cluster) from archival VLA observations obtained in the A and BC configurations.

A thorough study of the radio properties was performed by Taylor et al. (2002) and our total intensity image of VLA A configuration data is consistent with their results, where the radio emission shows a bright nuclear source, radio jets and lobes with the western lobe bending towards east.

The interaction with the hot X-ray atmosphere is clearly present, as the radio plasma pushed out the hot gas and created cavities (Taylor et al. 2006; Panagoulia et al. 2014; Sanders et al. 2016). Interestingly, González-Martín et al. (2006) found only a diffuse morphology without a clear point-like emission in the hard X-ray bands as a sign of a central star-bursting activity. They also noted that the X-rays could be just obscured by the dust and gas. The ongoing AGN activity is supported by our VLA A configuration data together with the VLBA observation of a small-scale one-sided jet detected by Taylor et al. (2006).

The cold extended molecular gas and warm ionized gas and dust were discussed in the recent publication by Olivares et al. (2019) and references therein. Moreover, Mittal et al. (2011) observed a cooling [CII] line in the central region.

5.34 NGC 4778

NGC 4778 or NGC 4761 is the only one lenticular (S0) galaxy in our sample and the CDG of a bright compact group, HCG 62 (Hickson 1982). It is in the process of merging with its companion NGC 4776 [or NGC 4759][](Spavone et al. 2006). A small point source-like central radio emission is observed in both archival VLA A (Vrtilek et al. 2002) and D configuration total intensity images (Figure 3.2e).

Moreover, looking at the lower radio frequencies with GMRT, Gitti et al. (2010) found the expected radio lobes, coincident with the observed X-ray cavities (Morita et al. 2006; Panagoulia et al. 2014) and Giacintucci et al. (2011) detected a possible second outer set of radio lobes.

The Hα emission in NGC 4778 was detected and studied by Valluri & Anupama (1996).

5.35 NGC 4782

The radio source known as 3C 278 is hosted by the giant elliptical galaxy NGC 4782 in the center of the group LGG 316.

Radio emission, shown in the archival high resolution A configuration image (Figure 3.5f) is rather peculiar as already noted by Borne & Colina (1996) and Machacek et al. (2006). The radio jets emanating from the core are, at first invisible due to the high relativistic velocities. After $\sim$ 2 kpc the eastern side of the jet is tilted to the north, whereas the western side continues in a straight line up to 15 kpc, where it bents to the north as well. When using a more compact B configuration, a more diffuse radio emission is observed, which not only traces the peculiar bent of the jets, but also fills the space between and around the jet structure.

The X-ray images reveal an interaction with the neighbor NGC 4783, which could be responsible for the observed bent of the jet. Moreover, X-ray cavities have been observed at the position of both radio lobes (Borne & Colina 1996; Machacek et al. 2006).

A nuclear (within 2 kpc from the core) warm ionized nebula was detected with SOAR (Lakhchaura et al. 2018), otherwise no cool gas or dust was found in this giant elliptical galaxy.

5.36 NGC 4936*

The radio emission from the giant elliptical galaxy NGC 4936 in our new VLA A configuration total intensity image (Figure 3.2f), shows a point-like radio emission from the nucleus.

Macchetto et al. (1996) studied the warm ionized gas and found Hα+[NII] emission concentrated in a small disk similar to NGC 4872 (Section 5.35). The neutral gas, in the form of a double peaked H I line profile, was observed for this giant elliptical by Reid et al. (1994) (and references therein), together with strong emission from NII, SII and OI in the core of NGC 4936.

5.37 NGC 5044

NGC 5044 is the central dominant galaxy of the X-ray bright group NGC 5044, which is well known for its large cold gas reservoir.

Archival radio observations in the A, BnA and D configurations of the VLA presented in Figure 3.5g reveal emission from the central radio source with small-scale jets pointing to north-east and south-west (partly visible in the images analysed by Dunn et al. 2010). The previously unobserved indications for diffuse jet-like emission extending to about 6 kpc from the core in the east-west direction are seen in VLA B configuration contours. More diffuse oval-shaped radio emission extending up to $\sim$20 kpc is seen in the D configuration.

NGC 5044 has undergone (at least) three AGN outbursts. Gastaldello et al. (2009), David et al. (2011), Giacintucci et al. (2011), David et al. (2017), and Schellenberger et al. (2020b) presented GMRT and *Chandra* data, which revealed that the radio emission is consistent with the presence of the innermost southern X-ray cavity. They also found a second pair of more extended (up to $\sim$10 kpc) ghost X-ray cavities, which suggest another episode of an AGN outburst in NGC 5044. The last, the third, and most recent activity, is traced in the most recent study (Schellenberger et al. 2020a), where they also show the presence of small-scale radio jets seen in VLBI data.

Sloshing features are also observed at further distances from the center caused by the accretion of a less massive group (Gastaldello et al. 2009).

The filamentary morphology of the Hα+[NII] ionized nebulae extends up to 6 kpc (Ferrari et al. 1999), whereas the corresponding dust emission extends to only 1.3 kpc (Temi et al. 2007a,b), similar to NGC 4472 (Section 5.28).

Studies done by David et al. (2014a); Temi et al. (2018), and Schellenberger et al. (2020b) showed that CO emitting molecular gas clouds within $\sim$10 kpc from the core coincide well with the presence of the strong emission from the warm ionized gas (Hα filaments), the hot X-ray emitting gas, the innermost X-ray cavities (Schellenberger et al. 2020a) and the cold dust features in the central regions of NGC 5044 as well as [CII] line emission (Werner et al. 2014). Moreover, two CO absorption features were also detected within 5 pc from the core (Schellenberger et al. 2020a).

5.38 NGC 5129*

NGC 5129 is a radio-quiet giant elliptical and the dominant galaxy of a small group.

Our new A configuration data (Figure 3.5h) revealed a bright radio core with small-scale radio jets extending to about 2 kpc to the north-west and south-east from the core. We categorized this source as a compact radio source with radio jets. We find that the radio emission is offset by $\sim$1.2 arcsec from the X-ray and optical core of the galaxy. The point-like radio emission in NGC 5129 was previously observed by the NVSS survey (Condon et al. 1998).

The hot X-ray gas in the *Chandra* images has a disturbed morphology, which is not aligned with the direction of the radio jets. The X-ray gas properties were previously studied by Bharadwaj et al. (2014).

Warm ionized gas extending up to 2 kpc from the core was detected (Lakhchaura et al. 2018).

5.39 NGC 5419*

NGC 5419 is the CDG of the poor cluster A753, which hosts the radio source PKS B1400-33.

Our new A configuration VLA observations revealed extended radio emission in the core of the galaxy. Archival VLA CD configuration data (Figure 3.6a) (Goss et al. 1987) show a more extended emission, which forms an L-shaped radio tail to the south extending to about 35 kpc and a second prominent diffuse 120 kpc-in-diameter steep spectrum radio relic. This is a unusual feature for a poor cluster (previously observed by Subrahmanyan et al. 2003).

From the multifrequency data analysis, Subrahmanyan et al. (2003) suggests that this diffuse extended emission could be the remnant plasma of a radio lobe (although no parent optical source has been identified) injected into the poor cluster.

X-ray images showed that the hot gas coincides with the central radio emission of NGC 5419 (Balmaverde & Capetti 2006).

5.40 NGC 5813

NGC 5813 resides in the NGC 5846 group, where NGC 5846 (Section 5.41) is the brightest central galaxy.

Archival data in VLA A, B, and C configuration at $\sim$ 1.4 GHz (Randall et al. 2011) revealed signatures of AGN activity in radio images, when compared with the *Chandra* X-ray images (Figure 3.6b) (Randall et al. 2015). The position of the central radio core is consistent with the X-ray brightness peak and the radio lobe-like emission corresponds well with the innermost X-ray cavities, especially the northern part of the inner region (Randall et al. 2011; Panagoulia et al. 2014). Additionally, the compact C configuration data reveal more diffuse emission with small ripples to the north-east and south-west, but without a clear interaction with a second pair of more extended X-ray cavities Randall et al. (2015). The radio emission filling the second generation of cavities is found at lower frequencies with LOFAR (Bîrzan et al. 2020) and GMRT (Giacintucci et al. 2011).

The ionized gas shows a filamentary morphology and is coincident with dust emission (Ferrari et al. 1999). The ionised gas appears to be located in the wake of the rising AGN inflated bubbles (Randall et al. 2011). The cooling lines of [CII], [NII], and OI and warm nebulae were observed too (Werner et al. 2014; Lakhchaura et al. 2018).

5.41 NGC 5846

NGC 5846 is a giant elliptical galaxy and a CDG of the massive group holding the same name.

The innermost central region hosts a radio core surrounded by a more diffuse radio emission (Figure 3.6c), which also appears to fill the innermost X-ray cavities (Trinchieri & Goudfrooij 2002; Dunn et al. 2010; Machacek et al. 2011; Panagoulia et al. 2014). The extended and diffuse emission, with a total extent of $\sim$ 12 kpc, is traced by the contours of the archival CnD configuration image. The results of the presented VLA data were previously published in Machacek et al. (2011).

The X-ray image analysis revealed multiple signatures of sloshing in NGC 5846 (Machacek et al. 2011), although, without a distinctive X-ray core in the central regions (Trinchieri & Goudfrooij 2002; Satyapal et al. 2005; González-Martín et al. 2006).

The ionized and molecular plasma coincides with the disturbed nuclear X-ray emission, [CII] line emission and cold, dusty features in the central regions of NGC 5846. (Macchetto et al. 1996; Caon et al. 2000; Trinchieri & Goudfrooij 2002; Werner et al. 2014; Temi et al. 2007b, 2009; Mathews et al. 2013; Lakhchaura et al. 2018).

5.42 NGC 7619*

The giant elliptical galaxy, NGC 7619, is the CDG of the Pegasus I group.

Our new VLA data in the A configuration have revealed a central radio source with a small extension to the east of the core (Figure 3.2g), consistent with previously observed point-like morphology in the archival VLA C configuration data. This findings are consistent with the emission in NVSS (Condon et al. 1998) and with GMRT observations at lower frequencies (at 610 MHz) by Giacintucci et al. (2011).

The X-ray image analysis revealed a ram-pressure-stripped tail (to the south-west of the nuclear region) as a result of NGC 7619 falling towards the center of the Pegasus cluster and interacting with the companion NGC 7626 with radio jets/lobes morphology (Randall et al. 2009) located 415 arcseconds (102 kpc) from NGC 7619. The study of ionized gas performed by Macchetto et al. (1996) showed a circumnuclear emission with an additional extended tail from the north-east to south-west. Although, the subsequent long slit spectroscopy and narrow band imaging observations with SOAR did not confirm the previous findings of Hα+[NII] emission (Lakhchaura et al. 2018). CO line emission was detected by Temi et al. (2007a) for this giant elliptical galaxy.

Chapter 6

Powerful AGN Jets and Unbalanced Cooling in the Hot Atmosphere of IC 4296

R. Grossová,[1,2] *N. Werner,*[3,1,4] *K. Rajpurohit,*[5] *F. Mernier,*[3,6,7] *K. Lakhchaura,*[3,8] *K. Gabányi,*[8,9] *R. E. A. Canning,*[10] *P. Nulsen,*[11,12] *F. Massaro,*[2] *M. Sun,*[13] *T. Connor,*[14] *A. King,*[10] *S. W. Allen,*[10] *R. L. S. Frisbie,*[15] *M. Donahue,*[15] *A. C. Fabian*[16]

[1]Department of Theoretical Physics and Astrophysics, Faculty of Science, Masaryk University, Kotlářská 2, Brno, 611 37, Czech Republic
[2]Dipartimento di Fisica, Universita degli Studi di Torino, via Pietro Giuria 1, I-10125 Torino, Italy
[3]MTA-Eötvös University Lendület Hot Universe Research Group, Pázmány Péter sétány 1/A, Budapest, 1117, Hungary
[4]School of Science, Hiroshima University, 1-3-1 Kagamiyama, Higashi-Hiroshima 739-8526, Japan
[5]Dipartimento di Fisica e Astronomia, Universitá di Bologna, Via Gobetti 93/2, 40131, Bologna, Italy
[6]SRON Netherlands Institute for Space Research, Sorbonnelaan 2, 3584 CA Utrecht, The Netherlands
[7]Institute of Physics, Eötvös University, Pázmány Péter sétány 1/A, Budapest, 1117, Hungary
[8]MTA-Eötvös University Extragalactic Astrophysics Research Group, Pázmány Péter sétány 1/A, Budapest, 1117, Hungary
[9]Konkoly Observatory, MTA Research Center for Astronomy and Earth Sciences, Konkoly Thege Miklós út 15-17, H-1121 Budapest, Hungary
[10]Kavli Institute for Particle Astrophysics and Cosmology, Stanford University, 452 Lomita Mall, Stanford, CA 94305-4085, USA
[11]Harvard Smithsonian Centre for Astrophysics, 60 Garden Street, Cambridge, MA 02138, USA
[12]ICRAR, University of Western Australia, 35 Stirling Hwy, Crawley, WA 6009, Australia
[13]Department of Physics and Astronomy, University of Alabama in Huntsville, Huntsville, AL 35899, USA
[14]The Observatories of the Carnegie Institution for Science, 813 Santa Barbara Street, Pasadena, CA 91101, USA
[15]Physics & Astronomy Department, Michigan State University, East Lansing, MI 48824-2320, USA
[16]Institute of Astronomy, University of Cambridge, Madingley Road, Cambridge CB3 0HA, UK

Received 2019 June 19 / Accepted 2019 June 19; in original form 2019 March 5
Published in Monthly Notices of the Royal Astronomical Society, volume 488, pages 1917-1925, 2019

Abstract

We present new Karl G. Jansky Very Large Array (VLA, 1.5 GHz) radio data for the giant elliptical galaxy IC 4296, supported by archival radio, X-ray (*Chandra*, *XMM-Newton*) and optical (SOAR, *HST*) observations. The galaxy hosts powerful radio jets piercing through the inner hot X-ray emitting atmosphere, depositing most of the energy into the ambient intra-cluster medium (ICM). Whereas the radio surface brightness of the A configuration image is consistent with a Fanaroff-Riley Class I (FR I) system, the D configuration image shows two bright, relative to the central region, large ($\sim 160\,\mathrm{kpc}$ diameter), well-defined lobes, previously reported by Killeen et al., at a projected distance $r \gtrsim 230\,\mathrm{kpc}$. The *XMM-Newton* image reveals an X-ray cavity associated with one of the radio lobes. The total enthalpy of the radio lobes is $\sim 7 \times 10^{59}\,\mathrm{erg}$ and the mechanical power output of the jets is $\sim 10^{44}\,\mathrm{erg\,s^{-1}}$. The jets are mildly curved and possibly re-brightened by the relative motion of the galaxy and the ICM. The lobes display sharp edges, suggesting the presence of bow shocks, which would indicate that they are expanding supersonically. The central entropy and cooling time of the X-ray gas are unusually low and the nucleus hosts a warm Hα+[NII] nebula and a cold molecular CO disk. Because most of the energy of the jets is deposited far from the nucleus, the atmosphere of the galaxy continues to cool, apparently feeding the central supermassive black hole and powering the jet activity.

6.1 Introduction

The oldest, largest known galactic structures in the Universe are giant elliptical galaxies. These systems are evolving contrary to the standard hierarchical galaxy formation scenario (Thomas et al. 2002). Observations and theoretical models indicate that they formed around 0.2–1 billion years after the Big Bang, went through a fast star-forming phase, and afterward grew only by dry mergers (Thomas et al. 2010; Onodera et al. 2015).

Initially, the evolution of giant ellipticals is dominated by dark matter, which clumps into haloes via gravity. When the mass of a halo reaches $\sim 10^{12}\,M_{\odot}$ (Correa et al. 2018), the inflowing gas passes through accretion shocks, and its temperature increases to several million Kelvin, forming an X-ray emitting atmosphere (further replenished by stellar mass loss; Pellegrini et al. 2018) and quenching star-formation (Cattaneo et al. 2009). These galaxies will continue to grow passively by interactions and dry mergers with other galaxies (Cattaneo et al. 2009). On the other hand, the sub-Eddington accretion rate of the gas onto the central supermassive black hole enables the so-called radio-mechanical (or radio mode) active galactic nucleus (AGN) feedback, thereby producing jets and lobes of relativistic plasma, visible in the radio band, which are able to propagate well outside their galaxy hosts.

Radio wavelength studies of giant elliptical galaxies are important for answering outstanding questions about the heating and cooling of their X-ray emitting atmospheres and about the physics of their AGNs (Brighenti & Mathews 2006). In clusters of galaxies, there is strong observational evidence for radio-mode AGN feedback balancing the cooling of the intra-cluster medium (ICM; e.g Churazov et al. 2000; Fabian et al. 2003; Bîrzan et al. 2004; Rafferty et al. 2006; Brüggen & Kaiser 2002) and preventing cooling flows and dramatic star formation (see Fabian 1994). It is believed that radio-mechanical feedback plays a critically important role also at smaller scales, in preventing atmospheric cooling in massive galaxies (Werner et al. 2019).

In the case of giant ellipticals, the so-called cooling flow problem is more severe. Shorter cooling time and larger amount of gas returned by the stellar populations over the lifetime of the galaxy (Cattaneo et al. 2009) place stronger demands on the AGN feedback as a source of heat balancing the radiative cooling. In some cases, the high-velocity radio jets are able to drill through the hot galactic atmospheres without significantly affecting the host galaxy, which may lead to unbalanced cooling in the innermost part of the galaxy (Sun et al. 2005b). Comprehensive studies of such systems are essential for our understanding of the role of AGN feedback in galaxies, galaxy groups, and galaxy clusters.

The powerful AGN jets penetrating the innermost hot galactic atmosphere and depositing most of their energy out at radii $r \gtrsim 230\,\mathrm{kpc}$ make the giant elliptical galaxy IC 4296, in the central region of the galaxy cluster Abell 3565, a source of high interest. Its radio counterpart, PKS 1333-33, has attracted the attention of astronomers for over 30 years. Historically, the first comprehensive studies were published by Killeen et al. (1986b,a) and Killeen & Bicknell (1988) using data from Very Large Arrray (VLA) at 1.3, 2, 6, and 20 cm. In particular, Killeen et al. (1986a) analysed X-ray data of the system from the imaging proportional counter (IPC) onboard the *Einstein* observatory. In addition to prominent jets extending over 35 arcmin, the authors reported a barely resolved diffuse X-ray source coinciding with the position of the galaxy.

In this paper, we present new radio data of IC 4296 obtained with the VLA in the A and D configurations at 1.5 GHz and compare them with archival observations available at lower frequencies in the TIFR GMRT Sky Survey (TGSS; Intema et al. 2017) and in the GaLactic and Extragalactic All-sky Murchison Widefield Array (GLEAM; Hurley-Walker et al. 2016).

While our paper presents new, deep radio observations, our goal is to study this system in a more comprehensive way. Therefore, we also analyse archival X-ray data from the *Chandra* and *XMM-Newton* observatories, as well as narrow-band Hα+[NII] images from the 4.1 meter Southern Astrophysical Research (SOAR) telescope and optical data from the Hubble Space Telescope (*HST*). This allows us to study the interaction between the jet/lobes and the surrounding hot and cold thermal gas phases.

Our paper is organized as follows: Section 6.2 includes the observational details and data reduction methods. Our results are presented and described in Section 6.3. A thorough discussion in Section 6.4 addresses the most important outcomes of our multiwavelength analysis connecting all these multiwavelength observations, with a particular emphasis on the relation between the radio and X-ray band. Finally, our conclusions and remarks are summarized in Section 7.1.

Throughout this paper, we used the following cosmological parameters: $\mathrm{H}_0 = 69.6\,\mathrm{km\,s^{-1}\,Mpc^{-1}}$ (Bennett et al. 2014), $\Omega_\mathrm{M} = 0.286$ and $\Omega_\Lambda = 0.714$. At the redshift of 0.0125 the distance of IC 4296 is $49\,\mathrm{Mpc}$ (Mei et al. 2000), estimated using the surface brightness fluctuation method, with the corresponding scale of $0.256\,\mathrm{kpc/arcsec}$. The spectral index α of the synchrotron radiation as a function of the flux density S_ν at the frequency ν is defined as $S_\nu \propto \nu^\alpha$. The elemental abundances are expressed with respect to the proto-solar values from Lodders et al. (2009).

6.2 Observations and Data Analysis

6.2.1 Radio Observations and Analysis

IC 4296 was observed on 2015 July 11 by the Karl G. Jansky VLA in A configuration (project code: 15A-305; PI: Werner) and on 2018 October 26 (project code: 18A-317, PI: Grossova) in D configuration. The L-band receiver covering the frequency range spanning from 1 to 2 GHz is divided into sixteen spectral windows with 64 1000 kHz wide channels. The one-hour long observations consist of ≈ 40 minutes integration time on the target and ≈ 10 minutes on both the standard VLA flux density calibrator 3C 286 and a nearby compact source J1316-3338 used as amplitude and phase calibrator. VLA data were reduced and imaged using the

National Radio Astronomy Observatory (NRAO) pipeline Common Astronomy Software Applications (CASA, McMullin et al. 2007), v4.7.2 and v5.0.0 for A and D configuration data, respectively.

A careful approach was followed to flag Radio Frequency Interferences (RFI). First, we used the auto-flagging algorithm `tfcrop` in CASA to identify the outliers in the time-frequency plane. Then, we used the Offringa's RFI software AOFLAGGER (Offringa et al. 2012). The combination of the two strategies, for the A configuration, flagged in total 46 % of the data, with spectral windows 2, 3, 8 and 9 almost entirely flagged. In the case of the D configuration, more than half of the data had to be flagged.

Afterwards, we used a model for the flux calibrator 3C 286 provided by the CASA package to set up the flux density scale determined by Perley & Butler (2013). The initial gain calibration was performed for central channels on both calibrators to average over small variations of phase with time in the bandpass. Next, we performed the bandpass calibration. The relative delays of each antenna in comparison with the reference antenna were derived and complex bandpass solutions were calculated to include variations in gain with frequency. The next step determined the complex gains for both calibrators. Finally, the derived calibration solutions were applied to the target.

The deconvolution and imaging were performed by the CASA `clean` algorithm in the multifrequency synthesis mode. We produced images over a wide range of resolutions and with different uv-tapers and weighting schemes to emphasize the radio emission on various spatial scales. A second-order Taylor polynomial (`nterms = 2`, McMullin et al. 2007) was used, to take into account the spectral behaviour of bright sources. To refine the calibration for the target, we performed two cycles of phase and one cycle of amplitude and phase self-calibration.

We also constructed a spectral index map using the VLA D configuration image at 1.5 GHz and a GLEAM radio image at 158 MHz. To create a reliable spectral index map, it is essential to compare the images using the same resolution and the same pixel size. First, we deconvolved the two-dimensional VLA calibrated data using the `uvtaper` option within the CASA `clean` algorithm to create a total flux intensity image close to the resolution of the GLEAM image. Then, we smoothed the image with the exact GLEAM restoring beam size[1] using the CASA task `imsmooth`. Secondly, the GLEAM image was regridded to get the same pixel size as the VLA D configuration image. We used the CASA `immath` task, to calculate flux densities, spectral indices, and their uncertainties following Rajpurohit et al. (2018). We assumed flux density uncertainties ($f_{\rm err}$) of 4 % for the VLA data (Perley & Butler 2013) and 8 % for the GLEAM data (Hurley-Walker et al. 2017).

6.2.2 Archival X-ray Observations

Archival *Chandra* observations and analysis

IC 4296 was observed by the *Chandra* Advanced CCD Imaging Spectrometer in the S-array (ACIS-S) on 2001 September 10 (Obs. ID: 2021) and 2001 December 15 (Obs. ID: 3394) with a total clean exposure time of 48 ks. The on-axis point-spread function (PSF) is better than 1 arcsec for *Chandra*. The data reduction and analysis are described in detail in Lakhchaura et al. (2018).

Archival *XMM-Newton* observations and analysis

In addition to *Chandra*, we also used an archival *XMM-Newton* observation (Obs. ID: 0672870101) of IC 4296, which was performed on 2011 July 11. We took advantage of both the EPIC (MOS 1, MOS 2, and pn) and RGS (RGS 1 and RGS 2) instruments to fully investigate this system. The on-axis PSF of the X-ray telescopes on *XMM-Newton* is of the order of 10 arcsec.

The entire EPIC data reduction procedure and EPIC (European Photon Imaging Camera) imaging extraction were done using the XMM Science Analysis System (SAS) software v17.0.0 following Mernier et al. (2015) to which we refer for further details. After filtering the EPIC data from flaring events, the cleaned exposures are 46, 47, and 44 ks for MOS 1, MOS 2, and pn, respectively.

The EPIC spectral analysis reported in Section 6.3.2 follows the general prescription detailed in Mernier et al. (2015). We used the spectral fitting package SPEX v3.04 (Kaastra et al. 1996; Kaastra et al. 2017) to analyse the obtained EPIC spectra. Since the signal-to-noise ratio in the extracted EPIC regions is much weaker than in the central regions analysed with *Chandra* ACIS-S (Section 6.3.2), a careful modelling of the background is necessary here. This modelling, taking into account the galactic thermal emission, the local hot bubble, the unresolved point sources (or cosmic X-ray background), the quiescent particle background, and the residual soft-proton background is also fully described in Mernier et al. (2015), and references therein. Finally, we modelled the X-ray emission of IC 4296 with a redshifted and absorbed collisional ionisation equilibrium plasma model (`cie`), in which the abundances are fixed to 0.3 proto-solar (Urban et al. 2017). The MOS 1, MOS 2, and pn spectra were fitted simultaneously and the spectra were deprojected using the `dsdeproj` tool (Russell et al. 2008). The free parameters are thus the temperature (kT) and the SPEX normalisation.

The RGS data reduction was performed using the SAS task `rgsproc`, which also takes care of filtering the data from flared events and of estimating the background from the RGS CCD 9 (where no source counts are expected). The first order RGS 1 and RGS 2 raw spectra, extracted within 0.8 arcmin (i.e. 90 % of the PSF) in the cross-dispersion direction, are then background-subtracted and combined using the SAS task `rgscombine`. Compared to EPIC, the RGS spectra are in principle much better suited for investigating the heating-cooling balance in the central X-ray atmosphere of IC 4296 (Section 6.3.2). Therefore, in addition to the

[1]The GLEAM restoring beam is $155.57'' \times 143.65''$.

cie emission, we model our combined RGS spectrum with a classical 'cooling-flow' (cf) component. The multiplicative component lpro (calculated from the MOS 1 detector image in the 0.3–2 keV band) is also applied to account for the instrumental broadening of the lines due to the spatial extent of the source. The lower and higher temperature limits of the cf model are respectively fixed to 0.1 keV and tied to the temperature of the cie model. The free parameters are the normalization of the cie component, the cooling rate of the cf component, and the O, Ne, and Fe abundances. The other abundances are tied to that of Fe, with the exception of Mg which is tied to the O abundance.

6.2.3 Archival Optical Observations and Analysis

Narrow-band Hα+[NII] imaging of IC 4296 was obtained by Sun et al. (in prep.) with the 4.1 m SOAR telescope using the SOAR Optical Imager (SOI). The full description of these observations is given in the survey paper (Sun et al. in prep.), but we briefly summarize them here. IC 4296 was observed on 2015 July 21 for 1800 s in both on (6649/76) and off (6737/76) band filters[2]. Basic reduction was performed using SOI-specific IRAF scripts based on the mscred package.

In addition to the SOAR image, we used archival *HST* Imaging with the Advanced Camera for Surveys (ACS) High Resolution Channel (HRC) obtained as part of the program GO-9838 (PI: L. Ferrarese) observed on 2004 August 7. ACS/HRC images are in the F435W filter and the FR656N filter, which was tuned to a central wavelength of 6644.3 Å; this tuning samples Hα at the redshift of IC 4296. These observations were previously discussed by Dalla Bontà et al. (2009) and presented also in Lauer et al. (2005) and Balmaverde & Capetti (2006). We did not continuum-subtract the ACS/HRC images, but a strong nuclear source is seen in the FR656N image that is not seen in the corresponding F435W image. As was discussed by Dalla Bontà et al. (2009), there is strong Hα+[NII] emission that extends beyond the central dust disk visible in the right panel of Figure 6.7 (for more details see also Section 6.3.3).

6.3 Results

6.3.1 Radio Morphology

The 1.5 GHz VLA A configuration radio image is shown in Figure 6.1 (left) with a resolution of $3.94'' \times 3.26''$ and a root-mean-square (rms) noise of 0.06 mJy beam^{-1}. The total intensity image clearly reveals a bright nucleus and extended emission in two jets, with several knots on both sides, terminating in diffuse radio plumes. The two well-collimated and almost symmetric jets emit via synchrotron radiation in the central regions. However, interestingly, the jets show noticeable re-brightening further away from the nucleus at $r \sim 10\,\mathrm{kpc}$, where the radio plumes broaden, as mentioned previously by Killeen & Bicknell (1988). Based on our VLA data obtained in A configuration (which is less sensitive to extended structures), the total extent of the radio structure is $\sim 120\,\mathrm{kpc}$ with the northwestern jet extending out to $r \sim 70\,\mathrm{kpc}$ and the southeastern to $r \sim 50\,\mathrm{kpc}$. The total integrated flux density of the source in A configuration is $3.98 \pm 0.40\,\mathrm{Jy}$. IC 4296 shows a gradual decrease in surface brightness from the centre, which is typical of Fanaroff-Riley (FR I) radio galaxies.

The low-resolution D configuration image is shown in Figure 6.1 (right). The image has a resolution of $90.15'' \times 23.02''$ and the rms noise level is $\sim 0.2\,\mathrm{mJy\,beam^{-1}}$. The total integrated flux density of IC 4296 in D configuration is $8.30 \pm 0.83\,\mathrm{Jy}$. The difference between the extracted integrated flux density values in A and D configurations lies in the fact that the A configuration data with the missing short baselines are not able to recover the highly peaked signal from the more extended diffuse emission in the jets and lobes. Two well-confined lobes are visible in the D configuration image at a projected distance of ∼230 kpc and 290 kpc from the bright nuclear region, in the northwestern and southeastern directions, respectively.

Since the plumes and/or lobes in FR I and FR II radio galaxies tend to have steep radio spectra, we also inspected the archival TGSS radio maps at 153 MHz. These revealed a radio structure close to that observed at 1.5 GHz in our VLA A configuration image, but also a weak diffuse lobe-like emission extending far beyond the A configuration image (black contours in Figure 6.2). The GLEAM data at 154–162 MHz also confirm the two extended lobe-like structures (white contours in Figure 6.2).

The spectral index map created using the GLEAM data at 158 MHz and the VLA D configuration data at 1.5 GHz is shown in Figure 6.3. As expected, the central regions of the galaxy show a flat spectral index of -0.5 and a steepening is present in the lobes. They both have steep spectra with indices of -0.7 and -1.1, respectively (Figure 6.3). The spectral index map appears uniform over the two lobes in agreement with the lack of clear hot spots that would have flatter radio spectra. The uncertainties on the spectral index are of the order of a few percent.

The radio power of $\sim 10^{24}\,\mathrm{W\,Hz^{-1}}$ at 1.4 GHz[3] obtained from CASA total intensity D configuration image is close to the boundary radio power of the FR dichotomy of $\sim 10^{24.5}\,\mathrm{W\,Hz^{-1}}$ at 1.4 GHz (Owen & Ledlow 1994). With its absolute R-band magnitude of $M_\mathrm{R} = -23.33 \pm 0.24\,\mathrm{mag}$, IC 4296 is placed below the boundary division line of the Ledlow-Owen diagram, where most of the FR I sources are located.

[2]CTIO (Cerro Tololo Inter-American Observatory) H_α filter 6649/76 (λ_cen = 6650Å, FWHM = 77Å) and 6737/76 (λ_cen = 6746Å, FWHM = 86Å).

[3]With corresponding flux density $\sim 8\,Jy$.

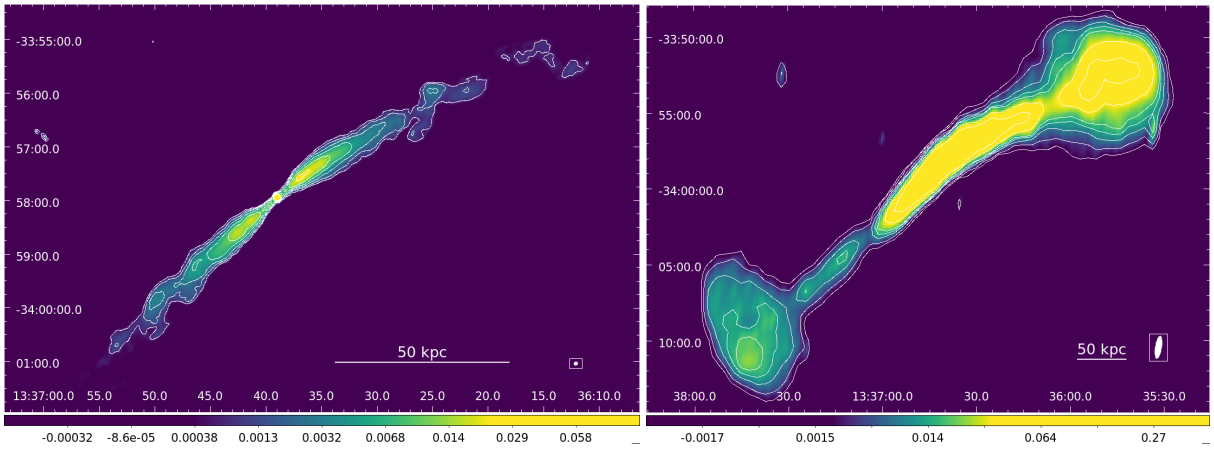

Figure 6.1: VLA total intensity images of IC 4296 at 1.5 GHz. **Left**: A configuration image shows that the surface brightness of jets decreases as a function of radius, although we also see re-brightening in the radio plumes at $\sim$ 10 kpc from the nucleus. The restoring beam size is $3.94'' \times 3.26''$ and is shown in the bottom right corner. **Right**: D configuration image revealed well-confined radio lobes extending up to almost 300 kpc from the central regions of IC 4296, previously reported by Killeen et al. (1986b). The restoring beam is $90.15'' \times 23.02''$ and is shown in the bottom-right corner. The contour levels are at [-1,1,2,4,8,16] $\times$ 5 rms noise, with corresponding rms noise of $0.06\,\mathrm{mJy\,beam^{-1}}$ and of $0.2\,\mathrm{mJy\,beam^{-1}}$ for VLA A and D configuration data, respectively.

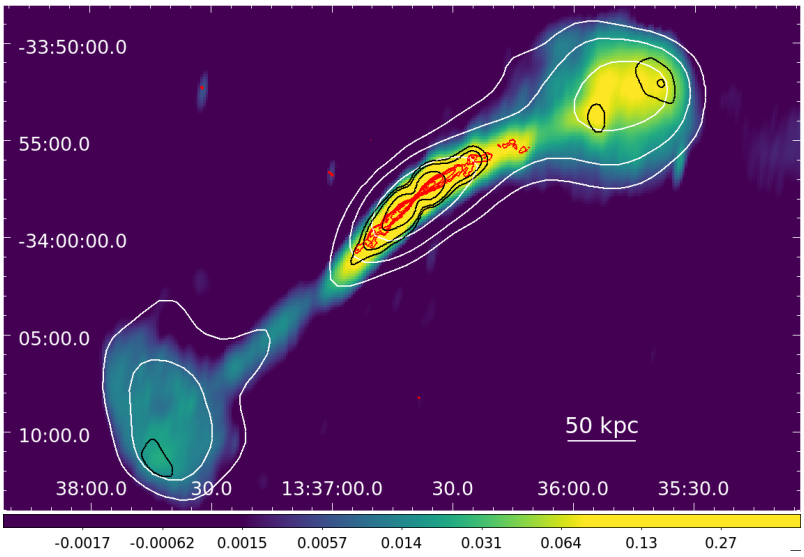

Figure 6.2: VLA D configuration radio map at 1.5 GHz overplotted with the TGSS radio contours at 153 MHz (in black), VLA A configuration contours at 1.5 GHz (in red), and the GLEAM radio maps at 154–162 GHz (in white). Contours levels were created at $[-1, 1, 2, 4, 8, 16] \times 5$ rms noise for the TGSS, GLEAM, VLA A configuration data with corresponding rms noise of 3, 0.12, and $0.06\,\mathrm{mJy\,beam^{-1}}$.

6.3.2 Comparison with the X-ray Data

The characteristic radius of the X-ray atmosphere in Figure 6.4 (left) observed by *Chandra* ACIS-S (see also Pellegrini et al. 2003) is much smaller than the total extent of the radio jets. The jets emanating from the nuclear region are at first well-collimated and, after piercing through the innermost parts of the hot X-ray emitting atmosphere, at $r \sim 10\,\mathrm{kpc}$, they widen significantly, as previously noticed by Killeen & Bicknell (1988).

Lakhchaura et al. (2018) investigated the radial profiles of the entropy and the cooling time ($t_{\rm cool}$) over free-fall time ($t_{\rm ff}$) ratio. The cooling time and entropy decrease with decreasing radius down to $< 1\,\mathrm{kpc}$. The power-law fit of the radial entropy profile

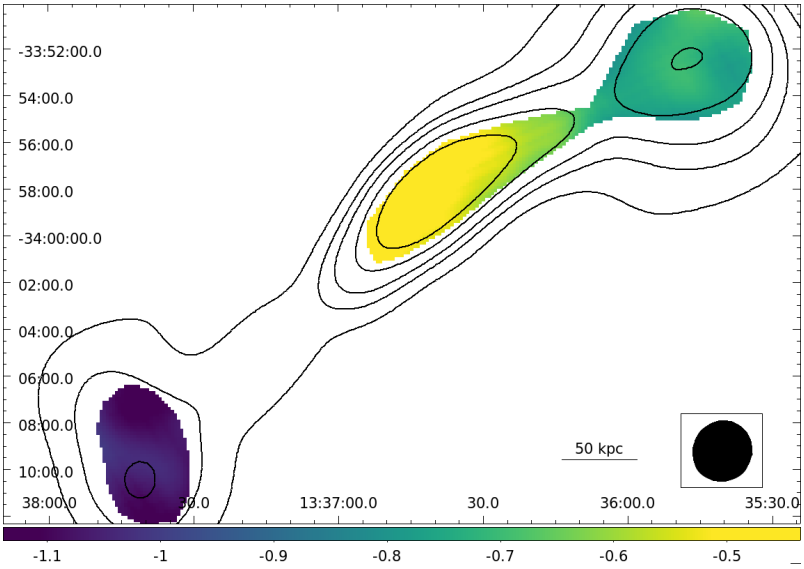

Figure 6.3: The spectral index map for IC 4296 reveals a flat spectral index in the central region of the jet, whereas in the two lobes we observe a steep spectral index of -0.7 and -1.1. The map was created using the 158 GHz GLEAM and the 1.5 GHz VLA D configuration image at $155'' \times 143''$ resolution (the beam is shown in the right corner of the map) and it is overlaid with VLA contours corresponding to the VLA smoothed image, in respect to GLEAM image to reach the same beam size. The rms noise reached value of $\sim 1.5\,\mathrm{mJy\,beam^{-1}}$. Contour levels are $[-1, 1, 2, 4, 8, 16] \times 5\,\mathrm{rms\,noise}$.

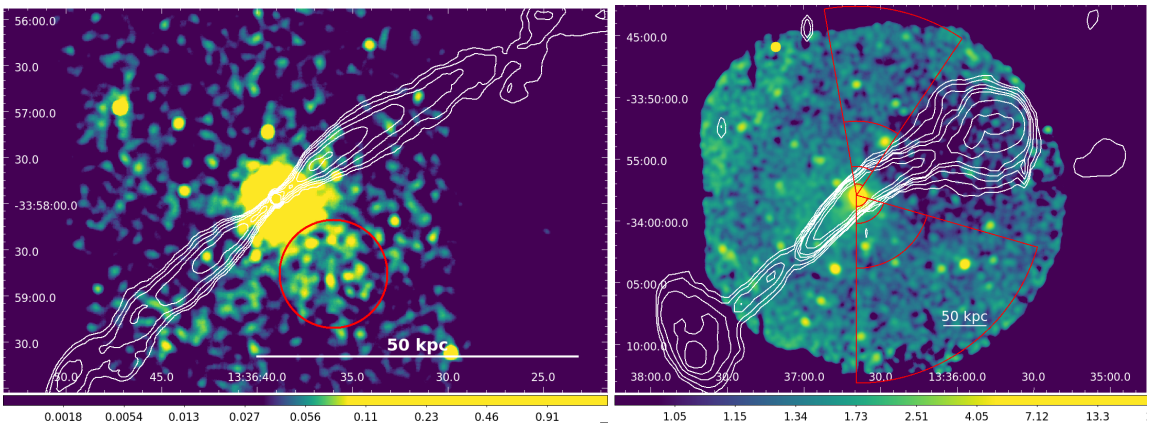

Figure 6.4: **Left:** The *Chandra* X-ray image at 0.5–5 keV overlaid with white contours of our VLA map at 1.5 GHz obtained in A configuration with same contour levels as defined in Figure 6.1. The image reveals an excess of the X-ray emission, marked by a red circle, to the southwest of IC 4296. **Right:** The background-subtracted, exposure-corrected *XMM-Newton* EPIC image (combining MOS 1, MOS 2, and pn) in the 0.3–2 keV band overlaid with contours of the VLA D configuration image same as in Figure 6.1 (right). The X-ray image reveals a decrement, a likely cavity, corresponding to the northwestern radio lobe. The over-plotted red partial annuli indicate the spectral extraction regions used to determine the temperature and the density of the ICM outside of the northern radio lobe.

reveals a steep slope with an index of $\sim$ 1.2. Even below 2 kpc, the slope of the entropy profile remains steep with an index of $\sim$ 1.0, and in the innermost radial bin the entropy reaches a value of $K_0 \sim 1.5\,\mathrm{keV\,cm^2}$ (see the appendix in Lakhchaura et al. 2018). In fact, IC 4296 has the steepest entropy profile of all galaxies in the sample of Lakhchaura et al. (2018), followed by that of NGC 4261 (see Figure 6.5; right). This will be discussed further in Section 6.4.2.

The cooling time in the centre of IC 4296 is $t_{\rm cool} < 11.2\,\mathrm{Myr}$. The ratio of the cooling time to free-fall, time $t_{\rm cool}/t_{\rm ff}$, reaches a

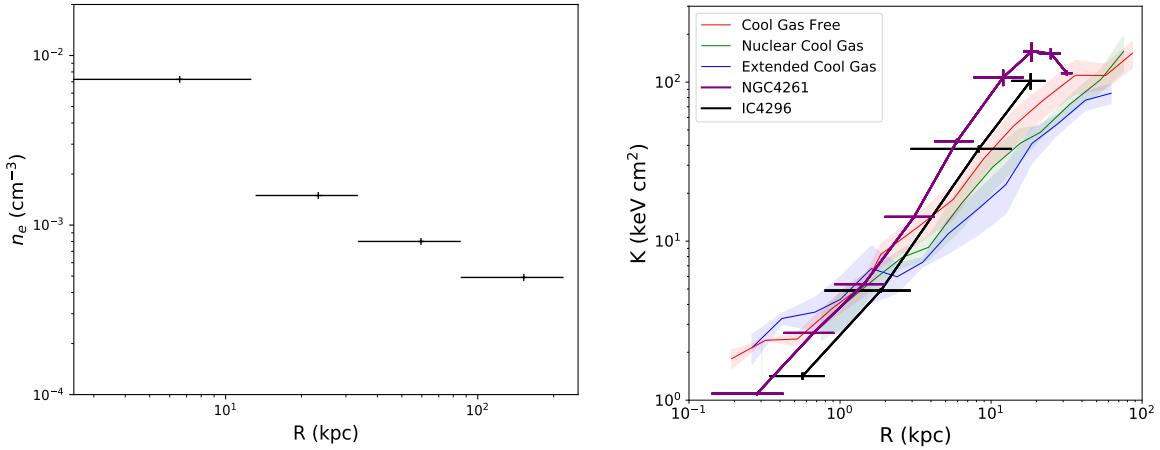

Figure 6.5: **Left:** Deprojected electron density profile for the gas surrounding the northwestern cavity of IC 4296. The two spectral extraction regions, whose values have been combined and averaged in this figure, are shown by the red sectors in Figure 6.4 (right). **Right:** The entropy profiles of IC 4296 and NGC 4261 in comparison with the sample of Lakhchaura et al. (2018). The red, green and blue solid lines show median profiles for cool gas free, nuclear cool gas and extended cool gas systems, respectively and the shaded regions show the median absolute deviation (MAD) spreads about the medians. The entropy profiles of IC 4296 and NGC 4261 show much steeper trends than the other galaxies in the sample.

value close to 10 in the centre of the galaxy, where the atmosphere most likely continues to cool, feeding the central supermassive black hole and powering the jets.

The archival *Chandra* X-ray image reveals an excess of X-ray emission in the southwestern part of the structure, in between the northwestern and southeastern side of the jet, as marked by a red circle in the *Chandra* X-ray image in Figure 6.4 (left). The detection significance of such X-ray diffuse emission is above $5\,\sigma$. Surface brightness profiles derived along this extended X-ray emission do not reveal any sharp edges.

Our *XMM-Newton* EPIC image extracted in the 0.3–2.0 keV band reveals a cavity with a diameter of $\sim$ 160 kpc associated with the northwestern radio lobe (see Figure 6.4; right). We find a small misalignment between the radio lobe and the X-ray cavity. It could be the result of projection effects, where the part of the cavity closer to the mid-plane of the source is clearly visible in the X-ray image, while the part associated with the visible radio emission could be offset from the mid-plane and thus not seen clearly in the images.

We extracted and fitted the deprojected spectra from four partial spherical shells in the direction of the northwestern jet (traced by the red sectors in Figure 6.4 right). The corresponding radial profile of the electron density (n_e) is shown in Figure 6.5 (left). We have subtracted the emission contribution of the gas at larger radii (i.e. beyond our field of view), which we estimated by extrapolating a beta model fit to our initial density profile. The temperature and total density (electrons plus ions) of the gas surrounding the cavity (i.e. the last radial bin in Figure 6.5; left) are respectively $kT = 0.95 \pm 0.01$ keV and $n = 9.6 \pm 0.05 \times 10^{-4}$ cm^{-3}, which corresponds to a pressure of $nkT = 9.12 \times 10^{-4}$ keV cm^{-3}. Assuming the northwestern cavity is spherical with a radius of 80 kpc, the $4pV$ work performed by the jet to displace the ICM is $\sim 3.7 \times 10^{59}$ erg. Assuming a similar enthalpy for the southeastern cavity, which is outside of the *XMM-Newton* field-of-view, we obtain a total enthalpy of $\sim 7 \times 10^{59}$ erg.

The combined *XMM-Newton* RGS 1+RGS 2 spectrum is shown in Figure 6.6. Some lines (e.g. Fe XVII at 15Å and 17Å, O VIII at 19Å, rest frame) are clearly identified as they are typical of a cool ($\lesssim$1 keV) gas. Our best-fit model provides a temperature of 0.79 ± 0.05 keV and an Fe abundance of 0.13 ± 0.02 for the `cie` component, as well as a cooling rate of $4.5 \pm 1.0\ M_\odot$ yr^{-1} for the `cf` component. In this spectrum of limited quality, however, the cooling rate and Fe abundance parameters seem to share some degeneracy, with our inferred cooling rate dropping to $2.1 \pm 0.6\ M_\odot$ yr^{-1} when fixing the abundances to 0.3 proto-solar. This is further discussed in Section 6.4.2.

6.3.3 Comparison with the Optical Data

The narrow band SOAR Hα+[NII] image shown in Figure 6.7 (right) indicates that the ionized gas is circumnuclear and the ionized disk is perpendicular to the jets. The SOAR data also provide a hint for entrainment along the northwestern radio plume. The *HST* data show a warped, dust disk with a 0.9 radius (see Figure 6.7; left), which does not appear to be perpendicular to the jets (see Schmitt et al. 2002, for more details) and is visible on smaller scales than the emission in the SOAR image (Figure 6.7;

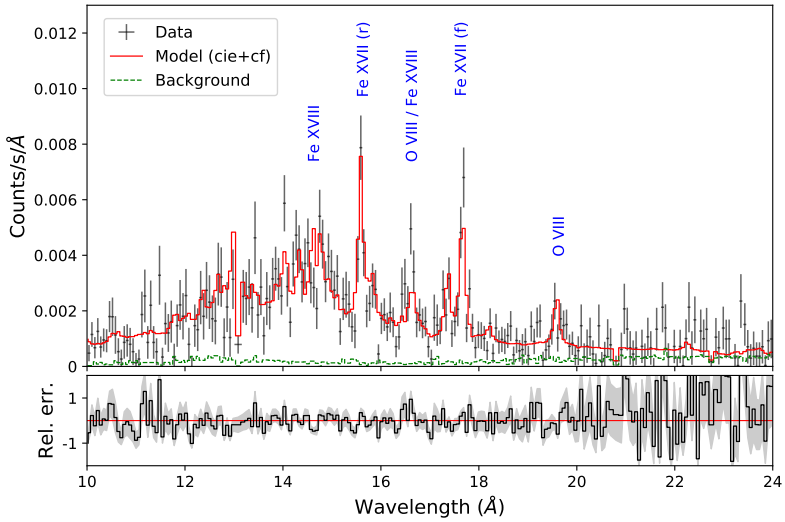

Figure 6.6: Combined first order RGS 1+RGS 2 spectrum of IC 4296, extracted within 0.8 arcmin in the cross-dispersion direction. Our best-fit model (cie+cf, see text) is overplotted in red.

right).

Interestingly, recent studies of CO emission from a sample of giant elliptical galaxies by Boizelle et al. (2017) and Ruffa et al. (2019) revealed the presence of a circumnuclear molecular gas disk, which is co-spatial with the dust (Ruffa et al. 2019).

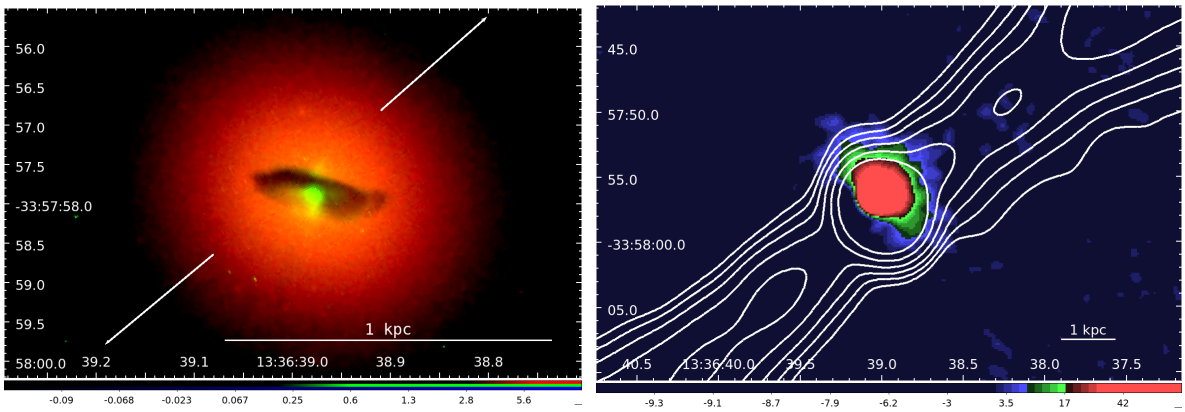

Figure 6.7: **Left:** The *HST* image of a dust disk in IC 4296. The narrow band Hα image (in green) was obtained using ramp filter adjusted to the redshift of the galaxy. Two white arrows represent jets emitted from the central nuclear regions. **Right:** The narrow band Hα+[NII] image from the SOAR telescope overlaid with the VLA A configuration radio contours.

6.4 Discussion

6.4.1 The Nature of the Radio Source

Our new VLA data in D configuration at 1.5 GHz confirm the presence of the two lobes previously detected by Killeen et al. (1986b). While the extended emission resembles the radio morphology of FR II radio galaxies, the lobes lack compact hot spots. The total extent of the radio structure is $\approx 500\,\mathrm{kpc}$, which is in agreement with Killeen et al. (1986b). The compactness of the radio lobes relative to their distance from the galaxy core, make IC 4296 very similar to other powerful radio galaxies.

From the X-ray analysis, we conclude that it would take $1.5 \times 10^8\,\mathrm{yr}$ to inflate the northwestern X-ray cavity with a radius of $\sim 80\,\mathrm{kpc}$ at the sound speed of $c_\mathrm{s} \sim 500\,\mathrm{km\,s^{-1}}$ for $kT = 1\,\mathrm{keV}$ gas. Assuming this expansion time, we obtain a jet power of

$1.6 \times 10^{44}\,\mathrm{erg\,s^{-1}}$. Another estimate considers the sound-crossing time of the projected distance of the cavity from the centre of the galaxy of $2.2 \times 10^{8}\,\mathrm{yr}$ resulting in a jet power of $10^{44}\,\mathrm{erg\,s^{-1}}$.

The radio morphology of the source indicates a possible supersonic expansion. In the boundary layer, where the well-defined northwestern radio lobe meets the ambient ICM (Figure 6.1; right), the surface brightness is increased and the end of the jet forms a lobe with a sharp-edged morphology. According to 3-dimensional hydrodynamic simulations by Massaglia et al. (2016) and Perucho & Martí (2007), this sharp head of the jet is consistent with bow shocks, which are typical indicators of the supersonic expansion relative to the surrounding medium. The inconsistency with the classical FR I class, low power radio sources with subsonic expansion, lies in the re-brightenings and sharp-edged structure of the northwestern radio lobe suggesting its supersonic expansion.

The radio morphology of IC 4296 shows similarities with the morphology of 3C 348 (Hercules A, often classified as a FR I/II radio source; Siebert et al. 1996; Gizani & Leahy 2003), which is one of the most luminous radio sources with a total power comparable to the Cygnus A galaxy (Gizani et al. 2005). Hercules A also has missing compact hotspots and possesses an unusual morphology dominated by jets and inflated steep spectrum lobes.

The jets, piercing through the galactic atmosphere and depositing their energy into the surrounding intra-cluster medium, are also present in the FR I radio source NGC 4261 (a.k.a. 3C 270; O'Sullivan et al. 2005). Interestingly, we find that the derived enthalpy for the cavities/lobes of IC 4296 is ~ 30 times larger than for NGC 4261 (O'Sullivan et al. 2011b), mainly due to the size of the radio lobes (~ 6 times larger in the case of IC 4296). As further discussed in Section 6.4.2, in these two cases the central regions also show steep entropy (see Figure 6.5; right) and cooling time profiles (Werner et al. 2012; Voit et al. 2015b) and a prominent nuclear dust disk fueling the AGN closely related to powerful radio jets (Jaffe et al. 1993; Jaffe & McNamara 1994), which could have cooled from the hot X-ray emitting atmosphere of the galaxy. Such a dust and molecular disk are also present in the brightest cluster galaxy of Hydra A, which also displays powerful jet activity (McNamara 1995; Taylor 1996).

6.4.2 The Unbalanced Cooling in IC 4296

The X-ray image overlaid with the radio contours in Figure 6.4, indicates that while in the inner part of the galaxy, at $r \lesssim 10\,\mathrm{kpc}$, the radio jets are well-collimated by the thermal pressure of the hot atmosphere, their width increases at larger radii. Nevertheless, these powerful radio jets pierce through the inner hot X-ray emitting atmosphere of the galaxy and extend to radii over $r \gtrsim 230\,\mathrm{kpc}$, where they deposit their energy into the outer galactic atmosphere and the ambient ICM.

Similarly to NGC 4261, the entropy profile of IC 4296 (Figure 6.5; right) shows a steeper slope than for all other giant elliptical galaxies analysed by Lakhchaura et al. (2018). In fact, it appears to be decreasing all the way to $r < 1\,\mathrm{kpc}$ (see also Panagoulia et al. 2014; Babyk et al. 2018). At $r < 1\,\mathrm{kpc}$, $t_{\mathrm{cool}}/t_{\mathrm{ff}}$ drops to $\approx$10 and the gas may become thermally unstable (Sharma et al. 2012; Gaspari et al. 2012b; Kunz et al. 2012; McCourt et al. 2012; Gaspari et al. 2013; Voit et al. 2015a). These results suggests that, whereas the expanding radio jets and lobes may be able to heat the surrounding gas at $r \gtrsim 10\,\mathrm{kpc}$, the inner, well-collimated, part of the jets do not appear to be depositing sufficient heat to the innermost rapidly cooling X-ray atmosphere.

At first glance, this picture is in line with our analysis of the *XMM-Newton* RGS spectra, as they are consistent with an appreciable mass deposition rate of $4.5 \pm 1.0\,M_{\odot}\,\mathrm{yr^{-1}}$. This rate is particularly high compared to other elliptical galaxies and groups whose RGS spectra reveal mass deposition rates typically less than $1\ M_{\odot}\ \mathrm{yr^{-1}}$ (Liu et al. 2019). We caution, however, that this measurement suffers from large systematic uncertainties because the limited quality of the data implies degeneracies between some parameters. For example, fixing all the abundances to 0.3 proto-solar (which is more realistic than our best-fit 0.13 proto-solar value; e.g. Urban et al. 2017) yields a lower mass deposition rate of $2.1 \pm 0.6\,M_{\odot}\,\mathrm{yr^{-1}}$. Moreover, we cannot exclude even higher abundances (i.e. close to the proto-solar value) in the inner $\sim$10 kpc region, which would then further revise lower inferred cooling rates. Future deeper observations will thus be important to confirm (or disprove) the unusually high cooling rate in this source. Assuming nevertheless our initial deposition rate and that the bulk of this material accretes onto the central supermassive black hole and is converted into jets with a 10 % efficiency, it will result in a jet power of $\sim\ 2.6 \times\ 10^{46}\,\mathrm{erg\,s^{-1}}$. This is more than two orders of magnitude higher than the actual jet power estimated in Section 6.4.1 ($\sim\ 10^{44}\,\mathrm{erg\,s^{-1}}$). We therefore conclude that the currently assumed rate of cooling is largely sufficient to effectively produce the observed radio jets.

In the centre of the galaxy, a disc of ionized and molecular gas (Boizelle et al. 2017; Ruffa et al. 2019) is observed, which is also visible in the *SOAR* image in the right panel of Figure 6.7. The circumnuclear dust disc seen by *HST* in the right panel of Figure 6.7., could be covering the central engine of the galaxy, offering a possible explanation for the apparent strongly sub-Eddington nuclear luminosity of $L_{\mathrm{bol}}/L_{\mathrm{Edd}}$[4]$\sim 2\times 10^{-5}$ (Pellegrini et al. 2003). The true Eddington ratio necessary to explain the acceleration of jets penetrating through the ambient medium could be significantly higher. On the other hand, the low Eddington ratio could also be a result of an advection-dominated accretion flow (ADAF), where the heat generated via viscous dissipation in the disk is "advected" inwards with the accreting gas (Narayan & Yi 1994).

6.4.3 Peculiar Bending Jets in Hot Atmosphere

The radio and X-ray morphologies of IC 4296 resemble those of some other systems, such as NGC 1265, where the powerful radio jets penetrate through the atmosphere of hot gas bound to the host galaxy, with little impact on the X-ray gas (Sun et al. 2005a). In NGC 1265, the two-sided jet emerges from the atmosphere into the ICM of the Perseus cluster. Since NGC 1265 is moving at high

[4]The Eddington luminosity for IC 4296 is $\sim 1.2\times\ 10^{47}\,\mathrm{erg\,s^{-1}}$.

speed relative to the ICM, we see bright radio knots in its jet where they impinge on the ICM and are deflected (O'Dea & Owen 1987). Although IC 4296 differs in important respects from NGC 1265, we cannot exclude that the observed re-brightening in its jet at $r \sim 10\,\mathrm{kpc}$ could have a similar origin.

The presence of a possible X-ray tail seen in the *Chandra* image and the location of IC 4296 in the centre of Abell 3565 is consistent with the sloshing of the ambient ICM in the potential well of the cluster (see Markevitch & Vikhlinin 2007). Given the relative motion, the radio jets emerging from the central atmosphere run into the ICM and are deflected in the direction opposite to the galaxy's travel, as also noted by Kemp (1994). Assuming that the jets are supersonic, they could be deflected in a succession of inclined weak shocks or via magnetohydrodynamical instabilities (Massaglia et al. 2019), converting jets' kinetic energy to thermal energy. Alternatively, the brightening could result from the dissipation of turbulence driven by the interaction between the jets and the external medium (Burns 1998). In either case, the additional thermal energy will raise the pressure (and density) in the jet plasma, causing it to expand (e.g. Gizani & Leahy 1999). This would account for the increase in the width of the radio source in the regions $\sim 10\,\mathrm{kpc}$ from the central AGN, also noticed by Killeen & Bicknell (1988).

The apparent curvature of the jets is rather weak and we may be viewing the system from a direction nearly parallel to the velocity vector. The location of the tail and the radio source curvature are both consistent with a projected relative velocity towards the northeast.

Chapter 7

Summary and Future perspectives

7.1 Summary and Conclusions

The most important results of our statistical radio study of a large sample of optically and X-ray brightest nearby early-type galaxies as well as the comprehensive single-source study of IC 4296, are summarized here.

First of all, the final results of our VLA statistical study are the following:

- A large, volume-, optical and X-ray luminosity-limited sample of 42 early-type galaxies observed with multiple configurations of the VLA reveals the presence of a radio source in almost all galaxies. Our radio source detection rate is as high as 41/42 (98%), with the remaining source detected in archival single dish observations (Dressel & Condon 1978; Condon & Broderick 1988), reported in the NVSS survey (Brown et al. 2011), and at low frequencies using LOFAR (Bîrzan et al. 2020). The radio emission has an extended morphology in at least 67% (28 out of 42) of sample galaxies. 34 sources out of 42 (81%) display a decrease in the X-ray surface brightness due to the hot gas being displaced out by jets creating X-ray cavities in the hot atmosphere.
- Significant correlations are found between the radio power and the luminosity of the central X-ray point source, and between the radio flux density and the largest linear size of the emission. When we compare the radio power with the jet power, we find a hint of positive correlation. On the other hand, no correlation was found between the radio power and the luminosity of the X-ray atmospheres, the mass of the supermassive black hole, the cooling time or the entropy of the hot gas, or the luminosity of the Hα+[NII] line emission.
- The central spectral indices show a large variety, with approximately 1/3 of the sources having relatively flat spectra, indicating the presence of fresh relativistic particles injected by the AGN, which could mean that the AGN has been switched on recently. The majority of our sources have steep spectra, indicating that the relativistic plasma has undergone significant aging in the nuclear regions of the host galaxies since the last major cycle of AGN activity.
- On the one hand, the analysis of FUV fluxes suggests that the observed radio emission at 1.5 GHz for 5 of 14 low-power early-type galaxies with point-like radio morphologies could be dominated by star formation. On the other hand, we also observe ghost cavities in 4 of those 5 galaxies, suggesting the interaction of radio lobes inflated by the AGN with the hot X-ray atmospheres and thus, the presence of radio-mechanical AGN feedback.
- Importantly, for four (potentially five) sources, we found an offset between the radio emission and the optical centre of the galaxy, which could indicate that the central supermassive black hole has acquired a significant velocity due to gravitational recoil following a merger.

Secondly, the results of new VLA radio observations of the peculiar giant elliptical galaxy IC 4296, obtained in the A and D configuration and combined with complementary X-ray and optical data are:

- The new high-resolution VLA data in A configuration reveal the bright central region of IC 4296 and two almost symmetrical knotty radio jets extending far beyond the host galaxy. With the VLA D configuration data, we confirm the presence of well-defined radio lobes first reported by Killeen et al. (1986b). The lobes, without significant hot spots, have large diameters of $\sim$160 kpc at radii $r \gtrsim$230 kpc and are undetected in the higher resolution A configuration VLA maps.
- The *XMM-Newton* data reveal the presence of an X-ray cavity associated with one of the large radio lobes indicating a remarkable total enthalpy $\sim 7 \times 10^{59}$ erg. For comparison, this enthalpy is 30 times larger than for NGC 4261, due to the 6 times larger size of the radio lobes.
- The observed radio morphology is consistent with 3D hydrodynamical simulations (e.g. Massaglia et al. 2016) of supersonically expanding jets/lobes, with bow shocks created at the boundary layer of the radio lobes interacting with the ambient ICM.

- The jets are bent likely due to the relative motion of the ICM with respect to IC 4296 and magneto-hydrodynamic instabilities, advecting the plasma in long narrow plumes. The relative motion of the galaxy with respect to the ICM is also supported by a possible X-ray tail seen in the *Chandra* image.
- The powerful jets piercing through the hot galactic atmosphere do not appear to be depositing sufficient heat in the innermost gas to prevent it from cooling, with the bulk of their energy deposited well beyond 10 kpc from the nucleus. The atmosphere of the galaxy can therefore continue to cool rapidly, feeding the central supermassive black hole and powering the jets. This is supported by the steep entropy and cooling time profiles of the hot galactic atmosphere which continue to drop all the way to the nucleus, where a warm Hα+[NII] nebula and a cold molecular CO disk are clearly seen. As for a handful of other examples, such as NGC 4261, the cooling continues despite the powerful jet activity.

In the last section, we will envision some of the future prospects for finding the answers to these crucial questions about AGN feedback and the evolution and life cycle of early-type galaxies.

7.2 Future Prospects

Our research, which focused solely at high-resolution observations at gigahertz frequencies with VLA, offers many insights into the AGN activity of early-type galaxies, but information about the more diffuse and extended emission components could be missing. Novel insights into to the steep spectrum, low surface brightness emission from early-type galaxies will be provided by observations with the Low-Frequency Array (LOFAR), which is due to the high sensitivity and high resolution (up to subarcsecond scales) at lower frequencies of 30–240 MHz excellent for the study of multiple generations of AGN activity (Lonsdale 2005).
Especially interesting will be the studies of galaxies with point-like radio morphologies or Fanaroff-Riley Class 0 (FR 0) , which show signatures of small-scale interactions with hot X-ray gas in the form of cavities. The older radio plasma filling those cavities could be potentially revealed by observations with LOFAR.

Important breakthroughs in AGN science are also expected from the upcoming high-quality radio data from the Square Kilometer Array (SKA), which is a set of next generation telescopes that are combining wide-frequency coverage with unprecedented sensitivity and are scheduled for the end of 2021. Within phase one, SKA1 will be divided into SKA1-Low (50–350 MHz) and SKA1-Mid (0.35–15 GHz) components with the sensitivity surpassing current radio arrays like LOFAR or VLA. Therefore, its surveys will serve as a unique tool to distinguish between AGN and star forming emission or to detect the radio counterparts of most galaxies identified in current surveys. The wide frequency coverage will offer observations at different resolutions and therefore, the state, age, composition, magnetic field, particle populations, as well as plasma properties on all scales of the radio jets/lobes. In phase two, SKA2 will improve the sensitivity by another order of magnitude as well as the dynamic range, which will allow us to resolve, model, and study the weakest radio structures in the most powerful AGN (Agudo et al. 2015; Eckert et al. 2021).

Exciting follow-up studies also include imaging and spectral index maps of the innermost central parsec-scale regions at miliarcsecond scales with Very Long Baseline Interferometer (VLBI) or Very Long Baseline Array (VLBA), a European and American version of very long baseline interferometers. Our analysis can serve as a motivation for a more in-depth investigation of the nuclear activity of AGN at high resolutions. The observations from very long baseline arrays would offer a closer look at the central regions and their most recent state of activity or its multiple generations. Recent study done by Schellenberger et al. (2020a) using VLBA observations, confirms that the giant elliptical galaxy, NGC 5044, has an ongoing jet activity on parsec-scales and discusses the presence of multiple generations of X-ray cavities and associated radio emission.

Chapter 8

Overview of Publications and Author Contributions

8.1 Annex I: Paper I

***R*omana Grossová**, N. Werner, F. Massaro, K. Lakhchaura, Tomáš Plšek, K. Gabányi, K. Rajpurohit, R. E. A. Canning, P. Nulsen, Ewan O'Sullivan, Steven W. Allen, Andrew Fabian (Submitted) VLA Radio Study of a Sample of Nearby X-ray and Optically Bright Early-Type Galaxies. Astrophysical Journal Supplement.

RG reduced and analyzed the radio data, led the writing of the manuscript, and finalized the manuscript after comments from all authors under the supervision of the supervisors NW and FM.

8.2 Annex II: Paper II

***R*omana Grossová**, N. Werner, K. Rajpurohit, F. Mernier, K. Lakhchaura, K. Gabányi, R. E. A. Canning, P. Nulsen, F. Massaro, M. Sun, T. Connor, A. King, S. W. Allen, R. L. S. Frisbie, M. Donahue, A. C. Fabian (2019) Powerful AGN jets and unbalanced cooling in the hot atmosphere of IC 4296. Monthly Notices of the Royal Astronomical Society. 488:1917-1925.

RG reduced and analyzed the radio data, led the writing of the manuscript, and finalized the manuscript after comments from all authors under the supervision of the supervisors NW and FM.

8.3 Annex III: Paper III and Paper IV

R.L.S. Frisbie, M. Donahue, G.M. Voit, T. Connor, Y. Li, M. Sun, K. Lakhchaura, N. Werner and ***R*omana Grossová** (2020) Properties of the Hot Ambient Medium of Early-type Galaxies Hosting Powerful Radio Sources. Astrophysical Journal. 899:1-10.

RG provided radio data analysis and detailed comments on the manuscript.

Jimenez-Gallardo, A., F. Massaro, A. Capetti, M.A. Prieto, A. Paggi, R.D. Baldi, ***R*omana Grossová**, L. Osorero, A. Siemiginowka and S. Viada (2019) COMP2CAT: hunting compact double radio sources in the local Universe. Astronomy & Astrophysics. 627:1-21.

RG helped with the morphological classification of the sources for the catalog and provided comments on the manuscript.

References

Abell, G. O., Corwin, Harold G., J., & Olowin, R. P. 1989, ApJS, 70, 1, doi: 10.1086/191333

Agudo, I., Boettcher, M., Falcke, H. D. E., et al. 2015, in Advancing Astrophysics with the Square Kilometre Array (AASKA14), 93. https://arxiv.org/abs/1501.00420

Alamo-Martínez, K. A., West, M. J., Blakeslee, J. P., et al. 2012, A&A, 546, A15, doi: 10.1051/0004-6361/201219285

Algaba, J. C., Anczarski, J., Asada, K., et al. 2021, arXiv e-prints, arXiv:2104.06855. https://arxiv.org/abs/2104.06855

Allen, S. W., Dunn, R. J. H., Fabian, A. C., Taylor, G. B., & Reynolds, C. S. 2006, MNRAS, 372, 21, doi: 10.1111/j.1365-2966.2006.10778.x

Allen, S. W., Taylor, G. B., Nulsen, P. E. J., et al. 2001, MNRAS, 324, 842, doi: 10.1046/j.1365-8711.2001.04315.x

Andernach, H., Feretti, L., Giovannini, G., et al. 1992, A&AS, 93, 331

Arp, H. C. 1967, Astrophys. Lett., 1, 1

Ascasibar, Y., & Markevitch, M. 2006, ApJ, 650, 102, doi: 10.1086/506508

Babyk, I. V., McNamara, B. R., Nulsen, P. E. J., et al. 2018, ApJ, 862, 39, doi: 10.3847/1538-4357/aacce5

Babyk, I. V., McNamara, B. R., Tamhane, P. D., et al. 2019, ApJ, 887, 149, doi: 10.3847/1538-4357/ab54ce

Baldi, A., Forman, W., Jones, C., et al. 2009, ApJ, 707, 1034, doi: 10.1088/0004-637X/707/2/1034

Baldi, R. D., Capetti, A., & Giovannini, G. 2015, A&A, 576, A38, doi: 10.1051/0004-6361/201425426

Baldi, R. D., Capetti, A., & Massaro, F. 2018, A&A, 609, A1, doi: 10.1051/0004-6361/201731333

Balmaverde, B., & Capetti, A. 2006, A&A, 447, 97, doi: 10.1051/0004-6361:20054031

Barnes, J. E. 1989, in Bulletin of the American Astronomical Society, Vol. 21, 1170

Barrows, R. S., Comerford, J. M., Greene, J. E., & Pooley, D. 2016, ApJ, 829, 37, doi: 10.3847/0004-637X/829/1/37

Batcheldor, D., Robinson, A., Axon, D. J., Perlman, E. S., & Merritt, D. 2010, ApJ, 717, L6, doi: 10.1088/2041-8205/717/1/L6

Bell, E. F. 2003, ApJ, 586, 794, doi: 10.1086/367829

Bennett, C. L., Larson, D., Weiland, J. L., & Hinshaw, G. 2014, ApJ, 794, 135, doi: 10.1088/0004-637X/794/2/135

Best, P. N., Kauffmann, G., Heckman, T. M., et al. 2005, MNRAS, 362, 25, doi: 10.1111/j.1365-2966.2005.09192.x

Beuing, J., Dobereiner, S., Bohringer, H., & Bender, R. 1999, MNRAS, 302, 209, doi: 10.1046/j.1365-8711.1999.02108.x

Bharadwaj, V., Reiprich, T. H., Schellenberger, G., et al. 2014, A&A, 572, A46, doi: 10.1051/0004-6361/201322684

Bianchi, L., Herald, J., Efremova, B., et al. 2011, Ap&SS, 335, 161, doi: 10.1007/s10509-010-0581-x

Bílek, M., Cuillandre, J. C., Gwyn, S., et al. 2016, A&A, 588, A77, doi: 10.1051/0004-6361/201526608

Biller, B. A., Jones, C., Forman, W. R., Kraft, R., & Ensslin, T. 2004, ApJ, 613, 238, doi: 10.1086/423020

Binney, J., & Tabor, G. 1995, MNRAS, 276, 663, doi: 10.1093/mnras/276.2.663

Birkinshaw, M., & Davies, R. L. 1985, ApJ, 291, 32, doi: 10.1086/163038

Bîrzan, L., Rafferty, D. A., McNamara, B. R., Wise, M. W., & Nulsen, P. E. J. 2004, ApJ, 607, 800, doi: 10.1086/383519

Bîrzan, L., Rafferty, D. A., Nulsen, P. E. J., et al. 2012, MNRAS, 427, 3468, doi: 10.1111/j.1365-2966.2012.22083.x

Bîrzan, L., Rafferty, D. A., Brüggen, M., et al. 2020, MNRAS, 496, 2613, doi: 10.1093/mnras/staa1594

Blakeslee, J. P., Jordán, A., Mei, S., et al. 2009, ApJ, 694, 556, doi: 10.1088/0004-637X/694/1/556

Blandford, R., Meier, D., & Readhead, A. 2019, ARA&A, 57, 467, doi: 10.1146/annurev-astro-081817-051948

Blandford, R. D., & Znajek, R. L. 1977, MNRAS, 179, 433, doi: 10.1093/mnras/179.3.433

Blanton, E. L., Sarazin, C. L., McNamara, B. R., & Clarke, T. E. 2004, ApJ, 612, 817, doi: 10.1086/422677

Blecha, L., Civano, F., Elvis, M., & Loeb, A. 2013, MNRAS, 428, 1341, doi: 10.1093/mnras/sts114

Blecha, L., Cox, T. J., Loeb, A., & Hernquist, L. 2011, MNRAS, 412, 2154, doi: 10.1111/j.1365-2966.2010.18042.x

Blecha, L., Sijacki, D., Kelley, L. Z., et al. 2016, MNRAS, 456, 961, doi: 10.1093/mnras/stv2646

Boizelle, B. D., Barth, A. J., Darling, J., et al. 2017, ApJ, 845, 170, doi: 10.3847/1538-4357/aa8266

Boizelle, B. D., Walsh, J. L., Barth, A. J., et al. 2021, ApJ, 908, 19, doi: 10.3847/1538-4357/abd24d

Borne, K., & Colina, L. 1996, in Roentgenstrahlung from the Universe, ed. H. U. Zimmermann, J. Trümper, & H. Yorke, 427–428

Bower, G. A., Heckman, T. M., Wilson, A. S., & Richstone, D. O. 1997, ApJ, 483, L33, doi: 10.1086/310723

Braine, J., & Dupraz, C. 1994, A&A, 283, 407

Bridle, A. H., Davis, M. M., Fomalont, E. B., Willis, A. G., & Strom, R. G. 1979, ApJ, 228, L9, doi: 10.1086/182892

Briggs, D. S. 1995, 27, 1444

Brighenti, F., & Mathews, W. G. 2006, ApJ, 643, 120, doi: 10.1086/502645

Brown, M. J. I., Jannuzi, B. T., Floyd, D. J. E., & Mould, J. R. 2011, ApJ, 731, L41, doi: 10.1088/2041-8205/731/2/L41

Brüggen, M., & Kaiser, C. R. 2002, Nature, 418, 301
Buote, D. A., & Barth, A. J. 2018, ApJ, 854, 143, doi: 10.3847/1538-4357/aaa971
Burke-Spolaor, S., Gültekin, K., Postman, M., et al. 2017, ApJ, 849, 59, doi: 10.3847/1538-4357/aa9064
Burns, J. O. 1990, AJ, 99, 14, doi: 10.1086/115307
—. 1998, Science, 280, 400, doi: 10.1126/science.280.5362.400
Campanelli, M., Lousto, C., Zlochower, Y., & Merritt, D. 2007, ApJ, 659, L5, doi: 10.1086/516712
Caon, N., Macchetto, D., & Pastoriza, M. 2000, ApJS, 127, 39, doi: 10.1086/313315
Capetti, A., Celotti, A., Chiaberge, M., et al. 2002, A&A, 383, 104, doi: 10.1051/0004-6361:20011714
Capetti, A., de Ruiter, H. R., Fanti, R., et al. 2000, A&A, 362, 871. https://arxiv.org/abs/astro-ph/0009056
Capetti, A., Massaro, F., & Baldi, R. D. 2017a, A&A, 598, A49, doi: 10.1051/0004-6361/201629287
—. 2017b, A&A, 601, A81, doi: 10.1051/0004-6361/201630247
Cappellari, M., Emsellem, E., Krajnović, D., et al. 2011, MNRAS, 416, 1680, doi: 10.1111/j.1365-2966.2011.18600.x
Carilli, C. L., & Barthel, P. D. 1996, A&A Rev., 7, 1, doi: 10.1007/s001590050001
Carroll, B. W., & Ostlie, D. A. 2006, An introduction to modern astrophysics and cosmology
Cash, W. 1979, ApJ, 228, 939, doi: 10.1086/156922
Cattaneo, A., Faber, S. M., Binney, J., et al. 2009, Nature, 460, 213, doi: 10.1038/nature08135
Cavaliere, A., & Fusco-Femiano, R. 1976, A&A, 500, 95
Chen, R., Peng, B., Strom, R. G., & Wei, J. 2012, MNRAS, 420, 2715, doi: 10.1111/j.1365-2966.2011.20245.x
Chiaberge, M., Ely, J. C., Meyer, E. T., et al. 2017, A&A, 600, A57, doi: 10.1051/0004-6361/201629522
Churazov, E., Brüggen, M., Kaiser, C. R., Böhringer, H., & Forman, W. 2001, ApJ, 554, 261, doi: 10.1086/321357
Churazov, E., Forman, W., Jones, C., & Böhringer, H. 2000, A&A, 356, 788
Churazov, E., Sunyaev, R., Forman, W., & Böhringer, H. 2002, MNRAS, 332, 729, doi: 10.1046/j.1365-8711.2002.05332.x
Clarke, T. E., Blanton, E. L., Sarazin, C. L., et al. 2009, ApJ, 697, 1481, doi: 10.1088/0004-637X/697/2/1481
Colbert, J. W., Mulchaey, J. S., & Zabludoff, A. I. 2001, AJ, 121, 808, doi: 10.1086/318758
Combes, F., Young, L. M., & Bureau, M. 2007, MNRAS, 377, 1795, doi: 10.1111/j.1365-2966.2007.11759.x
Condon, J. J. 1992, ARA&A, 30, 575, doi: 10.1146/annurev.aa.30.090192.003043
Condon, J. J., & Broderick, J. J. 1988, AJ, 96, 30, doi: 10.1086/114788
Condon, J. J., Cotton, W. D., Greisen, E. W., et al. 1998, AJ, 115, 1693, doi: 10.1086/300337
Condon, J. J., Darling, J., Kovalev, Y. Y., & Petrov, L. 2017, ApJ, 834, 184, doi: 10.3847/1538-4357/834/2/184
Condon, J. J., & Ransom, S. M. 2016, Essential Radio Astronomy
Conroy, C., Graves, G. J., & van Dokkum, P. G. 2014, ApJ, 780, 33, doi: 10.1088/0004-637X/780/1/33
Cornwell, T. J. 2009, A&A, 500, 65, doi: 10.1051/0004-6361/200912148
Correa, C. A., Schaye, J., Wyithe, J. S. B., et al. 2018, MNRAS, 473, 538, doi: 10.1093/mnras/stx2332
Croston, J. H., Hardcastle, M. J., Birkinshaw, M., & Worrall, D. M. 2003, MNRAS, 346, 1041, doi: 10.1111/j.1365-2966.2003.07165.x
Croston, J. H., Hardcastle, M. J., Birkinshaw, M., Worrall, D. M., & Laing, R. A. 2008, MNRAS, 386, 1709, doi: 10.1111/j.1365-2966.2008.13162.x
Croton, D. J., Springel, V., White, S. D. M., et al. 2006, MNRAS, 365, 11, doi: 10.1111/j.1365-2966.2005.09675.x
Daddi, E., Renzini, A., Pirzkal, N., et al. 2005, ApJ, 626, 680, doi: 10.1086/430104
Dalla Bontà, E., Ferrarese, L., Corsini, E. M., et al. 2009, ApJ, 690, 537, doi: 10.1088/0004-637X/690/1/537
David, L. P., Vrtilek, J., O'Sullivan, E., et al. 2017, ApJ, 842, 84, doi: 10.3847/1538-4357/aa756c
David, L. P., O'Sullivan, E., Jones, C., et al. 2011, ApJ, 728, 162, doi: 10.1088/0004-637X/728/2/162
David, L. P., Lim, J., Forman, W., et al. 2014a, ApJ, 792, 94, doi: 10.1088/0004-637X/792/2/94
—. 2014b, ApJ, 792, 94, doi: 10.1088/0004-637X/792/2/94
Davis, D. S., Mushotzky, R. F., Mulchaey, J. S., et al. 1995, ApJ, 444, 582, doi: 10.1086/175632
Davis, T. A., Greene, J., Ma, C.-P., et al. 2016, MNRAS, 455, 214, doi: 10.1093/mnras/stv2313
de Menezes, R., Nemmen, R., Finke, J. D., Almeida, I., & Rani, B. 2020, MNRAS, 492, 4120, doi: 10.1093/mnras/staa083
De Villiers, J.-P., Hawley, J. F., & Krolik, J. H. 2003, ApJ, 599, 1238, doi: 10.1086/379509
Devereux, N., Eracleous, M., Hriljac, P., & Shearer, A. 2010, arXiv e-prints, arXiv:1008.2339. https://arxiv.org/abs/1008.2339
Disney, M. J., & Wall, J. V. 1977, MNRAS, 179, 235, doi: 10.1093/mnras/179.2.235
Donahue, M., Bruch, S., Wang, E., et al. 2010, ApJ, 715, 881, doi: 10.1088/0004-637X/715/2/881
Donato, D., Sambruna, R. M., & Gliozzi, M. 2004, ApJ, 617, 915, doi: 10.1086/425575
Dong, R., Rasmussen, J., & Mulchaey, J. S. 2010, ApJ, 712, 883, doi: 10.1088/0004-637X/712/2/883
Dressel, L. L., & Condon, J. J. 1978, ApJS, 36, 53, doi: 10.1086/190491
Duah Asabere, B., Horellou, C., Winkler, H., Jarrett, T., & Leeuw, L. 2014, arXiv e-prints, arXiv:1409.2474. https://arxiv.org/abs/1409.2474
Dunn, R. J. H., Allen, S. W., Taylor, G. B., et al. 2010, MNRAS, 404, 180, doi: 10.1111/j.1365-2966.2010.16314.x
Dunn, R. J. H., & Fabian, A. C. 2006, MNRAS, 373, 959, doi: 10.1111/j.1365-2966.2006.11080.x
Dunn, R. J. H., Fabian, A. C., & Taylor, G. B. 2005, MNRAS, 364, 1343, doi: 10.1111/j.1365-2966.2005.09673.x
Eckert, D., Gaspari, M., Gastaldello, F., Le Brun, A. M. C., & O'Sullivan, E. 2021, Universe, 7, doi: 10.3390/universe7050142
Ehlert, S., Werner, N., Simionescu, A., et al. 2013, MNRAS, 430, 2401, doi: 10.1093/mnras/stt060
Ekers, R. D., & Kotanyi, C. G. 1978, A&A, 67, 47

Ellison, D. C., Reynolds, S. P., Borkowski, K., et al. 1994, PASP, 106, 780, doi: 10.1086/133442
Escala, A., Larson, R. B., Coppi, P. S., & Mardones, D. 2005, ApJ, 630, 152, doi: 10.1086/431747
Ettori, S., & Fabian, A. C. 2000, MNRAS, 317, L57, doi: 10.1046/j.1365-8711.2000.03899.x
Event Horizon Telescope Collaboration, Akiyama, K., Algaba, J. C., et al. 2021, ApJ, 910, L13, doi: 10.3847/2041-8213/abe4de
Fabbiano, G., Kim, D. W., & Brickhouse, N. 2002, in American Astronomical Society Meeting Abstracts, Vol. 201, American Astronomical Society Meeting Abstracts, 14.04
Fabian, A. C. 1994, ARA&A, 32, 277, doi: 10.1146/annurev.aa.32.090194.001425
—. 2012, ARA&A, 50, 455, doi: 10.1146/annurev-astro-081811-125521
Fabian, A. C., & Nulsen, P. E. J. 1977, MNRAS, 180, 479, doi: 10.1093/mnras/180.3.479
Fabian, A. C., Sanders, J. S., Allen, S. W., et al. 2003, MNRAS, 344, L43, doi: 10.1046/j.1365-8711.2003.06902.x
Fabian, A. C., Walker, S. A., Russell, H. R., et al. 2016, MNRAS, 461, 922, doi: 10.1093/mnras/stw1350
Fanaroff, B. L., & Riley, J. M. 1974, MNRAS, 167, 31P, doi: 10.1093/mnras/167.1.31P
Feretti, L., Perley, R., Giovannini, G., & Andernach, H. 1999, A&A, 341, 29. https://arxiv.org/abs/astro-ph/9810305
Ferrarese, L., Ford, H. C., & Jaffe, W. 1996, ApJ, 470, 444, doi: 10.1086/177876
Ferrari, F., Pastoriza, M. G., Macchetto, F., & Caon, N. 1999, A&AS, 136, 269, doi: 10.1051/aas:1999465
Filho, M. E., Barthel, P. D., & Ho, L. C. 2002, ApJS, 142, 223, doi: 10.1086/341786
Filho, M. E., Fraternali, F., Markoff, S., et al. 2004, A&A, 418, 429, doi: 10.1051/0004-6361:20034486
Finoguenov, A., Arnaud, M., & David, L. P. 2001, ApJ, 555, 191, doi: 10.1086/321457
Fomalont, E. B., Ebneter, K. A., van Breugel, W. J. M., & Ekers, R. D. 1989, ApJ, 346, L17, doi: 10.1086/185568
Forbes, D. A., Ponman, T., Pearce, F., et al. 2006, PASA, 23, 38, doi: 10.1071/AS06002
Forman, W., Schwarz, J., Jones, C., Liller, W., & Fabian, A. C. 1979, ApJ, 234, L27, doi: 10.1086/183103
Forman, W., Nulsen, P., Heinz, S., et al. 2005, ApJ, 635, 894, doi: 10.1086/429746
Forman, W., Jones, C., Churazov, E., et al. 2007, ApJ, 665, 1057, doi: 10.1086/519480
Franceschini, A., Vercellone, S., & Fabian, A. C. 1998, MNRAS, 297, 817, doi: 10.1046/j.1365-8711.1998.01534.x
Freeman, P., Doe, S., & Siemiginowska, A. 2001, in Society of Photo-Optical Instrumentation Engineers (SPIE) Conference Series, Vol. 4477, Astronomical Data Analysis, ed. J.-L. Starck & F. D. Murtagh, 76–87, doi: 10.1117/12.447161
Frisbie, R. L. S., Donahue, M., Voit, G. M., et al. 2020, ApJ, 899, 159, doi: 10.3847/1538-4357/aba8a8
Fruscione, A., McDowell, J. C., Allen, G. E., et al. 2006, in Society of Photo-Optical Instrumentation Engineers (SPIE) Conference Series, Vol. 6270, Society of Photo-Optical Instrumentation Engineers (SPIE) Conference Series, ed. D. R. Silva & R. E. Doxsey, 62701V, doi: 10.1117/12.671760
Garcia, A. M. 1993, A&AS, 100, 47
Gaspari, M., Brighenti, F., D'Ercole, A., & Melioli, C. 2011, MNRAS, 415, 1549, doi: 10.1111/j.1365-2966.2011.18806.x
Gaspari, M., Ruszkowski, M., & Oh, S. P. 2013, MNRAS, 432, 3401, doi: 10.1093/mnras/stt692
Gaspari, M., Ruszkowski, M., & Sharma, P. 2012a, ApJ, 746, 94, doi: 10.1088/0004-637X/746/1/94
—. 2012b, ApJ, 746, 94, doi: 10.1088/0004-637X/746/1/94
Gaspari, M., Tombesi, F., & Cappi, M. 2020, Nature Astronomy, 4, 10, doi: 10.1038/s41550-019-0970-1
Gaspari, M., McDonald, M., Hamer, S. L., et al. 2018, ApJ, 854, 167, doi: 10.3847/1538-4357/aaaa1b
Gastaldello, F., Buote, D. A., Humphrey, P. J., et al. 2007, ApJ, 669, 158, doi: 10.1086/521519
Gastaldello, F., Buote, D. A., Temi, P., et al. 2009, ApJ, 693, 43, doi: 10.1088/0004-637X/693/1/43
Gastaldello, F., Di Gesu, L., Ghizzardi, S., et al. 2013, ApJ, 770, 56, doi: 10.1088/0004-637X/770/1/56
Giacintucci, S., O'Sullivan, E., Vrtilek, J., et al. 2011, ApJ, 732, 95, doi: 10.1088/0004-637X/732/2/95
Giacintucci, S., O'Sullivan, E., Clarke, T. E., et al. 2012, ApJ, 755, 172, doi: 10.1088/0004-637X/755/2/172
Gitti, M., O'Sullivan, E., Giacintucci, S., et al. 2010, ApJ, 714, 758, doi: 10.1088/0004-637X/714/1/758
Gizani, N. A. B., Cohen, A., & Kassim, N. E. 2005, MNRAS, 358, 1061, doi: 10.1111/j.1365-2966.2005.08849.x
Gizani, N. A. B., & Leahy, J. P. 1999, New A Rev., 43, 639, doi: 10.1016/S1387-6473(99)00069-X
—. 2003, MNRAS, 342, 399, doi: 10.1046/j.1365-8711.2003.06469.x
Gliozzi, M., Sambruna, R. M., & Brandt, W. N. 2003, A&A, 408, 949, doi: 10.1051/0004-6361:20031050
González-Martín, O., Masegosa, J., Márquez, I., Guainazzi, M., & Jiménez-Bailón, E. 2009, A&A, 506, 1107, doi: 10.1051/0004-6361/200912288
González-Martín, O., Masegosa, J., Márquez, I., Guerrero, M. A., & Dultzin-Hacyan, D. 2006, A&A, 460, 45, doi: 10.1051/0004-6361:20054756
Goss, W. M., McAdam, W. B., Wellington, K. J., & Ekers, R. D. 1987, MNRAS, 226, 979, doi: 10.1093/mnras/226.4.979
Goulding, A. D., & Alexander, D. M. 2009, MNRAS, 398, 1165, doi: 10.1111/j.1365-2966.2009.15194.x
Goullaud, C. F., Jensen, J. B., Blakeslee, J. P., et al. 2018, ApJ, 856, 11, doi: 10.3847/1538-4357/aab1f3
Governato, F., Bhatia, R., & Chincarini, G. 1991, ApJ, 371, L15, doi: 10.1086/185991
Grillmair, C. J., Forbes, D. A., Brodie, J. P., & Elson, R. A. W. 1999, AJ, 117, 167, doi: 10.1086/300661
Grossová, R., Werner, N., Rajpurohit, K., et al. 2019, MNRAS, 488, 1917, doi: 10.1093/mnras/stz1728
Gültekin, K., Burke-Spolaor, S., Lauer, T. R., et al. 2021, ApJ, 906, 48, doi: 10.3847/1538-4357/abc483
Haardt, F., & Maraschi, L. 1991, ApJ, 380, L51, doi: 10.1086/186171
Hardcastle, M. J., Worrall, D. M., & Birkinshaw, M. 1998, MNRAS, 296, 1098, doi: 10.1046/j.1365-8711.1998.01535.x
Harrison, C. M. 2017, Nature Astronomy, 1, 0165, doi: 10.1038/s41550-017-0165

Hickson, P. 1982, ApJ, 255, 382, doi: 10.1086/159838
Hlavacek-Larrondo, J., McDonald, M., Benson, B. A., et al. 2015, ApJ, 805, 35, doi: 10.1088/0004-637X/805/1/35
Ho, L. C., Filippenko, A. V., & Sargent, W. L. W. 1997, ApJ, 487, 579, doi: 10.1086/304642
Hogan, M. T. 2014, PhD thesis, Durham University
Hogan, M. T., McNamara, B. R., Pulido, F. A., et al. 2017, ApJ, 851, 66, doi: 10.3847/1538-4357/aa9af3
Högbom, J. A. 1974, A&AS, 15, 417
Högbom, J. A. 2003, in Astronomical Society of the Pacific Conference Series, Vol. 300, Radio Astronomy at the Fringe, ed. J. A. Zensus, M. H. Cohen, & E. Ros, 17
Horellou, C., Black, J. H., van Gorkom, J. H., et al. 2001, A&A, 376, 837, doi: 10.1051/0004-6361:20011039
Hubble, E. 1926, Contributions from the Mount Wilson Observatory / Carnegie Institution of Washington, 324, 1
Huchtmeier, W. K., Bregman, J. N., Hogg, D. E., & Roberts, M. S. 1988, A&A, 198, L17
Hurley-Walker, N., Callingham, J. R., Hancock, P. J., et al. 2016, VizieR Online Data Catalog, VIII/100
—. 2017, MNRAS, 464, 1146, doi: 10.1093/mnras/stw2337
Imanishi, M., Nakanishi, K., Izumi, T., & Wada, K. 2018, ApJ, 853, L25, doi: 10.3847/2041-8213/aaa8df
Intema, H. T., Jagannathan, P., Mooley, K. P., & Frail, D. A. 2017, A&A, 598, A78, doi: 10.1051/0004-6361/201628536
Jaffe, W., Ford, H. C., Ferrarese, L., van den Bosch, F., & O'Connell, R. W. 1993, Nature, 364, 213, doi: 10.1038/364213a0
Jaffe, W., & McNamara, B. R. 1994, ApJ, 434, 110, doi: 10.1086/174708
Jetha, N. N., Hardcastle, M. J., Babul, A., et al. 2008, MNRAS, 384, 1344, doi: 10.1111/j.1365-2966.2007.12829.x
Jimenez-Gallardo, A., Massaro, F., Capetti, A., et al. 2019, A&A, 627, A108, doi: 10.1051/0004-6361/201935104
Jones, C., Forman, W., Vikhlinin, A., et al. 2002, ApJ, 567, L115, doi: 10.1086/340114
Joye, W. A., & Mandel, E. 2003, in Astronomical Society of the Pacific Conference Series, Vol. 295, Astronomical Data Analysis Software and Systems XII, ed. H. E. Payne, R. I. Jedrzejewski, & R. N. Hook, 489
Kaastra, J. S., Ferrigno, C., Tamura, T., et al. 2001, A&A, 365, L99
Kaastra, J. S., Mewe, R., & Nieuwenhuijzen, H. 1996, in UV and X-ray Spectroscopy of Astrophysical and Laboratory Plasmas p.411, K. Yamashita and T. Watanabe. Tokyo : Universal Academy Press
Kaastra, J. S., Raassen, A. J. J., de Plaa, J., & Gu, L. 2017, SPEX X-ray spectral fitting package, doi: 10.5281/zenodo.2272992
Kaiser, C. R., & Binney, J. 2003, MNRAS, 338, 837, doi: 10.1046/j.1365-8711.2003.06131.x
Kelly, B. C. 2007, ApJ, 665, 1489, doi: 10.1086/519947
Kemp, S. N. 1994, A&A, 282, 425
Kenney, J. D. P., Tal, T., Crowl, H. H., Feldmeier, J., & Jacoby, G. H. 2008, ApJ, 687, L69, doi: 10.1086/593300
Killeen, N. E. B., & Bicknell, G. V. 1988, ApJ, 324, 198, doi: 10.1086/165890
Killeen, N. E. B., Bicknell, G. V., & Carter, D. 1986a, ApJ, 309, 45, doi: 10.1086/164576
Killeen, N. E. B., Bicknell, G. V., & Ekers, R. D. 1986b, ApJ, 302, 306, doi: 10.1086/163992
Kim, D.-W., & Fabbiano, G. 1995, ApJ, 441, 182, doi: 10.1086/175348
Kim, D.-W., Anderson, C., Burke, D., et al. 2018, ApJ, 853, 129, doi: 10.3847/1538-4357/aaa43a
—. 2019, ApJS, 241, 36, doi: 10.3847/1538-4365/ab0ca4
Kim, D.-W., Traynor, L., Paggi, A., et al. 2020, MNRAS, 492, 2095, doi: 10.1093/mnras/stz3530
Klein, U., Mack, K. H., Gregorini, L., & Vigotti, M. 2003, A&A, 406, 579, doi: 10.1051/0004-6361:20030825
Klein, U., Mack, K. H., Strom, R., Wielebinski, R., & Achatz, U. 1994, A&A, 283, 729
Kolokythas, K., O'Sullivan, E., Giacintucci, S., et al. 2015, MNRAS, 450, 1732, doi: 10.1093/mnras/stv665
Kolokythas, K., O'Sullivan, E., Raychaudhury, S., et al. 2018, MNRAS, 481, 1550, doi: 10.1093/mnras/sty2030
Kolokythas, K., O'Sullivan, E., Giacintucci, S., et al. 2020, MNRAS, 496, 1471, doi: 10.1093/mnras/staa1506
Komissarov, S. S. 2004, MNRAS, 350, 427, doi: 10.1111/j.1365-2966.2004.07598.x
Komossa, S. 2012, Advances in Astronomy, 2012, 364973, doi: 10.1155/2012/364973
Kormendy, J., Fisher, D. B., Cornell, M. E., & Bender, R. 2009, ApJS, 182, 216, doi: 10.1088/0067-0049/182/1/216
Kormendy, J., & Ho, L. C. 2013, ARA&A, 51, 511, doi: 10.1146/annurev-astro-082708-101811
Kraft, R. P., Forman, W. R., Churazov, E., et al. 2004, ApJ, 601, 221, doi: 10.1086/380427
Kraft, R. P., Forman, W. R., Jones, C., et al. 2011, ApJ, 727, 41, doi: 10.1088/0004-637X/727/1/41
Kraft, R. P., Roediger, E., Machacek, M., et al. 2017, ApJ, 848, 27, doi: 10.3847/1538-4357/aa8a6e
Krajnović, D., & Jaffe, W. 2002, A&A, 390, 423, doi: 10.1051/0004-6361:20020801
Krolik, J. H., & Hawley, J. F. 2010, General Relativistic MHD Jets, ed. T. Belloni, Vol. 794, 265, doi: 10.1007/978-3-540-76937-8_10
Kulkarni, S., Sahu, D. K., Chaware, L., Chakradhari, N. K., & Pandey, S. K. 2014, New A, 30, 51, doi: 10.1016/j.newast.2014.01.003
Kunz, M. W., Bogdanović, T., Reynolds, C. S., & Stone, J. M. 2012, ApJ, 754, 122, doi: 10.1088/0004-637X/754/2/122
Lacki, B. C., & Thompson, T. A. 2013, ApJ, 762, 29, doi: 10.1088/0004-637X/762/1/29
Laing, R. A., & Bridle, A. H. 1987, MNRAS, 228, 557, doi: 10.1093/mnras/228.3.557
Laing, R. A., Bridle, A. H., Parma, P., et al. 2008, MNRAS, 386, 657, doi: 10.1111/j.1365-2966.2008.13091.x
Laing, R. A., Canvin, J. R., Cotton, W. D., & Bridle, A. H. 2006, MNRAS, 368, 48, doi: 10.1111/j.1365-2966.2006.10099.x
Lakhchaura, K., Truong, N., & Werner, N. 2019, MNRAS, 488, L134, doi: 10.1093/mnrasl/slz114
Lakhchaura, K., Werner, N., Sun, M., et al. 2018, MNRAS, 481, 4472, doi: 10.1093/mnras/sty2565
Lal, D. V., Kraft, R. P., Randall, S. W., et al. 2013, ApJ, 764, 83, doi: 10.1088/0004-637X/764/1/83
Lanz, L., Jones, C., Forman, W. R., et al. 2010, ApJ, 721, 1702, doi: 10.1088/0004-637X/721/2/1702

Laor, A. 1990, MNRAS, 246, 369
Lara, L., Cotton, W. D., Feretti, L., et al. 2001, A&A, 370, 409, doi: 10.1051/0004-6361:20010254
Lauer, T. R., Faber, S. M., Gebhardt, K., et al. 2005, AJ, 129, 2138, doi: 10.1086/429565
Lauer, T. R., Faber, S. M., Richstone, D., et al. 2007, ApJ, 662, 808, doi: 10.1086/518223
Leahy, J. P. 1993, DRAGNs, ed. H.-J. Röser & K. Meisenheimer, Vol. 421, 1, doi: 10.1007/3-540-57164-7_74
Leahy, J. P., Bridle, A. H., & Strom, R. G. 2013, An Atlas of DRAGNs, An Atlas of DRAGNs
Lena, D., Robinson, A., Marconi, A., et al. 2014, ApJ, 795, 146, doi: 10.1088/0004-637X/795/2/146
Leon, S., Lim, J., Combes, F., & van-Trung, D. 2001, in QSO Hosts and Their Environments, ed. I. Márquez, J. Masegosa, A. del Olmo, L. Lara, E. García, & J. Molina, 185. https://arxiv.org/abs/astro-ph/0107498
Lidman, C., Suherli, J., Muzzin, A., et al. 2012, MNRAS, 427, 550, doi: 10.1111/j.1365-2966.2012.21984.x
Lindner, R. R., Baker, A. J., Hughes, J. P., et al. 2014, ApJ, 786, 49, doi: 10.1088/0004-637X/786/1/49
Liu, H., Pinto, C., Fabian, A. C., Russell, H. R., & Sanders, J. S. 2019, MNRAS, 456, doi: 10.1093/mnras/stz456
Liu, Y., Jiang, D. R., & Gu, M. F. 2006, ApJ, 637, 669, doi: 10.1086/498639
Liuzzo, E., Buttiglione, S., Giovannini, G., et al. 2013, A&A, 550, A76, doi: 10.1051/0004-6361/201220012
Liuzzo, E., Giovannini, G., Giroletti, M., & Taylor, G. B. 2010, A&A, 516, A1, doi: 10.1051/0004-6361/200913888
Lodders, K., Palme, H., & Gail, H. P. 2009, Landolt Börnstein, 4B, 712, doi: 10.1007/978-3-540-88055-4_34
Longair, M. S. 2011, High Energy Astrophysics
Lonsdale, C. J. 2005, in Astronomical Society of the Pacific Conference Series, Vol. 340, Future Directions in High Resolution Astronomy, ed. J. Romney & M. Reid, 547
López-Gonzaga, N., Burtscher, L., Tristram, K. R. W., Meisenheimer, K., & Schartmann, M. 2016, A&A, 591, A47, doi: 10.1051/0004-6361/201527590
López-Navas, E., & Prieto, M. A. 2018, MNRAS, 480, 4099, doi: 10.1093/mnras/sty2148
Ly, C., Walker, R. C., & Wrobel, J. M. 2004, AJ, 127, 119, doi: 10.1086/379855
Maccagni, F. M., Serra, P., Murgia, M., et al. 2021, IAU Symposium, 359, 141, doi: 10.1017/S1743921320004287
Maccagni, F. M., Murgia, M., Serra, P., et al. 2020, A&A, 634, A9, doi: 10.1051/0004-6361/201936867
Macchetto, F., Pastoriza, M., Caon, N., et al. 1996, A&AS, 120, 463
Machacek, M., Dosaj, A., Forman, W., et al. 2005, ApJ, 621, 663, doi: 10.1086/427548
Machacek, M., Nulsen, P. E. J., Jones, C., & Forman, W. R. 2006, ApJ, 648, 947, doi: 10.1086/505963
Machacek, M. E., Jerius, D., Kraft, R., et al. 2011, ApJ, 743, 15, doi: 10.1088/0004-637X/743/1/15
Mack, K. H., Klein, U., O'Dea, C. P., & Willis, A. G. 1997, A&AS, 123, 423, doi: 10.1051/aas:1997166
Makarov, D., Prugniel, P., Terekhova, N., Courtois, H., & Vauglin, I. 2014, A&A, 570, A13, doi: 10.1051/0004-6361/201423496
Maraston, C., Greggio, L., Renzini, A., et al. 2003, A&A, 400, 823, doi: 10.1051/0004-6361:20021723
Markevitch, M., & Vikhlinin, A. 2007, Phys. Rep., 443, 1, doi: 10.1016/j.physrep.2007.01.001
Marshall, H. L., Miller, B. P., Davis, D. S., et al. 2002, ApJ, 564, 683, doi: 10.1086/324396
Massaglia, S., Bodo, G., Rossi, P., Capetti, S., & Mignone, A. 2016, A&A, 596, A12, doi: 10.1051/0004-6361/201629375
—. 2019, A&A, 621, A132, doi: 10.1051/0004-6361/201834512
Mathews, W. G., Temi, P., Brighenti, F., & Amblard, A. 2013, ApJ, 768, 28, doi: 10.1088/0004-637X/768/1/28
McCourt, M., Sharma, P., Quataert, E., & Parrish, I. J. 2012, MNRAS, 419, 3319, doi: 10.1111/j.1365-2966.2011.19972.x
McDonald, M., Gaspari, M., McNamara, B. R., & Tremblay, G. R. 2018, ApJ, 858, 45, doi: 10.3847/1538-4357/aabace
McKinney, J. C., & Gammie, C. F. 2004, ApJ, 611, 977, doi: 10.1086/422244
McKinney, J. C., Tchekhovskoy, A., Sadowski, A., & Narayan, R. 2014, MNRAS, 441, 3177, doi: 10.1093/mnras/stu762
McMullin, J. P., Waters, B., Schiebel, D., Young, W., & Golap, K. 2007, 376, 127
McNamara, B. R. 1995, ApJ, 443, 77, doi: 10.1086/175504
McNamara, B. R., & Nulsen, P. E. J. 2007, ARA&A, 45, 117, doi: 10.1146/annurev.astro.45.051806.110625
—. 2012, New Journal of Physics, 14, 055023, doi: 10.1088/1367-2630/14/5/055023
McNamara, B. R., Nulsen, P. E. J., Wise, M. W., et al. 2005, Nature, 433, 45, doi: 10.1038/nature03202
McNamara, B. R., Russell, H. R., Nulsen, P. E. J., et al. 2016, ApJ, 830, 79, doi: 10.3847/0004-637X/830/2/79
Mei, S., Silva, D., & Quinn, P. J. 2000, A&A, 361, 68
Mernier, F., de Plaa, J., Lovisari, L., et al. 2015, A&A, 575, A37, doi: 10.1051/0004-6361/201425282
Mieske, S., Hilker, M., & Infante, L. 2005, A&A, 438, 103, doi: 10.1051/0004-6361:20041583
Miller, B., Ahumada, T., Puzia, T., et al. 2017, Galaxies, 5, 29, doi: 10.3390/galaxies5030029
Million, E. T., Allen, S. W., Werner, N., & Taylor, G. B. 2010, MNRAS, 405, 1624, doi: 10.1111/j.1365-2966.2010.16596.x
Milone, A., Barbuy, B., & Schiavon, R. P. 2000, AJ, 120, 131, doi: 10.1086/301434
Missaglia, V., Massaro, F., Capetti, A., et al. 2019, A&A, 626, A8, doi: 10.1051/0004-6361/201935058
Mittal, R., Hudson, D. S., Reiprich, T. H., & Clarke, T. 2009, A&A, 501, 835, doi: 10.1051/0004-6361/200810836
Mittal, R., O'Dea, C. P., Ferland, G., et al. 2011, MNRAS, 418, 2386, doi: 10.1111/j.1365-2966.2011.19634.x
Morganti, R., Peck, A. B., Oosterloo, T. A., et al. 2009, A&A, 505, 559, doi: 10.1051/0004-6361/200912605
Morita, U., Ishisaki, Y., Yamasaki, N. Y., et al. 2006, PASJ, 58, 719, doi: 10.1093/pasj/58.4.719
Morokuma-Matsui, K., Serra, P., Maccagni, F. M., et al. 2019, PASJ, 71, 85, doi: 10.1093/pasj/psz067
Mulchaey, J. S., & Zabludoff, A. I. 1999, ApJ, 514, 133, doi: 10.1086/306952
Murgia, M., Parma, P., Mack, K. H., et al. 2011, A&A, 526, A148, doi: 10.1051/0004-6361/201015302

Narayan, R., Igumenshchev, I. V., & Abramowicz, M. A. 2003, PASJ, 55, L69, doi: 10.1093/pasj/55.6.L69
Narayan, R., SÄ dowski, A., Penna, R. F., & Kulkarni, A. K. 2012, MNRAS, 426, 3241, doi: 10.1111/j.1365-2966.2012.22002.x
Narayan, R., & Yi, I. 1994, ApJ, 428, L13, doi: 10.1086/187381
North, E. V., Davis, T. A., Bureau, M., et al. 2021, MNRAS, 503, 5179, doi: 10.1093/mnras/stab793
Nulsen, P., Jones, C., Forman, W., et al. 2009, in American Institute of Physics Conference Series, Vol. 1201, The Monster's Fiery Breath: Feedback in Galaxies, Groups, and Clusters, ed. S. Heinz & E. Wilcots, 198–201, doi: 10.1063/1.3293033
Nulsen, P. E. J. 1986, MNRAS, 221, 377
Nulsen, P. E. J., Stewart, G. C., Fabian, A. C., et al. 1982, MNRAS, 199, 1089
Ocaña Flaquer, B., Leon, S., Combes, F., & Lim, J. 2010, A&A, 518, A9, doi: 10.1051/0004-6361/200913392
O'Dea, C. P. 1998, PASP, 110, 493, doi: 10.1086/316162
O'Dea, C. P., & Owen, F. N. 1987, ApJ, 316, 95, doi: 10.1086/165182
O'Donoghue, A. A., Owen, F. N., & Eilek, J. A. 1990, ApJS, 72, 75, doi: 10.1086/191410
Offringa, A. R., van de Gronde, J. J., & Roerdink, J. B. T. M. 2012, A&A, 539, A95, doi: 10.1051/0004-6361/201118497
Olivares, V., Salome, P., Combes, F., et al. 2019, A&A, 631, A22, doi: 10.1051/0004-6361/201935350
Onodera, M., Carollo, C. M., Renzini, A., et al. 2015, ApJ, 808, 161, doi: 10.1088/0004-637X/808/2/161
O'Sullivan, E., Combes, F., Hamer, S., et al. 2015, A&A, 573, A111, doi: 10.1051/0004-6361/201424835
O'Sullivan, E., Forbes, D. A., & Ponman, T. J. 2001, MNRAS, 328, 461, doi: 10.1046/j.1365-8711.2001.04890.x
O'Sullivan, E., Sanderson, A. J. R., & Ponman, T. J. 2007, MNRAS, 380, 1409, doi: 10.1111/j.1365-2966.2007.12229.x
O'Sullivan, E., Vrtilek, J. M., Kempner, J. C., David, L. P., & Houck, J. C. 2005, MNRAS, 357, 1134, doi: 10.1111/j.1365-2966.2005.08749.x
O'Sullivan, E., Vrtilek, J. M., Read, A. M., David, L. P., & Ponman, T. J. 2003, MNRAS, 346, 525, doi: 10.1046/j.1365-2966.2003.07108.x
O'Sullivan, E., Worrall, D. M., Birkinshaw, M., et al. 2011a, MNRAS, 416, 2916, doi: 10.1111/j.1365-2966.2011.19239.x
—. 2011b, MNRAS, 1180, doi: 10.1111/j.1365-2966.2011.19239.x
O'Sullivan, E., Combes, F., Salomé, P., et al. 2018, A&A, 618, A126, doi: 10.1051/0004-6361/201833580
Owen, F. N., Eilek, J. A., & Kassim, N. E. 2000, ApJ, 543, 611, doi: 10.1086/317151
Owen, F. N., & Ledlow, M. J. 1994, Astronomical Society of the Pacific Conference Series, 54, 319
Owen, F. N., & Rudnick, L. 1976, ApJ, 205, L1, doi: 10.1086/182077
Paggi, A. 2014, in X-ray View of Galaxy Ecosystems, 28. https://arxiv.org/abs/1404.5315
Pahre, M. A., Ashby, M. L. N., Fazio, G. G., & Willner, S. P. 2004, ApJS, 154, 229, doi: 10.1086/423320
Panagoulia, E. K., Fabian, A. C., Sanders, J. S., & Hlavacek-Larrondo, J. 2014, MNRAS, 444, 1236, doi: 10.1093/mnras/stu1499
Paolillo, M., Fabbiano, G., Peres, G., & Kim, D. W. 2002, ApJ, 565, 883, doi: 10.1086/337919
—. 2003, ApJ, 586, 850, doi: 10.1086/367718
Parma, P., de Ruiter, H. R., Fanti, C., & Fanti, R. 1986, A&AS, 64, 135
Pellegrini, S., Ciotti, L., Negri, A., & Ostriker, J. P. 2018, ApJ, 856, 115, doi: 10.3847/1538-4357/aaae07
Pellegrini, S., Venturi, T., Comastri, A., et al. 2003, ApJ, 585, 677, doi: 10.1086/346184
Pence, W. D. 1986, ApJ, 310, 597, doi: 10.1086/164712
Perley, R., Napier, P., Jackson, J., et al. 2009, IEEE Proceedings, 97, 1448, doi: 10.1109/JPROC.2009.2015470
Perley, R. A., & Butler, B. J. 2013, ApJS, 204, 19, doi: 10.1088/0067-0049/204/2/19
Perley, R. A., Chandler, C. J., Butler, B. J., & Wrobel, J. M. 2011, ApJ, 739, L1, doi: 10.1088/2041-8205/739/1/L1
Perley, R. A., Willis, A. G., & Scott, J. S. 1979, Nature, 281, 437, doi: 10.1038/281437a0
Perucho, M., & Martí, J. M. 2007, MNRAS, 382, 526, doi: 10.1111/j.1365-2966.2007.12454.x
Peterson, J. R., & Fabian, A. C. 2006, Phys. Rep., 427, 1, doi: 10.1016/j.physrep.2005.12.007
Peterson, J. R., Paerels, F. B. S., Kaastra, J. S., et al. 2001, A&A, 365, L104
Pizzolato, F., & Soker, N. 2005, ApJ, 632, 821, doi: 10.1086/444344
Planck Collaboration, Ade, P. A. R., Aghanim, N., et al. 2016, A&A, 594, A13, doi: 10.1051/0004-6361/201525830
Prandoni, I., Laing, R. A., de Ruiter, H. R., & Parma, P. 2010, A&A, 523, A38, doi: 10.1051/0004-6361/201015456
Rafferty, D. A., McNamara, B. R., & Nulsen, P. E. J. 2008, ApJ, 687, 899, doi: 10.1086/591240
Rafferty, D. A., McNamara, B. R., Nulsen, P. E. J., & Wise, M. W. 2006, ApJ, 652, 216, doi: 10.1086/507672
Rajpurohit, K., Hoeft, M., van Weeren, R. J., et al. 2018, ApJ, 852, 65, doi: 10.3847/1538-4357/aa9f13
Randall, S., Nulsen, P., Forman, W. R., et al. 2008, ApJ, 688, 208, doi: 10.1086/592324
Randall, S. W., Jones, C., Kraft, R., Forman, W. R., & O'Sullivan, E. 2009, ApJ, 696, 1431, doi: 10.1088/0004-637X/696/2/1431
Randall, S. W., Forman, W. R., Giacintucci, S., et al. 2011, ApJ, 726, 86, doi: 10.1088/0004-637X/726/2/86
Randall, S. W., Nulsen, P. E. J., Jones, C., et al. 2015, ApJ, 805, 112, doi: 10.1088/0004-637X/805/2/112
Rau, U., & Cornwell, T. J. 2011, A&A, 532, A71, doi: 10.1051/0004-6361/201117104
Reid, N., Boisson, C., & Sansom, A. E. 1994, MNRAS, 269, 713, doi: 10.1093/mnras/269.3.713
Ruffa, I., Prandoni, I., Laing, R. A., et al. 2019, MNRAS, 484, 4239, doi: 10.1093/mnras/stz255
Russell, H. R., Sanders, J. S., & Fabian, A. C. 2008, MNRAS, 390, 1207, doi: 10.1111/j.1365-2966.2008.13823.x
Russell, H. R., McNamara, B. R., Fabian, A. C., et al. 2019, MNRAS, 490, 3025, doi: 10.1093/mnras/stz2719
Rybicki, G. B., & Lightman, A. P. 1979, Radiative processes in astrophysics
Ryle, M. 1972, Nature, 239, 435, doi: 10.1038/239435a0

Sabater, J., Best, P. N., Hardcastle, M. J., et al. 2019, A&A, 622, A17, doi: 10.1051/0004-6361/201833883
Sage, L. J., & Galletta, G. 1993, ApJ, 419, 544, doi: 10.1086/173507
Sage, L. J., & Wrobel, J. M. 1989, ApJ, 344, 204, doi: 10.1086/167789
Saglia, R. P., Opitsch, M., Erwin, P., et al. 2016, ApJ, 818, 47, doi: 10.3847/0004-637X/818/1/47
Sahu, S. K., Pandey, S. K., Chaware, L., & Pand ge, M. B. 2016, in From Interstellar Clouds to Star-Forming Galaxies: Universal Processes?, ed. P. Jablonka, P. André, & F. van der Tak, Vol. 315, E70, doi: 10.1017/S1743921316008322
Saikia, D. J., & Jamrozy, M. 2009, Bulletin of the Astronomical Society of India, 37, 63. https://arxiv.org/abs/1002.1841
Salim, S., Rich, R. M., Charlot, S., et al. 2007, ApJS, 173, 267, doi: 10.1086/519218
Sanders, J. S., Fabian, A. C., Taylor, G. B., et al. 2016, MNRAS, 457, 82, doi: 10.1093/mnras/stv2972
Santos, W. A., Mendes de Oliveira, C., & Sodré, Laerte, J. 2007, AJ, 134, 1551, doi: 10.1086/521341
Satyapal, S., Dudik, R. P., O'Halloran, B., & Gliozzi, M. 2005, ApJ, 633, 86, doi: 10.1086/449304
Schellenberger, G., David, L. P., Vrtilek, J., et al. 2020a, arXiv e-prints, arXiv:2010.13804. https://arxiv.org/abs/2010.13804
Schellenberger, G., Vrtilek, J. M., David, L., et al. 2017, ApJ, 845, 84, doi: 10.3847/1538-4357/aa7f2e
Schellenberger, G., David, L. P., Vrtilek, J., et al. 2020b, ApJ, 894, 72, doi: 10.3847/1538-4357/ab879c
Schmitt, H. R., Pringle, J. E., Clarke, C. J., & Kinney, A. L. 2002, ApJ, 575, 150, doi: 10.1086/341211
Schure, K. M., Kosenko, D., Kaastra, J. S., Keppens, R., & Vink, J. 2009, A&A, 508, 751, doi: 10.1051/0004-6361/200912495
Schweizer, F. 1980, ApJ, 237, 303, doi: 10.1086/157870
Shabala, S. S., & Godfrey, L. E. H. 2013, ApJ, 769, 129, doi: 10.1088/0004-637X/769/2/129
Sharma, P., McCourt, M., Quataert, E., & Parrish, I. J. 2012, MNRAS, 420, 3174, doi: 10.1111/j.1365-2966.2011.20246.x
Shin, J., Woo, J.-H., & Mulchaey, J. S. 2016, ApJS, 227, 31, doi: 10.3847/1538-4365/227/2/31
Shurkin, K., Dunn, R. J. H., Gentile, G., Taylor, G. B., & Allen, S. W. 2008, MNRAS, 383, 923, doi: 10.1111/j.1365-2966.2007.12651.x
Siebert, J., Brinkmann, W., Morganti, R., et al. 1996, MNRAS, 279, 1331, doi: 10.1093/mnras/279.4.1331
Simionescu, A., Tremblay, G., Werner, N., et al. 2018, MNRAS, 475, 3004, doi: 10.1093/mnras/sty047
Singal, A. K. 1993, MNRAS, 263, 139, doi: 10.1093/mnras/263.1.139
Singh, K. P., Bhat, P. N., Prabhu, T. P., & Kembhavi, A. K. 1995, A&A, 302, 658
Sivakoff, G. R., Sarazin, C. L., & Carlin, J. L. 2004, ApJ, 617, 262, doi: 10.1086/425244
Skipper, C. J., & Browne, I. W. A. 2018, MNRAS, 475, 5179, doi: 10.1093/mnras/sty114
Smith, M. W. L., Gomez, H. L., Eales, S. A., et al. 2012, ApJ, 748, 123, doi: 10.1088/0004-637X/748/2/123
Smith, R. M., Martínez, V. J., Fernández-Soto, A., Ballesteros, F. J., & Ortiz-Gil, A. 2008, ApJ, 679, 420, doi: 10.1086/587454
Smith, R. M., Martínez, V. J., & Graham, M. J. 2004, ApJ, 617, 1017, doi: 10.1086/425890
Spavone, M., Iodice, E., Longo, G., Paolillo, M., & Sodani, S. 2006, A&A, 457, 493, doi: 10.1051/0004-6361:20065633
Stanger, V. J., & Warwick, R. S. 1986, MNRAS, 220, 363, doi: 10.1093/mnras/220.2.363
Storn, R. 1995, Technical report, International Computer Science Institute, 11. https://ci.nii.ac.jp/naid/20000924911/en/
Su, Y., Nulsen, P. E. J., Kraft, R. P., et al. 2017, ApJ, 851, 69, doi: 10.3847/1538-4357/aa989e
Su, Y., Kraft, R. P., Nulsen, P. E. J., et al. 2019, AJ, 158, 6, doi: 10.3847/1538-3881/ab1d51
Subrahmanyan, R., Beasley, A. J., Goss, W. M., Golap, K., & Hunstead, R. W. 2003, AJ, 125, 1095, doi: 10.1086/367797
Sun, M. 2009, ApJ, 704, 1586, doi: 10.1088/0004-637X/704/2/1586
Sun, M., Jerius, D., & Jones, C. 2005a, ApJ, 633, 165, doi: 10.1086/452620
Sun, M., Vikhlinin, A., Forman, W., Jones, C., & Murray, S. S. 2005b, ApJ, 619, 169, doi: 10.1086/425298
Tang, H., Scaife, A. M. M., Wong, O. I., et al. 2020, MNRAS, 499, 68, doi: 10.1093/mnras/staa2805
Tang, Y., Gu, Q. S., Huang, J. S., & Wang, Y. P. 2009, MNRAS, 397, 1966, doi: 10.1111/j.1365-2966.2009.15038.x
Taylor, G. B. 1996, ApJ, 470, 394, doi: 10.1086/177874
Taylor, G. B., Fabian, A. C., & Allen, S. W. 2002, MNRAS, 334, 769, doi: 10.1046/j.1365-8711.2002.05555.x
Taylor, G. B., Sanders, J. S., Fabian, A. C., & Allen, S. W. 2006, MNRAS, 365, 705, doi: 10.1111/j.1365-2966.2005.09705.x
Temi, P., Amblard, A., Gitti, M., et al. 2018, ApJ, 858, 17, doi: 10.3847/1538-4357/aab9b0
Temi, P., Brighenti, F., & Mathews, W. G. 2007a, ApJ, 660, 1215, doi: 10.1086/513690
—. 2007b, ApJ, 666, 222, doi: 10.1086/520123
—. 2009, ApJ, 707, 890, doi: 10.1088/0004-637X/707/2/890
Temi, P., Mathews, W. G., Brighenti, F., & Bregman, J. D. 2003, ApJ, 585, L121, doi: 10.1086/374326
Thomas, D., Greggio, L., & Bender, R. 1999, MNRAS, 302, 537, doi: 10.1046/j.1365-8711.1999.02138.x
Thomas, D., Maraston, C., & Bender, R. 2002, Reviews in Modern Astronomy, 15, 219
Thomas, D., Maraston, C., Schawinski, K., Sarzi, M., & Silk, J. 2010, MNRAS, 404, 1775, doi: 10.1111/j.1365-2966.2010.16427.x
Thorne, K. S. 1994, Black holes and time warps: Einstein's outrageous legacy
Tremblay, G. R., Quillen, A. C., Floyd, D. J. E., et al. 2006, ApJ, 643, 101, doi: 10.1086/502643
Tremmel, M., Quinn, T. R., Ricarte, A., et al. 2019, MNRAS, 483, 3336, doi: 10.1093/mnras/sty3336
Trinchieri, G., & Goudfrooij, P. 2002, A&A, 386, 472, doi: 10.1051/0004-6361:20020311
Urban, O., Werner, N., Allen, S. W., Simionescu, A., & Mantz, A. 2017, MNRAS, 470, 4583, doi: 10.1093/mnras/stx1542
Urry, C. M., & Padovani, P. 1995, PASP, 107, 803, doi: 10.1086/133630
Valluri, M., & Anupama, G. C. 1996, AJ, 112, 1390, doi: 10.1086/118106
van Cittert, P. H. 1934, Physica, 1, 201, doi: 10.1016/S0031-8914(34)90026-4
Venkatesan, T. C. A., Batuski, D. J., Hanisch, R. J., & Burns, J. O. 1994, ApJ, 436, 67, doi: 10.1086/174881

Verdoes Kleijn, G. A., Baum, S. A., de Zeeuw, P. T., & O'Dea, C. P. 1999, AJ, 118, 2592, doi: 10.1086/301135
Verdoes Kleijn, G. A., & de Zeeuw, P. T. 2005, A&A, 435, 43, doi: 10.1051/0004-6361:20042271
Voit, G. M. 2018, ApJ, 868, 102, doi: 10.3847/1538-4357/aae8e2
Voit, G. M., Bryan, G. L., Balogh, M. L., & Bower, R. G. 2002, ApJ, 576, 601, doi: 10.1086/341864
Voit, G. M., Donahue, M., Bryan, G. L., & McDonald, M. 2015a, Nature, 519, 203, doi: 10.1038/nature14167
Voit, G. M., Donahue, M., O'Shea, B. W., et al. 2015b, ApJ, 803, L21, doi: 10.1088/2041-8205/803/2/L21
Voit, G. M., Kay, S. T., & Bryan, G. L. 2005, MNRAS, 364, 909, doi: 10.1111/j.1365-2966.2005.09621.x
Voit, G. M., Babul, A., Babyk, I., et al. 2019, arXiv e-prints, arXiv:1903.11212. https://arxiv.org/abs/1903.11212
Vrtilek, J. M., Grego, L., David, L. P., et al. 2002, in APS April Meeting Abstracts, APS Meeting Abstracts, B17.107
Ward, C., Gezari, S., Frederick, S., et al. 2021, ApJ, 913, 102, doi: 10.3847/1538-4357/abf246
Welch, G. A., Sage, L. J., & Young, L. M. 2010, ApJ, 725, 100, doi: 10.1088/0004-637X/725/1/100
Werk, J. K., Prochaska, J. X., Tumlinson, J., et al. 2014, ApJ, 792, 8, doi: 10.1088/0004-637X/792/1/8
Werner, N., Allen, S. W., & Simionescu, A. 2012, MNRAS, 425, 2731, doi: 10.1111/j.1365-2966.2012.21245.x
Werner, N., McNamara, B. R., Churazov, E., & Scannapieco, E. 2018, arXiv e-prints. https://arxiv.org/abs/1811.05004
—. 2019, Space Sci. Rev., 215, 5, doi: 10.1007/s11214-018-0571-9
Werner, N., & Mernier, F. 2020, Hot Atmospheres of Galaxies, Groups, and Clusters of Galaxies, 279–310, doi: 10.1007/978-3-030-38509-5_10
Werner, N., Oonk, J. B. R., Sun, M., et al. 2014, MNRAS, 439, 2291, doi: 10.1093/mnras/stu006
White, D. A., Fabian, A. C., Johnstone, R. M., Mushotzky, R. F., & Arnaud, K. A. 1991, MNRAS, 252, 72
Wiklind, T., Combes, F., & Henkel, C. 1995, A&A, 297, 643
Willis, A. G., Strom, R. G., Bridle, A. H., & Fomalont, E. B. 1981, A&A, 95, 250
Wilson, C. D., Cridland, A., Foyle, K., et al. 2013, ApJ, 776, L30, doi: 10.1088/2041-8205/776/2/L30
Wolter, A., Esposito, P., Mapelli, M., Pizzolato, F., & Ripamonti, E. 2015, MNRAS, 448, 781, doi: 10.1093/mnras/stv054
Wood, R. A., Jones, C., Machacek, M. E., et al. 2017, ApJ, 847, 79, doi: 10.3847/1538-4357/aa8723
Worrall, D. M., Birkinshaw, M., & Hardcastle, M. J. 2003, MNRAS, 343, L73, doi: 10.1046/j.1365-8711.2003.06945.x
Worrall, D. M., Birkinshaw, M., Laing, R. A., Cotton, W. D., & Bridle, A. H. 2007, MNRAS, 380, 2, doi: 10.1111/j.1365-2966.2007.11998.x
Worrall, D. M., Birkinshaw, M., O'Sullivan, E., et al. 2010, MNRAS, 408, 701, doi: 10.1111/j.1365-2966.2010.17162.x
Xilouris, E. M., Georgakakis, A. E., Misiriotis, A., & Charmandaris, V. 2004, MNRAS, 355, 57, doi: 10.1111/j.1365-2966.2004.08289.x
Yi, S. K., Yoon, S. J., Kaviraj, S., et al. 2005, ApJ, 619, L111, doi: 10.1086/422811
Young, A. J., Wilson, A. S., & Mundell, C. G. 2002, ApJ, 579, 560, doi: 10.1086/342918
Young, L. M., Bureau, M., Davis, T. A., et al. 2011, MNRAS, 414, 940, doi: 10.1111/j.1365-2966.2011.18561.x
Zernike, F. 1938, Physica, 5, 785, doi: 10.1016/S0031-8914(38)80203-2
Zezas, A., Birkinshaw, M., Worrall, D. M., Peters, A., & Fabbiano, G. 2005, ApJ, 627, 711, doi: 10.1086/430044